Studies on Strong Correlation Effects in Half-Metallic Ferromagnets based on Spin-Resolved Electronic Structure

2019, March

Hirokazu Fujiwara

Graduate School of Natural Science and Technology
(Doctor’s Course)

OKAYAMA UNIVERSITY

ABSTRACT

This work investigated the nature of thermal spin depolarization in half-metallic ferromagnets based on electronic structure by means of spin-resolved and angle-resolved photoemission spectroscopy. Although half-metal-based magnetic tunneling junctions have been expected to be used for spintronics devices such as magnetoresistive random access memories, they have a critical issue: The tunneling magnetoresistance ratios, related to spin polarization, decrease rapidly with increasing temperatures, which cannot be explained from the macroscopic magnetization behaviors alone. There have been two proposed mechanisms of the thermal spin depolarization: interfacial effects and correlation effects. The interfacial effects have been investigated from both of theoretical and experimental aspects, while the correlation effects have been studied almost only from the theoretical aspect. The motivation of the present work is to reveal the contribution of the correlation effects to the thermal spin depolarization, through the electronic-structure investigations on candidates for half-metals, CrO_2 and CoS_2.

We have performed bulk-sensitive spin-resolved photoemission spectroscopy in order to clarify the intrinsic spin-resolved electronic states of half-metallic ferromagnet CrO_2. We used CrO_2 epitaxial films on $TiO_2(100)$, which shows a peak at 1 eV with a clear Fermi edge, consistent with the bulk- sensitive PES spectrum for CrO_2. In spin-resolved spectra at 40K, while the Fermi edge was observed in the spin up (majority spin) state, no states at the Fermi level (E_F) with an energy gap of 0.5 eV below E_F were observed in the spin down (minority spin) state. At 300 K, the gap in the spin down state closes. These results are consistent with resistivity measurements and magnetization curves of the fabricated CrO_2 film, constituting spectroscopic evidence for the half-metallicity of CrO_2 at low temperature and reducing the spin polarization at room temperature. Furthermore, from comparison of the spin-resolved photoemission spectra with the densities of states calculated within local spin density approximation with various U values, we revealed that the electronic correlation U must be considered in order to discuss the electronic states of CrO_2. These results also indicate that bulk-sensitive spin-resolved photoemission spectroscopy is a very powerful experimental tool to investigate intrinsic spin- resolved electronic states of half-metallic ferromagnets.

We have investigated the electronic states with a focus on non-quasiparticle (NQP) states derived from electron–magnon interactions. At 80 K, peculiar spin depolarization was observed at E_F, which is supported by theoretical calculations predicting NQP states. This suggests the

possible appearance of NQP states in CrO_2. Furthermore, in order to validate the existence of NQP states, we perform high-resolution spin-resolved photoemission spectroscopy measurements. We observe a distinct minority spin state near E_F and a corresponding depolarization that seldom contributes to demagnetization. The origin of this depolarization has been identified as the many-body effect characteristic of half-metallic ferromagnets, from comparison with electronic structures calculated within a dynamical mean field theory. Our investigation opens an experimental field of itinerant ferromagnetic physics focusing on phenomena with sub-meV energy scale.

Also, in order to reveal the half-metallicity of CoS_2, the spin-dependent band structure of CoS_2 being a candidate for a half-metallic ferromagnet was investigated by both of spin- and angle-resolved photoemission spectroscopy and theoretical calculations. We determined the three-dimensional Fermi surface and the band structure which has minority spin bands just below E_F as well as dispersive majority spin bands. We found that the majority spin bands cross the Fermi level, while the minority spin bands are slightly occupied in the close vicinity of E_F, providing spectroscopic evidence for nearly half-metallicity of CoS_2. Although the majority spin e_g bands are in good agreement with a theoretical band structure in which amount of the exchange-splitting is reduced, the minority spin e_g bands cannot be explained in terms of its bandwidth. The deviation between experiment and theory suggests strongly an occurrence of an anomalously large spin-dependent electronic correlation effect. We also reports temperature-dependence of the electronic structure across the Curie temperature and discuss the mechanism of the demagnetization. From comparison of the results of the present study with those of a study on half-metal CrO_2, it has been shown that the spin-dependent electronic correlation plays a crucial role in realizing half-metallic electronic structure at finite temperatures.

This study revealed that the correlation effects characteristic of half-metals contribute the thermal spin depolarization observed in magnetic tunneling junctions, based on the spin-resolved electronic structures. These findings emphasize the importance of many-body physics in half-metals, in improving the spintronic-device performance.

ACKNOWLEDGEMENTS

During my graduate experience in Okayama, I have been fortunate to come across many people from various places. This dissertation would not have been possible without the help and sincere support from them.

First of all, I would like to express my sincere gratitude my supervisor, Prof. Takayoshi Yokoya, for his support and encouragement throughout my doctor course. He introduced me to spin-resolved and angle-resolved photoemission spectroscopy (SARPES). I really had fun with this experimental technique because I had been interested in *observing* spins and *feeling* phenomena of quantum physics. When I joined the laboratory, he gave me works on building the SARPES apparatus, which is a valuable experience for me. He also let me freely challenge various experiments (and I experienced many failures), by which I have enjoyed my doctor course life. He often cared about me when I was conducting experiments and when I was visited by a flood disaster taking place in West Japan in July, 2018. I would like to appreciate again his supports in various aspects of my study life.

I would like to thank Prof. Yuji Muraoka for his technical support for sample fabrication, his deep insight for the subject, and his thoughtful guidance for my study and my career which gives me supportive pushes in various scenes. He has also taught me fundamentals of way of scientific thinking, and how to make good presentations.

I am grateful to Dr. Takanori Wakita for his support for starting my study, namely, for building a vacuum chamber and fabricating and evaluating bismuth films. I also thank his technical support for photoemission and low energy electron diffraction experiments on CrO_2 films at BL-5 in Hiroshima Synchrotron Radiation Center, and for experiments at other facilities (Photon Factory (PF), SPring-8, Institute for Solid State Physics (ISSP) in The University of Tokyo etc.). Furthermore, I would like to thank his supports when I visited Universitá di Roma “La Sapienza”, eliminating the barrier of my overseas life.

I would like to sincerely thank Dr. Kensei Terashima for his powerful support for SARPES experiments, data analysis, band calculations, writing papers, making presentations, and fruitful discussion for SARPES data, which developed my skills and knowledge, and greatly improved my study. He also supported my overseas life during beamtimes of BESSY II (Germany), ALBA (Spain), and ESRF (France), and during my stay in Rome, which become amazing experience for me. I really respect him as a physicist and as a mentor.

I would like to thank Dr. Keiji Kosaka for installing a calculation program and for valuable discussion for theoretical calculations.

I am grateful to Prof. Shik Shin for coordinating my SARPES experiments at ISSP. For the SARPES experiments, I would like to also thank Dr. Koichiro Yaji, Dr. Ayumi Harasawa, and Dr. Kenta Kuroda for their arrangement and technical support of the experiments, which helped me conduct the SARPES experiments smoothly. In fact, lots of photoemission data in this dissertation were taken with their laser SARPES apparatus. Besides, I thank their insightful advices for my study and papers, as well as their sociable relationship with me. I would like to also thank Sachiko Shinei and the people at “Kyodo Riyou” section of ISSP for their support.

I would like to thank Prof. Naurang Lal Saini for his kind reception of me and giving me the opportunity for joining his XAFS experiments at ALBA and ESRF. I had great experiences and really had a nice time in Europe, including the hillwalking to Fort de la Bastille in Grenoble. I am grateful to Prof. Takashi Mizokawa and his students for conducting experiments at ALBA and ESRF together with me.

I would like to thank Taichi Okuda and Koji Miyamoto for fruitful discussion about determination of S_{eff}. I also thank Toyohiko Kinoshita for the valuable discussion for data of my SARPES spectra.

Collaborations were indispensable for the work in this dissertation. In order to reliable photoemission measurements, high quality samples from Dr. Atsushi Teruya, Dr. Masashi Kakihana, Prof. Masato Hedo, Prof. Takao Nakama, and Prof. Yoshichika Ōnuki were very important. I am grateful to their kindness, cooperation, and guidance.

The collaboration with Dr. M. Minohara, Dr. Koji Horiba and Prof. Hiroshi Kumigashira was crucial to perform $h\nu$-dependent ARPES study at BL2A and BL28A in PF. I would like to also thank them for providing manganite ($La_xSr_{1-x}MnO_3$) samples.

I would like to thank Dr. Nayuta Takemori and Prof. Harald O. Jeschke for calculating electronic structure of CoS_2 and for their valuable discussion.

I am grateful to Dr. Kaya Kobayashi for providing $Nb_xBi_2Se_3$ samples. I would like to thank Dr. Hiroto Adachi, Dr. Seiichiro Onari, Prof. Masanori Ichioka, Prof. Naoshi Ikeda, Dr. Jun Kano, and Prof. Kozo Okada for their valuable discussion. I also thank Dr. T. Kambe, Prof. T. C. Kobayashi, and their students for help with the magnetization measurements.

I would like to thank my colleagues at Okayama University for the great experiences I shared with them. My special thanks go to Dr. Masanori Sunagawa for teaching me literacy of photoemission spectroscopy studies, and giving his grateful help. I am also grateful to Tomoko

Kittaka, Makoto Ogata, Yuka Matsuura, and Fumiya Yoshii for their technical support of synthesis of films, x-ray diffraction, electrical resistivity, and magnetization measurements. I would like to thank Seiko Inubushi, Takahiro Hamada, Taihei Jabuchi, Junki Sonoyama, Aya Takeda, Takanobu Nagayama, Tetsushi Fukura, Yuko Yano, Wataru Hosoda, Noriyuki Kataoka for their support for my photoemission experiments. I would like to also thank Yuki Suga, Misaki Kameoka, Daiki Yoshinaka, Takumi Taniguchi, Takumi Kawahara, and Yuki Fukuda for their help. I would like to thank Yayoi Kusano, Miwako Kakae, and Hiroko Asano for their administrative assistance (particularly procedures for overseas travels).

It is my greatest honor to thank my private friends, who have continuously supported and encouraged me throughout my life, and I would not have been able to accomplish this work without their presence. My special thanks go to Ryo Kataoka, Kohei Kawahara, Koudai Ono-Tanaka, Kai Taniuchi, Tomomi Nakakiya-Sakamoto, and their families. I must mention the exciting times with the members of Liners also.

On July 7th, 2018, many people including me were visited by a flood disaster taking place in Mabi-cho, Okayama, which made me suspend my research for a month. However, I would like to emphasize that I was able to return to my study at most after one month thanks to my relatives and volunteers. I would like to also thank Harada’s family and Hiroko Asano for their support. I am grateful to the government of Japan and the local government of Kurashiki city for their financial support for the disaster.

This work is supported by Research Fellowships of the Japan Society for the Promotion of Science (JSPS) for Young Scientists (DC1), and a Grant-in-Aid for JSPS Fellows (No. 16J03208) from the Ministry of Education, Culture, Sports, Science and Technology of Japan (MEXT). The laser-based SRPES experiments were conducted at ISSP with the approval of ISSP as the joint research. Parts of the ARPES experiments were performed under the Photon Factory Proposal No. 2018G127. This work is partially supported by the Motizuki Fund of Yukawa Memorial Foundation.

Lastly, I would like to express my sincere gratitude to my family: My brothers and mother. They have continuously supported me throughout my life. As all of my accomplishments would not have been possible without their supports, I dedicate this dissertation to my family.

And I dedicate this thesis to my late father.

CONTENTS

LIST OF ABBREVIATIONS AND SYMBOLS

AES	Auger electron spectroscopy
ARPES	angle-resolved photoemission spectroscopy
CVD	chemical vapor deposition
dHvA	de Haas–van Alphen
DMFT	dynamical mean-field theory
DOS	density of state
EDC	energy distribution curve
E_{F}	Fermi level
E_{k}	kinetic energy
FET	field effect transistor
FOM	figure of merit
FS	Fermi surface
GGA	generalized gradient approximation
GMR	giant-magnetoresistnce
HAXPES	hard x-ray photoemission spectroscopy
HDD	hard disc drive
HMF	half-metallic ferromagnet
ISSP	Institute for Solid State Physics
k_{F}	Fermi wave vector
LDA	local-density approximation
LEED	low-energy electron diffraction
LSDA	local spin-density approximation
MCP	multi-channel plate
MDC	momentum distribution curve
MRAM	magnetoresistive random access memory
MTJ	magnetic tunneling junction
NQP	non-quasiparticle
PCAR	point-contact Andreev reflection

PES	photoemission spectroscopy
PF	Photon Factory
SARPES	spin-resolved and angle-resolved photoemission spectroscopy
S_{eff}	effective Sherman function
SOC	spin-orbit coupling
SPLEED	spin-polarized low-energy electron diffraction
SQUID	superconducting quantum interference device
SRPES	spin-resolved photoemission spectroscopy
STT	spin transfer torque
TMR	tunneling magnetoresistance
UHV	ultra-high vacuum
VLEED	very-low-energy electron diffraction
VUV	vacuum ultraviolet
XMCD	x-ray magnetic circular dichroism

CHAPTER 1. INTRODUCTION

1.1 Spintronics

It has been predicted that the end of Moore's law stating that the number of transistors on a microprocessor chip will double every two years would happen in the early 2020s.[1] As one of “More than Moore” strategy, spintronics has been a promising technique. Spintronics is a multidisciplinary field whose central theme is the active manipulation of spin degrees of freedom in solid-state systems [2]. By giant-magnetoresistance (GMR) effect [3], of which the discovery was awarded Nobel Prize for Physics in 2007, and tunneling magnetoresistance (TMR) effect [4], memory capacity of the hard disc drives (HDDs) has been improved dramatically. This has been supporting the development of advancement of the highly information-based society.

Nevertheless, there are also a lot of potential spintronics devices which has not yet yielded practical applications. One of the devices is a magnetoresistive random access memories (MRAMs) based on magnetic tunneling junction (MTJ).[5,6] The structure is shown in Fig. 1.2(a). MRAM has a free magnetic layer as the information storage part. Therefore, MRAM has big advantages: nonvolatile, highly integrated, unlimited read and write endurance, high speed; from the feature, MRAM would be used as a promising universal memory doubled as a storage device. For scalability beyond 30 nm feature dimension, spin transfer torque (STT) and perpendicular MTJ techniques have been developed, which enable us to switch the direction of spins of MTJ by pass a spin-polarized current [7]. By these techniques, in 2016, 4Gbit density STT-MRAM was achieved by a research group constituted by SK Hynix Inc. and Toshiba Electronics Korea Corporation[8]. This is great progress for realizing a *normally-off computer* which turns off at any time when not in use off but operates instantly with full performance when needed, which provides low power innovation indispensable for sustainability [9].

The spin-polarized field effect transistor (FET) proposed by Datta and Das is also a promising device based on spintronics [10–12]. The source and the drain are ferromagnets acting as the injector and detector of the electron spin. The drain injects electrons with spins parallel to the transport direction. The electrons are transported ballistically through the channel. When they arrive at the drain, their spin is detected. In a simplified picture, the electron can enter the drain (ON) if its spin points in the same direction as the spin of the drain. Otherwise it is scattered away (OFF). The role of the gate is to generate an effective magnetic field, arising

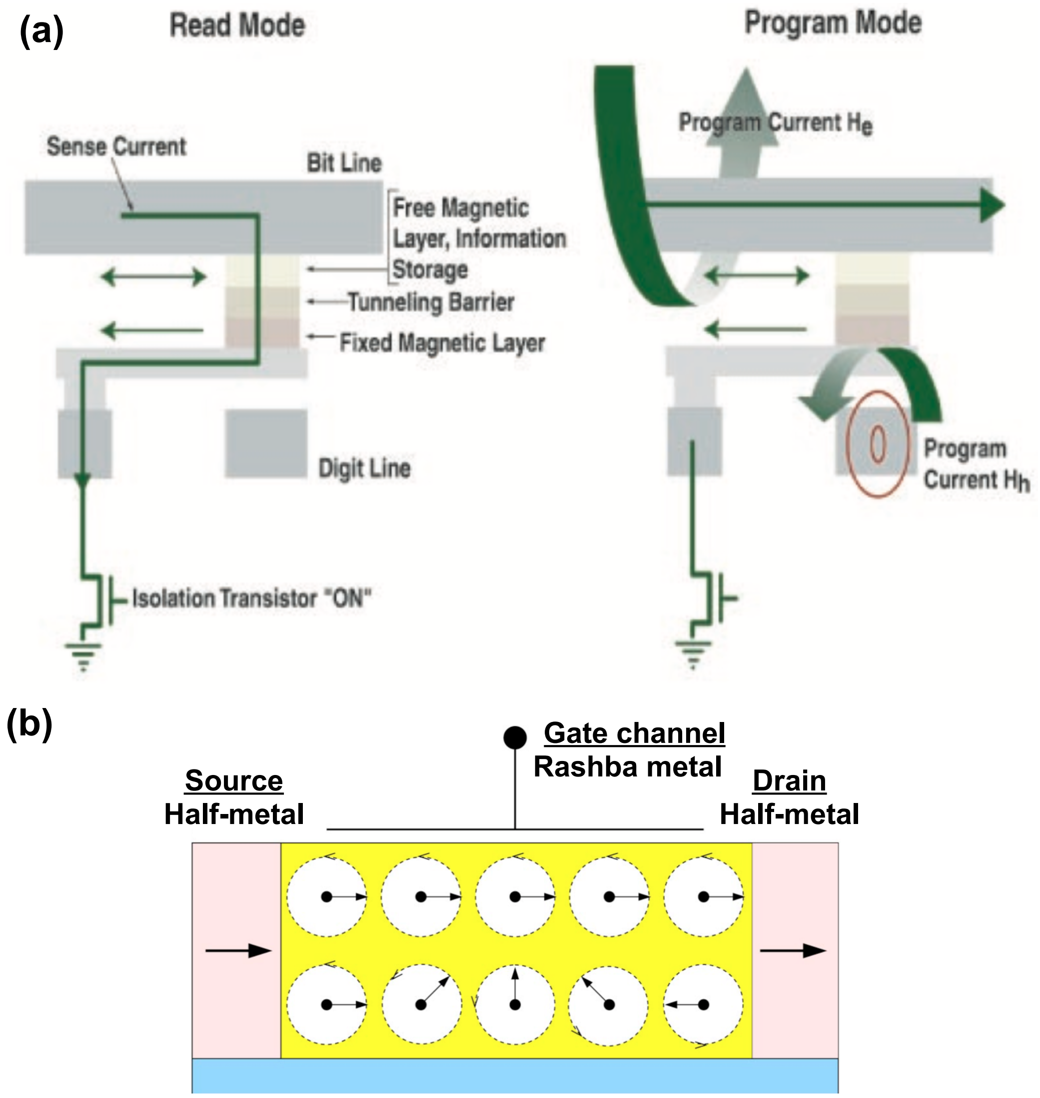

Fig. 1.1. (a) Scheme of the MRAM. Taken from [11]. (b) Scheme of the Datta-Das spin-polarized FET. Taken from [12].

from the spin-orbit coupling (SOC) in the substrate material, from the confinement geometry of the transport channel, and the electrostatic potential of the gate. This effective magnetic field causes the electron spins to process. By modifying the voltage, one can cause the precession to lead to either parallel or antiparallel electron spin at the drain, effectively controlling the current.

For the realization of the spin-polarized FET, we need mainly two materials: (i) Metals with large SOC and (ii) Ferromagnetic metals with completely spin-polarized conduction electrons as the spin injector and the spin detector. As large-SOC materials, heavy semimetals such as Bi and Sb[13–16], semiconductors such as InAs and BiTeI [17–20], and topological insulators such as Bi_2Se_3 [22,23] have been strenuously investigated, particularly for the last few decades. On the other hand, as the completely spin-polarized materials, half-metallic ferromagnets have

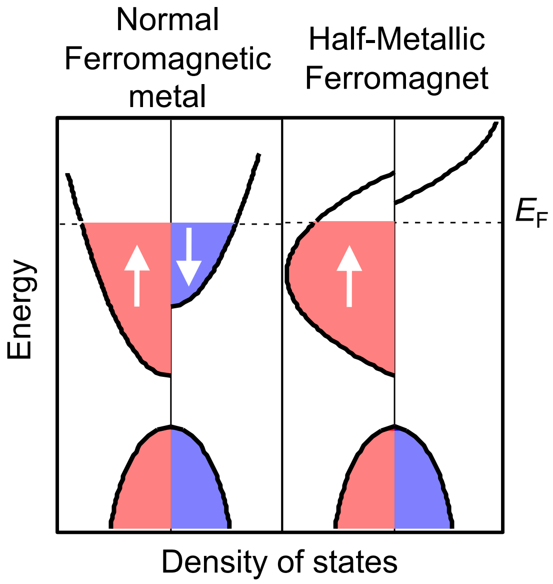

Fig. 1.2. Schematic diagram of electronic states of a normal ferromagnetic metal and a half-metallic ferromagnet.

been investigated [11,12,23–27]. Half-metallic ferromagnets have a metallic band structure with an energy gap at the Fermi level (E_F) in either one of electronic spin states, as shown in Fig. 1.2. This is ideal characteristics of spin injectors and spin detectors. However, in the half-metal-based MTJs, the TMR ratio drops exponentially with increasing temperatures, which does not obey the temperature dependence of macroscopic magnetization of the half-metals [28–32]. This mysterious behavior has prevented from the practical applications of the half-metal-based MTJ for the potential spintronics devices.

1.2 Half-Metallic Ferromagnets

1.2.1 Brief Introduction

Although nickel and cobalt metals, which are normal ferromagnetic metals, have fully spin-polarized *d*-bands, the Fermi level also crosses the unpolarized 4*s* band. On the other hand, half-metallic ferromagnets have no spin-unpolarized band crossing E_F. Half-metallic ferromagnetism, in which it is a metal with a Fermi surface only for electrons of one spin, was originally predicted for a half Heusler alloy NiMnSb by Groot *et al.* in 1983 [23]. Since then, half-metallic ferromagnetism has been demonstrated (theoretically and experimentally) for various systems: Full and half Heusler alloys (FeMnSb, Co_2MnSi etc.)[33–38], transition metal oxides (CrO_2 [39–44], normal-, double-, and quadruple perovskite oxides [45–49], magnetite [50–53] etc.), transition metal sulfides (CoS_2 [54–56], $Fe_{1-x}Co_xS_2$ [57–60], $Mn(Cr,V)S_4$ [61,62]), zinc-blend-structure materials (CrAs, CrSb, CaC, SrC etc.)[63–68], organic materials [69,70],

Table 1.1. Summary of the classification of half-metals by Coey *et al.* [25].

Type	Density of states	Conductivity	Majority spin electrons at E_F	Minority spin electrons at E_F
IA	Half-metal	Metallic	Itinerant	None
IB	Half-metal	Metallic	None	Itinerant
IIA	Half-metal	Nonmetallic	Localized	None
IIB	Half-metal	Nonmetallic	None	Localized
IIIA	Metal	Metallic	Itinerant	Localized
IIIB	Metal	Metallic	Localized	Itinerant

and two-dimensional materials (graphene, carbon nitride etc.) [71–74]. Experimentally, the highest spin polarization has been obtained for CrO_2 by both of point-contact Andreev reflection and spin-resolved photoemission spectroscopy. Although Heusler alloys have been investigated for practical applications because of its high Curie temperatures (for instance, T_C = 985 K for Co_2MnSi) [75], they show approximately 60% spin polarization even at low temperatures (below 4.2 K) [76–78]. Through the studies on Heusler alloys, it has been revealed that structural defects break the half-metallicity in Heusler alloys in terms of the electronic structure [6,35].

Half-metallic ferromagnets have been classified by Coey *et al.* as summarized in Table 1.1 [25,26]. Two situations where there is a single spin orientation at E_F are illustrated in Figs. 1.3(a) and (b). In either case there is a spin gap $\Delta_\uparrow$ or $\Delta_\downarrow$, where the index ↑(↓) represents majority (minority) spin, and a smaller gap Δ_{st} for spin–flip excitations from E_F. Half-metallic ferromagnets where the *s* states are pushed above E_F by hybridization with the *p* states are type I_A when there are less than five *d* electrons, but of type I_B when there are more than five. CrO_2 is a type I_A half-metal with majority spin electrons of mainly Cr t_{2g} character at E_F [39–41]. A type I_B half-metallic ferromagnet is double-perovskite oxide Sr_2FeMoO_6 [48], where the minority spin conduction electrons are mainly of Mo t_{2g} character.

Electrons in type II half-metals, lie in a band that is sufficiently narrow for them to be localized. The heavy carriers may form polarons and conduction is by hopping from one site to another with the same spin. Otherwise, the states in band tails can be localized by the presence of disorder. Magnetite Fe_3O_4 is a type II_B half-metal where minority spin electrons of Fe t_{2g} character hop among *B* sites in the spinel structure [26,79].

A third class of half-metals, known as the transport half-metals, have localized majority spin

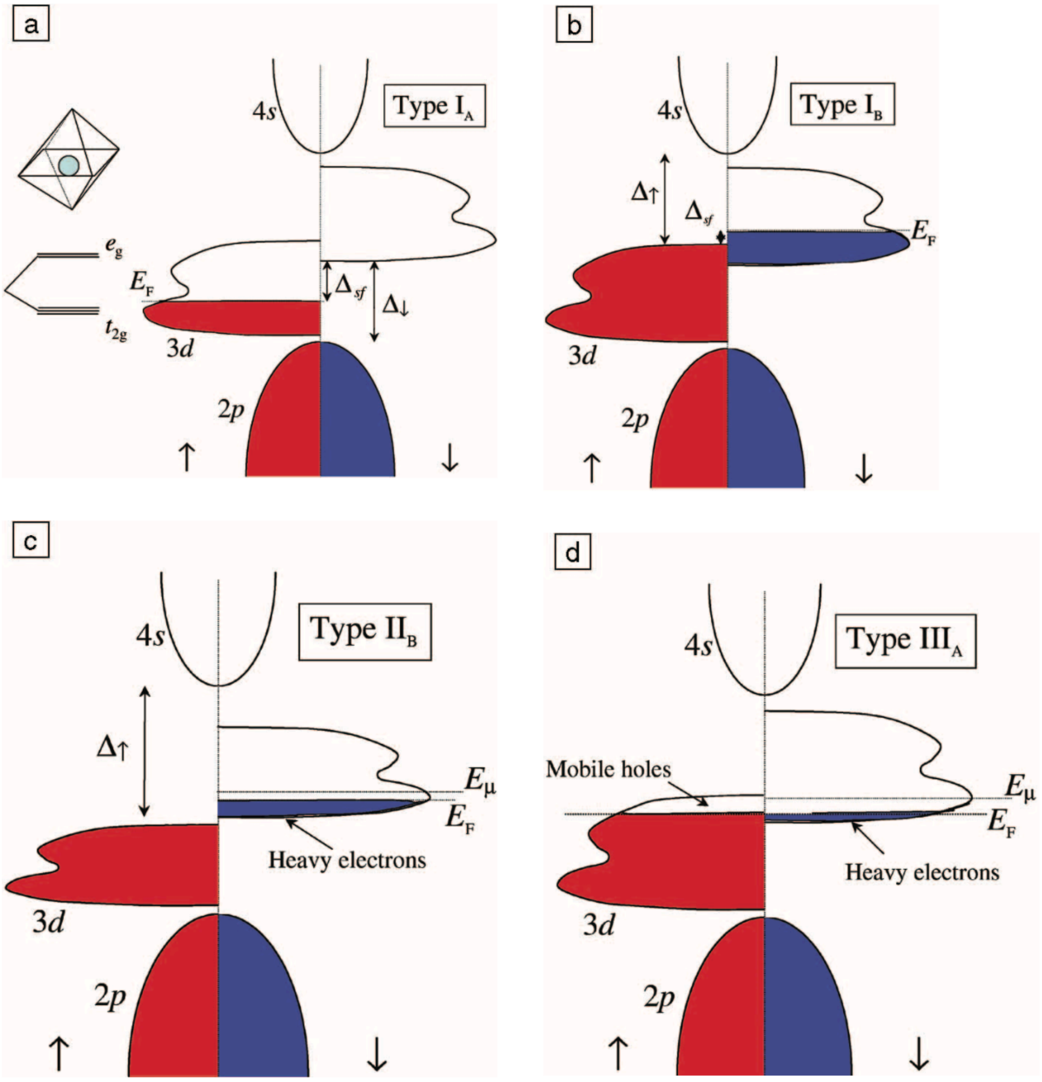

Fig. 1.3. Classification of half-metals. The diagrams show schematic densities of states for majority spin ↑ (red) and minority spin ↓ (blue) electrons. E_μ is the mobility edge energy, Δ is the gap for one electron spin, and Δ_{sf} is the spin-flip gap. (a) Type IA (e.g., CrO_2) and (b) Type IB (e.g., Sr_2FeMoO_6) half-metals have only ↑ or ↓ electrons at E_F, with a gap for the other spin direction. (c) Type II half-metals are similar to Type I, but have narrow bands where the electrons are localized, and conduction is by hopping; shown here is a Type IIB (e.g., Fe_3O_4). (d) Type III half-metals have a mixture of delocalized electrons with one spin direction and localized electrons with the other; shown here is a Type IIIA half-metal (e.g., $La_{0.7}Sr_{0.3}MnO_3$). Taken from [26].

carriers and delocalized minority spin carriers or *vice versa*. Although a density of states exists for both sub-bands at E_F, the carriers in one band have a much larger effective mass than those in the other. A schematic band structure of type IIIA is shown in Fig. 1.3(c). The heavy carriers give an activated conduction but they are short circuited by the light carriers which are metallic with resistivity given by Matthiessen's rule $\rho \sim \rho_0 + \rho(T)$. An example of type III$_A$ is the optimally doped manganite $La_{0.7}Sr_{0.3}MnO_3$, with mobile majority spin Mn e_g electrons and immobile minority spin Mn t_{2g} electrons at E_F.

Half-metallicity is not easy to detect experimentally. Unlike superconductors, metals, semiconductors, or insulators, there is no clear electrical signature. It is impractical to measure the intrinsic high-field susceptibility of a ferromagnet at low temperature sufficiently accurately to assert that it is zero. An indication of a type I or type II half-metal is metallic conduction in a solid with a spin moment at $T = 0$ which is precisely an integral number of Bohr magnetons per unit cell. In a stoichiometric compound, the number of electrons per unit cell $n = n^{\uparrow} + n^{\downarrow}$ is an integer. On account of the gap in one of the spin-polarized bands, $n^{\uparrow}$ or $n^{\downarrow}$ is also an integer. If both $n^{\uparrow}$ and $n^{\downarrow}$ are integers, the difference $n^{\uparrow} - n^{\downarrow}$, which is the spin moment in units of the Bohr magneton is also an integer. The integer spin moment criterion is a necessary but not a sufficient condition for half-metallicity, because spin–orbit coupling is neglected; it may destroy half-metallicity.

Detecting 100% spin polarization at E_F would rather provide the direct evidence for half-metallicity. The straightforward definition of spin polarization is

$$P_0 = \frac{N^{\uparrow} - N^{\downarrow}}{N^{\uparrow} + N^{\downarrow}} \tag{1.1}$$

where $N^{\uparrow(\downarrow)}$ are the density of states at E_F. However, in experiments involving ballistic or diffusive transport, the density of states must be weighted by the Fermi velocity of the electrons, v_F, or its square, respectively,

$$P_T = \frac{\langle N^{\uparrow} v_F^{\uparrow} \rangle - \langle N^{\downarrow} v_F^{\downarrow} \rangle}{\langle N^{\uparrow} v_F^{\uparrow} \rangle + \langle N^{\downarrow} v_F^{\downarrow} \rangle} \tag{1.2}$$

where the quantities with angle brackets represent $N^{\uparrow} v_F^{\uparrow}$ averaged for bands crossing E_F. By transport-based methods such as magnetotransport by MTJ and point-contact Andreev reflection (PCAR) measurement, P_T is dominantly observed, while P_0 can be directly observed just by SARPES.

Since SARPES can also observed energy band dispersions and Fermi surfaces for single-crystal samples, it can provide quite reliable evidence for the half-metallicity by determining whether the Fermi surface is constituted by electrons with one spin character or not. However it is not easy to demonstrate that there is really no Fermi surface with the minority spin character (for a type I_A half-metal) over the entire Brillouin zone. In order to observe the band dispersion

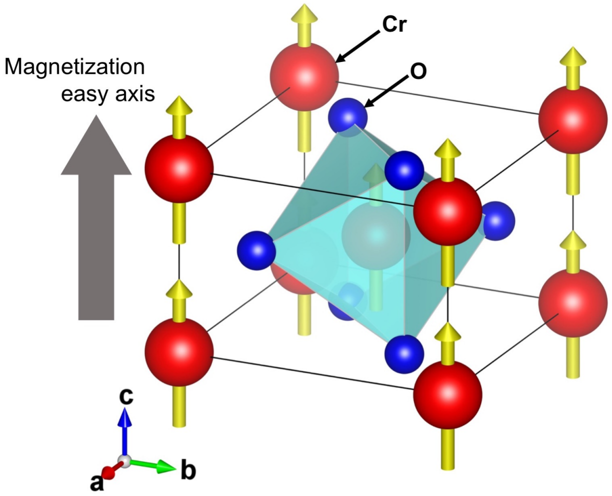

Fig. 1.4. Crystal structure of CrO_2 (Space group: $P4_2/mnm$). Yellow arrows represent magnetic moments of each Cr atom. Watery planes represent an octahedral structure formed by oxygen atoms surrounding a Cr atom.

over the entire Brillouin zone, SARPES measurements with wide momentum window have been daringly performed by using polycrystalline samples (or samples with polycrystalline surface).

1.2.2 CrO_2: Highly Spin-Polarized Half-Metal Candidate

Chromium dioxide (CrO_2) has a rutile-type crystal structure as shown in Fig. 1.4, and is the only binary oxide that is a ferromagnetic metal [80]. The half-metallicity of CrO_2 was predicted by Schwarz in 1986 by local-density approximation (LDA) calculations [39], as shown in Fig. 1.5.

The half-metallicity in CrO_2 has been explained as resulting from a self-doping effect and double-exchange interaction [40]. The self-doping effect arises as a result from negative charge-transfer gap. In general strongly correlated systems, there are two types of a band gap as shown in Fig. 1.6. One is the Mott-Hubbard gap, and another is the charge-transfer gap. The *d*-orbitals are relatively localized so that the Coulomb repulsion between *d*-electrons on the same site should be taken into account. Because of the repulsion, the band splitting whose energy is U is produced. If the band splitting corresponds to the band gap between valence and conduction bands, it is called Mott-Hubbard gap. Meanwhile, in some transition metal oxide insulators, the hybridization of oxygen *p*-electrons with transition metal *d*-electrons occurs and *p*-*d* hopping is allowed [81,82]. The charge excitations corresponding to a transfer of an electron from oxygen into a transition metal *d*-orbit need energy Δ. If $\Delta < U$, the band gap is called charge-transfer gap. In CrO_2, it is predicted $\Delta < 0$, namely *p*-band and *d*-band are mixing. Therefore

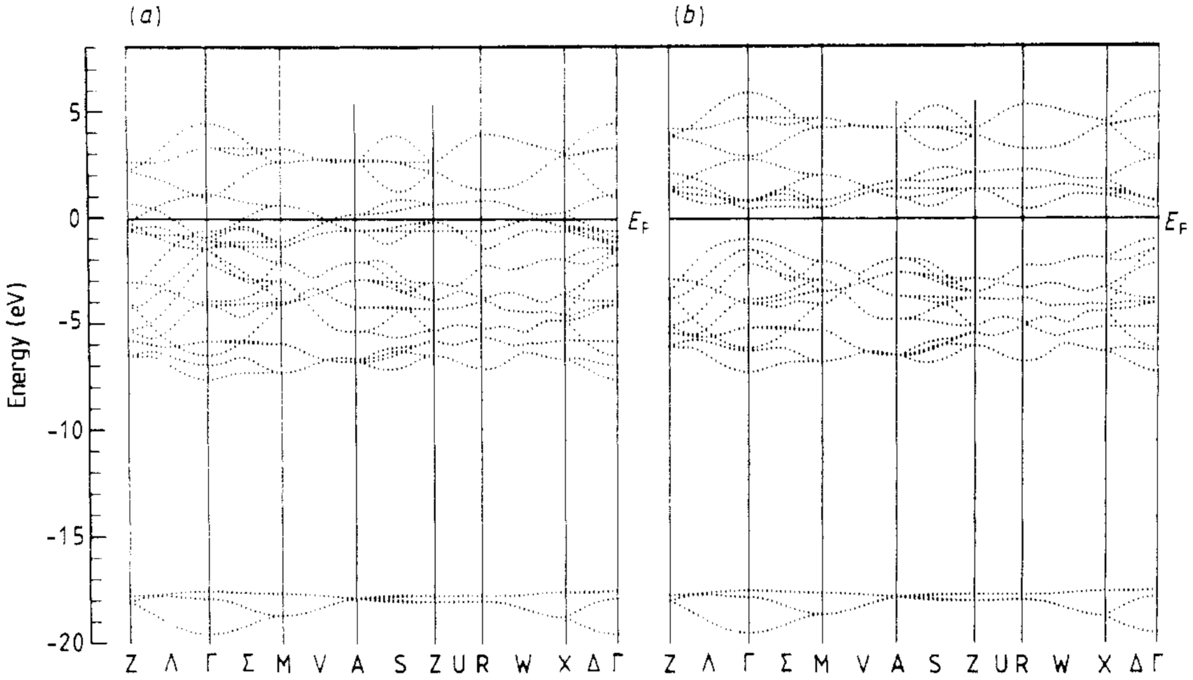

Fig. 1.5. Energy bands of CrO_2 for (a) majority-spin and (b) minority-spin electrons, calculated within LDA. Taken from [39].

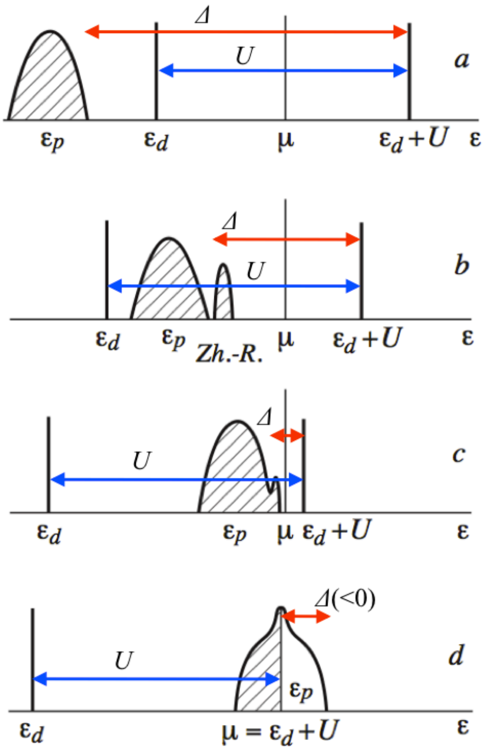

Fig. 1.6. Schematic illustration of electronic structure of strongly correlated materials. Taken from [81].

the ground state of *d*- and *p*-states is represented as following: $d^n + p^6 \rightarrow d^{n+1} + p^5$. This means that a hole, so-called “ligand hole”, is doped in an oxygen atom. This phenomenon is the self-doping effect playing a crucial role in the emergence of the metallic behavior of CrO_2[40].

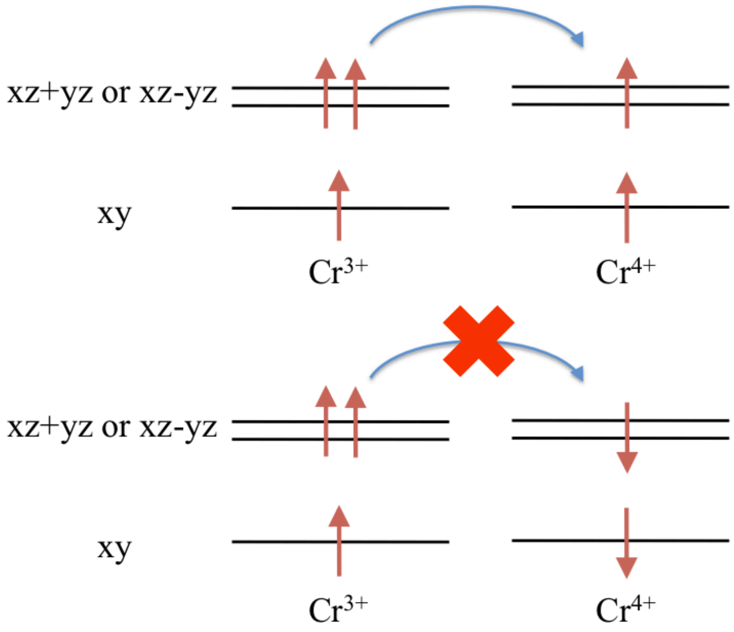

Fig. 1.7. Schematic view of the double exchange mechanism in CrO_2. Red arrows and black solid lines show the electron spins and the energy levels of Cr 3*d* (t_{2g}), respectively.

Additionally, it is predicted that the double exchange interaction is proposed as the origin of the ferromagnetic property in CrO_2 [40,83,84]. Figure 1.7 shows a schematic illustration of the double exchange model. CrO_2 has the rutile-type crystal structure, space group P^4/mnm, with a = 4.421 Å, c = 2.917 Å [85], so that the d-band splits into e_g and t_{2g} due to a crystal field effect. Moreover, for the rutile-type structure, the t_{2g} orbital splits into a lower xy state and higher $xz + yz$ and $xz - yz$ states. In the case of CrO_2, there are Cr ions which has two electrons or three electrons in t_{2g} orbitals because of the self-doping, as mentioned above. One electron in $xz + yz$ and $xz - yz$ orbitals of Cr ion having three electrons can hop to neighboring Cr ion only if the neighboring one has two 3d-electrons and the 3d-electrons are parallel to the hopping electron spin. If these 3d-electrons do not align, the hopping of the electron that Cr ($3d^3$) ion has is not allowed due to getting higher Coulomb energy. It is believed that one electron of Cr ($3d^3$) ion hops neighboring Cr site and as a result Cr 3d-electron spins aligns ferromagnetically because of the Hund's first rule. The double exchange interaction has been suggested as a mechanism of metallic and ferromagnetic behavior in $La_{1-x}Sr_xMnO_3$ (LSMO) and Fe_3O_4 (magnetite) [86]. For LSMO, the half-metallic electronic structure was confirmed in the ferromagnetic phase by spin-resolved photoemission spectroscopy (SRPES) studies [46,47], although the spin polarization obtained by PCAR measurements .

Spin polarization of CrO_2 was measured by PCAR and was determined to be 90% at 1.8 K

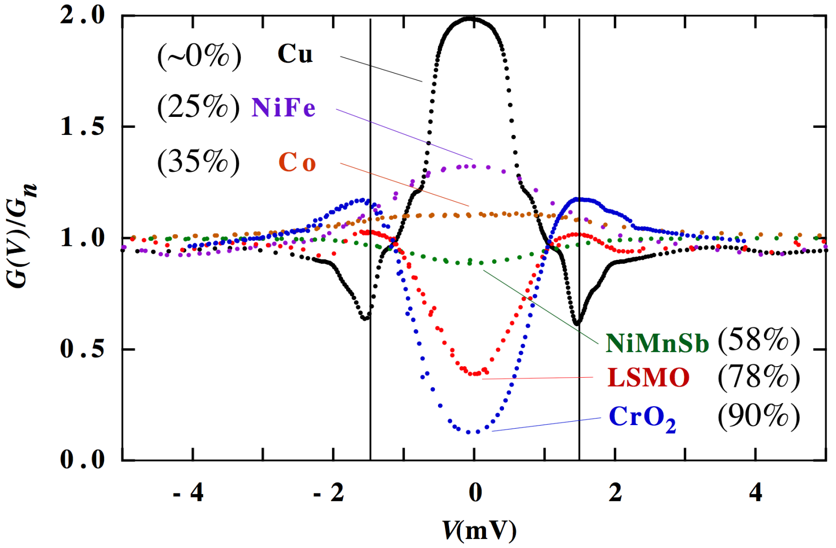

Fig. 1.8. The differential conductance for several spin-polarized metals via a superconducting Nb point contact, showing the suppression of Andreev reflection with increasing the spin polarization. The vertical lines denote the bulk gap of Nb: $\Delta(T = 0) = 1.5$ meV. Values in parentheses represent the obtained spin polarization. Taken from [76].

[76]. In the PCAR study, the spin polarization, 90%, is the highest value in measured half-metal candidates, as shown in Fig. 1.8. Before the PCAR report, a SARPES study reported the spin polarization to be almost 100% near E_F, although the SARPES spectrum has a peak located at 2 eV binding energy without a metallic Fermi edge [42]. Dedkov *et al*. re-examined the electronic structure by SARPES and reported that the spin polarization at E_F is 95% at room temperature, although the SARPES spectra show similar insulating-like spectral features [43]. These SARPES results are shown in Fig. 1.9. The insulating photoemission spectrum is inconsistent with the behavior of resistivity [85]. However, similar photoemission spectra have been reported by studies using polycrystalline bulk samples or epitaxial films grown on TiO_2 substrates[87–91]. Some of these studies suggested that the insulating spectra is derived from the electronic structure of a surface contaminant. Ventrice Jr. *et al*. have investigated surface-cleaning-procedure dependence of the photoemission spectra and compared each photoemission spectrum with that of Cr_2O_3 [90]. They indicated that all of the spectra taken under various sputtering and annealing conditions are remarkably similar to the photoemission spectra of Cr_2O_3. This implies that the surface contaminant Cr_2O_3 prevents from observing the intrinsic electronic structure of CrO_2. A recent photoemission study using soft x-ray synchrotron radiation and ultraviolet photon source has confirmed that photoemission spectra taken under bulk-sensitive condition have a peak located at 1 eV with a clear Fermi edge, while under surface-sensitive condition, the 1-eV peak shifts toward higher binding energy side and

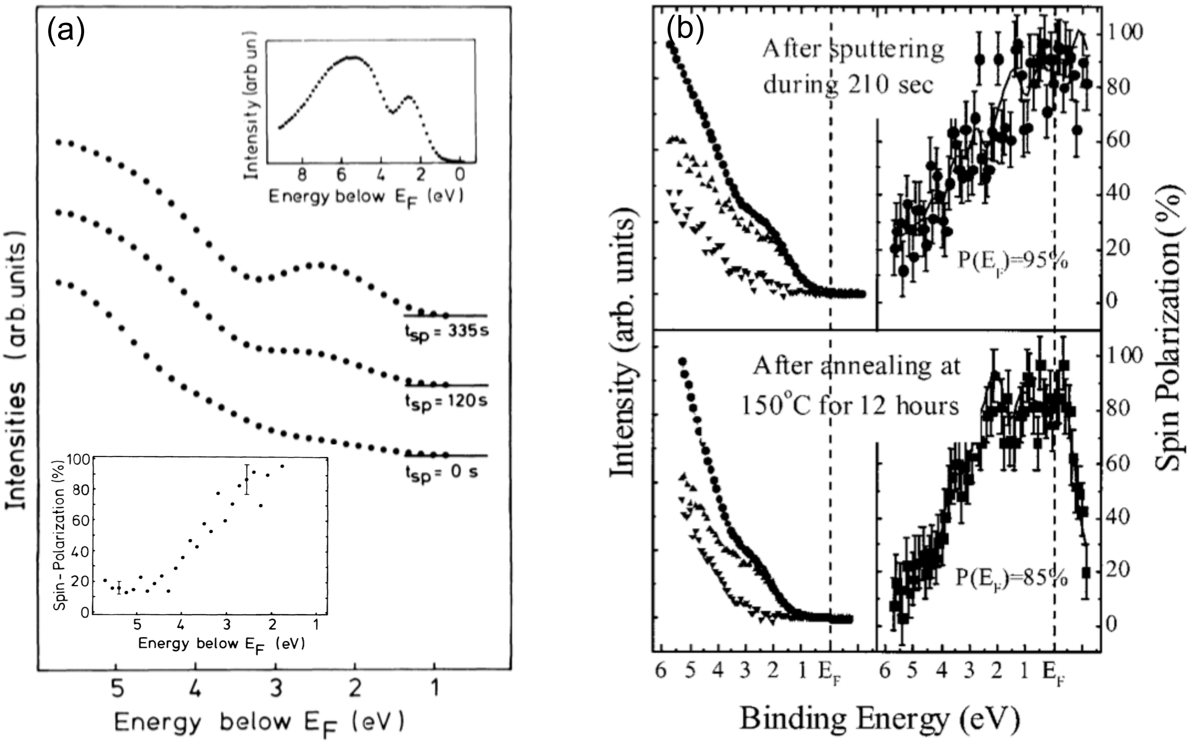

Fig. 1.9. (a) Previous photoemission EDCs of polycrystalline CrO_2 films at 300 K for *hv* = 21.2 eV and for different times (t_{sp}) of sputter cleaning, reported by Kämper *et al.* Upper inset shows EDC for t_{sp} = 335 s on a wide binding energy scale. Lower inset is binding energy dependence of spin polarization of a polycrystalline CrO_2 film at 300 K after 120 s of sputter cleaning. Taken from [42]. (b) Previous spin-resolved photoemission EDCs of epitaxial island CrO_2 films at 293 K for *hv* = 21.2 eV (left side) and its spin polarization (right side), reported by Dedkov *et al.* Upper panel is that after Ar^+ sputtering for 210 s at 500 eV. Lower panel is that after 750 s sputtering and an additional annealing treatment at 150°C for 12 h. Taken from [43].

the Fermi edge disappears, as shown in Fig. 1.10(a) [91]. These previous investigations evidently implies that the surface of CrO_2 tends to change to the antiferromagnetic insulator Cr_2O_3, and that it is not easy to remove the Cr_2O_3 contaminant by sputtering and annealing procedures.

In addition to a bulk-sensitive measurement, high-quality samples allow us to observe the intrinsic electronic structure of CrO_2. As a conventional preparation of a CrO_2 sample, a chemical vapor deposition method has been used. In the method, CrO_3 and TiO_2 are usually used as a precursor and a substrate, respectively [92]. Since CrO_3 is extremely hygroscopic, it gets various impurities in the atmosphere, which might change the deposition condition. Ivanov *et al.* reported that epitaxial CrO_2 thin films are successfully prepared by chemical vapor deposition (CVD) from a Cr_8O_{21} precursor [93]. Since Cr_8O_{21} is less hygroscopic and less toxic compared with CrO_3, it would be a more appropriate precursor. In addition, they have found from low-energy electron diffraction (LEED) observations that epitaxial growth of rutile-phase

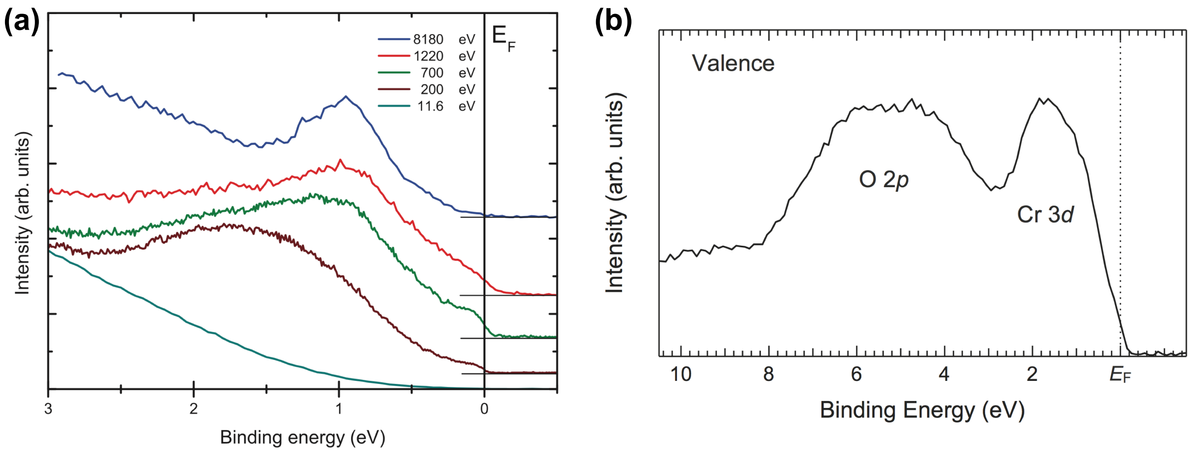

Fig. 1.10. (a) Valence band photoemission spectra of epitaxial CrO_2(100) films prepared by a conventional method at 20 K for different photon energies in normal emission. The surfaces are as grown, including a nominal Cr_2O_3 surface layer. Taken from [91]. (b) Valence band photoemission spectrum of an epitaxial CrO_2(100) film prepared by a closed-system CVD method. Taken from [85].

CrO_2 occurs to the top monolayer of the film. Furthermore, Iwai *et al.* fabricated a high quality sample which shows a peak at 1 eV with a clear Fermi edge in its surface-sensitive photoemission spectrum by developing a closed-system CVD method using a Cr_8O_{21} precursor [85], as shown in Fig. 1.10(b). By combining the high-quality CrO_2 sample and bulk-sensitive SARPES, it is expected that the intrinsic electronic structure and the spin polarization are directly observed, which reveals the half-metallicity of CrO_2.

Since CrO_2 is the simplest half-metal and shows the highest spin polarization in half-metal candidates, CrO_2 is an appropriate material for investigating phenomena characteristics of half-metals. It has been predicted that because spin-flip scattering of electrons is forbidden in half-metals, correlation effects, which do not occur in normal ferromagnetic metals such as Fe and Ni, may occur in half-metals when there are magnetic excitations in the system (described in Sec. 1.3).

1.2.3 CoS_2: Candidate for *Nearly* Half-Metal

Pyrite-type 3*d* transition-metal dichalcogenides MX_2 (M = Fe, Co, Ni, Cu; X = S, Se) exhibit a wide variety of electrical and magnetic properties [94]. The crystal structure (Space group: $Pa\bar{3}$, Lattice constant a = 5.539 Å at 300 K [95]) is shown in Fig. 1.11. As is the case with CrO_2, atoms of the chalcogen are octahedrally coordinated around those of the transition metal, but the chalcogen atoms form a chalcogen–chalcogen dimer. Therefore, the transition metal *d* bands

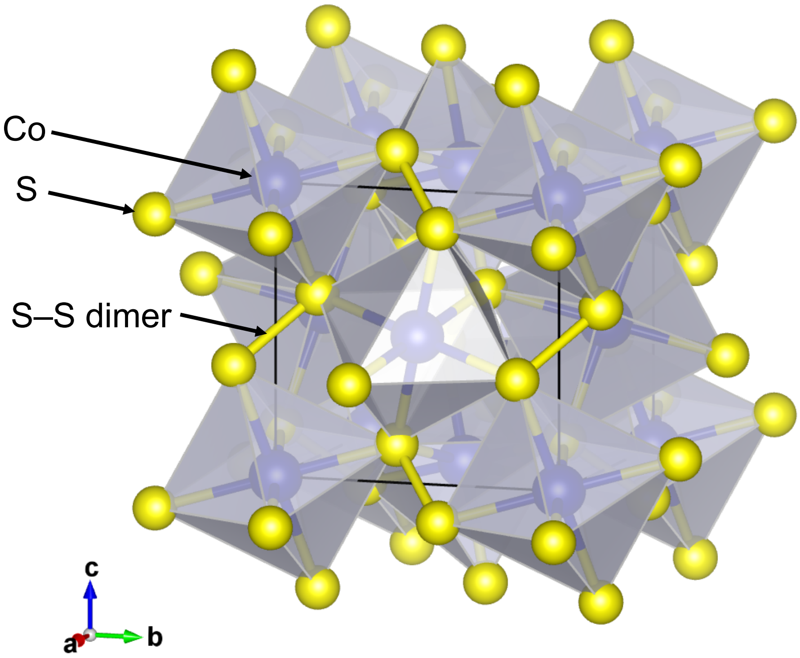

Fig. 1.11. Crystal structure of CoS_2 (Space group: $Pa\bar{3}$). Cube drawn by black lines represents the unit cell. Gray planes represent an octahedral structure formed by S atoms surrounding Co atoms.

split into t_{2g} and e_g, and the chalcogen p bands split into two bands of the bonding and antibonding orbitals. The transition-metal 3d electron configuration varies from $t_{2g}^6e_g^0$, $t_{2g}^6e_g^1$, and $t_{2g}^6e_g^2$ to $t_{2g}^6e_g^3$ for FeS_2, CoS_2, NiS_2 and CuS_2, respectively. FeS_2 is a semiconductor with a band gap of $E_g \sim 0.9$ eV [96]. CoS_2 is a ferromagnetic metal with the Curie temperature $T_C \sim$ 120 K, while $CoSe_2$ is a paramagnetic metal [56]. NiS_2 is an antiferromagnetic insulator with $E_g \sim 0.3$ eV and $T_N = 40$ K, while $NiSe_2$ is a paramagnetic metal [97,98]. CuS_2 is a superconductor with $T_c \sim 1.6$ K [99].

CoS_2 is a ferromagnetic metal with $T_C \sim 120$ K, as mentioned above, but the ferromagnetic order is suppressed by substituting S by Se and disappear by 11% substitution, through a metamagnetic phase[100,101]. CoS_2 has been also considered as a candidate for a half-metal because of its saturation magnetic moment of 0.85 μ_B/Co close to 1 μ_B/Co in a low-spin state of Co^{2+} (S=1/2 and $g = 2$) [102]. From a x-ray magnetic circular dichroism (XMCD) study, the orbital moment was estimated to be $L_z \sim 0.05\mu_B$ [103]. The half-metallicity is also supported by a theoretical band structure calculated within the generalized gradient approximation (GGA) [54], as shown in Fig. 1.12. CoS_2 has good lattice-constant matching with many semiconductors (GaAs, Si, ZnS, etc.) as reported by Kirczenow [104]. This feature is advantageous for spintronics devices.

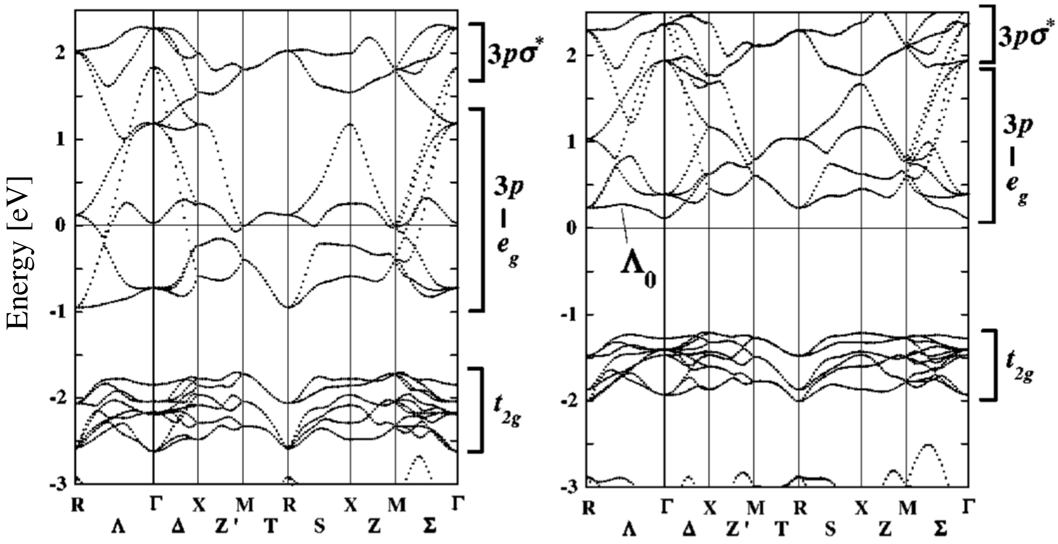

(a) GGA; Majority spin

(b) GGA; Minority spin

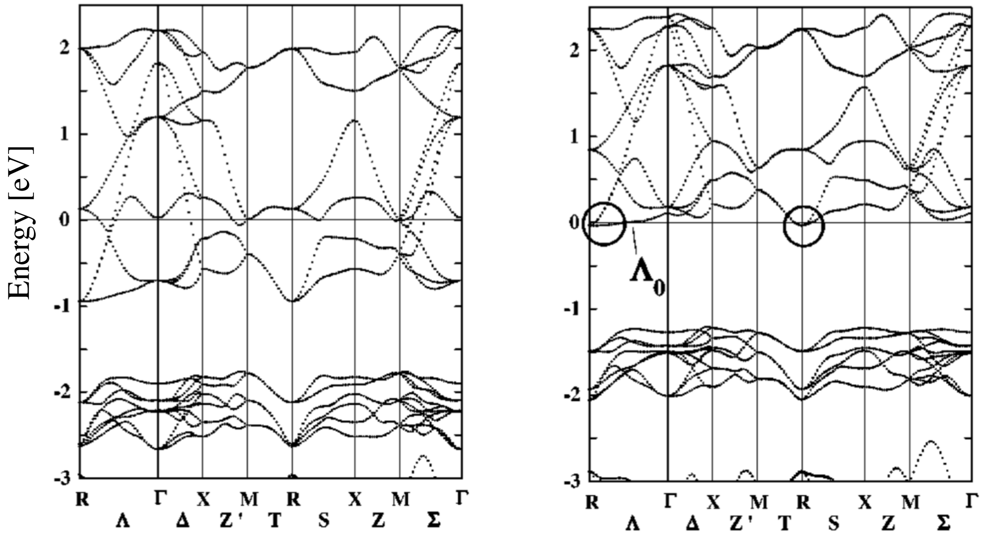

(c) LSDA; Majority spin

(d) LSDA; Minority spin

Fig. 1.12. Band structure of CoS_2 calculated within GGA for (a) majority spin electrons and (b) minority spin electrons. (c), (d) Same as (a) and (b), but calculated within LSDA. Taken from [54].

However, the half-metallicity of CoS_2 is still an open question. The half-metallicity has been supported by GGA calculations [54], an experimental study of the de Haas–van Alphen (dHvA) effect [56], and an optical study measuring reflectivity of CoS_2 [105]. On the other hand, the results of band calculation within local spin-density approximation (LSDA) [106–109], PCAR [110], XMCD [111], and photoemission spectroscopy measurements [112,113] indicated that CoS_2 has a “nearly” half-metallic electronic structure in which a bottom of the minority spin e_g band touches or slightly crosses E_F near the R point.

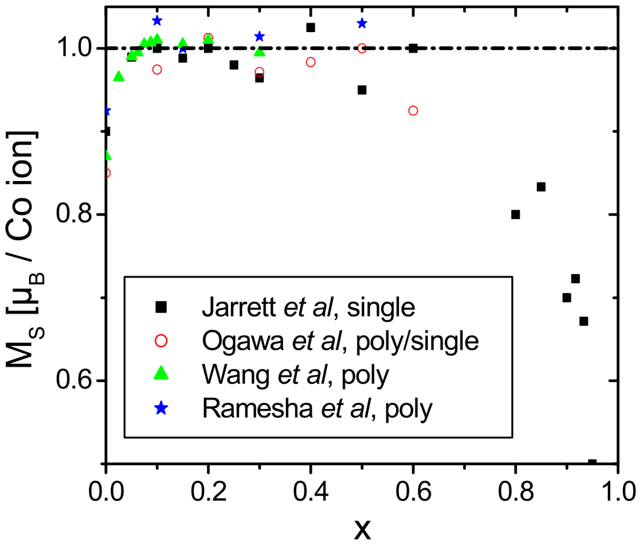

Fig. 1.13. Fe doping dependence of the saturation magnetization per Co ion (assuming zero moment on the Fe sites). Taken from a review article [57].

The band-structure picture of the nearly half-metallic ferromagnet is also supported by PCAR studies on $Co_{1-x}Fe_xS_2$ [57,59,114,115]. By substituting Co by Fe, holes are introduced in to the system, and then the position of E_F is depressed toward the low energy side. By the shift of E_F, minority spin e_g bands are pushed up relatively. Accordingly, the minority spin e_g band produces a gap at E_F, while the majority spin e_g band still crosses E_F. This band structure is just half-metallic one. This band picture has been confirmed experimentally [57], as shown in Fig. 1.13.

If CoS_2 has the nearly half-metallic electronic structure, it is expected that CoS_2 shows intermediate physical properties between a normal ferromagnet and a half-metal. Therefore, by comparison of characteristics of CoS_2 with those of normal ferromagnets, we might find key features for realizing half-metallic electronic structure.

1.3 Thermal Spin Depolarization in Half-Metallic Ferromagnet

1.3.1 Macroscopic Characteristics of Half-Metal-Based Magnetic Tunneling Junctions

Because of the completely spin-polarized carrier of half-metals, half-metals have been used for realizing MTJ-based spintronics devices [2,11,12]. However, they have a critical issue: the tunneling magnetoresistance rapidly decreases with increasing temperature [28–32]. Figures

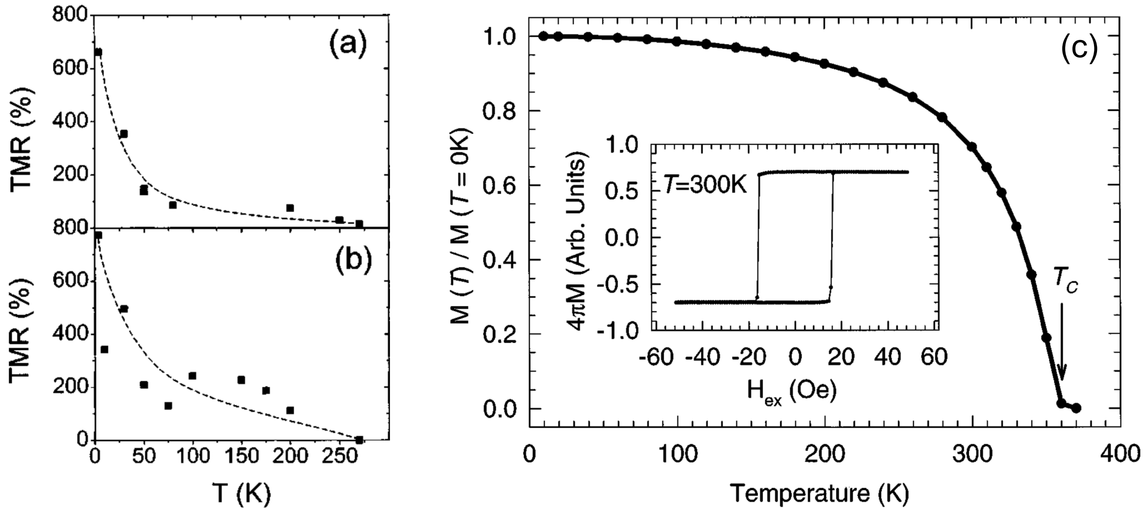

Fig. 1.14. Temperature dependence of the TMR measured with V_{dc} = 10 mV for two junctions: 2×6 $\mu\mathrm{m}^2$ (a) and 1.4×4.2 $\mu\mathrm{m}^2$ (b). Dashed lines are guides to the eye. Taken from [116]. (c) Temperature dependence of magnetization measured SQUID at 200 Oe. The inset shows the magnetization M vs applied magnetic field H hysteresis loop. Taken from [47].

1.14(a) and (b) show an example of T-dependent TMR ratio of a half-metal/barrier/half-metal MTJ, in which $La_{2/3}Sr_{1/3}MnO_3$ (LSMO) is used as the half-metal [116]. The TMR ratio shows an exponential fall with elevated temperature; the T-dependence does not obey the T-dependence expected from its macroscopic magnetization shown in Fig. 1.14(c) [47]. Similar behavior has been obtained for CrO_2-based MTJs [117]. As a spin-depolarization mechanism in half-metals, Skomski and Dowben have proposed a spin-mixing effect, but this effect alone cannot explain the rapid decrease of the TMR ratio because this effect produces spin depolarization with temperature dependence same as that of the magnetization [118–121].

As possible origins of the rapid decrease of TMR, two effects have been pointed out as:

1. Interfacial effects in MTJs
2. Many-body effects in half-metals

The interfacial effects have been investigated religiously for LSMO-based MTJs. Teresa *et al.* found that the sign of TMR ratio depends on the barriers inserted between LSMO and Co films [122], although the sign should be determined from the combination of the ferromagnetic electrodes, based on Julliére's expression for TMR ratio:

$$\frac{\Delta R}{R}=\frac{R_{\mathrm{AP}}-R_{\mathrm{P}}}{R_{\mathrm{P}}}=\frac{2P_1P_2}{1-P_1P_2} \tag{1.3}$$

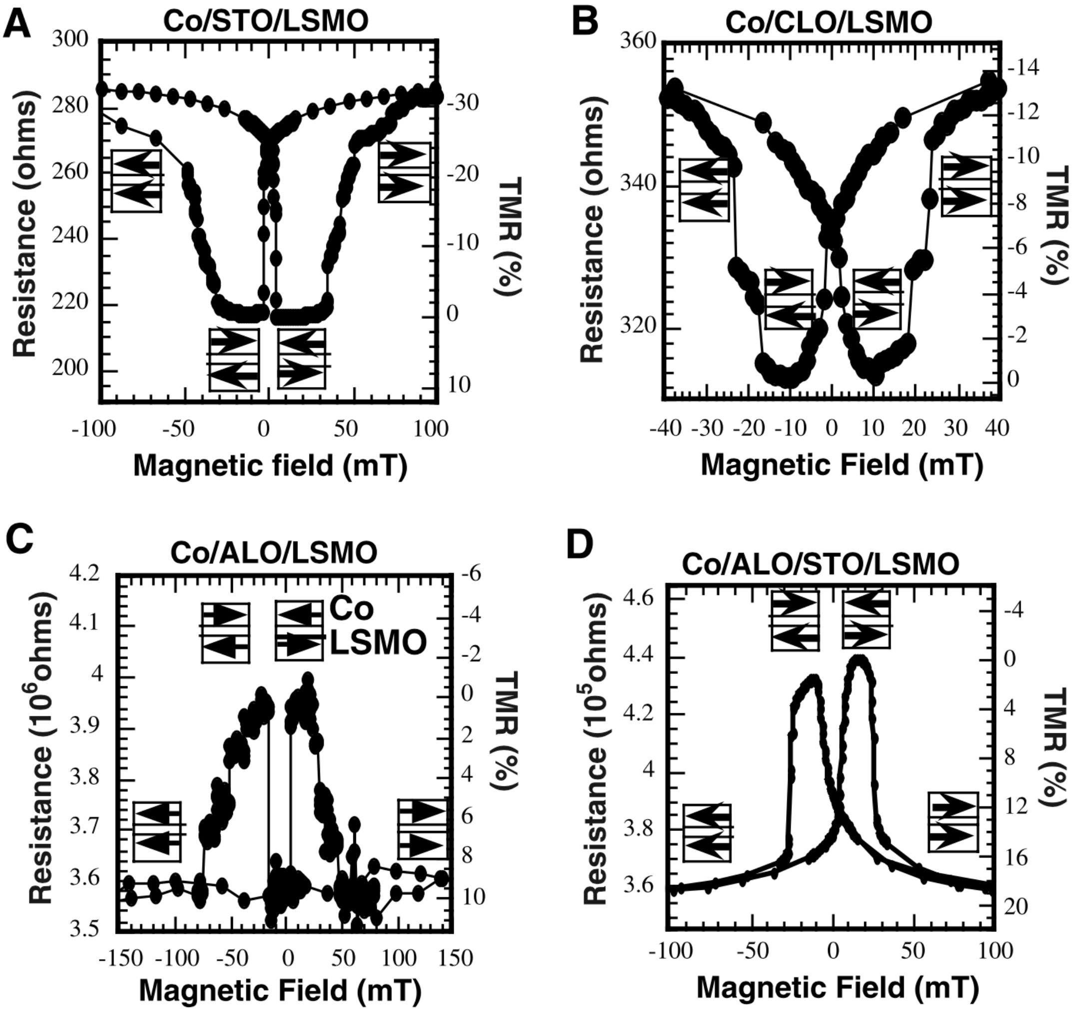

Fig. 1.15. TMR curves recorded at 40 K with a bias of –10 mV for (A) Co/STO/LSMO, (B) Co/CLO/LSMO, (C) Co/ALO/LSMO, (D) Co/ALO/STO/LSMO junctions. Taken from [122].

where R_{AP} and R_P are the resistances in the antiparallel and parallel states, respectively, and P_1 and P_2 are the electron spin polarizations of the two electrodes. Figure 1.15 shows TMR ratios of Co/barrier/LSMO-TMJs for various tunneling barriers. The factor P_1P_2 of the TMJ with an alumina barrier (Al_2O_3: ALO) is positive, but it is negative when the barrier is strontium titanate ($SrTiO_3$: STO) or cerium lanthanite ($Ce_{0.69}La_{0.31}O_{1.845}$: CLO). These results suggest that spin polarization observed by TMJ does not determined by the combination of the electrode alone, and that electronic structures of the interface are also important. Since the magnetization due to the interfacial electronic structure does not so much contribute to the macroscopic magnetization, the interfacial effect is a candidate for the explanation for the rapid decrease of spin polarization in half-metal-based MTJs.

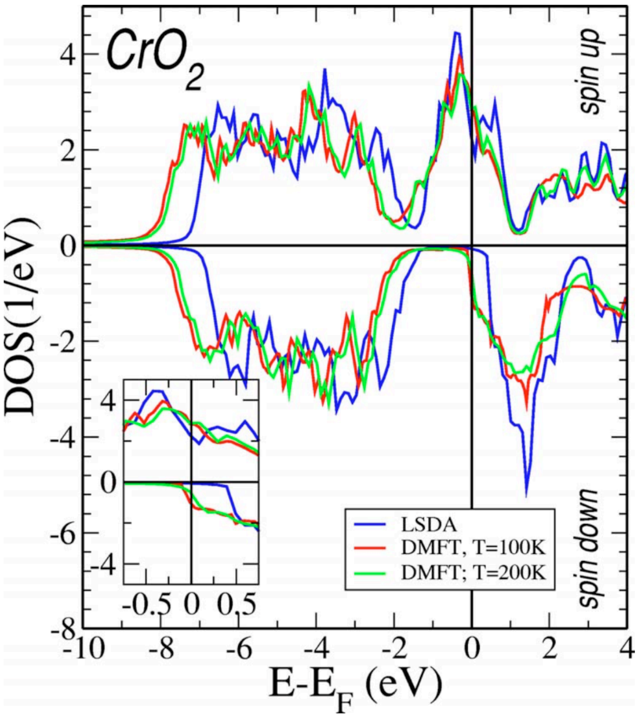

Fig. 1.16. Density of states obtained within the LSDA and LSDA+DMFT calculations for different temperatures. The inset shows the results for a smaller energy window around E_F. Taken from [135].

Furthermore, a spin-filtering effect was proposed based on the symmetry of wave functions. Yuasa *et al*. fabricated fully single-crystal Fe/MgO/Fe MTJs and reported a TMR ratio of 180% at room temperature, which was impossible with previous material systems [123,124]. Butler *et al*. considered the symmetry of wave functions and focused on the electron state and the continuity of the wave functions of barriers in their theory [125,126]. In a MgO barrier, a band named Δ1 with the smallest attenuation is responsible for the conductance. In contrast, the Δ1 band electrons in the Fe electrodes have high spin polarization. Therefore, only the Δ1 band with high spin polarization contributes to the tunnel conduction for the above MTJs, thus achieving a high TMR ratio.

In contrast, for many-body effects, theoretical studies have preceded experimental studies [127–131]. The completely spin-polarized band structure of half-metals results in an important role for incoherent states (called *non-quasiparticle*: NQP) which occur near E_F owing to correlation effects. The origin of these states is connected with ‘spin-polaron’ processes: the spin-down low-energy electron excitations, which are forbidden for HMF in the one-particle picture, turn out to be possible as a superposition of spin-up electron excitations and virtual magnons. The density of NQP states has been calculated from first principles for a prototype half-metal, NiMnSb, as well as for other Heusler alloys, zinc-blende structure compounds, and

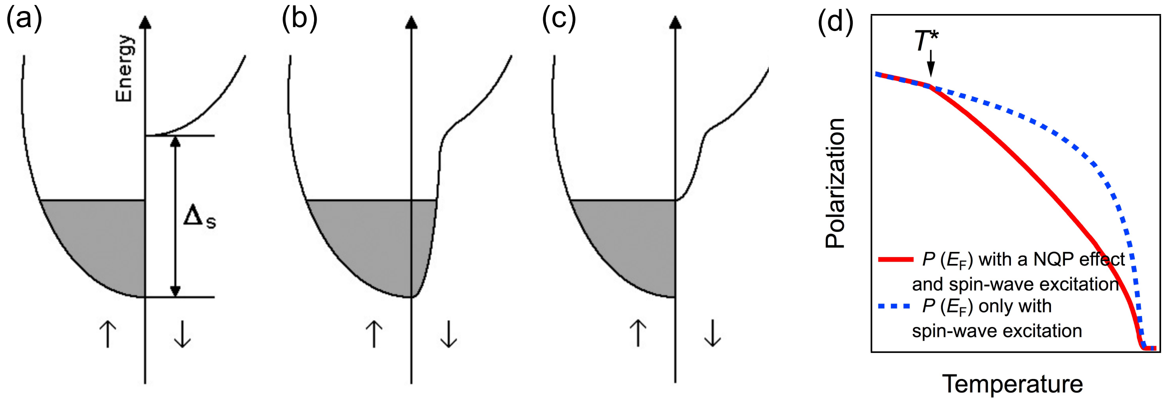

Fig. 1.17. Schematic density of states in a type IA half-metal: (a) one-electron ground state, (b) effect of spin mixing at $T > 0$, and inclusion of NQP states. Taken from [118]. (d) Schematic illustration of T-dependent spin polarization at E_F with both of a NQP effect and spin-wave excitation (red solid line), and just with spin-wave excitation (blue dotted line).

CrO_2 [24, 132–135]. Figure 1.16 shows the calculated density of states of CrO_2 for various temperatures [135]. In the ground state calculated within local spin density approximation (LSDA), CrO_2 has a half-metallic electronic structure. However, at finite temperatures, a minority spin tail state is broadened and crosses E_F. Since the bottom of the minority spin state is located at $E - E_F \sim 100$ meV, the change of the electronic structure has little influence on the macroscopic magnetization, while it may strongly affects the magnetotransport properties. An indication of the NQP states was provided by Chioncel *et al.* through a study using Co_2MnSi-based MTJ [136]. Nevertheless, the NQP states have not yet been detected directly by SARPES or spin-polarized scanning tunneling microscopy. So far, the contribution of the NQP states to TMR ratio has not been unclear.

1.3.2 Theoretical Spin-Depolarization Mechanisms in Half-Metals

Far below T_C , the densities of states of normal ferromagnets are only weakly modified by thermal fluctuations, because k_BT is much smaller than the Fermi energy and band-structure distortions are small. Essentially, low-temperature thermal disorder leads to slight modifications of the spin-dependent exchange potential and of the spin-up and spin-down densities of state. However, as elaborated on in Refs. [119–121], half-metallic ferromagnets are an exception, they exhibit qualitatively new low-temperature effects.

Figures 1.17(a)–(c) shows schematic band diagrams of a half-metal at the ground state, that at a finite temperature including a spin-mixing effect due to spin-wave excitation proposed by

Skomski and Dowben, and that at a finite temperature including NQP states [118]. By the spin-mixing effect, the minority spin states develop over the spin-polarized energy region. Here, the density of states of the minority spin state is represented as:

$$D_{\downarrow}(E)=\frac{M_0-M_{\mathrm{s}}(T)}{M_0+M_{\mathrm{s}}(T)}D_{\uparrow}(E) \tag{1.4}$$

where $D_{\uparrow/\downarrow}(E)$ is the majority/minority spin density of states, $M_{\mathrm{s}}(T)$ is the spontaneous magnetization, and $M_0 = M_{\mathrm{s}}(0)$. Equation 1.4 indicates that $D_{\downarrow}(E)$ shows the same energy dependence as $D_{\uparrow}(E)$ and that the temperature dependence of spin polarization obtained by $P = (D_{\uparrow}(E) - D_{\downarrow}(E))/(D_{\uparrow}(E) + D_{\downarrow}(E))$ is strictly in line with that of the normalized spontaneous magnetization $M_{\mathrm{s}}(T)/ M_0$. On the other hand, NQP states appear just near E_{F} and decrease the spin polarization above a crossover temperature T^*, as shown in Fig. 1.17(d).

The NQP states were first considered theoretically by Edwards and Hertz in work on electron–magnon interaction in a broad-band Hubbard model of itinerant electron ferromagnets [128]. Later it was demonstrated that for a narrow-band Hubbard model, the whole spectral weight for one spin projection belongs to NQP states, which is of importance for the problem of stability of Nagaoka's ferromagnetism [137] and for adequate description of the corresponding excitation spectrum [129]. The NQP states in the *s–d* exchange model of magnetic semiconductors have been considered in Ref. [138]. It was indicated that depending on the sign of the *s–d* exchange integral, they can occur either only below E_{F} or only above it. Later it was realized that half-metals are natural substances for theoretical and experimental investigation of NQP effects, and a variety of these effects in electronic and magnetic properties have been considered [130,139].

Since the half-metals can be characterized by the absence of magnon decay into Stoner excitations (electron–hole pairs with the opposite spins), spin waves are well defined in the whole Brillouin zone. Therefore, unlike the usual itinerant ferromagnets, the effects of electron–magnon interaction, so-called spin-polaron effects, are not masked by Stoner excitations in the half-metals [129,131]. This electron–magnon interaction results in the occurrence of NQP states.

The NQP theory has been built based on the standard *s–d* exchange model:

$$\mathcal{H}=\sum_{\boldsymbol{k}\sigma} t_{\boldsymbol{k}} c_{\boldsymbol{k}\sigma}^{\dagger} c_{\boldsymbol{k}\sigma} - I\sum_{\boldsymbol{q}\boldsymbol{k}\alpha\beta} \boldsymbol{S}_{\boldsymbol{q}} c_{\boldsymbol{k}\sigma}^{\dagger}\sigma_{\alpha\beta} c_{\boldsymbol{k}-\boldsymbol{q}\beta} - \sum_{\boldsymbol{q}} J_{\boldsymbol{q}} \boldsymbol{S}_{\boldsymbol{q}} \boldsymbol{S}_{-\boldsymbol{q}} \tag{1.5}$$

where $c_{\boldsymbol{k}\sigma}^{\dagger}$, $c_{\boldsymbol{k}\sigma}$ and $\boldsymbol{S}_{\boldsymbol{q}}$ are operators for conduction electrons and localized spins in the

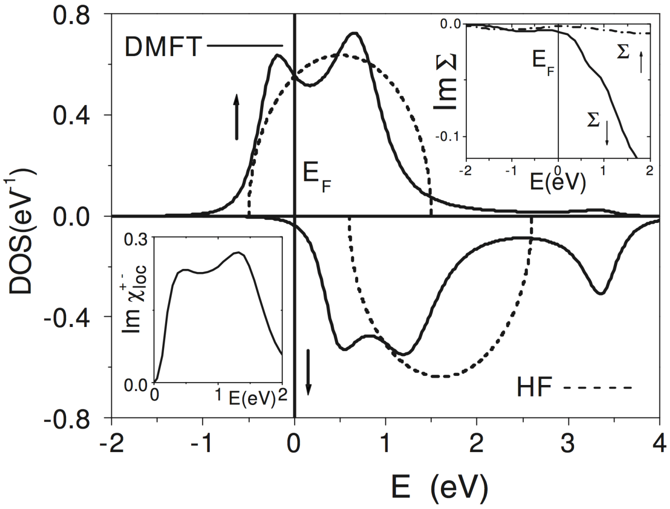

Fig. 1.18. Density of states for half-metals in the Hartree-Fock approximation (dashed line) and in the quantum Monte Carlo solution of the DMFT problem for the semi-circular model (solid line) with bandwidth $W = 2$ eV, Coulomb interaction $U = 2$ eV, $\Delta = 0.5$ eV, chemical potential $\mu = -1.5$ eV, and temperature $T = 0.25$ eV. Insets: Imaginary part of the spin-flip susceptibility (left) and imaginary part of self-energy (right). Taken from [132].

quasimomentum representation, the electron spectrum $t_{\boldsymbol{k}}$ is referred to E_{F}, I is the *s–d* exchange parameter and $\boldsymbol{\sigma}$ are the Pauli matrices. Based on the *s–d* model and the Dyson equation, we obtain a simple expression for the electron density of states as:

$$N_\sigma(E) = \sum_{\boldsymbol{k}} \delta(E - t_{\boldsymbol{k}\sigma}) - \sum_{\boldsymbol{k}} \delta'(E - t_{\boldsymbol{k}\sigma}) \mathrm{Re}\Sigma_{\boldsymbol{k}\sigma}(E) - \frac{1}{\pi} \sum_{\boldsymbol{k}} \frac{\mathrm{Im}\Sigma_{\boldsymbol{k}\sigma}(E)}{(E - t_{\boldsymbol{k}\sigma})^2} \tag{1.6}$$

where $t_{\boldsymbol{k}\sigma} = t_{\boldsymbol{k}} - \sigma I \langle S^z \rangle$ is the mean-field electron spectrum and $\Sigma_{\boldsymbol{k}\sigma}(E)$ is the self-energy which describes the electron–magnon interaction. The second term on the right-hand side of Eq. 1.6 describes the renormalization of quasiparticle energies. The third term, which arises from the branch cut of the self-energy $\Sigma_{\boldsymbol{k}\sigma}(E)$, describes the NQP contribution owing to scattering by magnons. Under a half-metallic condition ($2|I|S > E_{\mathrm{F}}$), the contribution of NQP states to temperature dependence of spin polarization at E_{F}, $P_{\mathrm{NQP}}(T)$, is described as:

$$P_{\mathrm{NQP}}(T) \propto P(0) \left(1 - T \ln \frac{T}{T^*}\right) \tag{1.7}$$

where T^* represents a crossover temperature above which Eq. 1.7 is defined. This indicates that the spin depolarization drastically drop around T^* due to NQP states [136].

In order to obtain the density of states of NQP for various systems, the dynamical mean-field theory (DMFT) has been used [24]. Combination of the local density approximation (LDA) scheme with the DMFT has described electronic structures of strongly correlated systems [140–142]. Figure 1.18 shows the density of states for half-metals in the solution of the DMFT problem. The DMFT calculation predicted that by considering the Coulomb interaction and fluctuations due to a finite temperature, the exchange-splitted bands are broadened and the subband with the spin-down character crosses E_F. The DMFT calculations have predicted the band-broadening effect for various half-metals (NiMnSb, Co_2MnSi, CrO_2 etc.) [132–135]. However, as mentioned above, since the NQP states shown by the DMFT calculations have not observed directly, the contribution of the NQP states to the rapid spin depolarization in half-metals has been unclear. Revealing behavior of the NQP states must provide a hint for realizing completely spin-polarized materials at room temperature.

1.4 Motivation and Brief Outline of This Dissertation

Half-metals are regarded as important materials not only for spintronic materials producing completely spin-polarized current but also for model materials for investigating many-body physics. Through electronic-structure studies, we can understand the mechanisms of the rapid thermal spin depolarization of half-metals in relation to the many-body effects. However, so far, there is the lack of full information on the evolution of electronic structure due to the many-body effects characteristic of half-metals, because we have two problems addressing the electronic-structure investigation: (i) CrO_2 is the only material, where the indication of the predicted half-metallicity has been provided experimentally by several different techniques. Furthermore, CrO_2 surface tends to change to antiferromagnetic insulator Cr_2O_3, preventing from observing the intrinsic electronic structure of CrO_2. (ii) There is no appropriate experimental technique to directly observe the spin-resolved fine electronic structure in the vicinity of E_F. SARPES is a promising technique, but the achieved energy resolution of conventional SARPES apparatus is approximately 100 meV, which is insufficient to detect NQP states.

The motivation of the present work is to reveal the origins of the thermal spin depolarization in half-metals by investigating the temperature dependence of the spin-polarized electronic structure of half-metal CrO_2 and of nearly half-metal CoS_2 by means of the most-advanced SARPES techniques: Bulk-sensitive SARPES and high-resolution SARPES. The authors sets the goal of present study to be threefold: (i) to clarify the intrinsic spin-resolved electronic structure of a high-quality CrO_2 film, (ii) to check if there is some change of electronic structure and spin polarization in the close vicinity of E_F; and if some change is observed, (iii) to reveal if the electronic-structure change is an universal feature of half-metals or not, by investigation on CoS_2.

This dissertation is organized as follows. After this introductory chapter, experimental aspects of this dissertation including the principles of photoemission spectroscopy and of spin detectors in Chapter 2. Details of the two kinds of SARPES apparatus which are keys for accomplishing the present work are described in Chapter 3. In Chapter 4, bulk-sensitive SARPES investigation on CrO_2 which reports spectroscopic evidence for the half-metallicity of CrO_2 is described. Chapter 5 describes the discovery of fine spin depolarization originating from the many-body effect in CrO_2 by high-resolution SARPES. Thorough electronic-structure investigation on CoS_2 which reveals the half-metallicity and anomalously large spin-dependent correlation effects is described in Chapter 6. Summary and possible future outlook are mentioned in Chapter 7.

1.5 References

[1] M. M. Waldrop, Nature **530**, 144 (2016).

[2] Y. Ando, Jpn. J. Appl. Phys. **54**, 070101 (2015).

[3] M. N. Baibich, J. M. Broto, A. Fert, F. Nguyen Van Dau, F. Petroff, P. Etienne, G. Creuzet, A. Friederich, and J. Chazelas, Phsy. Rev. Lett. **61**, 2472 (1988).

[4] M. Julliere, Phys. Rev. Lett. A **54**, 225 (1975).

[5] S. Tehrani, J.M. Slaughter, E. Chen, M. Durlam, J. Shi, and M. DeHerrera, IEEE Trans. Magn. **35**, 2814 (1999).

[6] S. Tehrani, B. Engel, J. M. Slaughter, E. Chen, M. DeHerrera, M. Durlam, P. Naji, R. Whig, J. Janesky, and J. Calder, IEEE Trans. Magn. **35**, 2752 (2000).

[7] A. V. Khvalkovskiy, D. Apalkov, S. Watts, R. Chepulskii, R. S. Beach, A. Ong, X. Tang, A. Driskill-Smith, W. H. Butler, P. B. Visscher, D. Lottis, E. Chen, V. Nikitin, and M. Krounbi, J. Phys. D: Appl. Phys. **46**, 139601 (2013).

[8] AS.-W. Chung, T. Kishi, J. W. Park, M. Yoshikawa, K. S. Park, T. Nagase, K. Sunouchi, H. Kanaya, G. C. Kim, K. Noma, M. S. Lee, A. Yamamoto, K. M. Rho, K. Tsuchida, S. J. Chung, J. Y. Yi, H. S. Kim, Y.S. Chun, H. Oyamatsu, and S. J. Hong ,Proc. IEEE Int. Electron Devices Meeting, 27.1.1 (2016).

[9] K. Ando, S. Fujita, J. Ito, S. Yuasa, Y. Suzuki, Y. Nakatani, T. Miyazaki, and H. Yoda, J. Appl. Phys. **115**, 172607 (2014).

[10] S. Datta and B. Das, Appl. Phys. Lett. **56**, 665 (1990).

[11] S. A. Wolf, D. D. Awschalom, R. A. Buhrman, J. M. Daughton, S. von Molnár, M. L. Roukes, A. Y. Chtchelkanova, and D. M. Treger, Science **294**, 1488 (2001).

[12] I. Žutić, J. Fabian, S. Das Sarma, Rev. Mod. Phys. **76**, 323 (2004).

[13] A. Takayama, T. Sato, S. Souma, and T. Takahashi, Phys. Rev. Lett. **106**, 166401 (2011).

[14] H. Miyahara, T. Maegawa, K. Kuroda, A. Kumura, K. Miyamoto, H. Namatame, M. Taniguchi, and T. Okuda, e-J. Surf. Sci. Nanotech. **10**, 153 (2012).

[15] A. Takayama, T. Sato, S. Souma, T. Oguchi and T. Takahashi, Phys. Rev. Lett. **114**, 066402 (2015).

[16] A. Takayama, T. Sato, S. Souma, and T. Takahashi, New J. Phys. **16**, 055004 (2014).

[17] D. Grundler, Phys. Rev. Lett. **84**, 6074 (2000).

[18] T. Matsuyama, R. Kürsten, C. Meißner, and U. Merkt, Phys. Rev. B **61**, 589 (2000).

[19] K. Ishizaka, M. S. Bahram, H. Murakawa, M. Sakano, T. Shimojima, T. Sonobe, K.

Koizumi, S. Shin, H. Miyahara, A. Kimura, K. Miyamoto, T. Okuda, H. Namatame, M. Taniguchi, R. Arita, N. Nagaosa, K. Kobayashi, Y. Murakami, R. Kumai, Y. Kaneko, Y. Onose, and Y. Tokura, Nat. Mat. **10**, 521 (2011).

[20] A. Crepaldi, L. Moreschini, G. Autès, C. Tournier-Colletta, S. Moser, N. Virk, H. Berger, Ph. Bugnon, Y. J. Chang, K. Kern, A. Bostwick, E. Rotenberg, O. V. Yazyev, and M. Grioni, Phys. Rev. Lett. **109**, 096803 (2012).

[21] Y. Zhang, K. He, C.-Z. Chang, C.-L. Song, L.-L. Wang, X. Chen, J.-F. Jia, Z. Fang, X. Dai, W.-Y. Shan, S.-Q. Shen, Q. Niu, X.-L. Qi, S.-C. Zhang, X.-C. Ma, and Q.-K. Xue, Nat. Phys. **6**, 584 (2010).

[22] Z.-H. Zhu, G. Levy, B. Ludbrook, C. N. Veenstra, J. A. Rosen, R. Comin, D. Wong, P. Dosanjh, A. Ubaldini, P. Syers, N. P. Butch, J. Paglione, I. S. Elfimov, and A. Damascelli, Phys. Rev. Lett. **107**, 186405 (2011).

[23] R. A. de Groot, F. M. Mueller, P. G. van Engen, and K. H. J. Buschow, Phys. Rev. Lett. **50**, 2024 (1983).

[24] M. I. Katsnelson, V. Yu. Irkhin, L. Chioncel, A. I. Lichtenstein, and R. A. de Groot, Rev. Mod. Phys. **80**, 315 (2008).

[25] J. M. D. Coey and M. Venkatesan, J. Appl. Phys. **91**, 8345 (2002).

[26] J. M. D. Coey and C. L. Chien, MRS Bull. **28**, 720 (2003).

[27] A. M. Haghiri-Gosnet, T. Arnal, R. Soulimane, M. Koubaa, and J. P. Renard, Phys. Stat. Sol. (a) **201**, 1392 (2004).

[28] A. Gupta and J. Z. Sun, J. Magn. Magn. Mater. **200**, 24 (1999).

[29] K.-I. Kobayashi, T. Kimura, H. Sawada, K. Terakura, and Y. Tokura, Nature **395**, 677 (1998).

[30] H.Y. Hwang, S.-W. Cheong, N.P. Ong, and B. Batlogg, Phys. Rev. Lett. **77**, 2041 (1996).

[31] H.Y. Hwang, S.-W. Cheong, Nature **389**, 942 (1997).

[32] H.Y. Hwang, S.-W. Cheong, Science **278**, 1607 (1997).

[33] D. Orgassa, H. Fujiwara, T. C. Schulthess, and W. H. Butler, Phys. Rev. B **60**, 237 (1999).

[34] D. Comtesse, B. Geisler, P. Entel, P. Kratzer, and L. Szunyogh, Phys. Rev. B **89**, 094410 (2014).

[35] S. Picozzi, A. Continenza, and A. J. Freeman, Phys. Rev. B **69**, 094423 (2004).

[36] I. Galanakis1 and Ph. Mavropoulos, J. Phys.: Condens. Matter **19**, 315213 (2007).

[37] S. Fujii, IEEE Trans. Magn. **50**, 1001003 (2014).

[38] M. Jourdan, J. Minár, J. Braun, A. Kronenberg, S. Chadov, B. Balke, A. Gloskovskii, M.

Kolbe, H.J. Elmers, G. Schönhense1, H. Ebert, C. Felser, and M. Kläui, Nat. Commun. 5:3974 doi: 10.1038/ncomms4974 (2014).

[39] K. Schwarz, J. Phys. F: M: Met. Phys. **16**, L211 (1986).

[40] M. A. Korotin, V. I. Anisimov, D. I. Khomskii, and G. A. Sawatzky, Phys. Rev. Lett. **80**, 4305 (1998).

[41] H.-T. Jeng and G. Y. Guo, J. Appl. Phys. **92**, 951 (2002).

[42] K. P. Kämper, W. Schmitt, G. Güntherodt, R. J. Gambino, and R. Ruf, Phys. Rev. Lett. **59**, 2788 (1987).

[43] Yu. S. Dedkov, M. Fonine, C. König, U. Rüdiger, G. Güntherodt, S. Senz, and D. Hesse, Appl. Phys. Lett. **80**, 4181 (2002).

[44] Y. Ji, G. J. Strijkers, F. Y. Yang, C. L. Chien, J. M. Byers, A. Anguelouch, Gang Xiao, and A. Gupta, Phys. Rev. Lett. **86**, 5585 (2001).

[45] J. D. Burton and E. Y. Tsymbal, Phil. Trans. R. Soc. A **370**, 4840 (2012).

[46] J.-H. Park, E. Vescovo, H.-J. Kim, C. Kwon, R. Ramesh, and T. Venkatesan, Nature **392**, 794 (1998).

[47] J.-H. Park, E. Vescovo, H.-J. Kim, C. Kwon, R. Ramesh, and T. Venkatesan, Phys. Rev. Lett. **81**, 1953 (1998).

[48] T. Saitoh, M. Nakatake, A. Kakizaki, H. Nakajima, O. Morimoto, Sh. Xu, Y. Moritomo, N. Hamada, and Y. Aiura, Phys. Rev. B **66**, 035112 (2002).

[49] W.-T. Chen, M. Mizumaki, H. Seki, M. S. Senn, T. Saito, D. Kan, J. P. Attfield, and Y. Shimakawa. Nat. Commun. 5:3909 doi: 10.1038/ncomms4909 (2014).

[50] R. Masrour, E.K. Hlil, M. Hamedoun, A. Benyoussef, O. Mounkachi, and H. El Moussaoui, J. Magn. Magn. Mater. **378**, 37 (2015).

[51] Yu. S. Dedkov, U. Rüdiger, and G. Güntherodt, Phys. Rev. B **65**, 064417 (2002).

[52] M. Fonin, Yu. S. Dedkov, R. Pentcheva, U Rüdiger, and G. Güntherodt, J. Phys.: Condens. Matter **19**, 315217 (2007).

[53] J. G. Tobin, S. A. Morton, S. W. Yu, G. D. Waddill, I. K. Schuller. and S. A. Chambers, J. Phys.: Condens. Matter **19**, 315218 (2007).

[54] T. Shishidou, A. J. Freeman, R. Asahi, Phys. Rev. B **64**, 180401(R) (2001).

[55] Y. J. Jin and J. I. Lee, Phys. Rev. B **73**, 064405 (2006).

[56] A. Teruya, F. Suzuki, D. Aoki, F. Honda, A. Nakamura, M. Nakashima, Y. Amako, H. Harima, M. Hedo, T. Nakama, and Y. Ōnuki, J. Phys. Soc. Jpn. **85**, 064716 (2016).

[57] C. Leighton, M. Manno, A. Cady, J. W. Freeland, L. Wang, K. Umemoto, R. M.

Wentzcovitch, T. Y. Chen, C. L. Chien, P. L. Kuhns, M. J. R. Hoch, A. P. Reyes, W. G. Moulton, E. D. Dahlberg, J. Checkelsky, and J. Eckert, J. Phys.: Condens. Matter **19**, 315219 (2007).

[58] K. Umemoto, R. M. Wentzcovitch, L. Wang, and C. Leighton, Phys. Status Solidi b **243**, 2117 (2006).

[59] L. Wang, K. Umemoto, R. M. Wentzcovitch, T. Y. Chen, C. L. Chien, J. Checkelsky, J. Eckert, E. D. Dahlberg, and C. Leighton, Phys. Rev. Lett. **94**, 056602 (2005).

[60] I. I. Mazin, Appl. Phys. Lett. **77**, 3000 (2000).

[61] M. S. Park, S. K. Kwon, and B. I. Min, Phys. Rev. B **64**, 100403(R) (2001).

[62] B. I. Min, M. S. Park, and J. H. Park, J. Phys.: Condens. Matter **16**, S5509 (2004).

[63] H. Akinaga, T. Manago, and M. Shirai, Jpn. J. Appl. Phys. **39**, L1118 (2000).

[64] B.-G. Liu, Phys. Rev. B **67**, 172411 (2003).

[65] W.-H. Xie, B.-G. Liu, and D. G. Pettifor, Phys. Rev. B **68**, 134407 (2003).

[66] W.-H. Xie, Y.-Q. Xu, and B.-G. Liu, Phys. Rev. Lett. **91**, 037204 (2003).

[67] G. Y. Gao, K. L. Yao, E. Şaşıoğlu, L. M. Sandratskii, Z. L. Liu, and J. L. Jiang, Phys. Rev. B **75**, 174442 (2007).

[68] G. Y. Gao and K. L. Yao, Appl. Phys. Lett. **91**, 082512 (2007).

[69] L. Zhou, S.-W. Yang, M.-F. Ng, M. B. Sullivan, V. B.C. Tan, and L. Shen, J. Am. Chem. Soc. **130**, 4023 (2008).

[70] H. Xiang, J. Yang, J. G. Hou, and Q. Zhu, J. Am. Chem. Soc. **128**, 2310 (2006).

[71] Y.-W. Son, M. L. Cohen, and S. G. Louie, Nature **444**, 347 (2006).

[72] S. Dutta, A. K. Manna, and S. K. Pati, Phys. Rev. Lett. **102**, 096601 (2009).

[73] A. Du, S. Sanvito, and S. C. Smith, Phys. Rev. Lett. **108**, 197207 (2012).

[74] F. Zheng, G. Zhou, Z. Liu, J. Wu, W. Duan, B.-L. Gu, and S. B. Zhang, Phys. Rev. B **78**, 205415 (2008).

[75] P. J. Webster, J. Phys. Chem. Solids **32**, 1221 (1971).

[76] R. J. Soulen Jr., J. M. Byers, M. S. Osofsky, B. Nadgorny, T. Ambrose, S. F. Cheng, P. R. Broussard, C. T. Tanaka, J. Nowak, J. S. Moodera, A. Barry, and J. M. D. Coey, Science **282**, 85 (1998).

[77] L. Ritchie, G. Xiao, Y. Ji, T. Y. Chen, C. L. Chien, M. Zhang, J. Chen, Z. Liu, G. Wu, and X. X. Zhang, Phys. Rev. B **68**, 104430 (2003).

[78] L. Makinistian, M. M. Faiz, R. P. Panguluri, B. Balke, S. Wurmehl, C. Felser, E. A. Albanesi, A. G. Petukhov, and B. Nadgorny, Phys. Rev. B **87**, 220402(R) (2013).

[79] J. Loos and P. Novák, Phys. Rev. B **66**, 132403 (2002).

[80] J. M. D. Coey, in *Magnetism and Magnetic Materials*, p.412 (Cambridge University Press, New York, 2010).

[81] D. Khomskii, e-print arXiv:cond-mat/0101164v1.

[82] W. Weber, Z. Phys. B Condensed Matter **70**, 323 (1988).

[83] I. V. Solovyev, I. V. Kashin, and V. V. Mazurenko, Phys. Rev B **92**, 144407 (2015).

[84] P. Schlottmann, Phys. Rev. B **67**, 174419 (2003).

[85] K. Iwai, Y. Muraoka, T. Wakita, M. Hirai, T. Yokoya, Y. Kato, T. Muro, and Y. Tamenori, J. Appl. Phys. **108**, 043916 (2010).

[86] S. Blundell, *Magnetism in Condensed Matter*, Oxford University Press, 2014.

[87] R. Cheng, B. Xu, C. N. Borca, A. Sokolov, C. -S. Yang, L. Yuan, S. -H. Liou, B. Doudin, and P. A. Dowben, Appl. Phys. Lett. **79**, 3122 (2001).

[88] R. Cheng, T. Komesu, H.-K. Jeong, L. Yuan, S.-H. Liou, B. Doudin, P. A. Dowben, and Ya. B. Losovyj, Physics Letters A **302**, 211 (2002).

[89] C. F. Chang, D. J. Huang, A. Tanaka, G. Y. Guo, S. C. Chung, S.-T. Kao, S. G. Shyu, and C. T. Chen, Phys. Rev. B **71**, 052407 (2005).

[90] C. A. Ventrice, Jr., D. R. Borst, H. Geisler, J. van Ek, Y. B. Losovyj, P. S. Robbert, U. Diebold, J. A. Rodriguez, G. X. Miao, and A. Gupta, J. Phys. Condens. Matter **19**, 315207 (2007).

[91] M. Sperlich, C. König, G. Güntherodt, A. Sekiyama, G. Funabashi, M. Tsunekawa, S. Imada, A. Shigemoto, K. Okada, A. Higashiya, M. Yabashi, K. Tamasaku, T. Ishikawa, V. Renken, T. Allmers, M. Donath, and S. Suga, Phys. Rev. B **87**, 235138 (2013).

[92] S. Ishibashi, T. Namikawa, and M. Satou, Mater. Res. Bull. **14**, 51 (1979).

[93] P. G. Ivanov, S. M. Watts, and D. M. Linda, J. Appl. Phys. **89**, 1035 (2001).

[94] K. Sato, Prog. Cryst. Growth Charact. **11**, 109 (1985).

[95] P. J. Brown, K.-U. Neumann, A. Simon, F. Ueno. and K. R. A. Ziebeck, J. Phys.: Condens. Matter **17**, 1583 (2005).

[96] W. W. Kou and M. S. Seehra, Phys. Rev. B **18**, 7062 (1978).

[97] R. L. Kautz, M. S. Dresselhaus, D. Adler, and A. Linz, Phys. Rev. B **6**, 2078 (1972).

[98] S. Sudo and T. Miyadai, J. Phys. Soc. Jpn. **54**, 3934 (1985).

[99] Y. Takano, N. Uchiyama, S. Ogawa, N. Môri", Y. Kimishima, S. Arisawa, A. Ishii, T. Hatano, and K. Togano, Physica C **341**, 739 (2000).

[100] K. Sato, K. Adachi, T. Okamoto, and E. Tatsumoto, J. Phys. Soc. Jpn. **26**, 639 (1969).

[101] K. Adachi, M. Matsui, Y. Omata, H. Mollymoto, M. Motokawa, and M. Date, J. Phys. Soc. Jpn. **47**, 675 (1979).

[102] K. Adachi, K. Sato, and M. Takeda, J. Phys. Soc. Jpn. **26**, 631 (1969).

[103] T. Muro, T. Shishidou, F. Oda, T. Fukawa, H. Yamada, A. Kimura, S. Imada, S. Suga, S. Y. Park, T. Miyahara, and K. Sato, Phys. Rev. B **53**, 7055 (1996).

[104] G. Kirczenow, Phys. Rev. B **63**, 054422 (2001).

[105] R. Yamamoto, A. Machida, Y. Moritomo, and A. Nakamura, Phys. Rev. B **59**, 7793(R) (1999).

[106] H. Yamada, K. Terao, and M. Aoki, J. Magn. Magn. Mater. **177**, 607 (1998).

[107] S. K. Kwon, S. J. Youn, and B. I. Min, Phys. Rev. B **62**, 357 (2000).

[108] N. Wu, Y. B. Losovyj, D. Wisbey, K. Belashchenko, M. Manno, L. Wang, C. Leighton. and P. A. Dowben, J. Phys.: Condens. Matter **19**, 156224 (2007).

[109] G. L. Zhao, J. Callaway, and M. Hayashibara, Phys. Rev. B **48**, 781 (1993).

[110] L. Wang, T. Y. Chen, and C. Leighton, Phys. Rev. B **69**, 094412 (2004).

[111] V. N. Antonov, O. V. Andryushchenko, A. P. Shpak, A. N. Yaresko, and O. Jepsen, Phys. Rev. B **78**, 094409 (2008).

[112] T. Takahashi, Y. Naitoh, T. Sato, T. Kamiyama, K. Yamada, H. Hiraka, Y. Endoh, M. Usuda, and N. Hamada, Phys. Rev. B **63**, 094415 (2001).

[113] T. Sato, S. Souma, K. Sugawara, K. Nakayama, S. Raj, H. Hiraka, and T. Takahashi, Phys. Rev. B **76**, 113102 (2007).

[114] L. Wang, T. Y. Chen, C. L. Chien, and C. Leighton, Appl. Phys. Lett. **88**, 232509 (2006).

[115] L. Wang, T. Y. Chen, C. L. Chien, J. G. Checkelsky, J. Eckert, E. D. Dahlberg, K. Umemoto, R. M. Wentzcovitch, and C. Leighton, Phys. Rev. B **73**, 144402 (2006).

[116] M. Bowen, M. Bibes, A. Barthélémy, J.-P. Contour, A. Anane, Y. Lemaître, and A. Fert, Appl. Phys. Lett. **82**, 233 (2003).

[117] A. Gupta, X. W. Li, and G. Xiao, Appl. Phys. Lett. **78**, 1894 (2001).

[118] R. Skomski, J. Phys.: Condens. Matter **19**, 315202 (2007).

[119] R. Skomski and P. A. Dowben, Europhys. Lett. **58**, 544 (2002).

[120] P. A. Dowben and R. Skomski, J. Appl. Phys. **93**, 7948 (2003).

[121] P. A. Dowben and R. Skomski, J. Appl. Phys. **95**, 7453 (2004).

[122] J. M. De Teresa, A. Barthélémy, A. Fert, J. P. Contour, F. Montaigne, and P. Seneor, Science **286**, 507 (1999).

[123] S. Yuasa, A. Fukushima, T. Nagahama, K. Ando, and Y. Suzuki, Jpn. J. Appl. Phys. **43**,

L588 (2004).

[124] S. Yuasa, T. Nagahama, A. Fukushima, Y. Suzuki, and K. Ando, Nat. Mater. **3**, 868 (2004).

[125] W. H. Butler, X.-G. Zhang, T. C. Schulthess, and J. M. MacLaren, Phys. Rev. B **63**, 054416 (2001).

[126] W. H. Butler, Sci. Technol. Adv. Mater. **9,** 014106 (2008).

[127] J. A. Hertz and D. M. Edwards, J. Phys. F **3**, 2174 (1973).

[128] J. A. Hertz and D. M. Edwards, J. Phys. F **3**, 2191 (1973).

[129] V. Yu. Irkhin and M. I. Katsnelson, J. Phys. C **18**, 4173 (1985).

[130] M. I. Katsnelson and V. Yu. Irkhin, Phys. –Usp, **37**, 659 (1994).

[131] V. Yu. Irkhin, M. I. Katsnelson, and A. I. Lichtenstein, J. Phys.: Condens. Matter **19**, 315201 (2007).

[132] L. Chioncel, M. I. Katsnelson, R. A. de Groot, and A. I. Lichtenstein, Phys. Rev. B **68**, 144425 (2003).

[133] L. Chioncel, E. Arrigoni, M. I. Katsnelson, and A. I. Lichtenstein, Phys. Rev. B **79**, 125123 (2009).

[134] L. Chioncel, M. I. Katsnelson, G. A. de Wijs, R. A. de Groot, and A. I. Lichtenstein, Phys. Rev. B **71**, 085111 (2005).

[135] L. Chioncel, H. Allmaier, E. Arrigoni, A. Yamasaki, M. Daghofer, M. I. Katsnelson, and A. I. Lichtenstein, Phys. Rev. B **75**, 140406(R) (2007).

[136] L. Chioncel, Y. Sakuraba, E. Arrigoni, M. I. Katsnelson, M. Oogane, Y. Ando, T. Miyazaki, E. Burzo, and A.I. Lichtenstein, Phys. Rev. Lett. **100**, 086402 (2008).

[137] Y. Nagaoka, Phys. Rev. **147**, 392 (1966).

[138] M. I. Auslender and V. Yu. Irkhin, J. Phys. C: Solid State Phys. **18**, 3533 (1985).

[139] V. Yu. Irkhin, and M. I. Katsnelson, J. Phys.: Condens. Matter **2**, 7151 (1990).

[140] V. I. Anisimov, A. I. Poteryaev, M. A. Korotin, A. O. Anokhin, and G. Kotliar, J. Phys.: Condens. Matter **9**, 7359 (1997).

[141] K. Haule, J. H. Shim, and G. Kotliar, Phys. Rev. Lett. **100**, 226402 (2008).

[142] J. Sánchez-Barriga, J. Braun, J. Minár, I. Di Marco, A. Varykhalov, O. Rader, V. Boni, V. Bellini, F. Manghi, H. Ebert, M. I. Katsnelson, A. I. Lichtenstein, O. Eriksson, W. Eberhardt, H. A. Dürr, and J. Fink, Phys. Rev. B **85**, 205109 (2012)

CHAPTER 2. SPIN- AND ANGLE-RESOLVED PHOTOEMISSION SPECTROSCOPY

2.1 Brief Introduction

Electronic structure is a dominant component for understanding the physical properties of a solid. Here, “electronic structure” includes energies, momenta, and spins of electrons in the system. Determining experimentally all of these quantities helps understand the material completely, especially for spin-polarized materials such as ferromagnets,[1–4] Rashba metals,[5–10] and topological materials[11–15]. However, determination of spin polarization is not easy, in fact. Although spin-resolved and angle-resolved photoemission spectroscopy (SARPES) [16–18], point-contact Andreev reflection (PCAR) [19–21], spin-polarized tunneling spectroscopy [22–25], and x-ray magnetic circular dichroism (XMCD) [26–29] etc. have been reported as methods to observe spin polarization, it is difficult to determine the absolute value of spin polarization by spin-polarized tunneling spectroscopy and XMCD, although they can determine relative variation of spin polarization. Moreover it is also difficult to obtain information of momentum by the methods except for SARPES. Therefore, so far, SARPES is the most powerful technique to completely determine the spin-polarized band structure and absolute value of spin polarization.

SARPES had been developed from the late 1980s to the 1990s [16]. The figure of merit (FOM) of SARPES using a Mott spin detector, which is a typical spin detector, in which a spin orbit interaction is used was about 10^{-4} times of that of the spin-integrated ARPES [10]. Hence it had the feature that we have to sacrifice energy and angular resolutions to increase photoelectron intensity. 100 meV has been the practicable energy resolution of traditional SARPES, which is almost two orders lower than spin-integrated ARPES. Therefore, at the period, the research target of SARPES were valence band structures of typical ferromagnetic metals, Fe, Co, and Ni, because the characteristic energy scale of ferromagnet, determined by the exchange splitting, is 0.1–1 eV.

However, in the 2000s, a field investigating spin textures on solid surfaces have attracted attention by development of the spintronics technology and by discovery of topological insulators [30–37]. In this field, the research targets are Rashba-splitting surface bands and spin-polarized Dirac bands protected topologically. To determine their spin texture, the energy resolution approximately 10 meV or less had to be achieved. In 2010, Souma *et al.* increased photoelectron intensity by combining the high-intensity xenon plasma discharge lamp [38] with a mini Mott detector, by which the energy resolution of SARPES apparatus mounted reaches 8 meV[39]. In addition, this development of low-energy photon source (XeIα line: $h\nu$ = 8.437 eV) included enhancement of the bulk-sensitivity of SARPES measurements by the low-energy photon[38,40]. Bulk-sensitive measurements can probe the spin-resolved bulk electronic structures which dominate physical properties of materials, so that this light source has been a powerful tool to investigate spin-related exotic properties originating from the bulk, such as ferromagnets, Weyl semimetals, and noncentrosymmetric materials.[41–47]

As another useful spin detector, there is a very-low-energy electron diffraction (VLEED) spin detector reported in 1989 [48–50]. By using the VLEED spin detector and high-brightness synchrotron radiation, Okuda *et al.* have achieved 7.5 meV energy resolution.[51] Furthermore, recently, Yaji *et al*. have built SARPES apparatus with a high-intensity low-energy laser and the VLEED spin detector, achieving almost 1 meV energy resolution.[52] By these efforts, we have been able to observe fine spin textures of solid surfaces, accelerating drastically the researches on Rashba metals and topological materials, as shown in Fig. 2.1.[4,44,53,54]

On the other hand, investigations on ferromagnetic materials with a focus on sub-meV electronic structure near E_F are also an important subject for realization of potential magnet-based spintronics devices such as spin-polarized field-effect transistor [55]. The emergence of

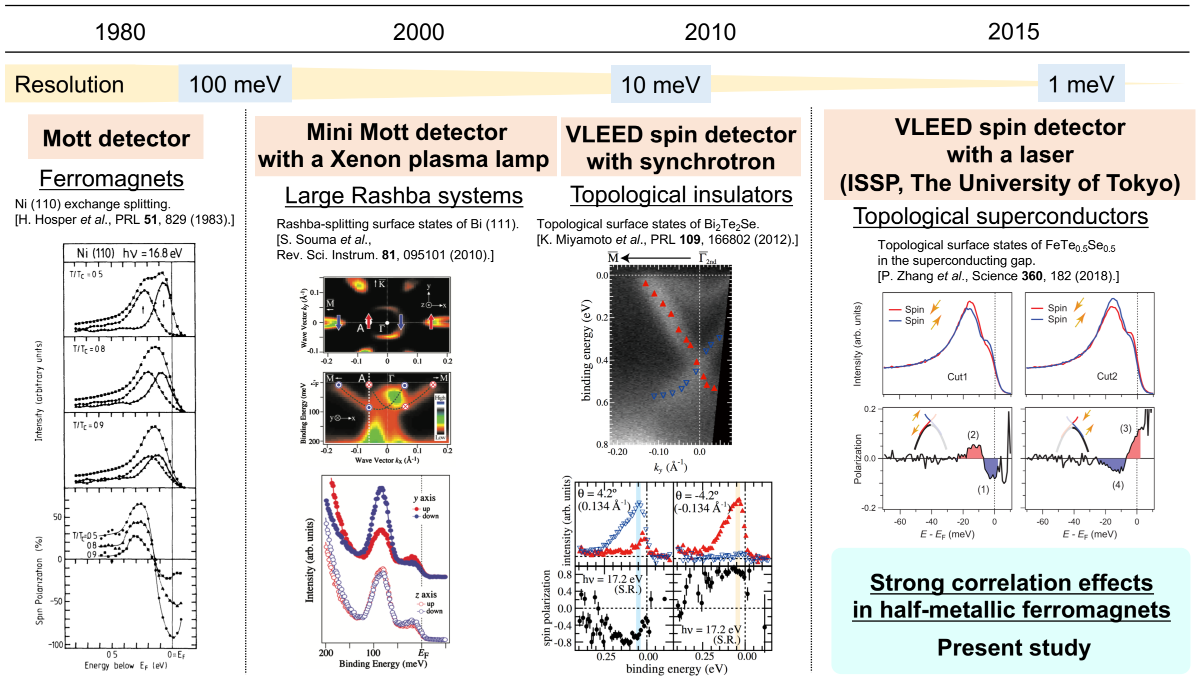

Fig. 2.1. Development of SARPES technique and history of subjects for SARPES study, with the position of the present study. Constructed by the author in reference to [4,44,53,54].

spintronics activated a foundation-research territory of ferromagnets dealing with many-body physics on spin-polarized conduction electrons [56,57]. An urgent issue for practical application of the potential spintronics devices is thermal spin depolarization of half-metals [30,31]. Although band models based on many-body physics have been proposed theoretically to explain the magnetotransport behavior through half-metal-based magnetic tunneling junctions [56], few SARPES studies have been reported so far, possibly due to the limitation of energy resolution. However, by the high-resolution SARPES apparatus, we can observe fine spin-resolved electronic structure of half-metals with sub-meV energy resolution. The spectroscopic studies can verify the theoretical models and would discover significant phenomena which has not attracted attention in the past.

In this chapter, we describe SARPES with a focus on fundamental principle of photoemission spectroscopy, spectral analysis, and spin detection.

2.2 Principles of Photoemission Spectroscopy

2.2.1 Theory of Photoemission

If a material is exposed to ultraviolet light, photoelectrons are emitted from its surface. The phenomenon is called *external photoelectric effect*, discovered by Heinrich Rudolf Hertz in 1887 [58]. Photoemission spectroscopy (PES) is the method in which the photoelectric effect is used. By PES, we can directly observe the energy distribution of electrons in a material. The process in which photoelectrons are emitted from a solid to vacuum is divided into the following three processes.

Process 1. Optical excitation of the electron in the solid
Process 2. Transport of the electron to the surface
Process 3. Escape of the electron into vacuum

This model which divides photoelectric emission into three processes is so-called *three-step model* [59].

In process 1, an electron absorbs a photon and transits to an excited state. The probability of this transition I obeys following relation:

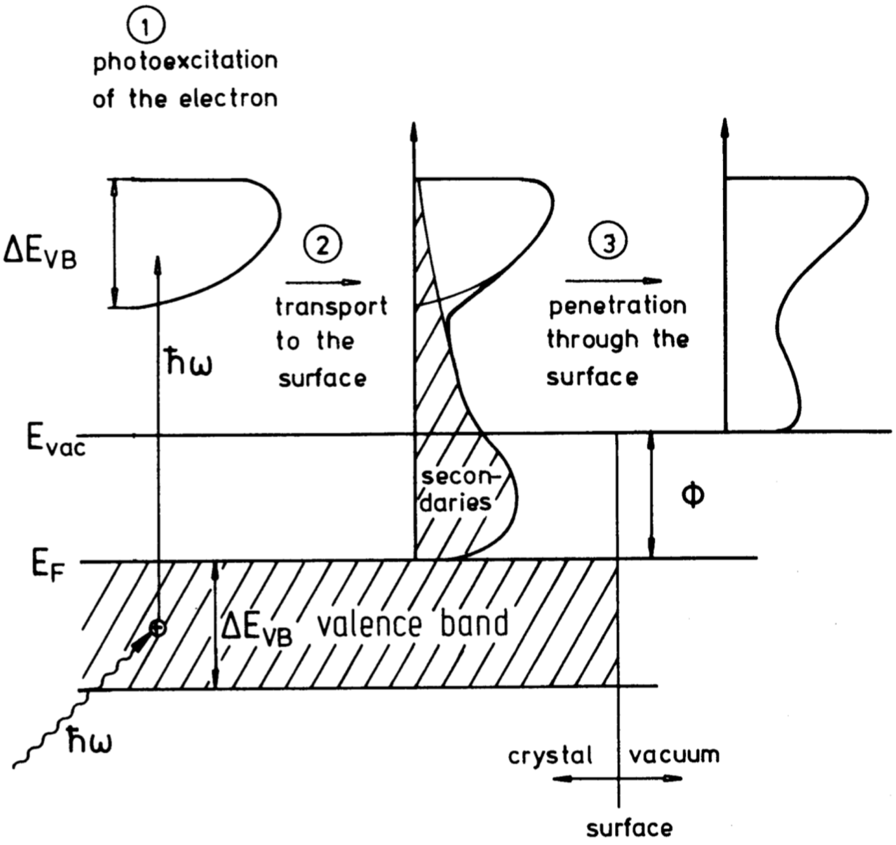

Fig. 2.2. Energy diagram for photoemission process based on three-step model. Taken from [60].

$$I \propto \left| \langle \Psi_f | \boldsymbol{A} \cdot \boldsymbol{p} | \Psi_i \rangle \right|^2 \tag{2.1}$$

where ψ_i and $\psi_f$represent wave functions of an initial state and a final state, respectively, and A and p are vector potential and the momentum operator, respectively. Equation 2.1 shows that this transition probability differs depending on the energy or polarization of light.

In process 2, the photoexcited electrons transfer to the solid surface with electron-electron and electron-phonon scattering. In this case, some electrons which scatters inelastically loses own energy. In addition, some electrons which are collided with the photoexcited electron obtains extra energy, and then the electrons escape from the atom. These electrons are called *secondary electrons*, and they are detected as background as shown as a shaded region in Fig. 2.2.

In process 3, only electrons whose component of the kinetic energy is sufficiently large to overcome the surface potential barrier can escape into the vacuum. However the electrons that do not have adequate kinetic energy are reflected inside the solid surface. This surface potential is called *work function* ϕ. The strict definition of work function is the temperature independent term of the work required to remove an electron from a metal.

In the photoelectron excitation, energy conservation is ideally held because one electron is excited by one photon. If electrons that have binding energy E_B in the solid are excited by photons whose energy is $h\nu$ and they are emitted into vacuum with kinetic energy E_K, we can write the binding energy E_B as

$$E_\mathrm{B} = h\nu - \phi - E_\mathrm{K} \tag{2.2}$$

We can obtain the binding energy of electrons by measuring the electron kinetic energy E_K and substituting the E_K into Eq. 2.2.

By measuring angular distribution of photoelectrons together with the kinetic energy, we can obtain band dispersions. This method is called angle-resolved photoemission spectroscopy (ARPES) which is a powerful tool to directly observe Fermi surface as well as band structures in metals. The key principle to determine the momentum of photoelectrons is space translation symmetry in crystals. In crystallized materials, the space translation symmetry is kept. At the surface, the space translation symmetry parallel to the surface is not broken also, while the symmetry perpendicular to the surface is broken. In general, a momentum is conserved when the space translation symmetry is held, as derived in quantum physics. Thus the parallel component of the wave vector $\mathrm{k}_{//}$ is conserved in the photoemission process:

$$k_{//} = K_{//} \tag{2.3}$$

where $k_{//}$ and $K_{//}$ are the crystal momentum in the crystal and the momentum out of the crystal, respectively. The relationship of Eq. 2.3 allows us to obtain the dispersion relation $E(k_{//})$ by ARPES. However the perpendicular component of the wave vector $k_\perp$ is not conserved and it is not even a good quantum number.

Showing the relationship between $K_{//}$ and E, we obtain the following equations:

$$\hbar K_{//} = \sqrt{2mE_\mathrm{K}}\sin\theta \tag{2.4}$$

$$\hbar K_{\perp} = \sqrt{2mE_\mathrm{K}}\cos\theta \tag{2.5}$$

where θ is an emission angle of a photoelectron, as defined in Fig. 2.3. Substituting Eq. 2.3 into Eq. 2.4, we obtain below:

$$\hbar k_{//} = \sqrt{2mE_\mathrm{K}}\sin\theta \tag{2.6}$$

On the other hand, in terms of the direction perpendicular to the surface, $K_\perp$ and $k_\perp$ are not equivalent. $k_\perp$ is shown as below:

$$\hbar k_{\perp} = \sqrt{2mE_\mathrm{K}\cos^2\theta + V_0} \tag{2.7}$$

where V_0 is an *inner potential* depending on materials. In the case of ideal two-dimensional materials, there is no $k_\perp$-dispersion, so that we can obtain the in-plane band dispersion at any $k_\perp$ points. However, in the case of three-dimensional materials, the inner potential should be

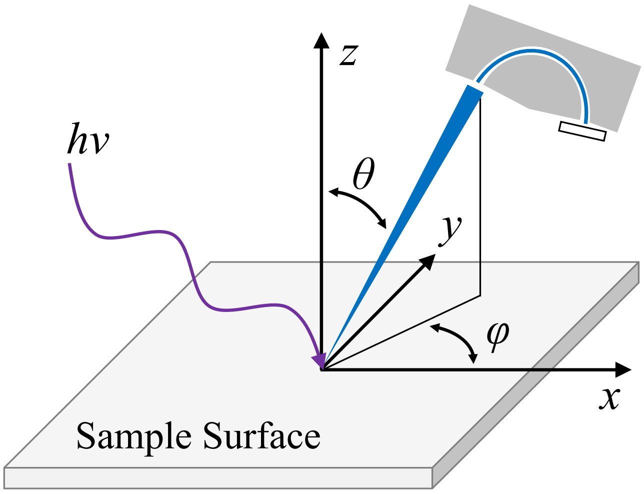

Fig. 2.3. Geometry of an ARPES experiment.

determined in order to identify the measuring $k_\perp$ point at the photon energy. From Eq. 2.7, we can determine V_0 by measuring photon-energy dependence of photoelectron intensity at $\theta = 0^\circ$, as known as the “normal-emission method”. By changing the excitation photon energy, we can vary E_K, corresponding to the change of $k_\perp$ as seen from Eq. 2.7. The energy distribution of photoelectrons varies periodically, because $k_\perp$-dispersion must have the periodicity of the Brillouin zone. By fitting the observed periodicity, we can determine V_0 experimentally.

In contrast, there is *one-step model* as another theoretical model explaining photoemission process. The one-step model takes inverse LEED wave functions for the final state of photoelectrons [61]. In this model, electrons of Bloch state are excited into a state that allows free propagation in vacuum but decays inside as leaving away from the surface. Then photoemission spectra can be calculated by the Fermi’s golden rule.

Along with the above-mentioned models, it should be noted that photoemission spectra are often calculated in terms of *sudden approximation*. Although a system can relax during the photoemission process, we assume that there is no time for the system to relax while the process. However, it is important to note that this approximation is true for high kinetic-energy photoelectrons.

2.2.2 One Particle Spectral Function

Starting from the three-step model, we can relate the photoemission spectra to the concept of one particle spectral function. For a given N-electron initial state ψ_i^N and a final state ψ_f^N, the transition probability for an optical excitation, w_{fi}, can be described by Fermi’s golden rule:

$$w_{fi} = \frac{2\pi}{\hbar}\left|\langle\psi_f^N|H_{\mathrm{int}}|\psi_i^N\rangle\right|^2\delta\left(E_f^N - E_i^N - h\nu\right)$$

(2.8)

where, $E_i^N = E_i^{N-1} - E_B^k$, $E_f^N = E_f^{N-1} - E_k$, H_{int} is the Hamiltonian describing the interaction between electrons and photons, E_B^k is the binding energy of the photoelectrons with kinetic energy of E_k and momentum k.

The Hamiltonian H_{int} takes the form as following:

$$H_{int} = \frac{e}{2mc}\left(\vec{A}\cdot\vec{p} + \vec{p}\cdot\vec{A}\right) - e\phi + \frac{e^2}{2mc^2}\vec{A}\cdot\vec{A}$$

$$\sim \frac{e}{mc}\vec{A}\cdot\vec{p}$$

(2.9)

where $\vec{A}$ and ϕ are vector and scalar potentials, respectively, and $\vec{p}$ is the momentum operator. In the second step of the equation, we assume: (i) $\phi = 0$, (ii) quadratic term in $\vec{A}$ is negligible with respect to the first term, which represents two photon processes, and (iii) $\nabla\cdot\vec{A} = 0$ because $\vec{A}$ is constant over atomic dimensions.

Within the sudden approximation, we can write the final state ψ_f^N as:

$$\psi_f^N = \Lambda\phi_f^{\vec{k}}\psi_f^{N-1} \tag{2.10}$$

where Λ is an antisymmetric operator, $\phi_f^{\vec{k}}$ is the wavefunction of photoelectron with momentum $\vec{k}$, and ψ_f^{N-1} is the wavefunction for the final state of remaining ($N-1$) electron system. The final state of ($N-1$) electron system can be one of the excited states m, defined by eigenfunction ψ_m^{N-1} and corresponding eigenvalue E_m^{N-1}. For calculating the total transition probability, one should integrate over all excited states m.

For the initial state, we assume Hartree-Fock formalism and simply use the form:

$$\psi_i^N = \Lambda\phi_i^{\vec{k}}\psi_i^{N-1} \tag{2.11}$$

By Eqs. 2.10 and 2.11, we can rewrite Eq. 2.8 as:

$$\langle\psi_f^N|H_{\mathrm{int}}|\psi_i^N\rangle = \left\langle\psi_f^{\vec{k}}\middle|H_{\mathrm{int}}\middle|\psi_i^{\vec{k}}\right\rangle\langle\phi_m^{N-1}|\phi_i^{N-1}\rangle \tag{2.12}$$

Here, we define $\left\langle\psi_f^{\vec{k}}\middle|H_{\mathrm{int}}\middle|\psi_i^{\vec{k}}\right\rangle \equiv M_{f,i}^{\vec{k}}$, and we call it the one-electron dipole matrix element.

Integrating Eq. 2.8 based on above equations, we obtain the photoemission intensity $I\left(\vec{k}, E_k\right)$ as:

$$I\left(\vec{k},E_k\right)=\sum_{f,i} w_{f,i}$$

$$\sim \sum_{f,i}\left|M^{\vec{k}}_{f,i}\right|^2 \sum_{m}\left|c_{m,i}\right|^2 \delta\left(E_k+E^{N-1}_m-E^N_i-h\nu\right)$$

(2.13)

where $\left|c_{m,i}\right|^2=\left\langle \phi^{N-1}_m \middle| \phi^{N-1}_i \right\rangle^2$ is the probability that removal of an electron results in the exited state *m* for the ($N-1$) electron system. Here, we obtain $\phi^{N-1}_i=\phi^{N-1}_{m_0}$, and the integral $\left|c_{m,i}\right|^2$ becomes unity for $m = m_0$. Then, if the dipole matrix element is nonzero, a photoemission spectrum become a set of delta functions given by the Hartree-Fock energy $E^{\vec{k}}_{\mathrm{B}}=-\epsilon_{\vec{k}}$, known as *Koopmans Theorem*. However, when electron correlation are not negligible in the system, Koopmans theorem is no longer true, and the photoemission spectra deviate from the one-electron spectra.

Although the above descriptions in terms of Fermi's golden rule provides the basics, one can alternatively utilize the formulation by Green's functions to deal with the photoemission in correlated electron systems. One-electron Green's function $\mathcal{G}\left(\vec{k},E\right)=G^{+}\left(\vec{k},E\right)+G^{-}\left(\vec{k},E\right)$ is described as:

$$G^{\pm}\left(\vec{k},E\right)=\sum_{m}\frac{\left|\left\langle \psi^{N\pm1}_m \middle| c^{\pm}_{\vec{k}} \middle| \psi^N_i \right\rangle\right|^2}{E-E^{N\pm1}_m+E^N_i\pm i\eta}$$

(2.14)

Where $c^{+(-)}_{\vec{k}}$ is the creation (annihilation) operator with wave vector $\vec{k}$. ψ^N_i is the *N*-particle initial state wavefunction, and we consider the sum over all ($N \pm 1$)-particle eigenstates with eigenenergies of $E^{N\pm1}_m$, and η is a positive infinitesimal number.

Using the Dirac identity:

$$\frac{1}{x\pm i\eta}=\mathcal{P}\left(\frac{1}{x}\right)\mp i\pi\delta(x) \quad (\mathcal{P}\text{: the principle value}) \tag{2.15}$$

And the equation that relates the retarded one-particle Green's function $G\left(\vec{k},E\right)=G^{+}\left(\vec{k},E\right)+\left[G^{-}\left(\vec{k},E\right)\right]^{*}$ to the one-particle spectral function $A\left(\vec{k},E\right)$:

$$G\left(\vec{k},E\right)=\int_{-\infty}^{\infty}dE'\frac{A\left(\vec{k},E\right)}{E-E'-i\eta}$$

(2.16)

One obtains:

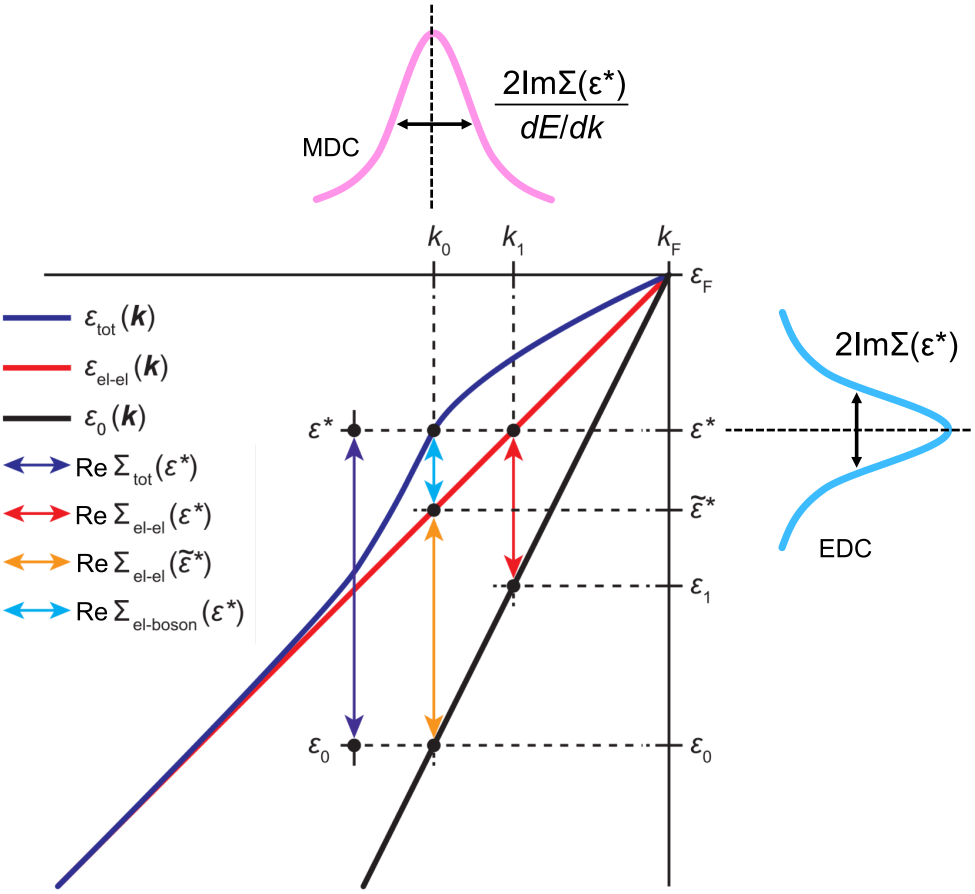

Fig. 2.4. Schematic illustration of the energy-band renormalization. Taken from [62].

$$A(\vec{k},E) = \frac{1}{\pi}\mathrm{Im}G(\vec{k},E)$$

(2.17)

Here,

$$A^{\pm}(\vec{k},E) = \sum_m \left|\langle\psi_m^{N\pm1}|c_{\vec{k}}^{\pm}|\psi_i^N\rangle\right|^2 \delta(E - E_m^{N\pm1} + E_i^N)$$

(2.18)

where $A^-(\vec{k},E)$ represents the one-particle removal spectra, which can be measured by photoemission spectroscopy. Alternatively, $A^+(\vec{k},E)$ represents the one-particle addition spectra, probed by inverse photoemission spectroscopy.

To incorporate electron–electron and/or electron–boson interaction, one can correct the Green's function with the electron's proper self-energy:

$$\Sigma(\vec{k},E) = \mathrm{Re}\Sigma + i\mathrm{Im}\Sigma$$

(2.19)

Here, $\Sigma_{\mathrm{tot}} = \Sigma_{\mathrm{el-el}} + \Sigma_{\mathrm{el\text{-}boson}} + \Sigma_{\mathrm{el\text{-}impurity}}$ where $\Sigma_{\text{el–el}}$, $\Sigma_{\text{el–boson}}$, $\Sigma_{\text{el–impurity}}$, and Σ_{tot} are self-energies derived from electron–electron correlation, electron–boson coupling, interaction with impurities, and total self-energy, respectively. Note that ReΣ provides the energy renormalization of an electron with band energy ϵ_k and momentum $\vec{k}$ in a correlated system, and ImΣ provides the lifetime of quasiparticle, obtained from width of a peak structure of a photoemission spectrum (see Fig. 2.4). Note also that ReΣ and ImΣ must obey Kramers-Kronig relation because of the causality. Then, Green's function and spectral function can be represented as:

$$G(\vec{k},E)=\frac{1}{E-\epsilon_k-\Sigma(\vec{k},E)} \tag{2.20}$$

$$A(\vec{k},E)=-\frac{1}{\pi}\frac{\mathrm{Im}\Sigma(\vec{k},E)}{\left[E-\epsilon_k-\mathrm{Re}\Sigma(\vec{k},E)\right]^2+\left[\mathrm{Im}\Sigma(\vec{k},E)\right]^2} \tag{2.21}$$

Therefore, useful information relevant to the self-energy of quasiparticles can be obtained from photoemission spectra.

2.2.3 Matrix Element Effect

The photocurrent can be varied significantly depending on the experimental conditions, since the one-electron dipole matrix element $\left|M_{f,i}^{\vec{k}}\right|^2$ depends on the electron momentum, the energy of incident photons, and the polarization of photons. Using the commutation relation $\vec{p}/m = -i/\hbar[\vec{x},H]$, we can express the matrix element as:

$$\left|M_{f,i}^{\vec{k}}\right|^2 \propto \left|\left\langle\psi_f^{\vec{k}}\middle|\vec{e}\cdot\vec{x}\middle|\psi_i^{\vec{k}}\right\rangle\right|^2 \tag{2.22}$$

where $\vec{e}$ shows the unit vector along the polarization direction of the vector potential.

Although actual matrix elements are very difficult to be evaluated, simple symmetry and parity arguments can tell if a given condition allows the emission of photoelectrons [63]. In order to have finite photoemission intensity, the whole integrand in the overlap integral must be even under the reflection with respect to the mirror plane. Furthermore, the final state wavefunction is restricted to be even; otherwise final states would be zero on the mirror plane and at the detector. These arguments lead us to the following general rule,

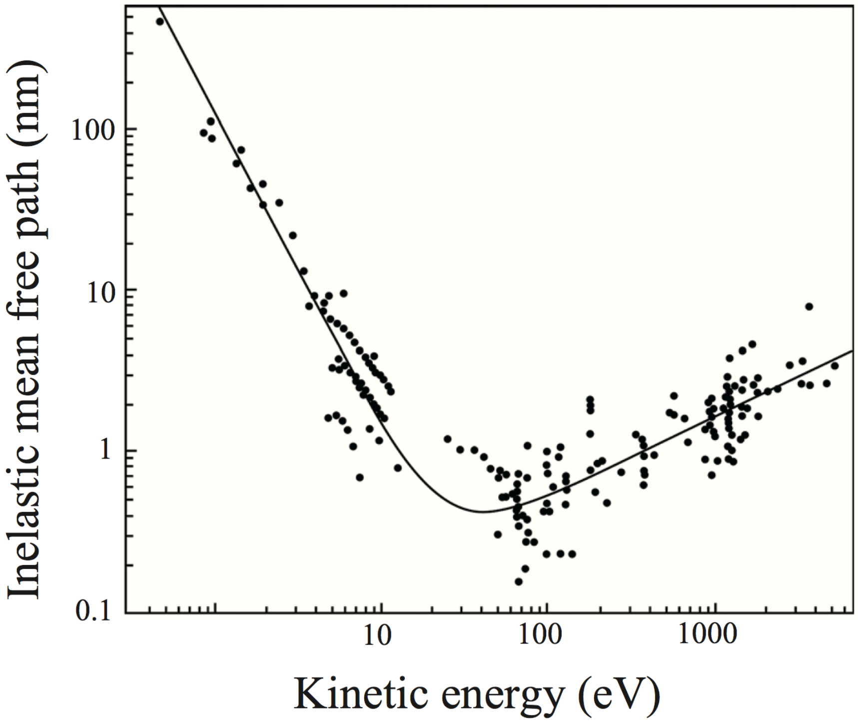

Fig. 2.5. Relationship between the kinetic energy of photoemitted electrons and inelastic mean free path. This relationship is usually referred as *Universal Curve*.Taken from [40].

$$\left\langle \psi_f^{\vec{k}} \middle| \vec{A}\cdot\vec{p} \middle| \psi_i^{\vec{k}} \right\rangle \begin{cases} \psi_i^{\vec{k}} \quad \text{even} \quad \langle + | + | + \rangle \quad \rightarrow \quad \vec{A}\ \text{even} \\ \psi_i^{\vec{k}} \quad \text{odd} \quad \langle + | - | - \rangle \quad \rightarrow \quad \vec{A}\ \text{odd} \end{cases} \tag{2.23}$$

where + and – symbols in the bracket represent even and odd parity, respectively. We can utilize the characteristics to obtain information of orbital-selective band structures.

2.2.4 Probing Depth

Photoemission spectroscopy is generally referred as a surface sensitive technique. The probing depth is mainly determined by the inelastic mean free path of photoelectrons in the solid. A relationship between the kinetic energy of photoelectrons and the inelastic mean free path, usually referred as a Universal Curve, is shown in Fig. 2.5. Even though photons in ultraviolet or soft x-ray regions can penetrate the sample by several thousands Å – several µm, there are various deexcitation processes that prevent excited photoelectrons from reaching the surface. One of the most important deexcitation processes is the interband transition due to electron–electron scattering which usually has the energy scale of several tens of electron volts. Therefore, photoelectrons, whose kinetic energy is around the energy scale of interband

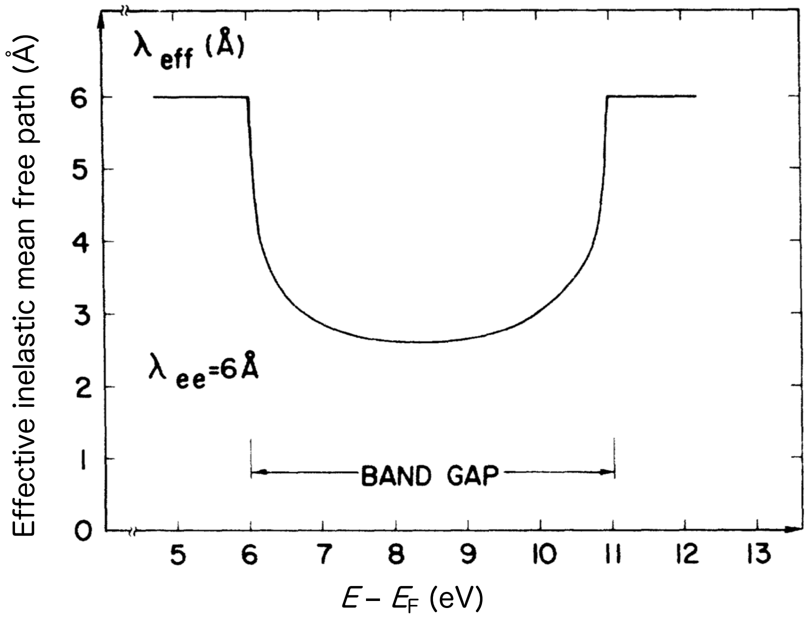

Fig. 2.6. Schematic diagram of the effective inelastic mean free path λ_{eff} for the band-gap case of photoemission. A constant bulk inelastic mean free path between electron–electron scattering λ_{ee} = 6 Å, corresponding to λ estimated from the Universal Curve, has been assumed, with a 5-eV band gap extending from 6 to 11 eV above E_{F}. Taken from [64].

transitions, are most easily scattered. Since low kinetic-energy photoelectrons cannot excite interband transitions and high-energy photoelectrons have smaller collision cross-sections, electron's inelastic mean free path shows its minimum at around E_{k} = 50–100 eV [40]. However, note that the probability of the interband transition depends on electronic structure of the material. Therefore, if there are a lot of bands closely located each other in the unoccupied side, for example in *d*- and *f*-electron systems, the probing depth does not perfectly obey the universal curve.

As one of the cases that the inelastic mean free path of photoelectrons does not obey the universal curve, 'band-gap case' is known. When an electron is excited into a band-gap region in which there is no state, the final state within the solid consists only of surface evanescent waves which rapidly decay into the solid with a decay length λ_{eff} [65]. An example of the simulated λ_{eff} is shown in Fig. 2.6. Note in Fig. 2.6 that even if the damping due to electron-electron scattering is large (e. g., $\lambda_{ee} \sim 6$ Å where λ_{ee} represents the inelastic mean free path between electron–electron scattering events), damping is significantly increased in the gap region ($\lambda_{\mathrm{eff}} \sim 3$ Å at 8.5 eV) due to the evanescent wave decay. This effect can strongly limit the probing depth of the photoemission spectroscopy, mainly when using low energy excitation photon below $h\nu = 10$ eV.

2.2.5 $k_\perp$-Broadening Effect

By photoemission spectroscopy measurements by typical ultraviolet light whose energy is 20–40 eV, the escape depth of photoelectrons is estimated to be 5–10 Å as described above. Since we can detect only photoelectrons initially confined in the surface region, the momentum along the direction parallel to the surface ($k_\perp$) is broadened due to the uncertainty $\Delta x \Delta p \geq \hbar$. If the probing depth is assumed to be 5 Å, the broadening of $k_\perp$ ($\Delta k_\perp$) is estimated to be 0.2 Å^{-1}. When observing the $k_\perp$-broadening effect, we obtain band structure integrated in a $k_\perp$ window in the Brillouin zone even if the measurements are performed along in-plane direction. This effect often prevents from observing clear band dispersions by ARPES.

2.2.6 Photoemission-Spectral Intensity

The photoemission-spectral intensity $I(k,\omega)$ observed by actual measurements can be represented as:

$$I^\sigma(k,\omega) = I_0^\sigma(k) \sum_{\delta k} \int d\omega' A^\sigma(k',\omega') f(\omega') R(\omega,\omega') + \mathrm{BG}^\sigma \tag{2.24}$$

where $I_0(k) \propto \left|\langle \psi_f^k | A \cdot p | \psi_i^k \rangle\right|^2$ including matrix element effects described above, $f(\omega)$ represents the Fermi-Dirac distribution function, R represents the energy resolution of the apparatus. The summation with respect to k is operated for describing the spectral broadening derived from the finite momentum resolution. BG is the background term including mainly two contributions: backgrounds due to second order light by using a grating and due to secondary electrons. The index σ indicates spin character, ↑ or ↓. Eq. 2.24 indicates that we can reproduce a photoemission spectrum from a spectral function by multiplying by Fermi-Dirac distribution function, convolving with a distribution function whose width corresponds to the energy resolution (typically Gaussian), multiplying by a coefficient $I_0(k)$, and adding background contribution.

2.2.7 Fermi-Dirac-distribution-function (FD) Dividing Analysis

One can obtain electronic structures above E_F by dividing the photoemission spectra by the Fermi-Dirac distribution function. A simple analysis is to divide the experimental photoemission spectrum without background above E_F by the Fermi-Dirac distribution function at measured temperatures convoluted with the experimental resolution. This analysis is valid when the spectral function $A(k, \omega)$ does not depend on energy ω in the energy region determined by the width of Fermi cut, $5k_BT$. In fact, this FD-dividing analysis has been applied for various systems [2,65–67].

Note that we have to consider effects of finite energy resolution of the photoemission measurements in the FD-dividing analysis. The FD-dividing analysis cannot be simply applied for systems which have a state standing at E_F. For this case, obtaining the spectral function from a photoemission spectrum should be treated as an “inverse problem”. That is, we have to extrapolate the spectral function from the photoemission spectrum by a deconvolution analysis: $\int d\omega' A^{\sigma}(k,\omega') f(\omega') R(\omega,\omega') \to A^{\sigma}(k,\omega) f(\omega)$. As a way to perform the deconvolution analysis, the maximum entropy method is used [68]. After the deconvolution analysis, we can easily obtain $A^{\sigma}(k, \omega)$ by dividing the deconvolution result by $f(\omega)$.

2.3 Spin Detector

2.3.1 Brief Introduction of Spin Detectors

Table 2.1. List of electron spin detectors with typical values of operation voltage, effective Sherman function (S_{eff}), figures of merit (FOM) showing total efficiency.

Detectors	**Detection Principle**	**Operation voltage**	S_{eff}	**FOM**	**Target**
Mott detector[39,69,70]	Spin-orbit interaction	20 ~ 100 keV	0.06 ~ 0.2	1 ~ 5 × 10^{-4}	Au or Th thin film
SPLEED[71,72]	Spin-orbit interaction	~ 150 eV	0.2 ~ 0.3	1 ~ 2 × 10^{-4}	W single crystal
Diffuse scattering[73]	Spin-orbit interaction	~150 eV	~ 0.2	~ 1 × 10^{-4}	Au thin film
VLEED[10,50,51]	Exchange interaction	6 ~ 10 eV	0.3 ~ 0.4	~ 10^{-2}	Fe – O on MgO(001)

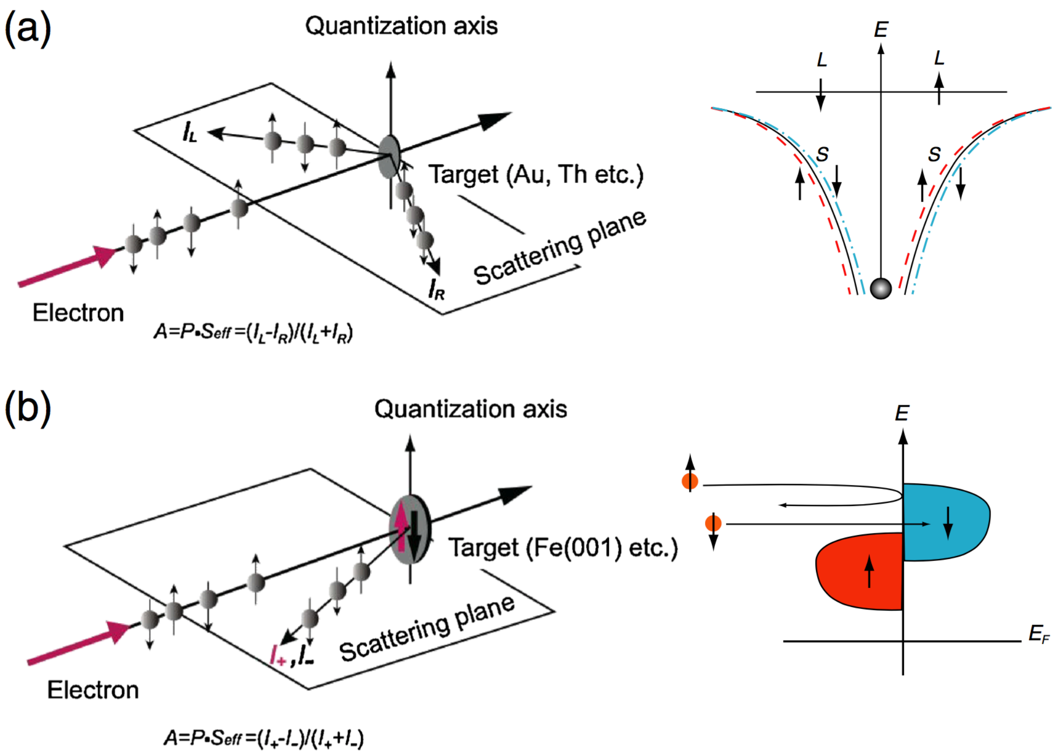

Fig. 2.7. Schematic illustrations of electron spin detection with (a) Mott spin detector and (b) VLEED spin detector. The principles of both methods are also schematically indicated on the right panels of each illustration. Taken from [10].

Generally, photoelectron spins are measured by adding a spin detector to an ARPES analyzer by SARPES technique. A part of photoelectrons from a material enter a spin detector after they pass through an energy analyzer. By leading a part of electrons to a spin detector, we can simultaneously observe energies and spins of photoelectrons. Interactions that have been commonly utilized for the spin-dependent scattering of electrons so far are spin–orbit and spin-exchange interactions. As summarized in Table 2.1, most of the techniques developed so far utilize spin–orbit interaction. These techniques are the Mott detector, spin low energy electron diffraction (SPLEED) detector, and diffuse scattering detector. All these detectors realize spin resolution by spin-dependent electron scattering by heavy material targets such as Au, although their operation energies (kinetic energy of injecting electron) are very high in a broad range from 300–500 eV to 100 keV. Among these spin–orbit interaction basis detectors, the Mott detector is most commonly used for SARPES measurement.

Mott spin detectors have high stability and measure SARPES spectra for 2 quantization axes simultaneously. However, the efficiency characterized by FOM is two orders lower than that of very-low-energy-electron diffraction (VLEED) detector. The most remarkable feature of VLEED detector is its high FOM defined as $(I/I_0)S_{\mathrm{eff}}$, where I_0 and I are intensities of electrons

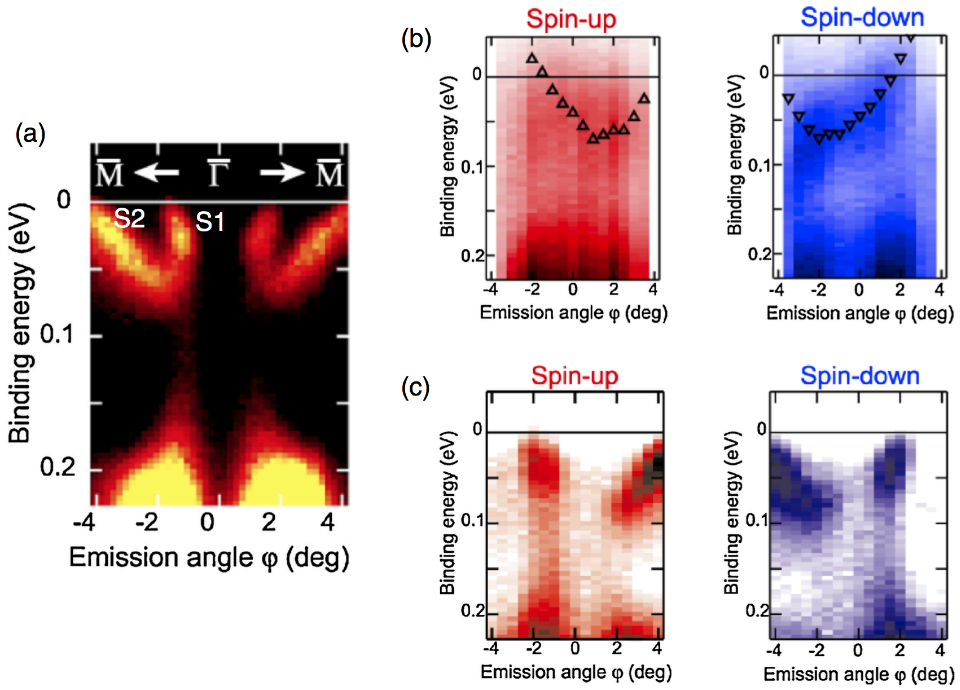

Fig. 2.8. Comparison of SARPES image map taken by apparatus with Mott spin detector with that taken by apparatus with VLEED spin detector .(a) Band dispersion of the surface states (S1 and S2) of Bi (111) obtained by the spin-integrated ARPES measurement. (b) Spin-up and spin-down dispersion of Bi(111) surface states observed by the conventional SARPES apparatus with Mott detector and (c) the same as (b) but by the SARPES apparatus with VLEED spin detector. Taken from [10].

entering the spin detector and of electrons detected after scattered by the target, respectively. S_{eff} is *effective Sherman function* used to obtain spin polarization as:

$$P = \frac{1}{S_{\mathrm{eff}}}\frac{I^{+} - I^{-}}{I^{+} + I^{-}} = \frac{I^{\uparrow} - I^{\downarrow}}{I^{\uparrow} + I^{\downarrow}} \tag{2.25}$$

where P is spin polarization, $I^{+(-)}$ is photoelectron intensity observed by the detector on configuration for detecting up (down) spin electrons. S_{eff} indicates the spin-resolving power of the spin detector, having a value between 1 and 0. From Table 2.1, since S_{eff} of VLEED spin detector is approximately at most 2 times larger than that of Mott spin detector, the main factor of the large FOM of VLEED spin detector is I/I_0. This means that the reflectance of photoelectrons for the target in VLEED spin detector is much larger than that in Mott spin detector. Nevertheless, VLEED spin detector has a disadvantage that the surface of the ferromagnetic target, mainly using Fe (001), is unstable, causing aging of the value of S_{eff}. This prevents from obtaining accurate spin polarization. For this disadvantage, it was reported that the stability of Fe (001) surface is highly improved by fabricating Fe(100)-p(1×1)O by

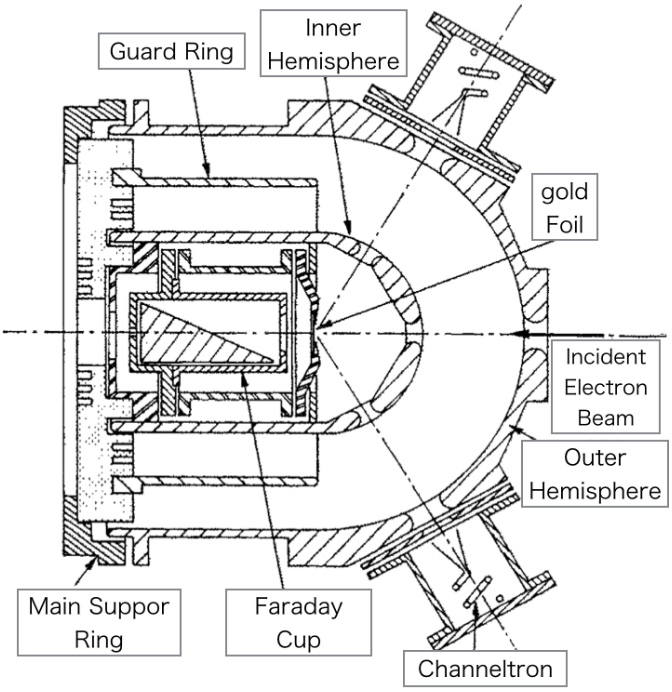

Fig. 2.9. Schematic illustration of Mott spin detector. Taken from [74].

oxidizing the Fe surface [50]. According Ref. 50, the target of the oxidized Fe surface can be used for several weeks. Even if the surface quality degrades, the spin-resolving power is repaired by annealing approximately at 600˚C. Furthermore, the asymmetry of the reflectance for spin up and spin down electrons of the oxidized surface is larger than that of Fe (100) clean surface, indicating that Fe (100)-p(1×1)O is one of the most ideal target for VLEED spin detector.

The schematic view of scattering and of principles for Mott spin detector and VLEED spin detector is shown in Fig. 2.7. In Mott spin detector, *Mott scattering* is used to resolved the electronic spins, while in VLEED spin detector, difference of reflectance for spin up and spin down electrons of the target is used. In measurements using Mott spin detector, we have to sacrifice the energy resolution due to its low FOM. On the other hand, by using VLEED spin detector, we can practically perform high-resolution measurements. In Fig. 2.8, the comparison of SARPES image map taken by apparatus with Mott spin detector with that taken by apparatus with VLEED spin detector. It is evident that the spin-polarized surface bands of Bi(111) obtained using VLEED spin detector is much clearer than that using Mott spin detector. By the dramatic improvement by development of VLEED spin detector, we can investigate spin-polarized fine band structures in a shorter time.

In following subsections, principles of the spin detectors are described with a focus on Mott

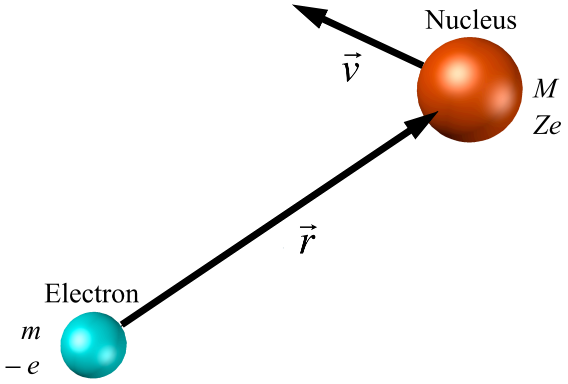

Fig. 2.10. Schematic view of static system of an electron in an atom.

detector and VLEED spin detector, used in the present study. In addition, procedures of data analysis of SARPES spectra are described.

2.3.2 Principle of Electron Spin Detection

A. Mott spin detector

A Mott spin detector has the structure shown in Fig. 2.9. Incident electrons accelerated by high-voltage are scattered at a target or are transmitted through a target. When incident electrons are scattered by a Au target in the spin detector, they are scattered depending on their own spin due to the spin-orbit interaction with an Au atom.

When we discuss the spin-orbit interaction, we focus on the system where a nucleus whose atomic number is Z circulates around an electron with an angular momentum L, as shown in Fig. 2.10. In this situation, the electron feels an effective magnetic field B_{eff} due to a circle movement of the nucleus. The electron has a magnetic moment μ_e due to its spin angular momentum. The Zeeman energy V_{LS} due to the interaction between μ_e and B_{eff} is given as:

$$V_{\mathrm{LS}} = -\boldsymbol{\mu}_{\mathrm{e}} \cdot \boldsymbol{B}_{\mathrm{eff}} \tag{2.26}$$

Then, using the nuclear velocity v and the electric field $\boldsymbol{E} = (Ze / r3)\ \boldsymbol{r}$ (bold-faced characters represent vector) which the electron feels from the nucleus, we can write $\boldsymbol{B}_{\mathrm{eff}}$ as:

$$\boldsymbol{B}_{\mathrm{eff}} = \frac{1}{c}\boldsymbol{v} \times \boldsymbol{E} = \frac{Ze}{cr^3}\boldsymbol{v} \times \boldsymbol{r} = \frac{Ze}{mcr^3}\boldsymbol{L} \tag{2.27}$$

By using an electron spin angular momentum $\boldsymbol{L}$ and Landé g factor, an electron magnetic moment $\boldsymbol{\mu}_{\mathrm{e}}$ is given as:

$$\boldsymbol{\mu}_{\mathrm{e}} = -\frac{g_{\mathrm{s}}e}{2mc}\boldsymbol{S} \tag{2.28}$$

From Eqs. 2.27 and 2.28, Eq. 2.26 is rewritten as:

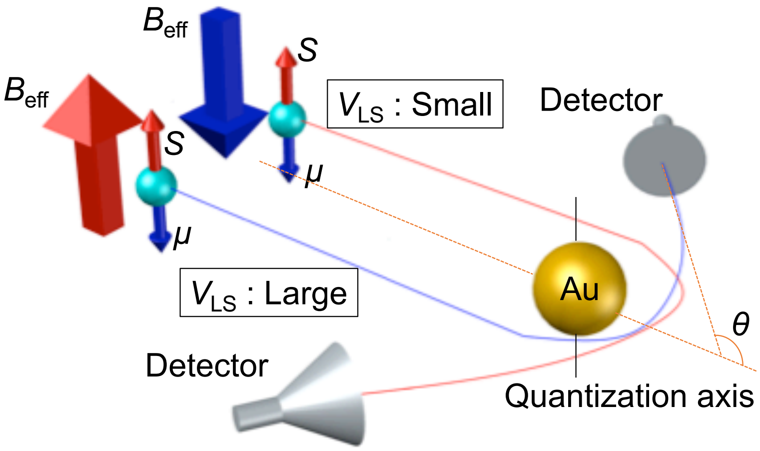

Fig. 2.11. Schematic view of scattering by spin-orbit interaction based on classical picture. Blue balls represent photoelectrons.

$$V_{\mathrm{LS}} = \frac{g_s e^2 Z}{2m^2 c^2 r^3} \boldsymbol{S} \cdot \boldsymbol{L} \tag{2.29}$$

Equation 2.29 is represented by the multiplication of an electron spin angular momentum $\boldsymbol{S}$ and a nuclear orbit angular momentum $\boldsymbol{L}$. Thus V_{LS} is called *spin-orbit interaction potential*. From Eq. 2.29, the higher the atomic number Z is or the nuclear velocity with respect to the electron is, the higher the spin-orbit interaction potential is. Thus, a stable Au polycrystalline thin film (atomic number $Z = 79$) are often used as a target of Mott detectors. In the detector, incident electrons are much accelerated to enhance the relativistic effect for electrons. The reason why a thin film is used as the target is that a rate of secondary electrons that lose their information of spins in a material by multiple scattering must be decreased.

Figure 2.11 shows a schematic view of scattering by spin-orbit interaction based on classical picture. An electron incident upon a Au target has potential V_{SL} represented in Eq. 2.29 which implies that the potential depends on the direction of rotation and the spin state of the incident electron.

For the scattering by the spin-orbit interaction, called *Mott scattering*, differential scattering cross-section $d\sigma(\theta)/d\Omega$ of electrons scattered with an angle θ defined in Fig. 2.11 which enter a Au thin film depends on a spin direction normal to scattering plane. $d\sigma(\theta)/d\Omega$ is given as:

$$\frac{d\sigma(\theta)}{d\Omega} = I_0(\theta)(1 + S(\theta)\boldsymbol{P} \cdot \hat{n}) \tag{2.30}$$

where $I_0(\theta)$, $\boldsymbol{P}$ and $\hat{\boldsymbol{n}}$ are differential scattering cross-section with respect to non-polarized electrons, spin polarization vector of incident electrons and unit vector normal to the scattering plane, respectively. Furthermore, the asymmetry function $A(\theta)$ is defined as:

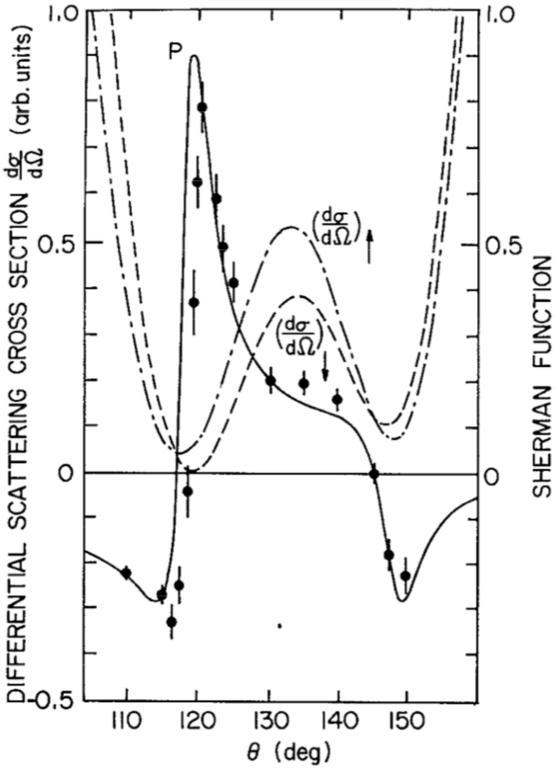

Fig. 2.12. Calculated differential scattering cross sections for spin up and spin down electrons incident at 300 eV on mercury atoms, and calculated Sherman function S(*θ*). Taken from [74].

$$A(\theta) \equiv \frac{\sigma_{\uparrow}(\theta) - \sigma_{\downarrow}(\theta)}{\sigma_{\uparrow}(\theta) + \sigma_{\downarrow}(\theta)} = PS(\theta) \tag{2.31}$$

where P and $S(\theta)$ are spin polarization of incident electrons and Sherman function, respectively. Sherman function is a quantity which relates spin polarization to asymmetry of the scattering. A θ-dependence of the Sherman function is shown in Fig. 2.12, which has the maximum at $\theta \sim 120^\circ$ [74]. Therefore, in Mott spin detectors, electron detectors, typically channeltrons, are generally mounted at $\theta = \pm 120^\circ$. The acceptance angle of channeltrons are optimized to maximize the FOM. "*Effective*" Sherman function, as mentioned above, is the intrinsic quantity of the apparatus, while Sherman function is determined by only a kind of a target atom.

B. VLEED spin detector

In VLEED spin detector, the asymmetry of the reflectance for spin up and spin down electrons is produced by the difference of unoccupied density of states (DOS) of the target. As in Fig. 2.7, in the VLEED spin detector, the target for scattering electron is ferromagnetic materials. The probability of electron absorption and reflection is proportional to the DOS of the unoccupied state of materials [75], and one can deduce information on unoccupied band structures of materials by measuring the absorption or reflection of a low energy electron as a function of its energy and injection angle. This is the principle of VLEED spin detection. In the case of the ferromagnetic materials, the unoccupied state is not in balance with the DOS owing to the exchange splitting of the electron bands. Therefore, the probabilities of electron absorption and reflection must be different between the case of up spin electron injection and down spin electron injection. If one measures the intensity of absorbed or reflected electrons by a magnetized target, one can determine the spin polarization of incoming electrons. In a real VLEED spin detector, we measure the intensities of reflected electrons by plus and minus magnetized ferromagnetic targets (I^+ and I^-) and obtain the asymmetry between the two. Target magnetization is changed by applying magnetic field to the target and the intensities, I^+ and I^-, are counted by a single electron detector. That is, the electron trajectories are the same in both I^+ and I^- electron measurements. Thus, in general, the VLEED spin detector possesses smaller instrumental asymmetry, allowing us to analyze SARPES data without cancel-out analysis for asymmetric contribution originating from apparatus, as described below.

2.3.3 Analysis of Spin-Polarized Photoemission Spectrum

For data taken by apparatus with Mott spin detector, the relation with spin polarization P, up (down) electron number $N_{\uparrow(\downarrow)}$ and number of electrons detected by a right (left) detector $N_{\mathrm{R(L)}}$ is given as:

$$P = \frac{N_\uparrow - N_\downarrow}{N_\uparrow + N_\downarrow} = \frac{1}{S_{\mathrm{eff}}(\theta)} \cdot \frac{N_\mathrm{R} - N_\mathrm{L}}{N_\mathrm{R} + N_\mathrm{L}} \tag{2.32}$$

As seen in Eq. 2.32, we cannot know the value of spin polarization P from N_R and N_L detected by the detector for which S_{eff} is not determined; in order to obtain P by SARPES, we must determine the S_{eff} of the detector. The way to determine S_{eff} is measuring electron spins from a material whose spin polarization P has been known. We can determine the S_{eff} from Eq. 2.32 by applying the measurement result (N_R, N_L).

If non-polarized electrons enter a spin detector, N_R and N_L are not equivalent generally, because of sensitivity of the channeltrons. An asymmetry factor A_i is also vital to determination of absolute values of spin polarization of materials, defined as:

$$A_i \equiv \frac{N'_\mathrm{R}}{N'_\mathrm{L}} \tag{2.33}$$

To determine the asymmetry A_i of apparatus, we may perform a SARPES measurement of a non-polarized material such as polycrystalline Au thin film. Using the asymmetry A_i, we can determine the spin polarization P by following relation:

$$P = \frac{1}{S_{\mathrm{eff}}(\theta)} \cdot \frac{N_{\mathrm{R}} - A_i N_{\mathrm{L}}}{N_{\mathrm{R}} + A_i N_{\mathrm{L}}} \tag{2.34}$$

In practice, we determine degree of spin polarization by using Eq. (2.34) when the material is not a ferromagnet as Rashba metals.

If the material is ferromagnetic one, the asymmetry of the SARPES apparatus can be totally calibrated by magnetization inversion. In this case, P is determined by the equation:

$$P = \frac{1}{S_{\mathrm{eff}}} \frac{\sqrt{N_{\mathrm{R}}^{\mathrm{N}} N_{\mathrm{L}}^{\mathrm{S}}} - \sqrt{N_{\mathrm{L}}^{\mathrm{N}} N_{\mathrm{R}}^{\mathrm{S}}}}{\sqrt{N_{\mathrm{R}}^{\mathrm{N}} N_{\mathrm{L}}^{\mathrm{S}}} + \sqrt{N_{\mathrm{L}}^{\mathrm{N}} N_{\mathrm{R}}^{\mathrm{S}}}} \tag{2.35}$$

where superscripts N and S represent magnetization direction of the sample [16].

For data taken by the apparatus with VLEED spin detector, we use the equation as:

$$P = \frac{1}{S_{\mathrm{eff}}} \frac{N^{+} - N^{-}}{N^{+} + N^{-}} \tag{2.36}$$

where $N^{+(-)}$ is the intensity of the electrons reflected by the positively (negatively) magnetized target. Eq. 2.36 is simpler than Eq. 2.35 because the VLEED spin detector possesses smaller instrumental asymmetry, as mentioned above.

After P is determined by SARPES, spin-resolved photoemission spectra can be obtained. In order to obtain the spin up and down spectra, the following equation is used:

$$N_{\uparrow,\downarrow} = \frac{N_{\mathrm{total}}}{2}\left(1 \pm P\right) = \frac{N_{\mathrm{R}} + N_{\mathrm{L}}}{2}\left(1 \pm \frac{1}{S_{\mathrm{eff}}} \frac{N_{\mathrm{R}} - N_{\mathrm{L}}}{N_{\mathrm{R}} + N_{\mathrm{L}}}\right) \tag{2.37}$$

where

$$N_{\mathrm{total}} = N_{\mathrm{R}} + N_{\mathrm{L}} \tag{2.38}$$

We can obtain Eq. 2.37 by solving Eqs. 2.32 and 2.38 for $N_{\uparrow}$ and $N_{\downarrow}$. Using Eq. 2.37, we can obtain spin-resolved EDCs calibrated by S_{eff}.

Here, note that spin polarization is never changed by the simple FD-dividing analysis. When the spin-resolved photoemission spectra $N_{\uparrow,\downarrow}$ are divided by the Fermi–Dirac function at the measured temperature convolved with the experimental resolution ($f^{\mathrm{conv}}(\omega)$), the $f^{\mathrm{conv}}(\omega)$ contribution is canceled out, as:

$$\begin{aligned} P &= \frac{\frac{N_\uparrow}{f^{\mathrm{conv}}(\omega)} - \frac{N_\downarrow}{f^{\mathrm{conv}}(\omega)}}{\frac{N_\uparrow}{f^{\mathrm{conv}}(\omega)} + \frac{N_\downarrow}{f^{\mathrm{conv}}(\omega)}} \\ &= \frac{N_\uparrow - N_\downarrow}{N_\uparrow + N_\downarrow} \end{aligned} \tag{2.39}$$

Therefore, structures observed in a spin-polarization spectrum does not originate from the simple FD-dividing analysis, but originate from the intrinsic electronic structure.

2.4 References

[1] M. Donath, Surf. Sci. Rep. **20**, 251 (1994).

[2] T. Greber, T. J. Kreutz, and J. Osterwalder, Phys. Rev. Lett. **79**, 4465 (1997).

[3] E. Kisker, K. Schröder, W. Gudat, and M. Campagna, Phys. Rev. B **31**, 329 (1985).

[4] H. Hopster, R. Raue, G. Güntherodt, E. Kisker, R. Clauberg, and M. Campagna, Phys. Rev. Lett. **51**, 829 (1983).

[5] A. Takayama, T. Sato, S. Souma, and T. Takahashi, Phys. Rev. Lett. **106**, 166401 (2011).

[6] T. Hirahara, K. Miyamoto, I. Matsuda, T. Kadono, A. Kimura, T. Nagao, G. Bihlmayer, E. V. Chulkov, S. Qiao, K. Shimada, H. Namatame, M. Taniguchi, and S. Hasegawa, Phys. Rev. B **76**, 153305 (2007).

[7] C. R. Ast and H. Höchst, Phys. Rev. Lett. **87**, 177602 (2001).

[8] A Takayama, T Sato, S Souma and T Takahashi, New J. Phys. **16**, 055004 (2014).

[9] A. Kimura, E. E. Krasovskii, R. Nishimura, K. Miyamoto, T. Kadono, K. Kanomaru, E. V. Chulkov, G. Bihlmayer, K. Shimada, H. Namatame, and M. Taniguchi, Phys. Rev. Lett. **105**, 076804 (2010).

[10] T. Okuda and A. Kimura, J. Phys. Soc. Jpn. **82**, 021002 (2013).

[11] K. Kuroda, M. Arita, K. Miyamoto, M. Ye, J. Jiang, A. Kimura, E. E. Krasovskii, E. V. Chulkov, H. Iwasawa, T. Okuda, K. Shimada, Y. Ueda, H. Namatame, and M. Taniguchi1, Phys. Rev. Lett. **105**, 076802 (2010).

[12] M. Nomura, S. Souma, A. Takayama, T. Sato, T. Takahashi, K. Eto, K. Segawa, and Y. Ando, Phys. Rev. B **89**, 045134 (2014).

[13] Y. Ando, J. Phys. Soc. Jpn. **82**, 102001 (2013).

[14] S.-Y. Xu, I. Belopolski, D. S. Sanchez, M. Neupane, G. Chang, K. Yaji, Z. Yuan, C. Zhang, K. Kuroda, G. Bian, C. Guo, H. Lu, T.-R. Chang, N. Alidoust, H. Zheng, C.-C. Lee, S.-M. Huang, C.-H. Hsu, H.-T. Jeng, A. Bansil, T. Neupert, F. Komori, T. Kondo, S. Shin, H. Lin, S. Jia, and M. Z. Hasan, Phys. Rev. Lett. **116**, 096801 (2016).

[15] S. Souma, K. Kosaka, T. Sato, M. Komatsu, A. Takayama, T. Takahashi, M. Kriener, K. Segawa, and Y. Ando, Phys. Rev. Lett. **106**, 216803 (2011).

[16] P. D. Johnson, Rep. Prog. Phys. **60**, 1217 (1997).

[17] M. Hoesch, T. Greber, V.N. Petrov, M. Muntwiler, M. Hengsberger, W. Auwärter, and J. Osterwalder, J. Electron Spectrosc. Relat. Phenom. **124**, 263 (2002).

[18] J.-H. Park, E. Vescovo, H.-J. Kim, C. Kwon, R. Ramesh, and T. Venkatesan, Nature **392**,

794–796 (1998).

[19] R. J. Soulen Jr., J. M. Byers, M. S. Osofsky, B. Nadgorny, T. Ambrose, S. F. Cheng, P. R. Broussard, C. T. Tanaka, J. Nowak, J. S. Moodera, A. Barry, and J. M. D. Coey, Science **282**, 85 (1998).

[20] R. J. Soulen, Jr., M. S. Osofsky, B. Nadgorny, T. Ambrose, P. Broussard, and S. F. Cheng, J. Appl. Phys. **85**, 4589 (1999).

[21] L. Makinistian, Muhammad M. Faiz, Raghava P. Panguluri, B. Balke, S. Wurmehl, C. Felser, E. A. Albanesi, A. G. Petukhov, and B. Nadgorny, Phys. Rev. B **87**, 220402(R) (2013).

[22] A. I. D’yachenko, V. A. D’yachenko, V. Yu. Tarenkov, and V. N. Krivoruchko, Phys. Solid State **48**, 432 (2006).

[23] A. Gupta and J. Z. Sun, J. Magn. Magn. Mater. **200**, 24 (1999).

[24] S. Yuasa and D. D. Djayaprawira, J. Phys. D: Appl. Phys. **40**, R337 (2007).

[25] J. M. D. Coey and M. Venkatesan, J. Appl. Phys. **91**, 8345 (2002).

[26] J. Stöhr, J. Magn. Magn. Mater. **200**, 470 (1999).

[27] V. Kanchana1, G. Vaitheeswaran1 and M. Alouani, J. Phys.: Condens. Matter **18**, 5155 (2006).

[28] V. N. Antonov, O. V. Andryushchenko, A. P. Shpak, A. N. Yaresko, and O. Jepsen, Phys. Rev. B **78**, 094409 (2008).

[29] T. Muro, T. Shishidou, F. Oda, T. Fukawa, H. Yamada, A. Kimura, S. Imada, S. Suga, S. Y. Park, T. Miyahara, and K. Sato, Phys. Rev. B **53**, 7055 (1996).

[30] Y. Ando, Jpn. J. Appl. Phys. **54**, 070101 (2015).

[31] K. Ando, S. Fujita, J. Ito, S. Yuasa, Y. Suzuki, Y. Nakatani, T. Miyazaki, and H. Yoda, J. Appl. Phys. **115**, 172607 (2014).

[32] M. König, S. Wiedmann, C. Brüne, A. Roth, H. Buhmann, L. W. Molenkamp, X.-L. Qi, and S.-C. Zhang, Science **318**, 766 (2007).

[33] J. Moore and L. Balents, Phys. Rev. B **75**, 121306(R) (2007).

[34] L. Fu and C. L. Kane, Phys. Rev. B **76**, 045302 (2007).

[35] D. Hsieh, D. Qian, L. Wray, Y. Xia, Y. S. Hor, R. J. Cava, and M. Z. Hasan, Nature **452**, 970 (2008).

[36] D. Hsieh, Y. Xia, L. Wray, D. Qian, A. Pal, J. H. Dil, J. Osterwalder, F. Meier, G. Bihlmayer, C. L. Kane, Y. S. Hor, R. J. Cava, and M. Z. Hasan, Science **323**, 919 (2009).

[37] M. Z. Hasan and C. L. Kane, Rev. Mod. Phys. **82**, 3045 (2010).

[38] S. Souma, T. Sato, T. Takahashi, and P. Baltzer, Rev. Sci. Instrum. **78**, 123104 (2007).

[39] S. Souma, A. Takayama, K. Sugawara, T. Sato, and T. Takahashi, Rev. Sci. Instrum. **81**, 095101 (2010).

[40] M. P. Seah and W. A. Dench, Surf. Interface Anal. **1**, 2 (1979).

[41] A. Chikamatsu, H. Wadati, H. Kumigashira, M. Oshima, A. Fujimori, M. Lippmaa, K. Ono, M. Kawasaki and H. Koinuma, Phys. Rev. B **76**, 201103(R) (2007).

[42] K. Horiba, M. Kitamura,1 K. Yoshimatsu, M. Minohara, E. Sakai, M. Kobayashi, A. Fujimori, and H. Kumigashira, Phys. Rev. Lett. **116**, 076401 (2016).

[43] I. Belopolski, S.-Y. Xu, D. S. Sanchez, G. Chang, C. Guo, M. Neupane, H. Zheng, C.-C. Lee, S.-M. Huang, G. Bian, N. Alidoust, T.-R. Chang, B. Wang, X. Zhang, A. Bansil, H.-T. Jeng, H. Lin, S. Jia, and M. Z. Hasan1, Phys. Rev. Lett. **116**, 066802 (2016).

[44] S. Souma, Z. Wang, H. Kotaka, T. Sato, K. Nakayama, Y. Tanaka, H. Kimizuka, T. Takahashi, K. Yamauchi, T. Oguchi, K. Segawa, and Y. Ando, Phys. Rev. B **93**, 161112(R) (2016).

[45] B. Q. Lv, H. M. Weng, B. B. Fu, X. P. Wang, H. Miao, J. Ma, P. Richard, X. C. Huang, L. X. Zhao, G. F. Chen, Z. Fang X. Dai, T. Qian, and H. Ding, Phys. Rev. X **5**, 031013 (2015).

[46] Y. Nishikubo, K. Kudo, and M. Nohara, J. Phys. Soc. Jpn. **80**, 055002 (2011).

[47] M. H. Fischer, T. Neupert, C. Platt, A. P. Schnyder, W. Hanke, J. Goryo, R. Thomale, and M. Sigrist, Phys. Rev. B **89**, 020509(R) (2014).

[48] D. Tillmann, R. Thiel, and E. Kisker, Z. Phys. B **77**, 1 (1989).

[49] F. U. Hillebrecht, R. Jugblut, L. Wiebusch, Ch. Roth, H. B. Rose, D. Knabben, C. Bethke, N. B. Weber, St. Manderla, U. Rosowski, and E. Kisker, Rev. Sci. Instrum. **73**, 1229 (2002).

[50] R. Bertacco, D. Onofrio, and F. Ciccacci, Rev. Sci. Instrum. **70**, 3572 (1999).

[51] T. Okuda, Y. Takeichi, Y. Maeda, A. Harasawa, I. Matsuda, T. Kinoshita, and A. Kakizaki, Rev. Sci. Instrum. **79**, 123117 (2008).

[52] K. Yaji, A. Harasawa, K. Kuroda, S. Toyohisa, M. Nakayama, Y. Ishida, A. Fukushima, S. Watanabe, C. Chen, F. Komori, and S. Shin, Rev. Sci. Instrum. **87**, 053111 (2016).

[53] K. Miyamoto, A. Kimura, T. Okuda, H. Miyahara, K. Kuroda, H. Namatame, M. Taniguchi, S. V. Eremeev, T. V. Menshchikova, E. V. Chulkov, K. A. Kokh, and O. E. Tereshchenko, Phys. Rev. Lett. **109**, 166802 (2012).

[54] P. Zhang, K. Yaji, T. Hashimoto, Y. Ota, T. Kondo, K. Okazaki Z. Wang, J. Wen, G. D. Gu, H. Ding, and S. Shin, Science **360**, 182 (2018).

[55] S. Datta and B. Das, Appl. Phys. Lett. **56**, 665 (1990).

[56] M. I. Katsnelson, V. Yu. Irkhin, L. Chioncel, A. I. Lichtenstein, and R. A. de Groot, Rev. Mod. Phys. **80**, 315 (2008).

[57] R. Skomski and P. A. Dowben, Europhys. Lett. **58**, 544 (2002).

[58] H. Hertz, Annalen der Physik **267**, 983 (1887).

[59] C. N. Berglund and W. E. Spicer. Phys. Rev. A **136** 1030 (1964).

[60] S. Hüfner, *Photoelectron Spectroscopy*, Springer-Verlag, Berlin, Heidelberg, 3rd 3 edition, 1995.

[61] J. B. Pendry, Surf. Sci. **57**, 679 (1976).

[62] H. Iwasawa, Y. Yoshida, I. Hase, K. Shimada, H. Namatame, M. Taniguchi, and Y. Aiura, Sci. Rep. **3**, 1930 (2013).

[63] A. Damascelli, Physica Scripta **T109**, 61 (2004).

[64] P. J. Feibelman and D. E. Eastman, Phys. Rev. B **10**, 4932 (1974).

[65] T. Kondo, M. Ochi, M. Nakayama, H. Taniguchi, S. Akebi, K. Kuroda, M. Arita, S. Sakai, H. Namatame, M. Taniguchi, Y. Maeno, R. Arita, and S. Shin, Phys. Rev. Lett. **117**, 247001 (2016).

[66] T. Ishiga, T. Wakita, R. Yoshida, H. Okazaki, K. Tsubota, M. Sunagawa, K. Uenaka, K. Okada, H. Kumigashira, M. Oshima, K. Yutani, Y. Muro, T. Takabatake, Y. Muraoka, and T. Yokoya, J. Phys. Soc. Jpn. **83**, 094717 (2014).

[67] T. Sato, S. Souma, K. Sugawara, K. Nakayama, S. Raj, H. Hiraka, and T. Takahashi, Phys. Rev. B **76**, 113102 (2007).

[68] W. von der Linden, M. Donath, and V. Dose, Phys. Rev. Lett. 71, 899 (1993).

[69] E. Kisker, R. Clauberg, and W. Gudat, Rev. Sci. Instrum. **53**, 1137 (1982).

[70] M. H. Berntsen, P. Palmgren, M. Leandersson, A. Hahlin, J. Ahlund, B. Wannberg, M. Mansson, and O. Tjernberg, Rev. Sci. Instrum. **81**, 035104 (2010).

[71] J. Kirschner and R. Feder, Phys. Rev. Lett. **42**, 1008 (1979).

[72] G. C. Wang, R. J. Celotta, and D. T. Pierce, Phys. Rev. B **23**, 1761 (1981).

[73] J. Unguris, D. T. Pierce, and R. J. Celotta, Rev. Sci. Instrum. **57**, 1314 (1986).

[74] T. J. Gay and F. B. Dunning, Rev. Sci. Instrum. **63**, 2 (1992).

[75] V. N. Strocov, R. Claessen, G. Nicolay, S. Hüfner, A. Kimura, A. Harasawa, S. Shin, A. Kakizaki, H. I. Starnberg, P. O. Nilsson, and P. Blaha: Phys. Rev. B **63**, 205108 (2001).

CHAPTER 3. SPIN- AND ANGLE-RESOLVED PHOTOEMISSION SPECTROSCOPY APPARATUS

3.1 Bulk-Sensitive Spin- and Angle-Resolved Photoemission Spectroscopy Apparatus with a Mott Spin Polarimeter at Okayama University

3.1.1 Overview of the SARPES Apparatus

In this chapter, SARPES apparatus at Research Institute for Interdisciplinary Science, Okayama University, is described. This apparatus consists of following main seven parts:

1. Hemispherical Electron Analyzer (OMICRON-SCIENTA R4000)
2. Mott Spin Detector (OMICRON-SCIENTA 2D-spin)[1]
3. Main Chamber
4. Preparation Chamber
5. Evaporation / Evaluation Chamber
    1. Heatable Manipulator (made by the Omicron)
    2. Evapolator (Omicron EFM 3)
    3. LEED/AES (SPECS ErLEED 3000D)
6. Load Lock Chamber
7. Rare gas discharge lamp[2]

    He (He Iα line: 21.18 eV, He IIα line: 40.814)
    Ne (Ne Iα line: 16.67 eV)
    Ar (Ar Iα line: 11.62 eV)
    Kr (Kr Iα: 10.03 eV)
    Xe (Xe Iα: 8.44 eV)

This apparatus has a gas-replacement-type discharge lamp in which various kinds of rare gas can be used. Since the photon energy can be changed by replacing the gas in the discharge lamp, we can measure band dispersion along $k_\perp$ direction. We can also perform bulk-sensitive measurements because the probing depth of ARPES using low-energy photon according to the Universal Curve shown in Fig. 2.5. The probing depth of a Xe I line ($h\nu$ = 8.44 eV) which is the lowest photon energy we can use in the apparatus is estimated to be ~50 Å. Indeed, it was

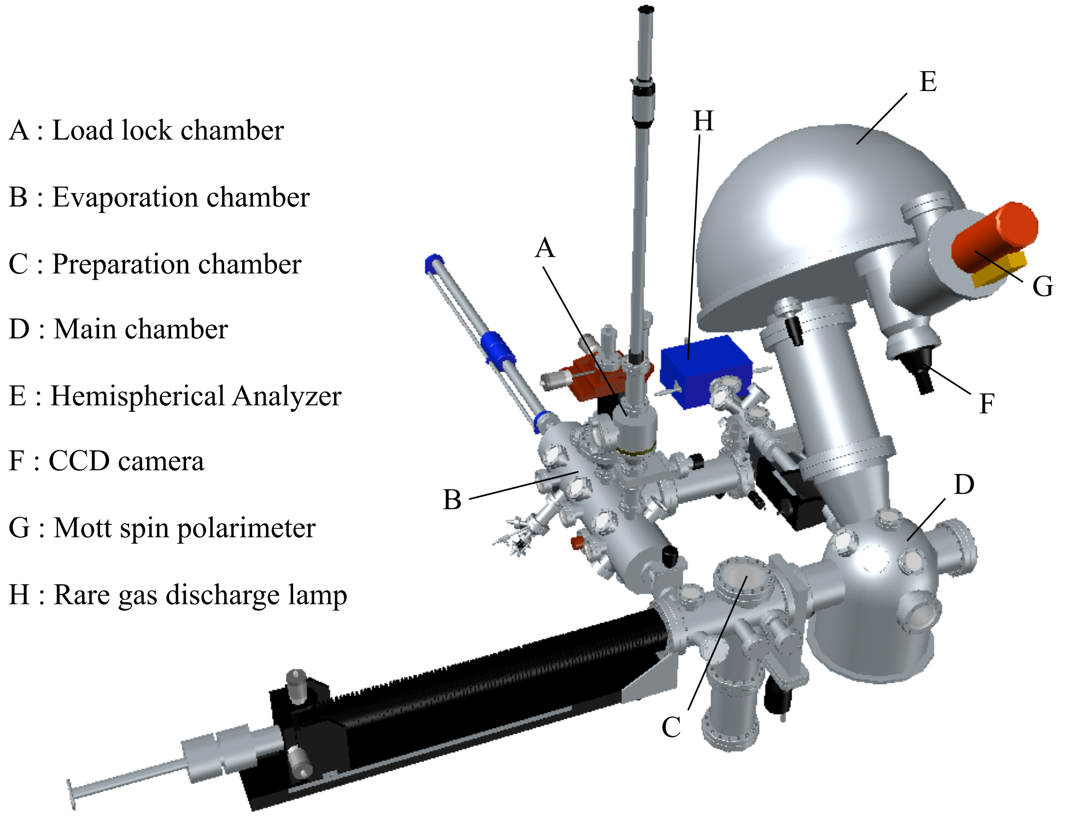

Fig. 3.1. Overview of our bulk-sensitive SARPES apparatus.

reported that the photoelectron intensity from a surface state of Yb is highly suppressed by using the Xe I line [2].

Table 3.1. The energy resolution of SARPES measurement as the function of the aperture and the entrance slit sizes, and the analyzer pass energy.

	Energy resolution (meV)			
Pass energy (eV)	#1	#2	#3	#4
1	2.3	4.6	6.9	9.2
2	4.6	9.2	14	18.5
5	12	23	35	46
10	23	46	69	92
20	46	92	139	185
50	116	231	347	462

Table 3.2. The angular resolution of SARPES measurement as the function of electron acceptance angle in different analyzer lens mode with different aperture size for spin detection channel. The numbers listed as lens mode roughly correspond to the acceptance angle.

	Angular resolution (degree)			
Lens mode	#1	#2	#3	#4
7	0.19	0.38	0.75	1.5
15	0.38	0.75	1.5	3
30	0.75	1.5	3	6

In the analyzer we can perform both of angle-integrated and angle-resolved measurements by using transmission mode and angular mode, respectively. When spin-resolved and angle-resolved PES measurements, we should adjust aperture size of the spin detector as well as the acceptance angle determined by the lens and in order to set a favorable angular resolution. The aperture size also affects the energy resolution of spin-resolved measurements. Table 3.1 and 3.2 show lists of the energy and angular resolution, respectively, made from the manual of VG Scienta (presently, Omicron Scienta) 2D-spin. The #1 to #4 correspond to aperture sizes. As seen from correspondences between the aperture size and resolution, the aperture size of #1 is the smallest size and that of #4 is the largest one.

By the Mott spin detector, we can simultaneously observe spin polarizations of photoelectrons for 2 quantization axes. Figure 3.2 shows a picture of the 2D Mott detector with schematic illustration of electronic spin detection. A polycrystalline Au thin film is used as a target (hidden in Fig. 3.2). Either one of the electronic spin directions corresponds to the in-plane spin direction parallel to the analyzer slit, and another corresponds to out-of-plane spin direction of the sample surface. By using a software named SES made by Scienta Omicron, we can measure both of the spin-up and spin-down spectra along the two directions, simultaneously. This highly contributes the enhancement of the measurement efficiency.

3.1.2 Apparatus Upgrade for Determination of the effective Sherman function

The effective Sherman function S_{eff} of the Apparatus was determined by measuring spin polarization originating from Rashba splitting on Bi(111) surface. S_{eff} can be determined by performing SARPES measurements for the materials whose spin polarization have been determined. The effective Sherman function is defined as $A = PS_{\mathrm{eff}}$ where A and P is observed

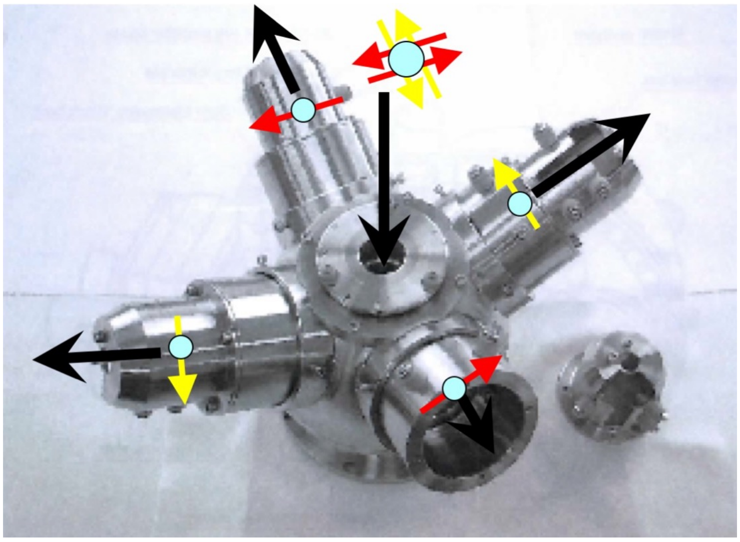

Fig. 3.2. Picture of the scattering chamber in the Mott spin detector. Blue circles and red and yellow arrows represent photoelectrons and spins.

spin asymmetry defined as $A = (I_R - I_L) / (I_R + I_L)$ and spin polarization, respectively. In order to determine spin polarization of materials, it is absolutely imperative to determine the effective Sherman function by measuring electronic spins from a material which meets following requirements:

1. Spin polarization has been determined.
2. Method of preparation has been established.
3. Intensity of photoelectrons excited by photons with $h\nu \sim 20$ eV from valence band is high enough to measure the intrinsic electronic spin state without aging in the SARPES measurement.

The efficiency of spin-resolved ARPES is much lower than spin-integrated ARPES.[2] Therefore we should measure a sample which has high intensity of photoelectrons of valence bands in order to obtain data which has high-S/N ratio and determine an accurate effective Sherman function. The most appropriate candidate is Bi/Si(111) thin film because it is known that a lot of SARPES studies on Bi thin films have been reported and the preparing method of Bi thin film has been established.[2–8]

In order to perform SARPES measurements of Bi/Si(111) thin film, it is necessary that the apparatus in which we can prepare Bi thin film in vacuum and perform *in-situ* SARPES measurements. The preparation procedures of a Bi/Si(111) thin film are divided into 3 parts: (i) Preparation of the Si(111)-7×7 surface. (ii) Forming a Bi film on the Si surface. (iii) Confirming

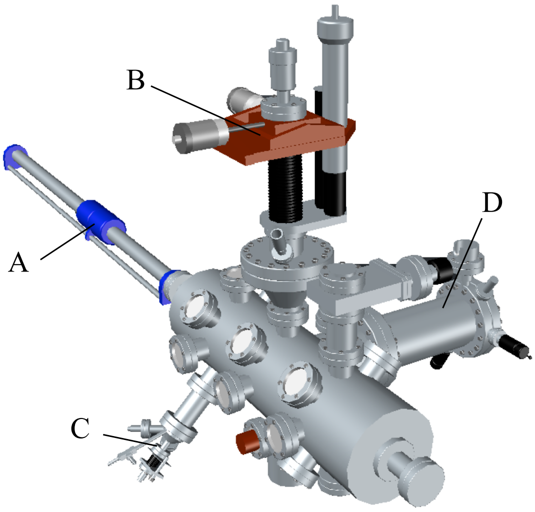

A. Transfer rod

B. Heating Manipulator

C. Evaporator
(Omicron EFM 3)

D. LEED / AES
(SPECS ErLEED 3000D)

Fig. 3.3. Overview of the evaporation/evaluation chamber.

the quality of the surface of Bi thin film.

For the preparation procedures, we built the evaporation and evaluation chamber, as shown in Fig. 3.3. For the formation of Si(111)-7×7 clean surface, we made a manipulator with a stage to heat a Si substrate electrically, as shown in Fig. 3.4(a). By the heating head, we can heat by 1200 °C by using electrical heating for low-doped Si substrates. Also we can heat by 800 °C in even cases when a substrate which cannot be heat directly is used because we can use radiation heating by filaments. Fig. 3.4 (b) shows the route of current when electrical heating. The current provided by a current generator flows along Si through a brush connecting with the manipulator head. Since the cramps of the brush side are isolated from the bottom of the sample holder by insulator ceramics, as shown in Fig. 3.4 (b), the current passes through only Si.

To evaporate Bi on the Si substrate, an electron-bombardment-based evaporator, Scienta Omicron UHV Evaporator EFM 3, as shown in Fig. 3.5 was used. In the evaporator, high-voltage (HV) is applied between the crucible and the filament. The accelerated thermoelectrons from the filament heat the Mo crucible and the evaporant by colliding with the crucible. By capturing ions of the evaporant with a flux monitor, we can monitor the amount of the flux of the vaporized material. As the modulation of the amount, there are three ways: (i) Adjustment of the shutter. (2) Adjustment of distance between the filament and the crucible. (3) Adjustment of HV or the filament current. The thermocouple is fixed as shown in Fig. 3.5 in order to monitor the temperature of the cooling shroud, because the overheating causes the melting of the shroud made of copper.

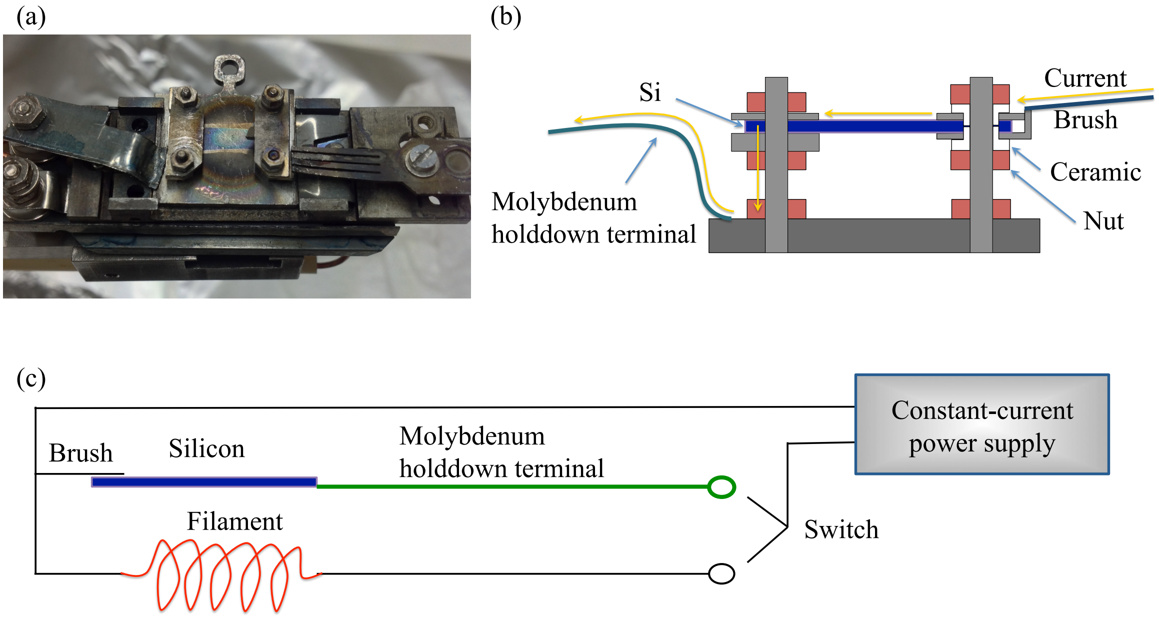

Fig. 3.4. (a) Picture of the assembly for electrical heating. (b) Cross-section view of the sample holder fixed on the manipulator head. (c) The circuit of the heating system.

In the case of evaporating Bi, there is a problem that the evaporant is somehow recrystallized on the inner side of the cooling shroud between the filament and the flux monitor. This problem occurs when we evaporate it for several hours (about 3 hours). In order to melt the recrystallized evaporant, we may heat the evaporator up to 250 °C by applying current through the filament without cooling water.

Low-energy electron diffraction (LEED) and Auger electron spectroscopy (AES) machine (SPECS ErLEED 3000D) is mounted on the evaporation/evaluation chamber for evaluation of the surface of the Bi thin film.

In order to perform *in-situ* SARPES measurements on the Bi thin film fabricated in the evaporation/evaluation chamber, we have to transfer the sample to the main chamber. For the sample transfer, sample stage was newly designed for the head of the SARPES-measurement manipulator with the helium cryostat, as shown in Fig. 3.6. The sample holder for current heating can be fixed by pressing the back of the holder by screws. When performing low-temperature measurements on half-metals and other bulk materials, we can use another copper plates for normal SARPES holder. Figure 3.6 shows each schematic view, one is for the holders for current heating (top) and another is for the normal SARPES holders (bottom).

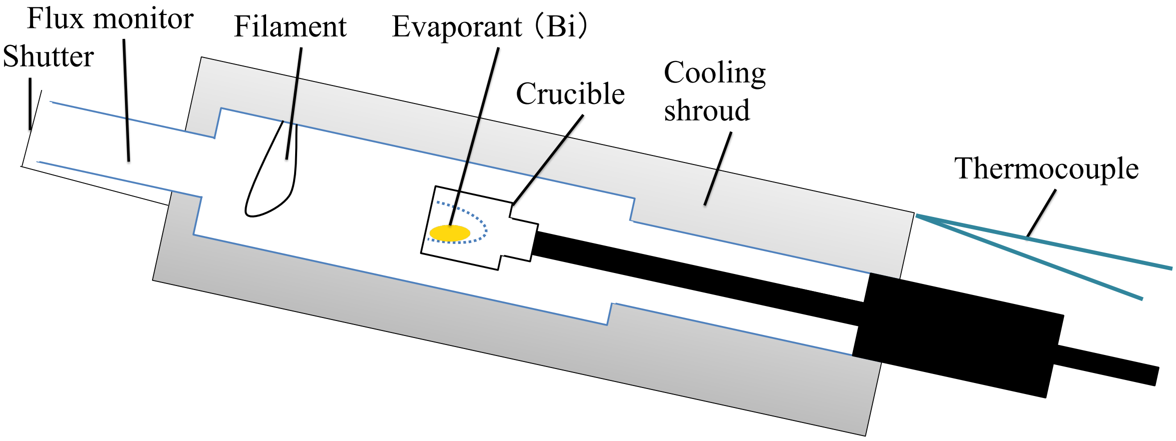

Fig. 3.5. Cross-section view of the electron-bombardment-based evaporator.

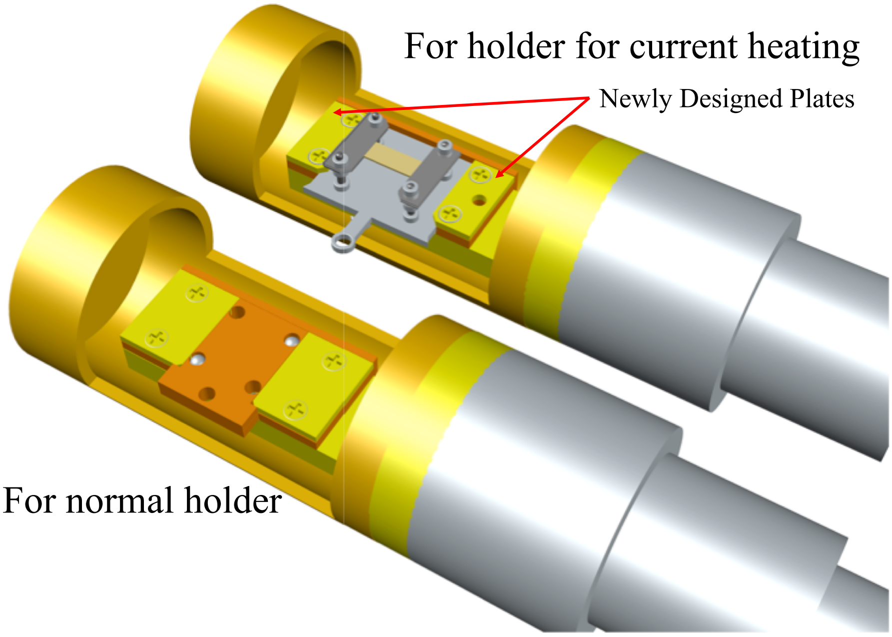

Fig. 3.6. Schematic drawing of the head on the manipulator with the helium cryostat.

3.1.3 Preparation of Bi Thin Film on Si(111)–7×7 Surface

We used a silicon wafer as a substrate of bismuth thin film. Silicon has diamond type crystal structure. Each silicon atom forms regular tetrahedrons. In the ideal plane of Si(111), there is one dangling bond for each silicon atom but in fact silicon atoms form zigzag chain by pairing every two columns to decrease the number of dangling bonds and form a surface structure of

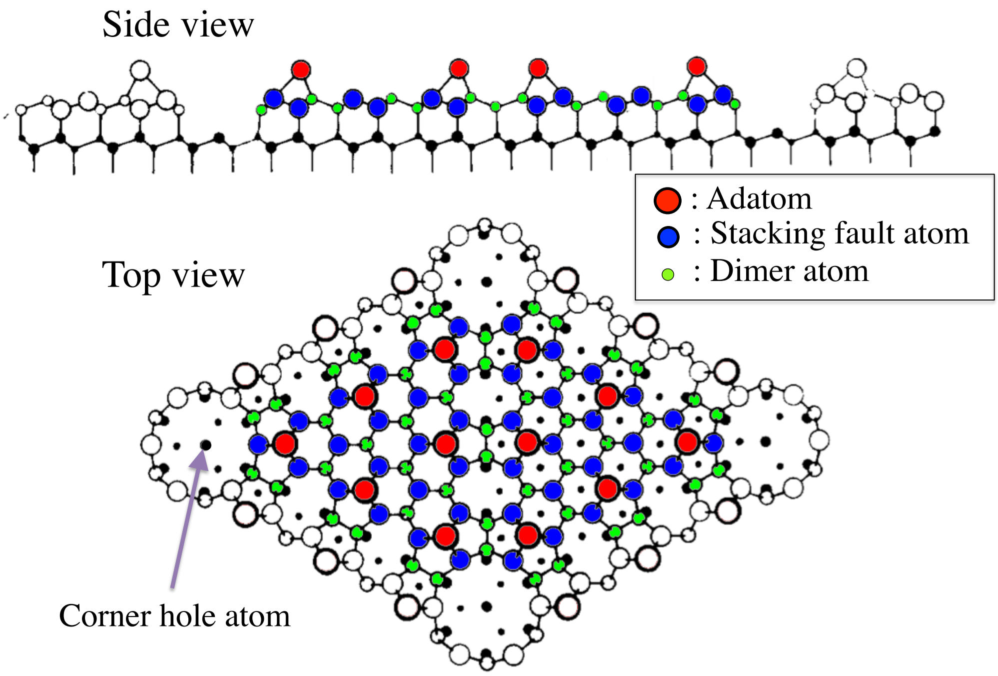

Fig. 3.7. DAS model for Si(111)–7×7. Taken from [5].

Si(111)–2×1 [3]. On the other hand, there is a more stable long-period structure of Si(111)–7×7 than the 2×1 structure. The 7×7 structure discovered by Binnig is obtained by heating about 900°C in ultrahigh vacuum [4]. The unit cell of 7×7 structure is suggested by K. Takayanagi *et al.* and so-called *DAS structure* (Dimer-Adatom-Stacking fault structure)[5]. The DAS structure is shown in Fig. 3.7. It includes 48 dimer atoms, 12 adatoms and 42 stacking fault atoms in its unit cell. Therefore 49 dangling bonds at first in 7×7 unit cell decrease to 19 dangling bonds: 12 from the adatoms, 6 from atoms which are in the first layer but are not bonded to the adatoms and 1 from the atom below the corner hole. Because of the decrease, the silicon surface state becomes stabilized but the silicon surface bonds the other adatom easily by these 19 dangling bonds.

We must heat silicon as quickly as possible from 850°C to 1000°C when we prepare a silicon clean surface, because in the temperature range it is known that a lot of step structures are formed [6]. Also, we need to keep the silicon wafer at higher than 870°C at which a silicon surface structure transforms from 1×1 to 7×7 structure in order to form Si(111)–7×7 structure more long-periodically. In order to obtain the Si clean surface, we repeated the process several times as following:

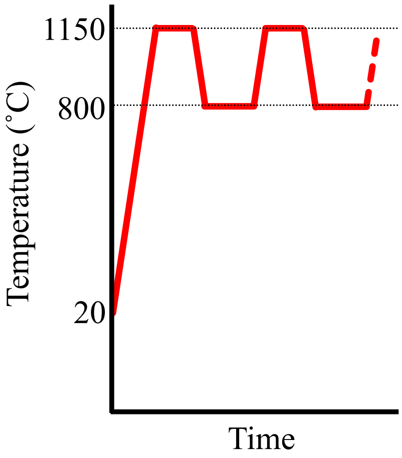

Fig. 3.8. Heating process for preparing the clean surface of Si(111)– 7×7.

Process 1. Heating up to 1150 ˚C quickly.
Process 2. Holding the temperature for a few seconds.
Process 3. Cooling down to 800 ˚C.

The schematic view of the process is also shown in Fig. 3.8.

In the actual procedures, before making the clean surface by above process, the Si wafer is degassed sufficiently. Temperatures of Si monitored to an accuracy of ±1 ◦C by a radiation thermometer (CHINO IR-AHS0). During the cleaning, a vacuum which is not exceed 1×10^{-6} Pa was maintained. After the surface cleaning, we took LEED pattern to evaluate the surface of the Si substrate, as shown in Fig. 3.9 (a). The LEED spots of three-fold symmetry and 7×7 superlattice spots was observed, indicating that the clean surface of the Si substrate is prepared. After the surface of the Si substrate is clean enough to observed the clear LEED pattern derived from the 7×7 structure, bismuth was evaporated onto the Si(111)–7×7 surface in the same vacuum chamber whose degree of vacuum is not exceed 3.0×10^{-8} Pa at room temperature for 20 minutes.

The surface crystallinity and elemental composition of Bi(111) thin film was also evaluated by LEED and AES measurements. Figure 3.9 (b) shows the LEED pattern of the fabricated Bi(111). The LEED image shows the clear spots without clear ring structures due to multi-domain component, which indicates that the single domain thin film of Bi was successfully fabricated.

Furthermore, we confirm the chemical state before and after forming the film by AES. Figure 3.10 (a) shows the differential wide AES spectra before and after the bismuth deposition. The blue spectrum shows a structure around 90 eV derived from VLL process of Si [7].

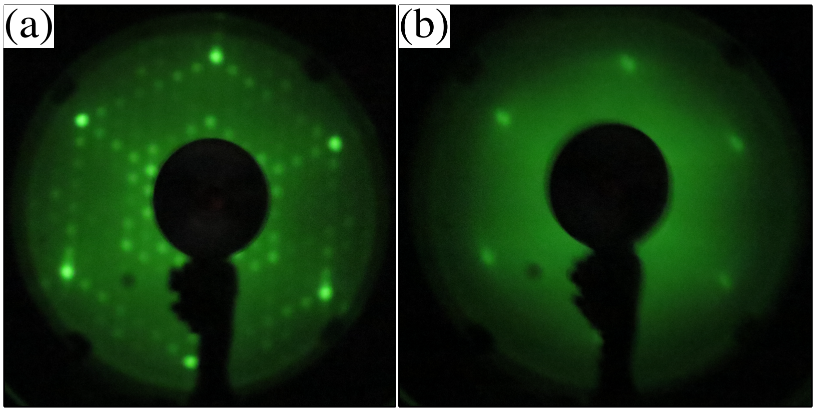

Fig. 3.9. (a) LEED image of Si substrate taken after the cleaning procedure. (b) Same as (a) but taken after evaporating bismuth.

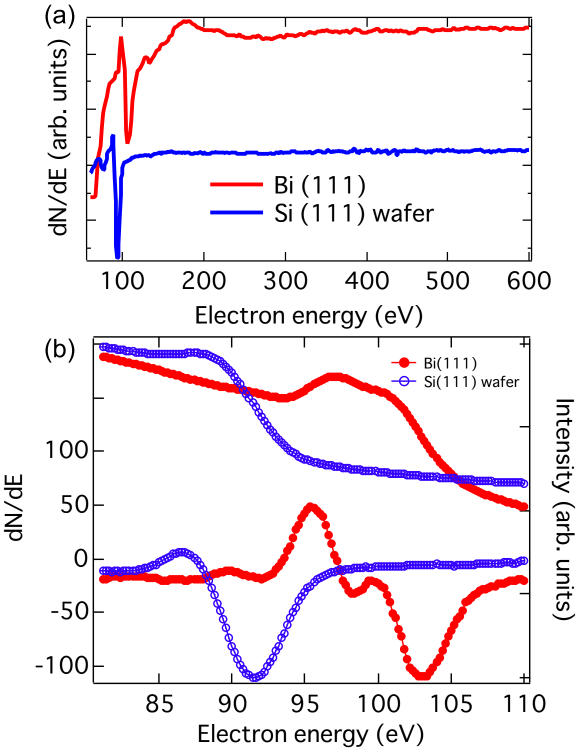

Fig. 3.10. (a) Wide AES spectra of Bi(111) and Si(111)–7×7. (b) Auger electron intensity (top) and its differential spectra (bottom) of the Si (111)–7×7 LVV process and Bi (111) NOO process.

Structures around 270 eV corresponding C KLL process[8] and around 500 eV corresponding O KLL process[7] was not found in the spectrum of Si, indicating again that a clean surface without any contaminants was prepared. In Fig. 3.10 (b), it was found that the AES signals of VLL process of Si disappeared after the bismuth deposition. The energy position of the structure at approximately 91 eV in the spectrum of the Bi film seems to be close to that of LVV process of the Si clean surface, but the derivation of structure around 91 eV is different from the LVV process because the energy of Auger electrons derived from the LVV process is 88 eV as seen in the spectrum of the Si clean surface. Therefore, we successfully made a thick Bi film for which we cannot observe any Si signals.

The reason why the structure of NOO process in Bi has two components is that there is energy splitting derived from spin-orbit coupling. In the NOO process, the electrons occupying $4f$ levels splitting into $4f_{7/2}$ whose binding energy is 156.6 eV and $4f_{5/2}$ whose binding energy is 161.9 eV due to the SOC are excited by irradiated electrons[9]. When $5d$ electrons whose binding energy is approximately 25 eV drop into the $4f$ levels, the energies of 131.6 eV and 136.9 eV is released. The electrons staying in the $5d$ level receive the released energies. If a $5d$ electron receives the energy of 131.6 eV, the electron is emitted with the energy $E_A = 131.6$ eV – 25 eV – W. If a $5d$ electron receives the energy of 136.9 eV, the electron is emitted with the energy $E_A = 136.9$ eV – 25 eV – W. Here, if it is assumed that work function is equal to 5 eV, the energies of the Auger electrons are approximately 101 eV and 107 eV, roughly consistent with the experimental values in the present study. Therefore the bismuth thin film was definitely formed on the Si (111)–7×7 surface.

3.1.3 Determination of the Effective Sherman Function

Figures 3.11 (a) and (b) show the ARPES intensity plot with respect to the E_F as a function of two-dimensional wave vectors and that of the previous study, respectively.[3] The shape of the Fermi surface was roughly consistent with that of the previous study, indicating again that Bi(111) surface was formed.

Figure 3.11 (c) shows the ARPES intensity map along the red line shown in Fig. 3.11 (a) and its second derivative image. The quantization axis is along x direction of the sample (parallel to $\bar{\Gamma}-\bar{K}$ direction in Fig. 3.11 (a). Energy distribution curves (EDCs) are also shown in Fig. 3.11 (d). Shape of the EDC at $k_y = 0$ Å^{-1} (blue line in Fig. 3.11 (d)) is perfectly in line with the total spectrum taken by the Mott spin detector, as shown by a black solid line in the Fig. 3.11 (d). This validates that angle-resolved measurement is successfully performed by our SARPES apparatus. Small differences of the spectral shape of I_R and I_L are also observed, which is reflected in the finite energy dependence of the asymmetry as shown by red and blue shaded area in Fig. 3.11(d). The energy dependence of the spectra of I_R, I_L, and the asymmetry are consistent with that of the previous study [10]. We determine the effective Sherman function of our SARPES apparatus by comparison of the spin polarization around 2.5 eV and 1.5 eV. From

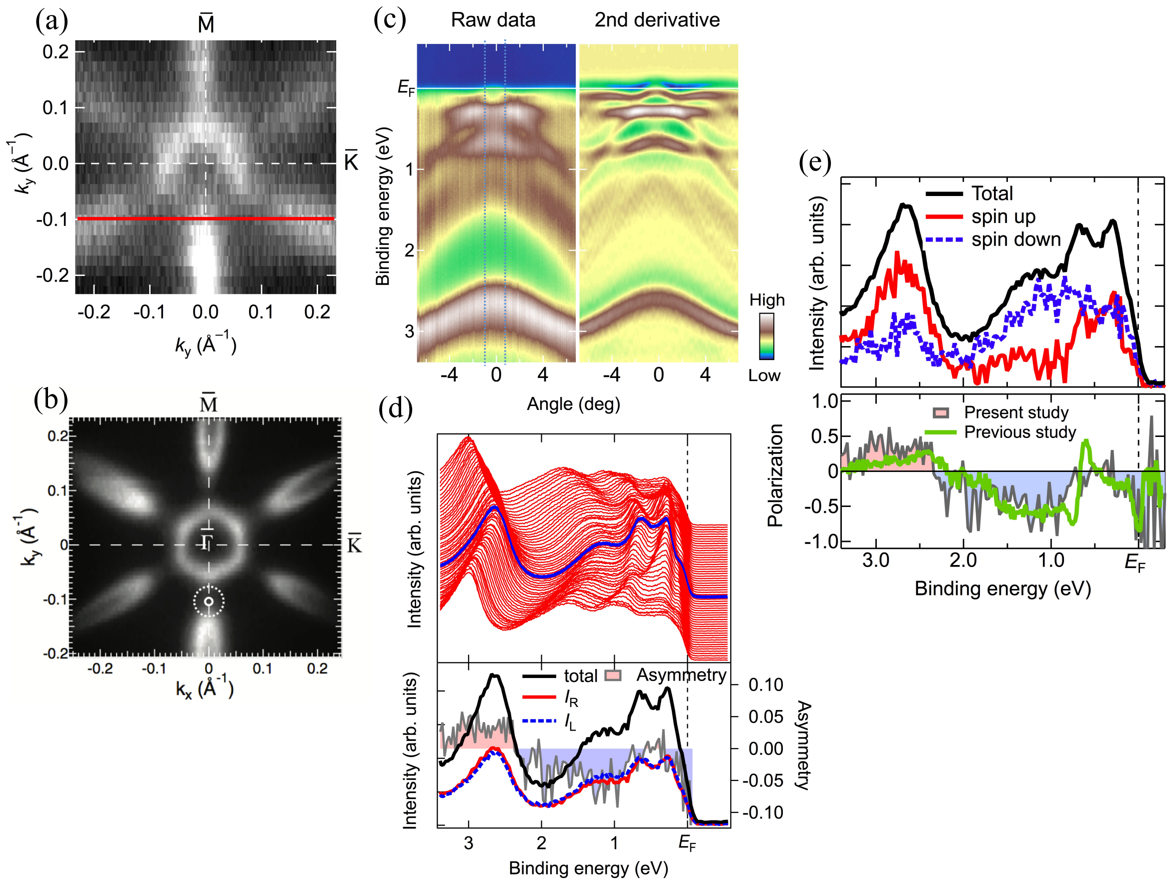

Fig. 3.11. (a) Fermi surface mapping of the Bi(111) film obtained by the two-dimensional detector of spin-integrated ARPES mode with the He discharge lamp ($h\nu = 21.2$ eV). (b) Same as (a) but reported by a previous study, taken from [10]. (c) ARPES intensity map taken along a red line shown in Fig. 3.11(a) (left) and its second derivative image (right). (d) (top) EDCs of the ARPES intensity map shown in Fig.3.11 (c). Blue spectrum corresponds to $k_y = 0$ Å^{-1}. (bottom) EDCs taken by right (red solid line) and left (blue dashed line) detector in the Mott spin detector, and corresponding asymmetry A determined from $A = (I_R - I_L) / (I_R + I_L)$. The angular resolution is ±0.75° corresponding to the width between blue dashed lines in the ARPES intensity map shown in (c). The spectrum shown by black line indicates the total spectrum obtained from $I_{total} = I_R + I_L$. (e) SARPES spectra and corresponding spin polarization calibrated by the effective Sherman function $S_{eff} = 0.1$ which is determined from $S_{eff} = A/P_{prev}$, where P_{prev} is spin polarization of the previous study [10].

$S_{eff} = A/P_{prev}$, where A is asymmetry observed in our SARPES and P_{prev} is the spin polarization of the previous study [10], the effective Sherman function S_{eff} of our SARPES apparatus was determined to be 0.10 ± 0.006. This value is a typical value of S_{eff} of Mott spin detectors.

Figure 3.11 (e) shows the spin polarization P obtained from the asymmetry by using 0.10 as the effective Sherman function S_{eff} (bottom) and spin up (red solid line) and spin down (blue dashed line) spectra obtained from the total spectrum ($I_{total} = I_R + I_L$, black solid line). In order to obtain the spin up and down spectra, Eq. 2.32 is used. The signal-to-noise (S/N) ratio of the spin up and down spectra is much higher than that of the raw SARPES data as seen in Fig. 3.11

(d), because the spectra $I_\uparrow$ and $I_\downarrow$ are determined by the spin polarization P calibrated by the effective Sherman function $S_{\mathrm{eff}} \ll 1$. If $S_{\mathrm{eff}} = 1$, the S/N ratio of $I_\uparrow$ and $I_\downarrow$ is exactly same as that of raw data I_{R} and I_{L}. The energy dependence of spin polarization in the present study is nicely in line with that of the previous study [10], as shown in Fig. 3.11 (e). One may notice that the energy dependence of the present study is broader than that of the previous study. The reason is attributed to the difference of the energy resolution. In the present study, energy resolution was approximately 100 meV, while it was 7.5 meV in the previous study. This difference does not influence the result of the value of S_{eff} determined in this study, because the energy region wider than the scale of these energy resolutions was used for determining the S_{eff}.

3.2 Ultrahigh-Resolution Spin- and Angle-Resolved Photoemission Spectroscopy Apparatus at The University of Tokyo

3.2.1 Overview of the SARPES Apparatus

Figures 3.12 (a) and (b) show the system for laser-based SARPES, which has been used extensively in this dissertation work [11]. The SARPES apparatus developed by Dr. Yaji *et al.* in Shin group (the Institute for Solid State Physics (ISSP), The University of Tokyo) consists of a low-energy laser source, a hemispherical electron analyzer Omicron-Scienta DA30-L, and twin VLEED spin detectors.

The laser is constructed from a frequency-tripled Nd:YVO_4 quasi-continuous wave laser with the repetition rate of 160 MHz and a nonlinear optical crystal of $KBe_2BO_3F_2$. The laser system provides the photons of $h\nu = 6.994$ eV, which correspond to the 6th harmonic of a basic wave of the laser. The spot size of the laser is approximately 100 μm in diameter on the sample. A photon flux with the laser power of 1 W is 1×10^{14} photons/s, which is practically available in the SARPES mode. On the other hand, the laser power has to be reduced in the ARPES mode to avoid the burnout of a multi-channel plate (MCP) by the intense photoelectrons. For the laser system, we offer linear horizontal and vertical polarizations as well as left and right circular polarizations, which are easily and simply yielded using $\lambda/2$ and $\lambda/4$ waveplates installed on the laser optic axis. For the linear polarization mode, one can arbitrarily adjust the direction of the electric field vector of the photon between the linear horizontal and vertical polarizations. For the circular polarization mode, we can provide elliptical polarization. Here, the degree of the polarization is tunable by individually rotating the $\lambda/2$ and $\lambda/4$ waveplates. These functions are

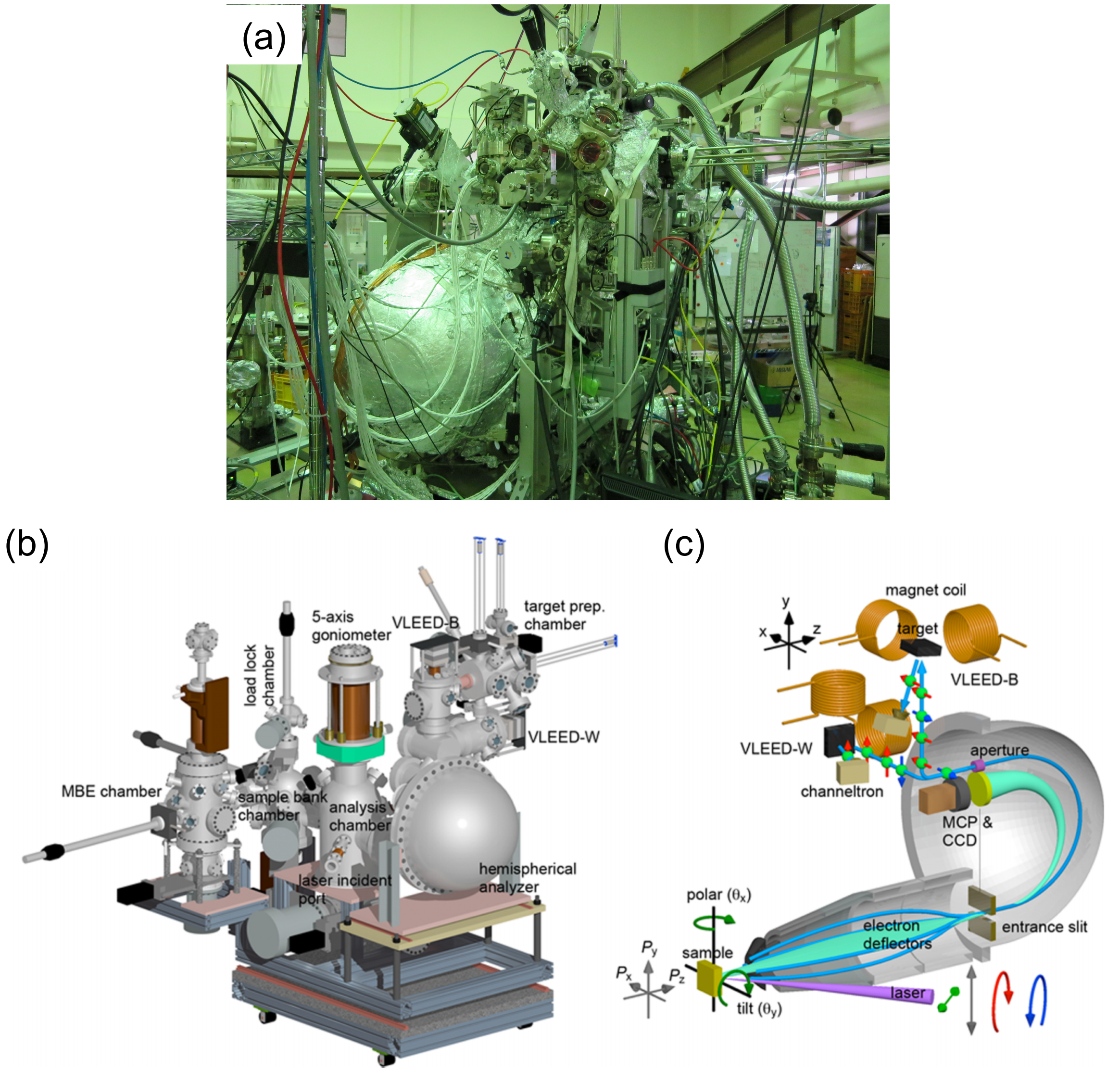

Fig. 3.12. (a) Picture of the laser-based SARPES spectrometer. (b) Overview of the laser-based SARPES spectrometer and related systems developed at the Laser and Synchrotron Research Laboratory at the Institute for Solid State Physics. (c) Schematic drawing of the detection systems of laser-based ARPES and laser-based SARPES. The angle between the laser and the analyzer is fixed at 50˚. Twin VLEED spin detectors arranged with orthogonal geometry are connected to the hemispherical photoelectron analyzer. The spectrometer is also equipped with electron deflectors at the multi-electron-lens part between the sample and the entrance slit. (b) and (c) are taken from [11].

useful for photon-polarization-dependent SARPES. In the SARPES system, a helium discharge lamp (Omicron Scienta VUV5000) with a photon flux of 4×10^{12} photons/s is also available as a photon source.

The photoelectron analyzer is equipped with electron detectors in a multi-electron-lens part between the sample and the entrance slit, different from R4000 analyzer employed in our SARPES apparatus as shown above. The electron detector system can control the passage of the photoelectrons using an electric field before they arrive at the entrance slit. Therefore, for the ARPES mode, the photoelectrons emitted in the θ_{y}, defined in Fig. 3.12(b), direction acceptance of 20° can reach the entrance slit and are imaged on the detector. For SARPES, one can selectively collect photoelectrons emitted in the acceptance cone of $(\theta_x \times \theta_y) = (30^\circ \times 20^\circ)$ without sample rotation. The detector function is in particular suitable for the spin-dependent band mapping of small samples. In addition, the polarization condition, i.e., the geometry of the incident laser and the sample angle with respect to the VLEED detectors, is also preserved in this procedure, which helps us to interpret the obtained spin polarizations.

The analysis chamber is equipped with a hemispherical photoelectron analyzer, twin VLEED spin detectors, and a five-axis goniometer with a liquid He cryostat. In this system, the home-made twin VLEED detectors are orthogonally placed with respect to each other in order to measure three components of spins. The targets of the VLEED spin detectors are Fe(100)-p(1×1) films terminated by oxygen (Fe(001)-O) grown on MgO(001) substrates, which are *in situ* prepared in the target preparation chamber. By the liquid He cryostat, we can cool the sample down to ~10 K.

Figure 3.12(c) indicates a schematic drawing of the spectrometer. The hemispherical electron analyzer is a custom-made Scienta Omicron DA30-L. The photoelectron analyzer is equipped with six types of entrance slits, with widths ranging between 0.1 mm and 3.0 mm. At the exit of the hemispherical analyzer, the MCP with the diameter of 40 mm and a CCD camera is installed, which enables us to perform the normal ARPES with two-dimensional (E–θ_x) detection with an acceptance angle of 30° in the θ_x direction (parallel to the entrance slit). Small rectangular apertures, which correspond to the exit slits for SARPES, are also placed at the exit of the hemispherical analyzer. The aperture sizes are as follows: (Energy direction (mm) × angular direction (mm)) = (3 × 2), (3×0.5), (2×1), (1×0.5), (0.2×0.5). The aperture size also determines the energy and angular resolutions of the SARPES measurements. One can choose a suitable combination of the entrance slit and the aperture for the SARPES measurements.

The photoelectrons passing through the aperture are guided to the VLEED spin detectors with a photoelectron transfer system. The photoelectrons scattered from the VLEED targets are detected by channeltrons. The Fe(001)-O targets are selectively magnetized with Helmholtz-type electric coils which are arranged with orthogonal geometry with respect to each other [only one side of each Helmholtz coil is illustrated in Fig. 3.12(c) for clarity]. The target of VLEED-B (VLEED-W) is magnetized in the x and z (y and z) directions, which correspond to the spin polarization directions of P_{x} and P_{z} (P_{y} and P_{z}) on the sample axis. Thus, the twin VLEED spin

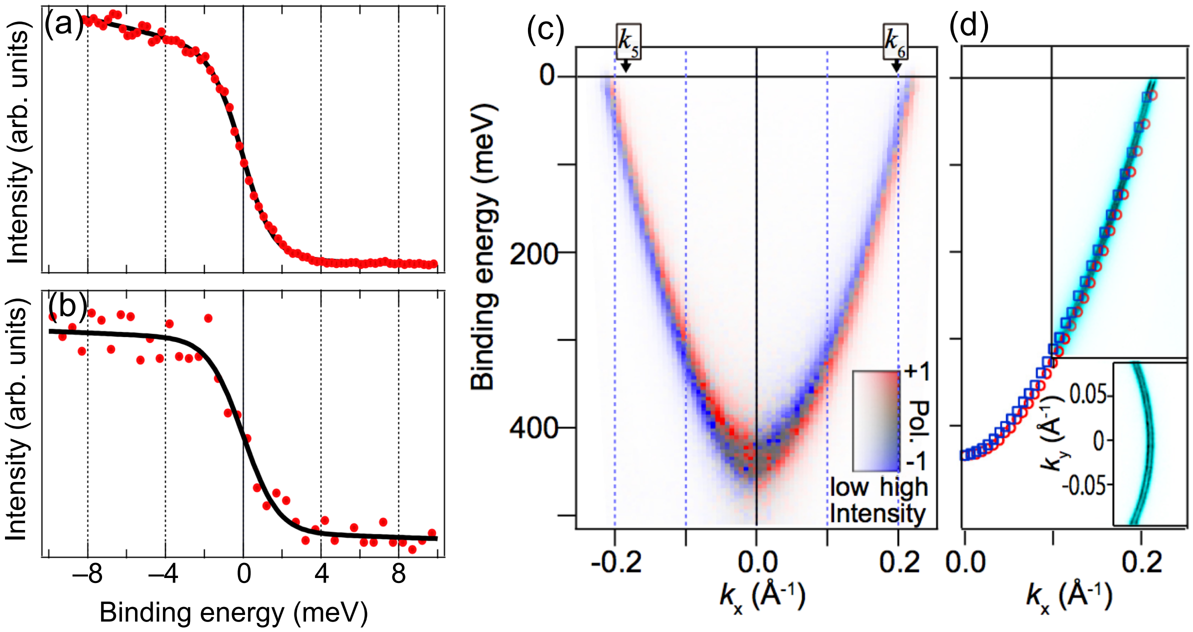

Fig. 3.13. The Fermi edges (circle plots) of a Au thick film recorded in (a) normal ARPES mode and (b) SARPES mode. Solid curves represent fitting results with the Fermi–Dirac distribution function and a polynomial background. (c) Spin-polarization and photoelectron intensity images of the Cu(111) surface state along $\overline{\Gamma}\overline{M}$ measured by high-resolution SARPES. The spin detector is arranged to be sensitive to the y component of the spin polarization P_y defined in Fig. 3.12 (c). (d) Peak positions of the spin-resolved EDCs together with the high-resolution ARPES intensity image. Red and blue symbols correspond to mutually opposite spin directions in the y direction. In the inset, the constant energy ARPES intensity map at E_F is displayed. The constant energy image is obtained by the summation of the photoelectron intensity within a 2-meV energy window centered at E_F. (a) and (b) is taken from [11], and (c) and (d) is taken from [13].

detectors enable us to analyze the spin vector of the electron three-dimensionally.

The effective Sherman function of the SARPES apparatus was estimated by measuring the surface states of Bi(111) at $k_{//} = 0.1$ Å on the $\overline{\Gamma}\overline{M}$ axis with the unpolarized photons from a He discharge lamp, as the same as our method for determining S_{eff} of SARPES apparatus at Okayama University, with the VLEED spin detector with the plus and minus magnetized target. Although the value of the effective Sherman function of the VLEED spin detector ranges between 0.2 and 0.4, depending on the quality of the target, we usually use the value of 0.25 as the effective Sherman function. This value is typical for the target just after surface cleaning, so that we always the surface cleaning before our SARPES measurements.

3.2.2 Energy Resolution

The achieved energy resolution was determined from the Fermi edge of a gold (Au) polycrystal film. Figure 3.13(a) shows the spectrum of the Fermi edge taken with the ARPES mode, with an analyzer pass energy of 1 eV and an entrance slit width of 0.2 mm. From the fitting with the Fermi–Dirac distribution function, the energy resolution was estimated to be 600 μeV.

Figure 3.13(b) shows the spectrum of the Fermi edge acquired in SARPES mode. The spectrum was recorded with an analyzer pass energy of 2 eV, entrance slit width of 0.2 mm, and aperture size of 0.2×0.5 mm^2. The acquisition time of the spectrum with the SARPES mode was 1.5 h. From the fitting, the energy resolution was estimated to be 1.7 meV, much higher than those of other SARPES machines using a noble gas discharge lamp and synchrotron radiation [10,12]. For practical measurements, one can choose a suitable energy resolution between 1.7 meV and 30 meV by changing the set of the pass energy, the entrance slit width, and the aperture size.

By using the laser-based high-resolution SARPES apparatus, spin-polarization derived from Rashba spin splitting on Cu(111) surface was observed, as shown in Figs. 3.13 (c) and (d) [13]. Since the atomic number of Cu is 29 which is comparatively small, the Rashba splitting is also expected to be small in comparison with Ag and Bi because the magnitude of the Rashba effect is generally proportional to the atomic number. In Fig. 3.13, the high-resolution SARPES observes the Rashba splitting on Cu(111) surface whose size at the Fermi wave vector between the spin-up and spin-down states is ~5 meV. The data certify the performance of the laser-based high-resolution SARPES apparatus.

3.2.3 Magnet Holder

For SARPES measurements on ferromagnetic materials, the ferromagnetic sample has to be magnetized in order to arrange the magnetization direction of each domain. Of course, the magnetization procedure must be performed for the sample whose temperature is below the Curie temperature T_C. Therefore, it is desired that the ferromagnetic sample is magnetized in a chamber connecting with the analysis system. However, we have to consider that the SARPES apparatus is shared with researchers all over the world, and that development of a fledged magnetization system with Helmholtz-type coils and magnetic circuit spends much time and money.

Hence, we devised a simple magnetization system and developed a totable magnet holder, as shown in Figs. 3.14 (a) and 3.14 (b). The magnet holder, the base plate, and the screws are made of non-magnetic materials. The SARPES apparatus has a carousel-type sample bank

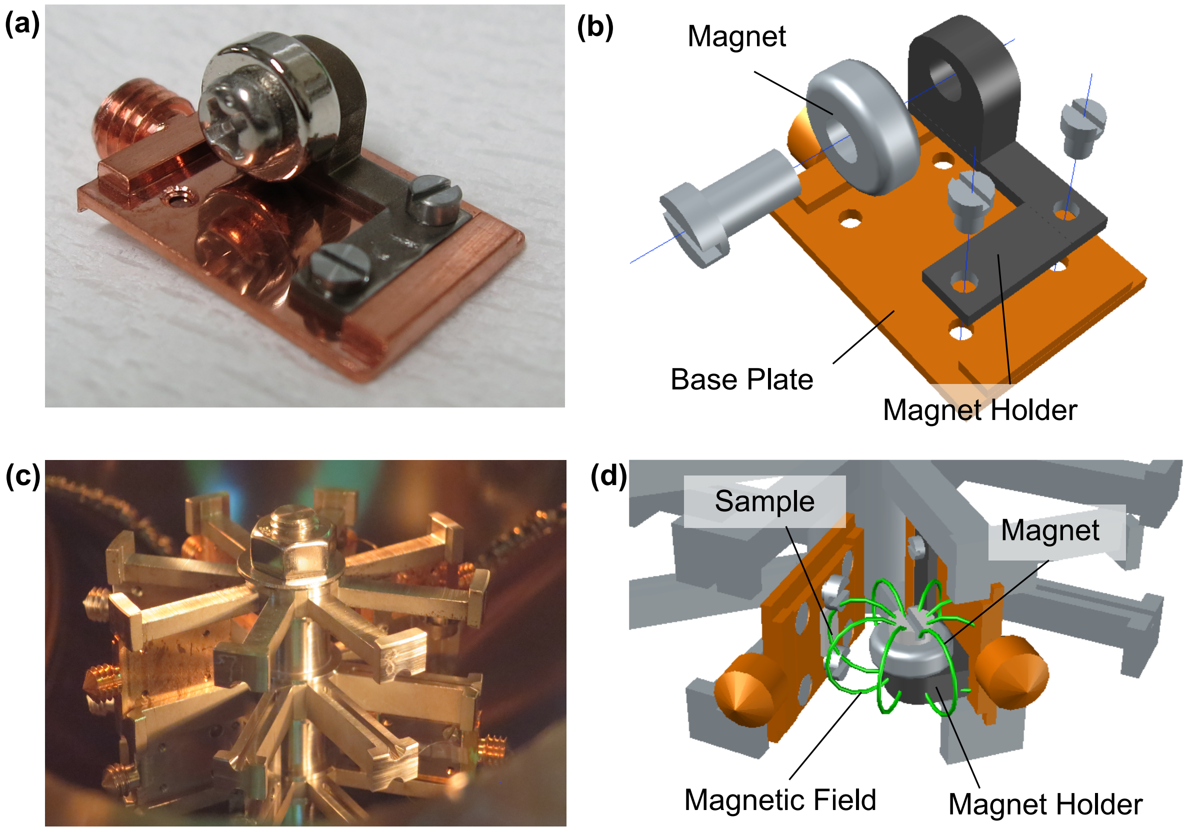

Fig. 3.14. (a) Picture of the magnet-holder assembly developed for magnetizing ferromagnetic samples *in situ*. (b) Schematic view of structure of the magnet holder. (c) Picture of the carousel-type sample bank. (d) Schematic drawing of the magnetization system built into the carousel-type sample bank.

chamber, as shown in Fig. 3.14 (c), neighboring the analysis chamber. Here, 16 samples (8 samples for upper stage, 8 samples for lower stage) can be stored under ultrahigh vacuum. By stocking a doughnut-shape magnet mounted on the magnet holder in the sample bank, we can magnetize the sample along the vertical direction by bringing the sample close to the magnet. In addition, we can transfer the sample between the sample bank chamber and the analysis chamber by one transfer rod. Therefore, by magnetizing the sample after cooling it with the transfer rod, we can magnetize the sample at low temperature, approximately below 40 K. For inversing the magnetization direction of the sample, we should prepare another set of the magnetization system in which the north pole and south pole of the magnet are inversed. The schematic illustration of the magnetization system is shown in Fig. 3.14 (d).

3.3 References

[1] M. H. Berntsen, P. Palmgren, M. Leandersson, A. Hahlin, J. Åhlund, B. Wannberg, M. Månsson, and O. Tjernberg, Rev. Sci. Instrum. **81**, 035104 (2010).

[2] S. Souma, A. Takayama, K. Sugawara, T. Sato, and T. Takahashi, Rev. Sci. Instrum. **81**, 095101 (2010).

[3] J. E. Northrup and M. L. Cohen, Phys. Rev. Lett. **49**, 1349 (1982).

[4] G. Binnig, H. Rohrer, Ch. Gerber, and E. Weibel, Phys. Rev. Lett. **50**, 120 (1983).

[5] K. Takayanagi, Y.Tanishiro, S. Takahashi, and M. Takahashi, Surf. Sci. **164**, 367 (1985).

[6] A. V. Latyshev, A.L. Aseev, A.B. Krasilnikov and S.I. Stenin Surf. Sci. **213**, 157 (1989).

[7] Y. Zhu and L. Cao, Appl. Surf. Sci. **133**, 213 (1998).

[8] Y. Mizokawa, T. Miyasato, S.Nakamura, K. M.Geib, and C. W. Wilmsen, Surf. Sci. **182**, 431 (1987).

[9] V.B. Nascimento, V. E. de Carvalho, R. Paniago, E. A. Soares, L. O. Ladeira, and H. D. Pfannes, J. Electron Spectrosc. Relat. Phenom. **104**, 99 (1999).

[10] T. Okuda, K. Miyamaoto, H. Miyahara, K. Kuroda, A. Kimura, H. Namatame, and M. Taniguchi, Rev. Sci. Instrum. **82**, 103302 (2011).

[11] K. Yaji, A. Harasawa, K. Kuroda, S. Toyohisa, M. Nakayama, Y. Ishida, A. Fukushima, S. Watanabe, C. Chen, F. Komori, and S. Shin, Rev. Sci. Instrum. **87**, 053111 (2016).

[12] S. Souma, A. Takayama, K. Sugawara, T. Sato, and T. Takahashi, Rev. Sci. Instrum. **81**, 095101 (2010).

[13] K. Yaji, A. Harasawa, K. Kuroda, R. Li, B. Yan, F. Komori, and S. Shin, Phys. Rev. B **98**, 041404(R) (2018).

CHAPTER 4. HALF-METALLICITY OF CrO_2 (100) FILMS

4.1 Introduction

Chromium dioxide, CrO_2, is a theoretically predicted half-metallic ferromagnet in which the spin polarization at E_F was expected to be 100%.[1–3] The half- metallic behavior of CrO_2 was experimentally proved by the point contact Andreev reflection measurement at 1.85K,[4] where the observed spin polarization at E_F was as high as 96%. This value has been the highest in the materials determined by the Andreev reflection measurements up to date. Therefore, the half-metallic ferromagnet CrO_2 has been regarded as one of the most hopeful materials for spintronics applications.

One of the key ingredients for practical usage is the temperature-dependence of spin polarization, i.e., the device performances at room temperature. Spin-resolved photoemission spectroscopy (SRPES) is a powerful technique for determining the half-metallicity as a function of temperature. In the earlier studies, the spin polarization of about 100% near E_F was found for the polycrystalline film and film island samples of CrO_2 at room temperature by spin-resolved PES using HeIα ($h\nu$ = 21.2 eV) as an excitation light source.[5,6] However, the reported energy positions of Cr 3*d* band were 2.7 eV (Ref. 5) and 2.3 eV (Ref. 6), away from the known value of ~1 eV, which was reported in spin-integrated PES by other groups.[7,8] In addition, the photoelectron intensity at E_F was too small to be regarded as a metal. It is well known that the surface of CrO_2 easily transforms into antiferromagnetic insulator Cr_2O_3,[9] whose energy position in photoemission spectra was reported to be ~2 eV.[10,11] In the previous spin-resolved PES study,[6] the maximum spin polarization was observed after removing the surface layer by moderate sputtering for certain optimum periods, and further sputtering reduced the spin polarization. Thus, it is likely that the Cr_2O_3 formed on the surface and sputtering procedure significantly influenced the results of the previous spin-resolved PES studies because of the surface sensitivity of the detected photoelectrons excited by HeIα. To determine the intrinsic spin-dependent electronic structure and discuss its half-metallicity, bulk-sensitive study has been anticipated. The escape depth of photoelectrons in a solid depends on their kinetic energies,[12] and the use of XeIα line ($h\nu$ = 8.44 eV) enables us to enhance the probing depth,[13] since the escape depth of excited photoelectrons is relatively long (~50 Å (Ref. 12)).

In this chapter, we present a bulk-sensitive SRPES study of high quality CrO_2 epitaxial

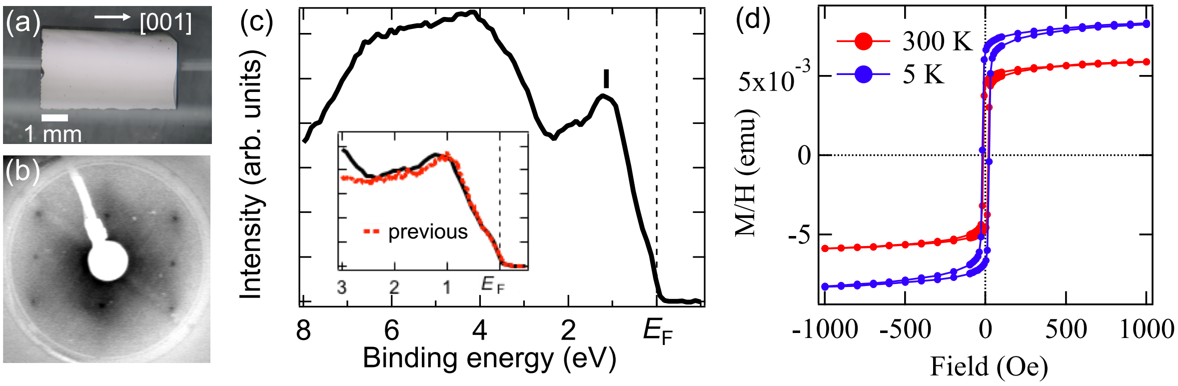

Fig. 4.1 (a) Picture of our $CrO_2/TiO_2(100)$ epitaxial film. (b) LEED pattern of the $CrO_2(100)$ epitaxial film on TiO_2 (100). The energy of incident electrons was set at 45 eV. (c) Valence band spin-integrated PES intensity at $h\nu$ = 70 eV. The inset shows comparison of this PES spectrum with the previous bulk-sensitive PES spectrum.[8] (d) Magnetic hysteresis curves for 300 K and 5 K.

films[7] at 40 K and 300 K. We have observed the intrinsic electronic states of CrO_2 peaked at 1.0 eV in the spin up spectra with a clear Fermi edge and the peak top of 1.0 eV in the spin up spectra at both 40K and 300K. A band gap of 0.5eV below E_F was observed in the spin down state at 40 K, which provides evidence for the half-metallicity of CrO_2 at low temperature, whose magnitude suggests that the electron correlation U firmly affects to the electronic states.

4.2 Preparation and Evaluation of $CrO_2/TiO_2(100)$ Epitaxial Films

The $CrO_2(100)$ films were prepared on $TiO_2(100)$ substrates with the same chemical vapor deposition (CVD) technique as what reported earlier by Iwai *et al.*[7] Cr_8O_{21} powder was used as a precursor, which was prepared by heating of CrO_3 at 250 ˚C for 8 h in flowing oxygen.[7] Because Cr_8O_{21} is less hygroscopic and less toxic compared with CrO_3, it would be a more appropriate precursor. The precursor and TiO_2 substrate were vacuum-encapsulated in a quartz tube. Then the precursor and substrate were heated to 300˚C and 390˚C for 150 minutes in an electric furnace.

After the synthesis, the CrO_2 film was taken from the quartz tube in an atmosphere and then immediately introduced into the ultra-high vacuum (UHV) at HiSOR BL-5 for PES and LEED measurements to evaluate the quality of the sample surface. As shown in Fig. 4.1(a), the rectangular-like pattern characteristic of tetragonal crystal structure was confirmed on the sample surface without any cleaning procedures including sputtering and annealing. The LEED pattern is consistent with that of $CrO_2(100)$ reported in the previous study.[14] The surface-sensitive PES spectrum of the valence band is shown in Fig. 4.1 (b) which shows a peak at 1 eV with a clear Fermi edge, consistent with the bulk-sensitive x-ray PES spectrum for CrO_2 as shown in the insert of Fig. 4.1 (b). This suggests that the high-quality sample surface was prepared, while a peak at 2 eV indicating the existence of Cr_2O_3 exists. The existence of a few amorphous Cr_2O_3 on the CrO_2 surface was also indicated in the LEED image as background signals.

Figure 4.1 (c) shows the magnetic hysteresis curves at 300 K and 40 K of the same CrO_2 sample as this spin-resolved PES measurement. The thickness of the film was estimated to be approximately 100 nm by assuming that the value of saturated magnetization at 5 K is $2\mu_B$ being that of bulk CrO_2 samples. The difference between values of saturated magnetization at 5 K and 300 K can be due to spin wave excitation. This effect affects the spin polarization measured by spin-resolved PES, as discussed in Sec. 5.3.

4.3 SRPES Experimental and Analysis

The spin-resolved PES measurements were carried out at 40 K and 300 K in a spin-resolved PES system with a base pressure of 1×10^8 Pa at Okayama University. The unpolarized light of HeIα line and XeIα line was used to excite photoelectrons for the experiments. The light of XeIα line was monochromated by a CaF_2 filter. The energy resolution, during the spin-integrated and spin-resolved PES, was approximately 35 meV and 100 meV, respectively. The spin-integrated and spin-resolved PES spectra were obtained in the transmission mode of the detector. The acceptance angle of the analyzer was ±15° along [001] direction (easy axis) and ±1° along [010] direction, corresponding to the ~ 50% Brillouin zone along [001] direction in the XMAR plane centered at the X point (k_z is unknown at present). However, actually, our ARPES spectrum does not indicate any clear angular dependence; therefore, our results can be considered to be angle-integrated. Calibration of E_F for the sample was achieved using a gold reference. To resolve the direction of the spin of photoelectrons, we used a mini Mott spin detector (VG Scienta 2D-spin)[15] whose target was an Au polycrystalline film. The effective Sherman function S_{eff} was determined to be 0.1 by spin- and angle-resolved PES measurements of Bi/Si(111) thin films (as shown in Sec. 3.1). The sensitivity of a pair of detectors in the Mott polarimeter was calibrated by non-polarized photoelectrons from Au polycrystalline film. We magnetized the sample along the easy axis by bringing a magnet close to the sample and measured spin polarization along the magnetized direction. Careful attention has been paid to hold the direction of magnetization when we took the magnet away from the sample.

The asymmetry including the sensitivity of a pair of the detectors in the Mott spin polarimeter was calibrated by magnetization reversal of the sample. We obtained the spin polarization by following equation: $P=\{\surd(I^+{}_L I^-{}_R)-\surd(I^-{}_L I^+{}_R)\}/\{\surd(I^+{}_L I^-{}_R)+\surd(I^-{}_L I^+{}_R)\}/S_{eff}$, where $I^{+(-)}{}_L$ and $I^{+(-)}{}_R$ are intensity observed by left and right channels, respectively, when magnetizing the sample in the "+ (–)" direction along the easy axis.[16] No background subtraction was applied as the data analysis because the background estimated by the intensity above E_F is much smaller than the signal at and below E_F.

4.4 Results and Discussion

Figure 4.2 (a) shows spin-integrated valence band PES spectra near E_F of epitaxial $CrO_2(100)$ film by the HeIα and the XeIα lines at 300K. In the spectrum of the HeIα line (He I spectrum), the peak positions were found to be approximately 1 eV and 2 eV. The intrinsic peak position derived from CrO_2 was reported to be at 1.0 eV by bulk sensitive hard x-ray photoemission spectroscopy (HAXPES);[8] therefore, we identify the peak of approximately 1 eV as Cr d_{xy} states of CrO_2. Existence of a structure approximately 2 eV indicates that small amount of Cr_2O_3 exists on the CrO_2 film, even if the only CrO_2 derived LEED pattern for the sample was observed. The relative intensity of 2 eV structure depends on films, and, for spin-resolved PES measurements, we used a film with negligible 2 eV structure. A clear Fermi edge in addition to the 1 eV structure was also observed in the He I spectrum, which indicates that the quality of samples used in the present study was higher than those of the previous studies.[5,6] In a previous resonant PES study of CrO_2,[14] the peak position of Cr 3*d* was found to be 1.9 eV with the LEED pattern of CrO_2 without Cr_2O_3-derived spots, similar to our measurements of the HeIα. In the Xe I spectrum, the spectral weight around 1 eV is relatively enhanced as compared to the He I spectrum, which implies that the energy distribution curve (EDC) of XeIα reflects more intrinsic electronic states of CrO_2 than that of the He I. Next, we discuss the spin polarization of the bulk electronic states of CrO_2 using the spin-resolved Xe I spectra.

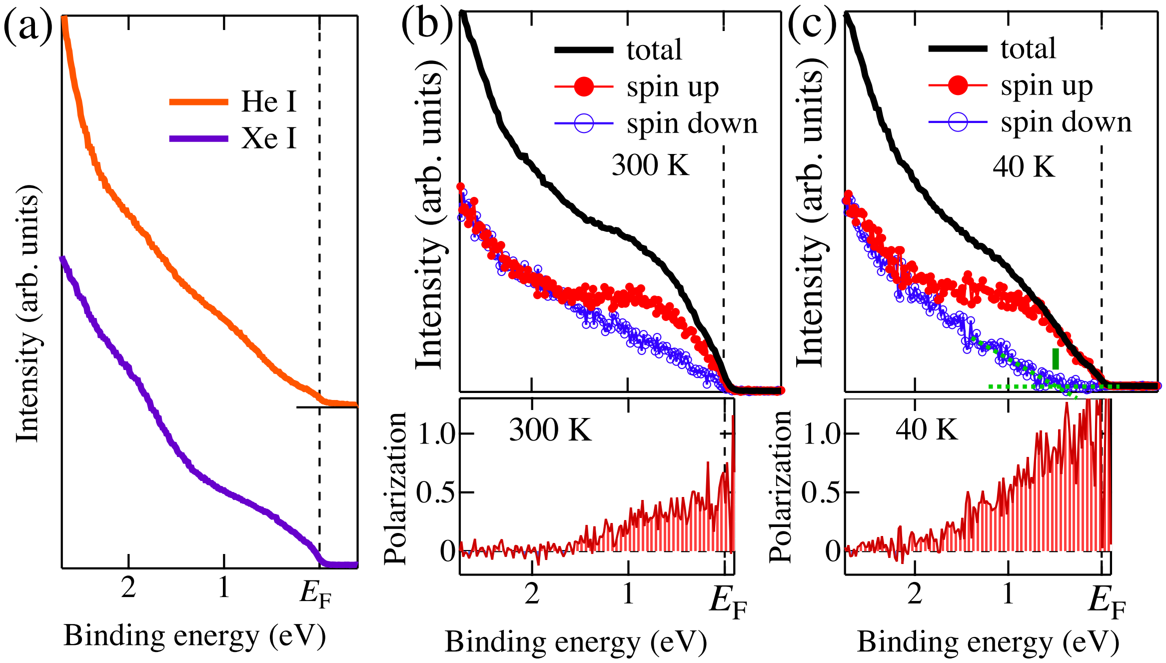

Fig. 4.2 (a) Valence band spin-integrated PES spectra measured by the He I line (21.2 eV) and a Xe I line (8.44 eV) at 300 K. (b), (c) Spin-resolved EDCs measured by the Xe I line and corresponding energy dependence of the spin polarization along the easy axis direction at 300 K and 40 K, respectively.

Figures 4.2 (b) and (c) show the spin-resolved EDCs of the CrO_2 film and the spin polarization as a function of binding energy at 300 K and 40 K, respectively. The spin polarization from E_F to 2 eV was observed both at 40 K and 300 K. It is clear from the figures that the spin down spectrum shows the insulating energy gap of 0.5 eV at least in the occupied side at 40 K (green thick line in Fig. 4.2 (c)), while the gap in the spin down spectrum at 300 K is closed. The degrees of spin polarization were 40 % and 100 % near E_F at 300 K and 40 K, respectively, which is consistent with our magnetization curve qualitatively. These results are different from the previous spin-resolved PES study[6] in three points: (i) The spin-polarized binding energy region (E_F ~ 2 eV) is narrower than the one in the previous study (E_F ~ 6 eV) and more consistent with the band calculation predictions. (ii) The spin polarization near E_F at room temperature of 40 % is smaller than the one of 95 % in the previous study and closer to the values expected from our magnetization curves. (iii) The clear Fermi edge is observed without any sputtering while the intensities of the Fermi edge in the previous studies are too small to be regarded as a metal even after the optimized sputtering procedures. Although we do not have a direct answer for the cause of these differences, we note that the experimental conditions, specifically, the excitation photon energy and the conditions of the film formation, are different. Since we performed more bulk-sensitive measurements on high quality

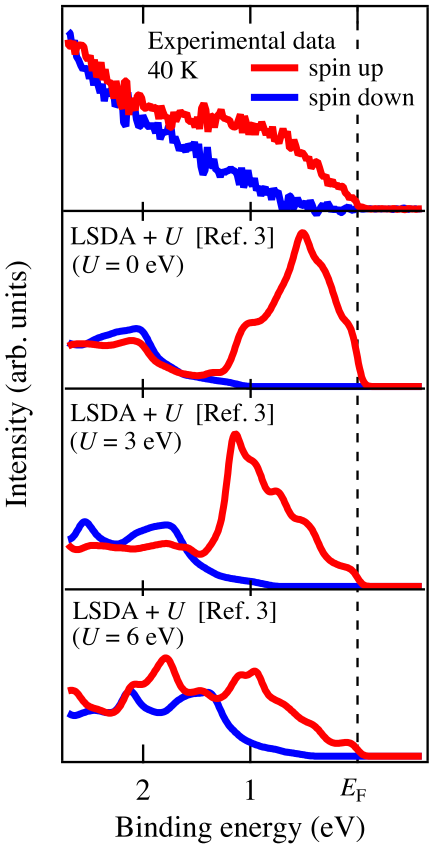

Fig. 4.3 Comparison of the experimental spin-resolved EDCs at 40 K in the present study with theoretical spin-resolved density of states calculated by Jeng and Guo.[3] These band calculations are multiplied by the Fermi-Dirac function and broadened by convoluting with a 100 meV Gaussian.

samples than the previous studies, we believe that the present results reflect the nature of intrinsic CrO_2 film with less influence of Cr_2O_3. One of the previous studies argued that the highly spin polarized results of the previous spin-resolved PES studies at room temperature might have suffered the Cr_2O_3 surface layer in a magnetically ordered single domain state on top of the CrO_2 film.[17] Our LEED patterns before and after SRPES measurements did not show the six-fold pattern derived from ordered Cr_2O_3, but with relatively high background, indicating that the Cr_2O_3 layer was in an amorphous state. The spin-polarized energy region corresponds to that of the coherent structure around 1eV of HAXPES spectra,[8] suggesting that the intrinsic electronic structure of CrO_2 was obtained. The consistency between the present SRPES spectra and the macroscopic measurements, i.e., magnetization and resistivity measurements, suggest that the effects of Cr_2O_3 on the CrO_2 film are small and support the reliability of our spin-resolved PES results.

Next, we discuss the possible reasons of depolarization near E_F at 300 K. As seen in Figs. 4.2 (b) and (c), the intensity between 2 eV and E_F in the spin down states increases with the increase in temperature, which primarily causes the decrease of spin polarization at 300 K. As the reasons why the spin polarization near E_F decreases at 300 K, the change of the amount of exchange splitting, formation of non-quasiparticle (NQP) states,[18] and/or enhancement of spin fluctuation are considered. In general, the energy scale of the change of the amount of exchange splitting below the Currie temperature ($0.3 < T/T_C < 0.8$) is 10–100 meV,[19,20] which is different from the energy region that the spin polarization decreases. The NQP states in CrO_2 were predicted by Chioncel *et al.*[21] who suggested that the NQP states can be produced near and above E_F. In this case, the down spin states in the vicinity of E_F would increase rather than those at the higher binding energy part, which contradicts to what observed here. In addition, the energy scale of NQP states below E_F has been argued to be about 100 meV based on their DMFT calculation, which does not explain the observed spin depolarization over a larger energy scale. Therefore, we concluded that the decrease of spin polarization at 300 K is mainly due to enhancement of spin fluctuation.[20] This picture is supported by the fact that the energy region where the spectral intensity of spin down states increases with increasing temperature matches well with the energy region where spin up states populate.

Finally, we discuss the on-site Coulomb interaction by comparison of experimental spin-resolved EDCs at 40 K with the density of states calculated by the LSDA+U method using 0, 3, and 6 eV as the electron correlation U,[3] as shown in Fig. 4.3. The spectral characteristics of spin-resolved PES, e.g., the peak position and the intensity at E_F of the spin up states and the gap on the occupied side of the spin down states, fit more closely with the band calculations using $U = 3$ eV or 6 eV rather than that of $U = 0$ eV, indicating that electron correlation U must have a finite value in CrO_2. Along with the previous hard x-ray PES and inverse PES study[8] which discuss the value of U, our spin-resolved PES study points out that electron correlation U must have been taken into account when considering the electronic structure of half-metallic ferromagnet CrO_2 system.

4.5 Summary

We have investigated the temperature dependence of the spin-dependent electronic structure of high quality CrO_2(100) epitaxial film by bulk-sensitive spin-resolved PES. A clear Fermi edge and spin polarization of about 100%, and a band gap of 0.5 eV in the spin down states, were observed at 40 K, providing the spectroscopic evidence for the half-metallicity of CrO_2 at low temperatures, at least in the probed momentum region of the Brillouin zone. In addition, the Fermi edge and spin polarization of 40% near E_F were observed at 300 K, which is consistent with earlier reports of resistivity measurements and magnetic hysteresis curves. The comparison of the spin-resolved PES spectra with LSDA+U calculations suggests that the electronic correlation U must be considered in order to discuss the electronic states of CrO_2. These results also indicate that bulk-sensitive spin-resolved PES is a powerful experimental tool to investigate intrinsic spin-resolved electronic states of half-metallic ferromagnets.

4.6 References

[1] K. Schwarz, J. Phys. F: Met. Phys. **16**, L211 (1986).

[2] M. A. Korotin, V. I. Anisimov, D. I. Khomskii, and G. A. Sawatzky, Phys. Rev. Lett. **80**, 4305 (1998).

[3] H.-T. Jeng and G. Y. Guo, J. Appl. Phys. **92**, 951 (2002).

[4] Y. Ji, G. J. Strijkers, F. Y. Yang, C. L. Chien, J. M. Byers, A. Anguelouch, G. Xiao, and A. Gupta, Phys. Rev. Lett. **86**, 5585 (2001).

[5] K. P. Kämper, W. Schmitt, G. Güntherodt, R. J. Gambino, and R. Ruf, Phys. Rev. Lett. **59**, 2788 (1987).

[6] Yu. S. Dedkov, M. Fonine, C. König, U. Rüdiger, G. Güntherodt, S. Senz, and D. Hesse, Appl. Phys. Lett. **80**, 4181 (2002).

[7] K. Iwai, Y. Muraoka, T. Wakita, M. Hirai, T. Yokoya, Y. Kato, T. Muro, and Y. Tamenori, J. Appl. Phys. **108**, 043916 (2010).

[8] M. Sperlich, C. König, G. Güntherodt, A. Sekiyama, G. Funabashi, M. Tsunekawa, S. Imada, A. Shigemoto, K. Okada, A. Higashiya, M. Yabashi, K. Tamasaku, T. Ishikawa, V. Renken, T. Allmers, M. Donath, and S. Suga, Phys. Rev. B **87**, 235138 (2013).

[9] R. Cheng, B. Xu, C. N. Borca, A. Sokolov, C.-S. Yang, L. Yuan, S.-H. Liou, B. Doudin, and P. A. Dowben, Appl. Phys. Lett. **79**, 3122 (2001).

[10] C. A. Ventrice, Jr., D. R. Borst, H. Geisler, J. van Ek, Y. B. Losovyj, P. S. Robbert, U. Diebold, J. A. Rodriguez, G. X. Miao, and A. Gupta, J. Phys.: Condens. Matter **19**, 315207 (2007).

[11] W.-Y. Howng and R. J. Thorn, J. Phys. Chem. Solids **41**, 75 (1980).

[12] M. P. Seah and W. A. Dench, Surf. Interface Anal. **1**, 2 (1979).

[13] S. Souma, T. Sato, T. Takahashi, and P. Baltzer, Rev. Sci. Instrum. **78**, 123104 (2007).

[14] Yu. S. Dedkov, A. S. Vinogradov, M. Fonin, C. König, D. V. Vyalikh, A. B. Preobrajenski, S. A. Krasnikov, E. Yu. Kleimenov, M. A. Nesterov, U. R€udiger, S. L. Molodtsov, and G. Güntherodt, Phys. Rev. B **72**, 060401 (2005).

[15] M. H. Berntsen, P. Palmgren, M. Leandersson, A. Hahlin, J. Åhlund, B. Wannberg, M. Månsson, and O. Tjernberg, Rev. Sci. Instrum. **81**, 035104 (2010).

[16] P. D. Johnson, Rep. Prog. Phys. **60**, 1217 (1997).

[17] P. A. Dowben, N. Wu, and C. Binek, J. Phys.: Condens. Matter **23**, 171001 (2011).

[18] M. I. Katsnelson, V. Yu. Irkhin, L. Chioncel, A. I. Lichtenstein, and R. A. de Groot, Rev.

Mod. Phys. **80**, 315 (2008).

[19] T. Greber, T. J. Kreutz, and J. Osterwalder, Phys. Rev. Lett. **79**, 4465 (1997).

[20] E. Kisker, K. Schröder, W. Gudat, and M. Campagna, Phys. Rev. B **31**, 329 (1985).

[21] L. Chioncel, H. Allmaier, E. Arrigoni, A. Yamasaki, M. Daghofer, M. I. Katsnelson, and A. I. Lichtenstein, Phys. Rev. B **75**, 140406 (2007).

CHAPTER 5. THERMAL SPIN DEPOLARIZATION IN CrO_2 DUE TO MANY-BODY EFFECT

5.1 Introduction

In the preceding parts, we discussed the overall characteristics of spin-resolved electronic structure of CrO_2. In this chapter, we focus on the electronic structure near E_F to discuss a fine-energy spin depolarization due to the NQP state investigated by high-resolution spin-resolved photoemission spectroscopy.

To entirely understand magnetic phenomena in itinerant electron ferromagnets has been one of the most significant goals of condensed-matter physics.[1] In itinerant electron ferromagnets, interaction between conduction electrons and thermal spin fluctuation is of crucial importance for understanding the physical properties. As a many-body state dominating the transport properties of ferromagnetic metals, the nonquasiparticle (NQP) state, also called spin-polaron state, was proposed in works on electron–magnon interaction.[2,3] For investigation of the behavior of the NQP state, half-metallic ferromagnets (HMFs), which have metallic electronic structures with an energy gap at the Fermi level (E_F) for any one electronic spin state in the ground state, are ideal substances, because it was predicted that in half-metallic ferromagnets the effect of electron–magnon interaction was not masked by Stoner excitations unlike usual itinerant ferromagnets and made observable modification of the electronic structure in the close vicinity of E_F.[4,5] Although many theoretical studies on NQP were reported,[6–8] only a few experimental studies suggesting the existence of NQP in HMFs were published to the present.[9,10] Experimental electronic-structure investigation of a HMF can reveal the behavior of the NQP state, which not only advances the formulation of many-body physics but also promotes application of HMFs for next-generation spintronic devices.[11]

Chromium dioxide (CrO_2), which has the rutile-type crystal structure, is the simplest half-metallic oxide without carrier doping. As a notable advantage, CrO_2 always shows almost 100% spin polarization, as validated in Chap. 4, which is the highest value exhibited by a candidate HMF at low temperature.[12–14] This completely spin-polarized feature is suitable for exploring the many-body state. In addition, recently, CrO_2 has been predicted to host triple point fermions, as well as additional Weyl points, attracting attention of material scientists.[15] According to magnetoresistance studies, the spin polarization drops exponentially at higher temperatures, the origin of which cannot be understood from bulk magnetization alone.[16–18]

As a cause of the rapid depolarization, the many-body effects have also been proposed.[19] Theoretical studies based on the dynamical mean-field theory (DMFT) showed that the many-body effects broadened the bandwidth of a minority spin state above E_F and that the tail of the state crossed E_F, which permitted spin-flip scattering of the conducting majority spin electrons.[6,19]

Spin-resolved photoemission spectroscopy (SRPES) is a powerful technique to directly observe spin-polarized electronic structures and determine absolute values of spin polarization based on simple analyses. In SRPES measurements using a conventional low-efficiency spin detector, the energy resolution is set to several 100 meV, which is not sufficient to observe the many-body states. However, recently, by using a high-efficiency spin detector and high-intensity low-energy light source, energy resolutions that were almost two orders higher were achieved,[20–22] as described in Sec. 3.2. This allows us to investigate the spin-polarized fine electronic structures such as the many-body states in HMFs.

There are pioneering works of SRPES on CrO_2.[23,24] In these studies, SRPES spectra show almost 100% spin polarization near E_F at room temperature. However, the energy resolutions were not good enough to discuss a depolarization near E_F characteristics of the many-body effects.

In this chapter, we present the temperature dependence of the electronic structure and spin polarization of half-metallic CrO_2(100) epitaxial films, measured by SRPES using the XeIα line and a laser, in order to clarify the origin of the depolarization in the magnetoresistance. First, we demonstrate the SRPES results obtained by the XeIα line, and following it, we demonstrate and discuss the results obtained by high-resolution SRPES measurements using the 7-eV laser and the high-efficient spin detector. Two spin depolarizations have been observed; Two types of spin depolarizations were observed: One developed over the entire spin-polarized energy range at a constant rate with respect to temperature. Above 80 K, another occurred in the close vicinity of E_F with an energy scale of several 10 meV. The tendency of the temperature dependence of the minority spin state is consistent with the DMFT calculations and NQP theories, which constitutes spectroscopic evidence for the many-body effect in CrO_2.

5.2 Experimental and Analysis

The CrO_2 (100) epitaxial films grown on a rutile-type TiO_2 (100) substrate were prepared by a closed-system chemical vapor deposition method.[25] After the synthesis, the CrO_2 film was removed from the quartz tube and then immediately placed under high vacuum for SRPES measurements. During the procedure, the CrO_2 sample was exposed to the atmosphere for approximately three minutes.

Our bulk-sensitive spin-resolved PES measurements were carried out at 40 K, 100 K, 150 K, 200K, and 300 K in a spin-resolved PES system with the Mott spin polarimeter (Scienta 2D-spin) whose target was a Au polycrystalline film at Okayama University. The effective Sherman function S_{eff} was determined to be 0.1 by comparison of our spin- and angle-resolved PES spectra of the Bi/Si(111) thin film with that of Ref. 21, as shown in Sec. 3.1. The monochromated beam of Xe I resonance line was used as the excitation beam to enhance the bulk-sensitivity. The energy resolution was set to 100 meV. The acceptance angle of the analyzer was ±15° along the [001] direction (easy axis) and ±1° along the [010] direction. We magnetized the sample along the magnetic easy axis by bringing a magnet close to the sample and then measured the spin polarization along the magnetized direction. Careful attention has been paid to maintain the direction of magnetization when we remove the magnet away from the sample. The asymmetry including the sensitivity of a pair of the detectors in the Mott spin polarimeter was calibrated by magnetization reversal of the sample. We obtained the spin polarization by following equation: $P=\{\sqrt{(I^{+}_{\mathrm{L}}I^{-}_{\mathrm{R}})}-\sqrt{(I^{-}_{\mathrm{L}}I^{+}_{\mathrm{R}})}\}/\{\sqrt{(I^{+}_{\mathrm{L}}I^{-}_{\mathrm{R}})}+\sqrt{(I^{-}_{\mathrm{L}}I^{+}_{\mathrm{R}})}\}/S_{\mathrm{eff}}$, where $I^{+(-)}_{\mathrm{L}}$ and $I^{+(-)}_{\mathrm{R}}$ are intensity observed by left and right channels, respectively, when magnetizing the sample in the "+ (–)" direction along the easy axis.[26,27] No background subtraction was applied as the data analysis because the background estimated by the intensity above E_{F} is much smaller than the signal at and below E_{F}.

For high-resolution measurements, spin-integrated and spin-resolved photoemission spectroscopy data were acquired by the laser-based spin-resolved ARPES (SARPES) apparatus at the Institute for Solid State Physics at the University of Tokyo.[22] The apparatus was equipped with highly efficient very-low-energy electron diffraction (VLEED) spin detectors whose effective Sherman function S_{eff} was 0.25 and a hemispherical analyzer (SCIENTA-OMICRON DA30L). We used a vacuum ultraviolet (VUV) laser ($h\nu = 6.994$ eV) with *p*-light-polarization as an excitation beam. During the measurement, the instrumental energy resolution was set to 20 meV and the base pressure was kept below 1×10^{-8} Pa. The acceptance angle of the spin detector was set to 0.7°, which reliably corresponded to approximately 1% of the Brillouin zone in the XMAR plane centered at the X point. However, actually, our ARPES spectrum does not indicate any clear angular dependence; therefore, our results can be considered to be angle-integrated. Calibration of E_{F} for the sample was achieved using a gold reference. We magnetized the CrO_2 (100) sample along the magnetic easy axis ([001] direction) by bringing the sample close to a magnet at room temperature. The approximate magnitude of the magnetic field at the sample position was 600 Oe. The schematic views of the experimental geometry and magnetization procedure are shown in Fig. 5.1.

In order to obtain absolute values of spin polarization using the VLEED detector, we used the equation $P = (1/S_{\mathrm{eff}})\,(I_+ - I_-)/(I_+ + I_-)$, where S_{eff} (=0.25) is the effective Sherman function of the apparatus and $I_{+(-)}$ is the intensity of the electrons reflected by the positively (negatively) magnetized target.[26] Then, we obtain the majority ($I_\uparrow$) and minority ($I_\downarrow$) spin spectra using $I_{\uparrow(\downarrow)} = (1 +(-)\, P)(I_{\mathrm{tot}}/2)$, where $I_{\mathrm{tot}} = I_+ + I_-$. After subtracting the background from $I_\uparrow$ and $I_\downarrow$, we obtain the resulting spin polarizations from $P = (I_{\uparrow\mathrm{BG}} - I_{\downarrow\mathrm{BG}})/(I_{\uparrow\mathrm{BG}} + I_{\downarrow\mathrm{BG}})$, where $I_{\uparrow(\downarrow)\mathrm{BG}}$ is the intensity of the majority (minority) spin electron without the background. The statistical error bars of the spin polarization were estimated from $1/(S_{\mathrm{eff}} I_{\mathrm{tot}}^{1/2})$.[27]

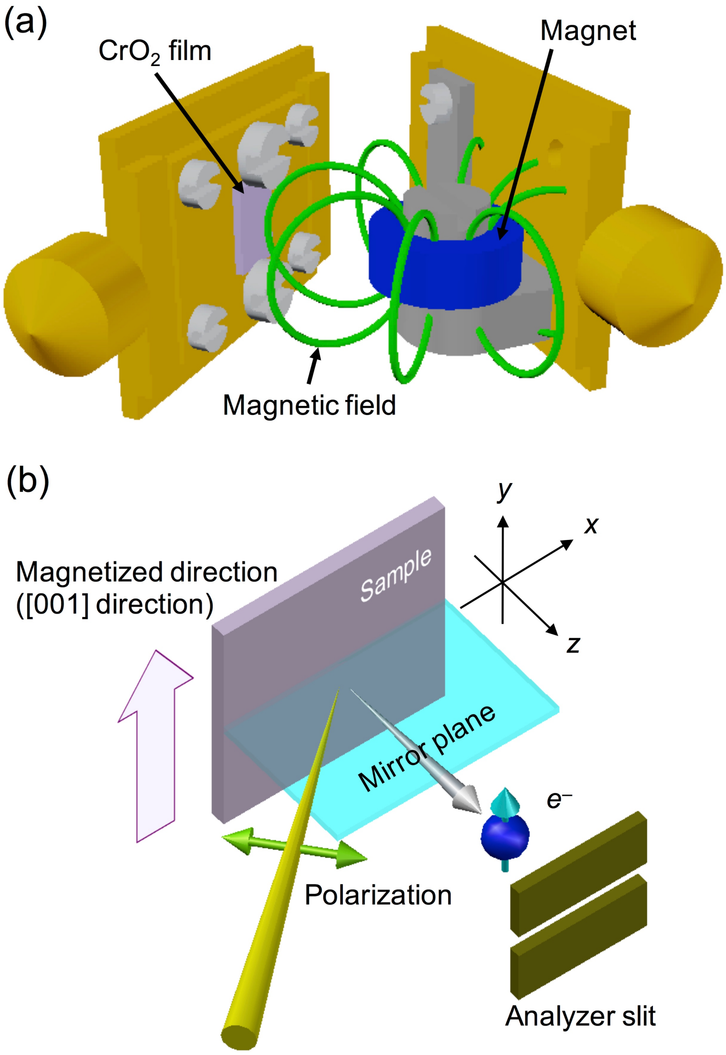

Fig. 5.1 Magnetization method and experimental geometry for SRPES measurements. (a) Schematic view illustrating how to magnetize our sample is shown. The magnet was mounted by a screw on our magnet holder. The real distance between the sample and the magnet was several millimeters, where magnitude of the magnetic field at the sample position was approximately 600 Oe. (b) Schematic view of the experimental geometry is represented. Both the magnetizing direction and measured spin polarization direction are parallel to the y axis. The angle between the laser light and the analyzer was fixed to 50°. The acceptance angle of the spin detector was 0.7° along x direction.

5.3 Results and Discussion

5.3.1 Bulk-Sensitive SRPES by the Xe Discharge Lamp and the Mott Detector

Figure 5.2 shows the temperature dependence of near-E_F SRPES spectra and the corresponding spin polarizations. At 40 K and 300 K, averaged values of the spin polarization between 600 meV BE and E_F, P(Ave.), are approximately 100% and 40%, respectively. This is consistent with the results of our previous measurements.[13] The spin polarization at 40 K is in good agreement with that obtained from the LDA calculations, as seen in Fig. 5.2. It should be noted that the spin polarization at 100 K significantly drops toward E_F from 150 meV. This narrow-range depolarization cannot be explained by the LDA calculations, shown by the yellow solid lines in Fig. 5.2. One of the possible origins of the narrow-range depolarization can be the NQP state in the minority spin gap. The green dotted lines in Fig. 5.2 show the spin polarization estimated from the DOS obtained within the LSDA+DMFT calculations for 100 K.[19] The green lines drop toward E_F from 150 meV while the yellow lines keep 100% spin polarization. According to Ref. 19, this depolarization seen in the green line is attributed to the NQP states in the minority spin gap. In order to directly compare the spin polarization curve from our experimental data with that from the theoretical calculations, we multiply the DOS obtained within the LSDA+DMFT calculations by the Fermi-Dirac function for 100 K and broaden it by convolving with a 100 meV Gaussian corresponding to the energy resolution of the measurement. The simulated spin polarization of the DMFT calculation is shown by the blue dashed lines in Fig. 5.2. The spectral shape of our experimental spin polarization at 100 K fits more closely with the blue line than the yellow line. This indirectly suggests the occurrence of the NQP state at 100 K in the CrO_2 film.

The wide-range depolarization, which we call *type I depolarization*, occurs over the entire spin-polarized energy range, namely, from more than $E_B \sim 1$ eV to E_F. This fact indicates that type I depolarization contributes predominantly to the demagnetization of the sample, which makes us speculate that the origin of type I depolarization is the same as that of demagnetization. In an earlier report, the $M(T)$ curve of CrO_2 powders followed Bloch's $T^{3/2}$ law and it was shown that the demagnetization was attributed to spin-wave excitation,[28] as same as our $M(T)$ curve. The spin-wave excitation caused a spin-mixing effect.[29] The magnitude of the spin-mixing contribution to the density of states was estimated to be $D_\downarrow(E) \approx (M_0 - M_s(T))/(M_0 + M_s(T))D_\uparrow(E)$, where $D_{\uparrow/\downarrow}(E)$ is the majority/minority spin density of states, $M_s(T)$ is the

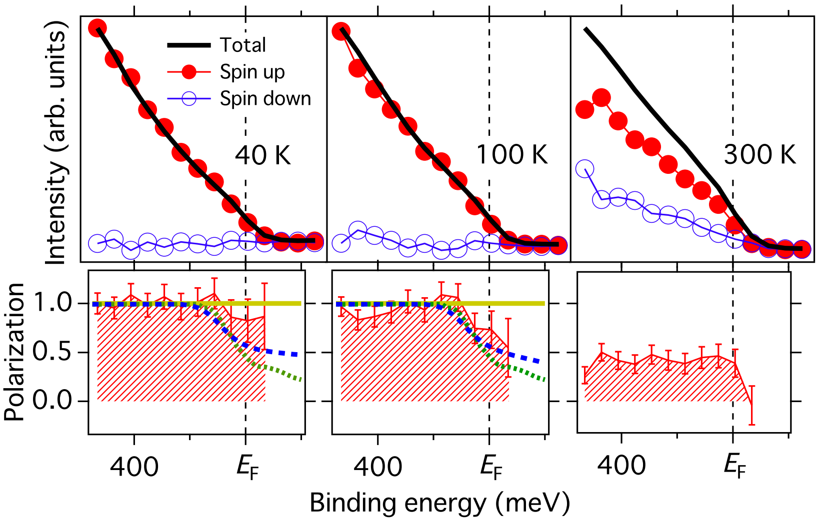

Fig. 5.2 Temperature dependence of near-E_F spin-resolved PES spectra (top) and spin polarization with statistical error bars (bottom) taken at $h\nu = 8.44$ eV. The error bars are estimated from $1/(S_{\text{eff}}I^{1/2})$ [24] where I is the total intensity. The yellow solid lines and green dotted lines in spin polarization at 40 K and 100 K show the energy dependence of spin polarization obtained from our LDA calculation and a DMFT calculation at 100 K from Ref. 14. The blue dashed lines show that obtained from the spin dependent DOS multiplied by the Fermi-Dirac function of each temperature and convoluted with a 100 meV Gaussian corresponding to the energy resolution of the measurement.

spontaneous magnetization, and $M_0 = M_s(0)$. This indicates that $D_\downarrow(E)$ shows the same energy dependence as $D_\uparrow(E)$ and that the corresponding spin polarization decreases over the entire spin-polarized energy range at elevated temperatures, which supports the present results from our SRPES measurements. Therefore, type I depolarization can be attributed mainly to the spin-wave excitation.

Next, we compare the average values in the energy region between 600 meV and E_F, P(Ave.), with the magnetization curve obtained from a SQUID measurement. P(Ave.) drops more rapidly with increasing temperature than the magnetization with increasing temperature. Similar behaviors were reported in an X-ray magnetic circular dichroism (XMCD) and spin-resolved PES study of $La_{0.7}Sr_{0.3}MnO_3$ (LSMO).[30] The LSMO study suggests that the more surface-sensitive the measurement, the more rapidly the obtained magnetization curve drops with increasing temperature. This is due to the effects of the surface boundary of the LSMO. The temperature dependence of P(Ave.) in Fig. 5.3 is similar to that of the magnetization curve obtained from the XMCD measurements in the LSMO study, which indicates that our SRPES measurements are more bulk-sensitive than those in the LSMO study. This is because a Xe I resonance line was used as an excitation beam. Nevertheless, the value of P(Ave.) at 300 K is quite small in comparison with that of the magnetization, which could be attributed to the

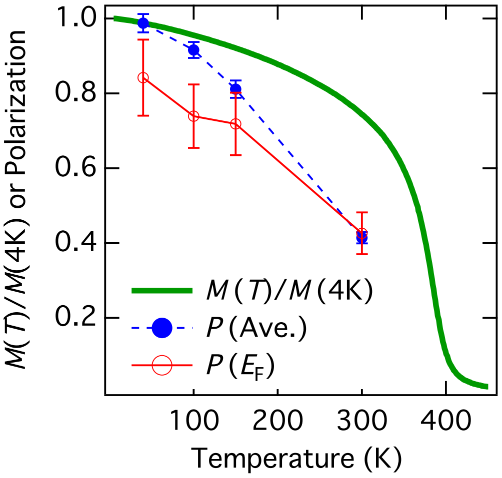

Fig. 5.3 Comparison of the temperature dependence of the spin polarization P obtained by our measurements with the magnetization along *b*-axis direction in an external magnetic field of 0.5 T from Ref. 25. The data points of the spin polarization P(Ave.) and $P(E_F)$ represent the average values in the region between 600 meV BE and E_F and between 100 meV BE and E_F, respectively. The statistical error bars are estimated from $1/(S_{eff}I_{sum}^{1/2})$ where I_{sum} is the intensity summed in the corresponding averaged energy region.

surface effect on the CrO_2 (100) film based on the LSMO study. Therefore, in order to investigate the behavior of the NQP states, it is sufficient to make *bulk-sensitive* and *low-temperature* (below 150 K) spin-resolved PES measurements on CrO_2, because type I depolarization derived from the surface effect is sufficiently suppressed in the low temperature region. The energy dependence of our experimental spin polarization at 40 K, reflecting the half-metallic electronic structure, is also consistent with that of band calculation for CrO_2 (100) surface.[31]

To validate the appearance of the narrow-range depolarization, which we call *type II depolarization*, we discuss the differences between the temperature dependence of P(Ave.) and that of $P(E_F)$. Figure 5.3 shows a comparison of the temperature dependence of the values of the spin polarization with the normalized magnetization curve from Ref. 25. At 300 K, $P(E_F)$ has the same value as P(Ave.). The difference between $P(E_F)$ and P(Ave.) is remarkable at lower temperature, showing that type II depolarization is more considerable at low temperature rather than at room temperature. The reason seems to be related to the suppression of type I depolarization. Around room temperature, type I depolarization is dominant in the SRPES measurements, so that the contribution of the NQP state is less considerable. In contrast, at low temperature, type I depolarization is strongly suppressed and as a result type II depolarization, characteristics of the NQP state, is more pronounced.

Nevertheless, further measurements with higher energy resolution, finer energy step, higher signal-to-noise ratio, and finer temperature step are needed in order to demonstrate the existence of the NQP state more clearly, because three problems are included in our results obtained by using a Xe I line: (i) At 40 K, there is another scenario in terms of the existence of the NQP state that type II depolarization cannot be observed due to the bad energy resolution although the NQP state occurs in the close vicinity of E_F. (ii) The error bars shown in Fig. 5.2 are still too large to discuss the existence of the NQP state at 100 K when the contribution of type I depolarization is included in the theoretical spin polarizations. (iii) The temperature step is too large to compare the SRPES results with that of a NQP theory and that of macroscopic magnetotransport measurements.[6,28,32] By using a high-intensity 7-eV laser and a high-efficient spin detector, we overcame these problems, as discussed below.

5.3.2 High-Resolution SRPES by the 7-eV Laser and the VLEED Spin Detector

From Fig. 5.4 (a) and (c), up to 70 K, the spin polarization decreases in the energy range above 80 meV, with the same binding-energy dependence; this corresponds to type I depolarization. We also found that the spin polarization evidently dropped toward E_F and produced a bending structure marked by a black arrow in Fig. 5.4 (c) above 80 K, which we regard as another type of depolarization named type II depolarization. With increasing temperature, the binding-energy dependence of the spin polarization seems to change slightly at 70 K. At 80 K, the spectral shape of the spin polarization clearly bends at $E_B = 10$ meV and the spin polarization drops toward E_F. Such a bending shape of the spin polarization is very evident at temperatures up to 120 K. Above 150 K, the bending point shifts toward the higher binding energy side and the bending structure gets broader. To eliminate the Fermi cutoff, the original curves shown in Fig. 5.4(a) are divided by the Fermi–Dirac (FD) function at each measured temperature convoluted with the experimental resolution in Fig. 5.4(b). With increasing temperature, from 20 K to 120 K, while the majority spin states do not change significantly, a finite state appears in the minority spin states at and above E_F. This minority state causes type II depolarization.

Here, we discuss comparison with the magnetization $M(T)$. The spin polarization measured by the laser decreases much more rapidly than the magnetization, with increasing temperature, although $P(80\text{ meV})$ in Fig. 5.4(d) should show the same temperature dependence as the $M(T)$ curve ideally. This behavior is quite similar to that of surface magnetism.[30,33] $P(80\text{ meV})$ also decreases more rapidly than what was observed in our bulk-sensitive SRPES study. These facts indicate that the present measurements obtained using the 7-eV laser–are quite surface sensitive. The probing depth of the present measurements is seemingly in contradiction to that

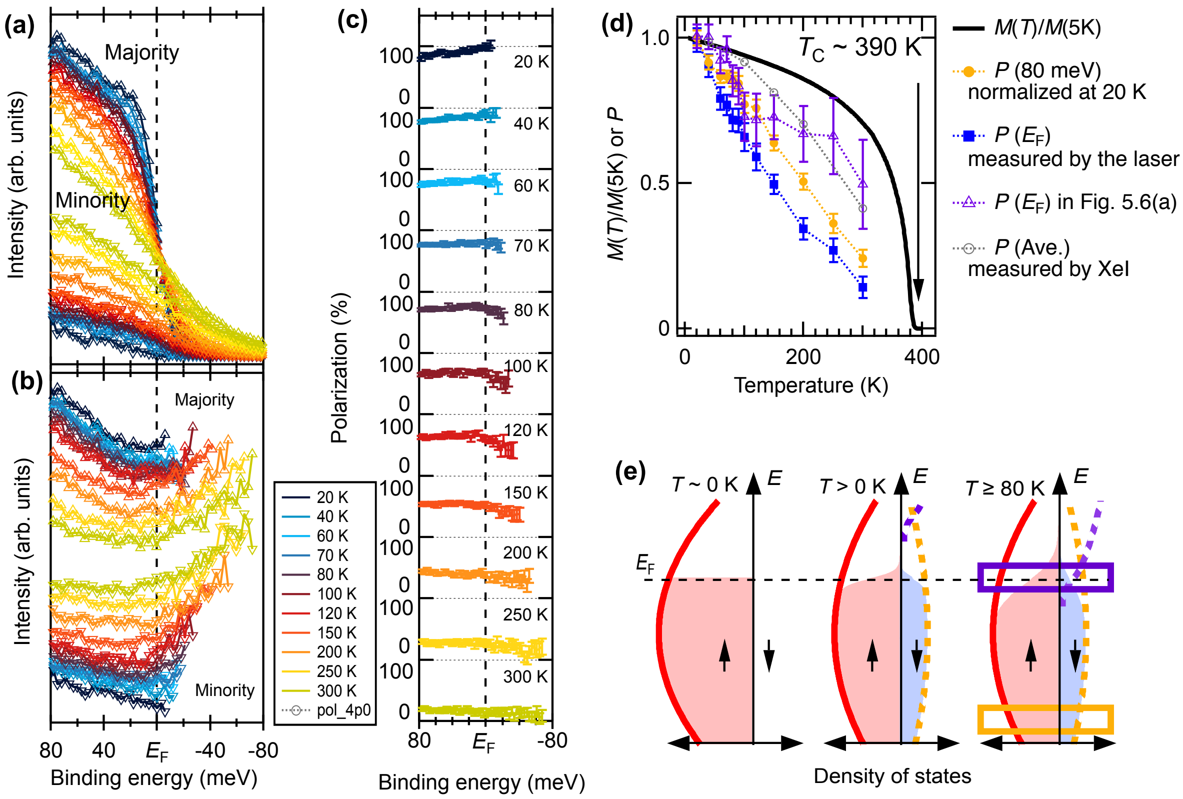

Fig. 5.4 Temperature-dependent spin-resolved electronic structures and corresponding spin polarizations. **(a)** Temperature dependences of spin-resolved spectra; **(b)** that divided by the FD functions added a constant background at measured temperatures convoluted with the experimental resolution; and **(c)** that of the corresponding spin polarization. In (a) and (b), triangle-up/down represents the majority/minority spin spectrum. In (c), the error is indicated by bars. The black arrow and gray dashed line show the bending point at 80 K and a visual guide representing the shift of the bending point, respectively. **(d)** Comparison of the temperature dependence of spin polarizations at various binding energies with that of the remnant magnetization along the *c*-axis direction for the CrO_2 sample, which was magnetized by a magnetic field of 1 T at 300 K. Yellow filled circles and blue filled squares show the spin polarizations at a binding energy E_B = 80 meV and at E_F, respectively. Purple triangles show the spin polarization at E_F, which is normalized by its value at 80 meV binding energy at 20 K after subtracting the background from majority and minority spin spectra. The spin polarization and the spin-resolved PES spectra used to obtain the purple-triangle points are shown in Fig. 2. Gray empty circles show spin polarization taken by a Xe I line averaged between 500 meV binding energy and E_F. **(e)** Schematic representation of density of states at the ground state and at finite temperatures. Red and blue areas represent the occupied states. Yellow and purple dashed lines represent the minority spin states causing type I and type II depolarizations, respectively (see text). Energy regions enclosed by yellow and purple rectangles, in which the spin polarizations are averaged to obtain the temperature dependence shown in (d), correspond to the *P*(80 meV) and *P*(E_F) in (d), respectively.

expected from the theoretical mean free path of photoelectrons.[34] One of the reasons for this inconsistency can be because lifetime of the photoexcited electrons is extremely short, as the final states are not in the unoccupied bulk bands; however, the surface electrons can escape

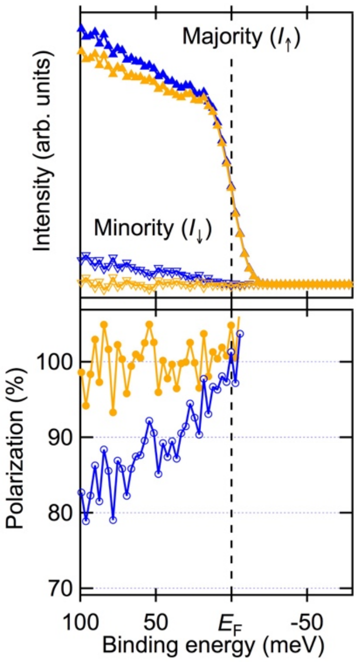

Fig. 5.5 SRPES spectra and spin polarization before and after subtracting the background. Majority (triangle-up) and minority (triangle-down) spin spectra before (blue) and after (yellow) subtracting the background (top), and corresponding spin polarization (bottom).

from the solid surface into vacuum by the short lifetime, as reported by theoretical and experimental photoemission studies.[35–37] This point is also supported by the electronic structures predicted during the band calculation of CrO_2.[38] Note that our success in observing the intrinsic electronic states of CrO_2, despite the surface-sensitive measurements, is because of our use of a high-quality sample with very few surface contaminants.

From Fig. 5.4(e), P(80 meV) includes the contribution of only type I depolarization, as mentioned above, while the spin polarization at E_F, $P(E_F)$, includes the contributions of both type I and type II depolarizations. Differences between these spin polarizations appear above 80 K, and the gap becomes wider for temperatures up to 120 K. In the higher temperature region, P(80 meV) and $P(E_F)$ are almost parallel and decrease at the same rate, implying that the contribution of type I depolarization is dominant and that of type II depolarization is rather enshrouded. Actually, the majority and minority EDCs divided by the FD function have approximately the same spectral shape above 200 K due to type I depolarization.

In order to clarify the temperature dependence of type II depolarization, we performed a background-subtraction analysis. Since we underestimate the spin polarization when non-negligible unpolarized background exists in a SRPES spectrum, we should remove the background to obtain intrinsic values of spin polarization.[26] Blue lines with triangle-up/down in Fig. 5.5 show the majority and minority spin EDCs measured by the VUV laser ($h\nu = 6.994$ eV) at 20 K, respectively. A clear Fermi edge was observed in the majority spin spectrum while no states at E_F with an energy gap of 10 meV below E_F were observed. These features are just those of half-metallic ferromagnet. However, in our bulk-sensitive SRPES studies, the gap size of the minority spin state is estimated to be 500 meV below E_F at 40 K where the degree of spin polarization is 100 % independent on binding energy, as shown above. The present minority spin EDC and spin polarization seem to be inconsistent with those of the bulk-sensitive SRPES study. This inconsistency can be attributed to the difference of the surface sensitivity of these measurements. Therefore, in our measurements by the laser, we may observe non-negligible intensity from the surface contaminants in addition to that of CrO_2. Based on this picture, the background seen in the minority spin spectrum at 20 K in Fig. 5.5 can be identified to be the tail of the electronic states of the surface contaminants as Cr_2O_3 which has a peak at 2 eV with no Fermi edge. Therefore, we subtracted the smoothed spectrum of the minority spin one from both majority and minority spin spectra at any temperatures. In addition, to eliminate the contribution of type I depolarization, we performed an analysis normalizing spin polarization by its value at binding energy $E_B = 80$ meV at which type II depolarization does not contribute. The normalized spin polarization is represented as $P_{\mathrm{nor}} = (1/S_{\mathrm{eff}}F_{\mathrm{nor}}(T))\ (I_+ - I_-)/(I_+ + I_-)$, where $F_{\mathrm{nor}}(T)$ is a normalize factor for each temperature. The error is represented as $1/(S_{\mathrm{eff}}F_{\mathrm{nor}}(T)I_{\mathrm{tot}}^{1/2})$. This error gets larger with increasing temperature, because $F_{\mathrm{nor}}(T)$ gets smaller with increasing temperature because the unnormalized spin polarizations get smaller with increasing temperatures. The spin polarization and SRPES spectra after these analysis are shown in Fig. 5.6.

Similar to Fig. 5.4(c), the normalized spin polarization indicated in Fig. 5.6 (a) shows type II depolarization at approximately 80 K. Furthermore, type II depolarization is enhanced and broadened systematically with the increase in temperature up to 300 K. In response to the change in the spin polarization, an extended peak structure appears in the minority spin EDCs. To clarify the peak structure further, we analyze the spin-resolved EDCs divided by the FD function shown in Figs. 5.6 (c) and (d). In the FD-divided minority EDCs, it is evident that a minority spin state exists at E_F above 80 K (purple shaded region). Moreover, this minority tail state becomes much broader and invades sufficiently below E_F. On the other hand, such considerable changes are not observed in the FD-divided majority EDCs. This fact is significant evidence that the minority tail state plays a central role in type II depolarization.

Note that the FD-dividing analysis does not reproduce spin-resolved DOS strictly. In order to reproduce the spin-resolved DOS more strictly, we must perform a deconvolution analysis,[39] as described in Sec. 2.2.8. We demonstrate the deconvoluted SRPES data at various temperatures in Fig. 5.7. We have adopted averaged data of 4 energy steps to make

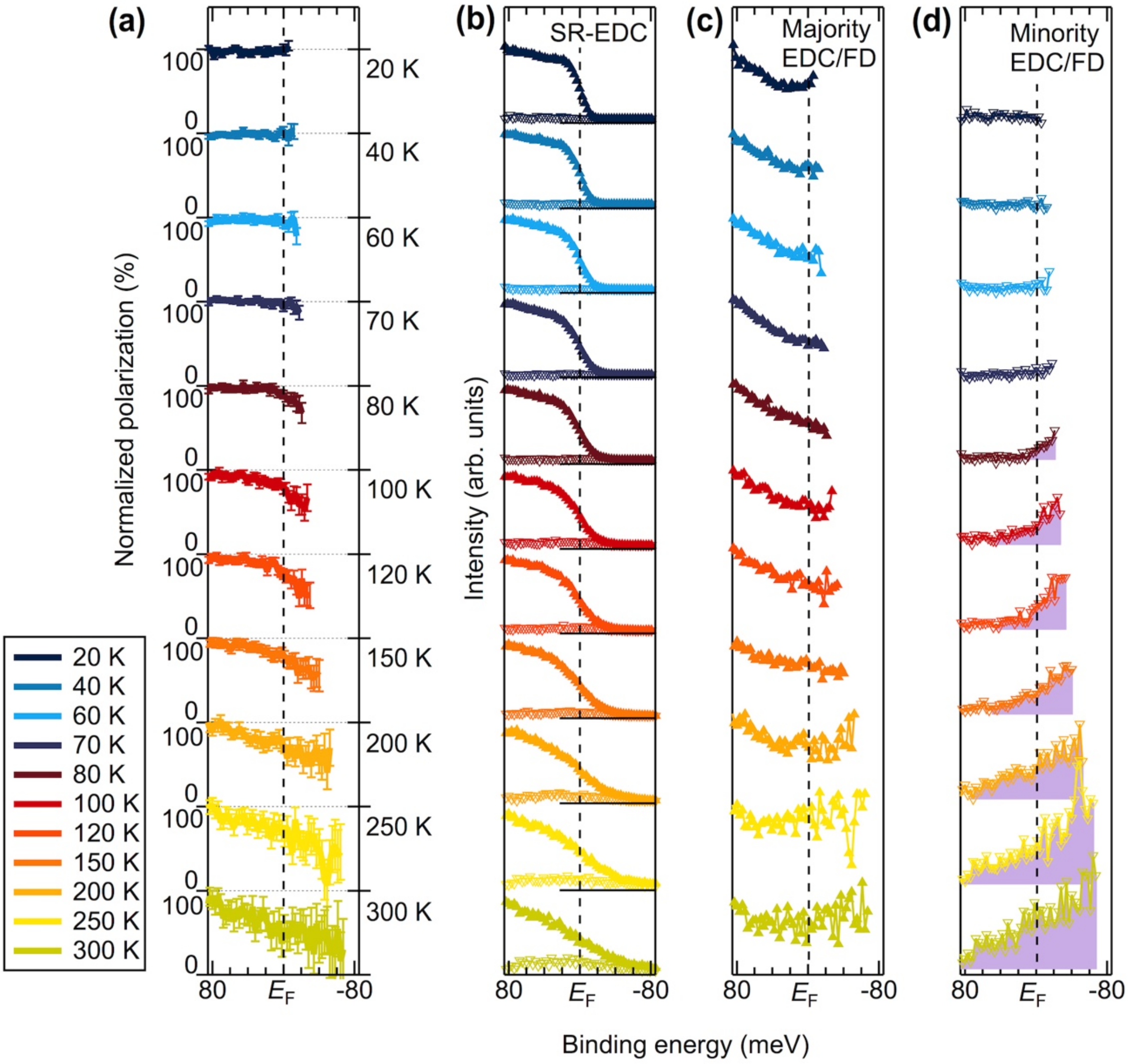

Fig. 5.6 Minority tail states at finite temperature. **(a)** Spin polarization obtained from majority and minority spin spectra subtracted background, and normalized by its value at E_B = 80 meV for various temperatures. Error is indicated by bars. **(b)** Spin-resolved EDCs calculated from $I_\uparrow = (1 + P_{nor})I_{tot}/2$ (triangle-up) and $I_\downarrow = (1 - P_{nor})I_{tot}/2$ (triangle-down) where P_{nor} is the normalized spin polarization shown in (a). **(c),(d)** Majority and minority EDCs divided by the FD function at the measured temperature convoluted with the experimental resolution.

1data point for deconvolution. The observed change in spin polarization has become slightly steeper in energy after deconvolution but the results remained essentially the same as before deconvolution, supporting the validity of our claim regarding type II depolarization.

We checked aging of the CrO_2 sample surface by irradiation by the 7-eV laser. Figure 5.8 shows spin polarizations and valence band PES spectra taken by the HeIIα line ($h\nu$ = 40.8 eV) before and after the SRPES measurements. The spin polarization after the measurements does not show significant change from those before the measurements. This indicates clearly that the

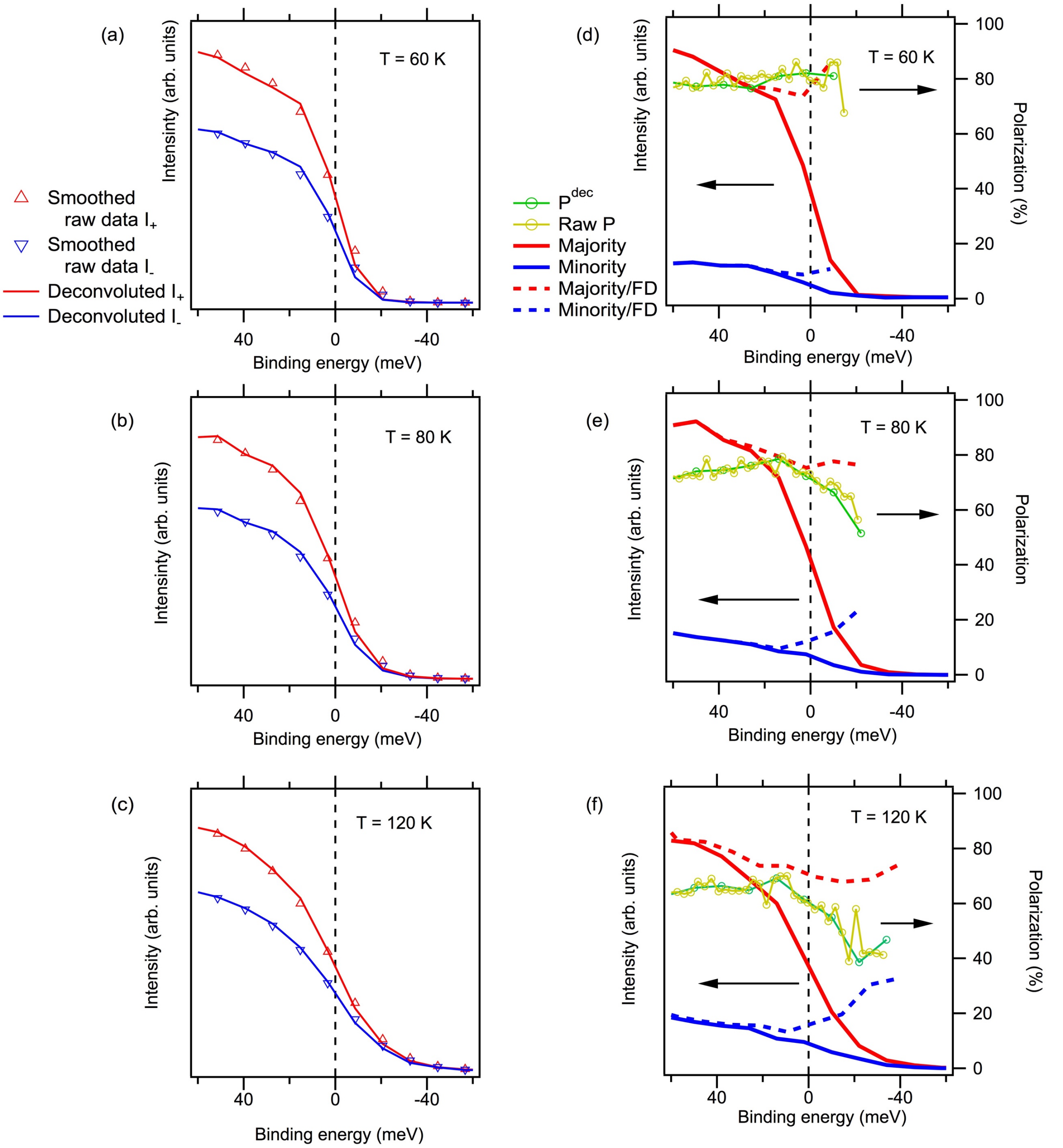

Fig. 5.7 Results of the deconvolution analysis using maximum entropy method. **(a)** Smoothed raw data for I_+ (red triangle-up), I_- (blue triangle-down), deconvoluted I_+ (red solid line) and I_- (blue solid line). **(b)** The same as (a) but $T = 80$ K. **(c)** The same as (a) but $T = 120$ K. **(d)** Majority spin spectrum $I_\uparrow$ (red solid line) at 60 K, that divided by non-convoluted FD function of the measured temperature (red broken line) and spin polarization P^{dec} (green solid line with circles) obtained using $P^{dec} = (1/S_{eff})(I_+^{dec} - I_-^{dec})/(I_+^{dec} + I_-^{dec})$, where $I_{+(-)}^{dec}$ is deconvoluted $I_{+(-)}$. Yellow solid line with circles shows spin polarization of original data shown in Fig. 5.4. **(e)** The same as (d) but $T = 80$ K. **(f)** The same as (d) but $T = 120$ K.

temperature-dependence of the SRPES spectra observed here is never due to extrinsic aging of the sample surface. That is, the observed temperature-dependent change is derived from change of the electronic structure of CrO_2. This is also supported by LEED pattern measured after the

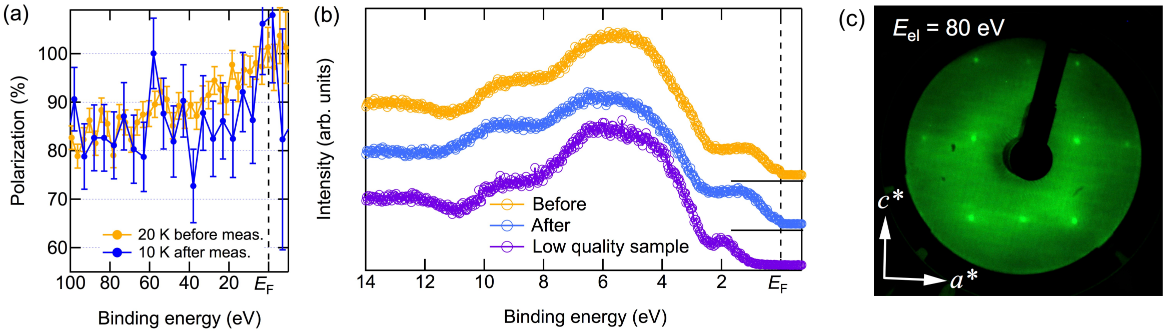

Fig. 5.8 Reproducibility of spin polarization and aging check of our sample. **(a)** Spin polarizations before (yellow) and after (blue) SRPES measurements at low temperatures. **(b)** Valence band photoemission spectra before (yellow) and after (light blue) SRPES measurements. Purple line with empty circles shows the spectrum of a low-quality sample of CrO_2 film whose surface seems to be almost covered by Cr_2O_3-like contaminants. (a) and (b) do not show significant aging near E_F while the SRPES measurement. **(c)** LEED pattern at an incident electron energy of 80 eV measured after high-resolution SRPES measurements.

measurements indicating a clear pattern derived from the rutile-type crystal structure, as shown in Fig. 5.8(c).

Let us discuss the origins of the minority tail state. A soft X-ray angle-resolved photoemission spectroscopy (ARPES) study of $CrO_2(100)$ films reported that the band structure of CrO_2 could be understood from the local spin density approximation with electron correlation U (LSDA + U) calculated with effective on-site Coulomb interaction $U_{eff} \approx 1$ eV.[40] The band structure has an energy gap in the minority spin states approximately 1 eV below E_F and 0.5 eV above E_F.[38,41,42] Therefore, considering the energy, the minority spin bands above E_F expected from LSDA + U cannot be observed by broadening the FD distribution even at 300 K.

In a theoretical study,[19] the minority state extending below E_F was interpreted as a NQP state arising from an electron–magnon interaction. Based on NQP theories,[2–6,9] the broadening of the minority spin state occurs at an energy scale in the order of the characteristic magnon energy. When the temperature exceeds the anisotropy gap in the magnon spectrum, the NQP state can exist in the occupied states. This indicates that spin polarization does not change as long as the thermal energy does not exceed the energy required to overcome the gap of the magnon spectrum; however, after it exceeds the energy, the spin polarization at E_F starts to drop instantly. The characteristics of the temperature dependence are consistent with those obtained from our measurements, shown as purple triangles in Fig. 5.4 (d). This suggests that the tail state in the minority spin state observed here can be attributed to the many-body effect. A study involving the DMFT + LSDA calculation predicted that the density of states of the minority spin above E_F was broadened by the many-body effect to cross E_F above 100 K.[19] This effect may cause band broadening to a larger energy extent than thermal energy. In a theoretical study, it was shown that the edge of the minority state above E_F at the ground state shifted to E_F and extended to E_B ~ 100 meV at 100 K, and then slightly shifted to the higher energy side with more broadening at 200 K. This tendency is consistent with our SRPES results.

However, curiously, the spin polarization at E_F at 200 K was higher than that at 100 K in the DMFT study,[19] which does not seem to be in line with the temperature dependence of our spin polarization. In Fig. 5.4 (d), the purple triangles falls precipitously from 70 K to 100 K, but between 100 K and 250 K, the spin polarization stays at approximately 70%. Since the trend of temperature dependence is not upward, but downward, with increase in temperature, the temperature dependence of our spin polarization cannot be completely explained by the DMFT + LSDA calculation. Furthermore, from the DMFT + LSDA calculation, the energy scale of the occupied minority spin state is estimated to be 100 meV which is approximately ten times larger than that obtained by our experiment. To understand our result, further theoretical studies are required.

Here, as an alternative depolarization mechanism, we discuss the effect of a Stoner-type collapse which may produce a spin depolarization with binding-energy dependence similar to that of type II depolarization. ARPES and SARPES studies on Ni metal reported that the exchange splitting Δ decreased from 280 meV to 130 meV with increasing temperatures from $0.47T_C$ to $0.80T_C$, and then vanished rapidly towards T_C.[43,44] The temperature dependence of Δ corresponded to the magnetization curve of Ni.[44,45] In the case of CrO_2, the minority-spin gap above E_F at the ground state can be estimated to be more than 500 meV based on ARPES and theoretical studies.[38,40–42] From this fact and our experimental results, the minority spin gap was reduced by as much as 500 meV with increasing temperatures up to $0.2T_C$ (~ 80 K), and then the gap was reduced by only 100 meV with increasing temperatures from $0.2T_C$ up to $0.75T_C$ (~ 300 K). This temperature dependence of Δ is different from that of Ni, which implies that type II depolarization is not attributed to the reduction of the exchange splitting.

From our results, we can improve our understanding of the peculiar reduction of the magnetoresistance of CrO_2. In CrO_2 with a surface-decomposed barrier, the magnetoresistance ratio decreases drastically at 50–100 K, different from the temperature dependence of its macroscopic magnetization.[16–18,46] From our results, it can be inferred that the depolarization near E_F, which seldom affects the demagnetization, occurs due to the emergence of the minority tail state. Since the contribution from the electrons near E_F is dominant in the

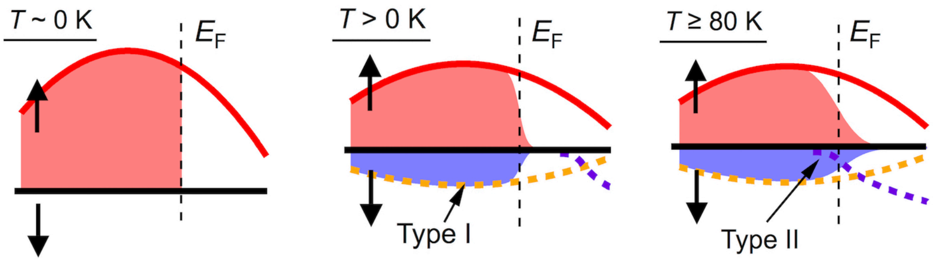

Fig. 5.9 Schematic representation of density of states at the ground state and at finite temperatures. Red and blue areas represent the occupied states. Yellow and purple dashed lines represent the minority states causing type I and type II depolarizations, respectively.

spin polarization obtained from magnetoresistance measurements, this depolarization must lead to the precipitous reduction of the magnetoresistance. A similar marked reduction in the magnetoresistance had been reported in the studies on $Tl_2Mn_2O_7$ [47] and $La_xSr_{1-x}MnO_3$ (LSMO),[48] though a spin polarization of 100% at 40 K was reported from an SRPES spectrum of LSMO with energy resolution of 200 meV.[30,49] In analogy with the case of CrO_2, the same change in the electronic structure of minority spin states possibly occurs in these materials.

Several studies on magnetotransport measurements support our experimental results.[28,32] The study on CrO_2(110) films suggested that spin-flip scattering events occurred above a certain temperature $T^* = 80$ K due to electron–magnon interaction.[32] This temperature T^* was in good agreement with the temperature at which type II depolarization was observed. This suggests that the electron–magnon interaction is associated with type II depolarization, supporting the NQP scenario mentioned above. Furthermore, the study in Ref. 32 reported that a crossover of the sign of the carriers from plus (hole-like) to minus (electron-like) occurred at T^*. We observed that the minority tail state seemed to move from the unoccupied side toward the higher binding energy side. We can speculate that the tail state is possibly an electron-like band and that it produces an electron pocket somewhere in the Brillouin zone. This variation in the electronic structure is consistent with that observed in the magnetotransport study.

Finally, we propose methods to preserve the high spin polarization at low temperatures up to room temperature, on the basis of the present results. In Fig. 5.9, we summarize the electronic structure of CrO_2 for the various temperatures discussed above. There are two depolarizations in CrO_2—type I and type II depolarizations. Since type I depolarization dominates the macroscopic demagnetization, in order to obtain higher spin polarization, we have to design materials with higher Curie temperatures, as already known. Type II depolarization occurs because of the broadened minority spin state above E_F. Therefore, optimizing the position of E_F is a promising way to improve the spin polarization at a finite temperature. In the case of CrO_2, it may be effective to move the position of E_F away from the minority spin state above E_F by elemental substitutions and/or interface effects such as band bending for hole doping. Furthermore, based on the NQP theories consistent with our results, the minority tail state crosses E_F when $k_BT > \hbar\omega_m$, where $\hbar\omega_m$ is the anisotropy gap in the magnon spectrum. [5,9,50] Therefore, another possible way is to increase the magnetic anisotropy, for instance, by using the strain from a substrate.[51] The NQP theories predict that the electronic structure changes, not only for CrO_2 but also for various other HMF candidates such as Heusler alloys and zinc-blende–structured compounds,[6] which suggests that the many-body effect observed here is a universal feature of HMFs. Therefore, these approaches from the perspective of material design can help preserve the high spin polarization in various HMFs at room temperature.

5.4 Summary

We performed low-energy bulk-sensitive spin-resolved PES measurements on half-metallic ferromagnet CrO_2 (100) epitaxial films to observe the NQP states. We found that averaged values of the spin polarization were approximately 100% and 40% at 40 K and 300 K, respectively, which is consistent with our previous report. At 100 K, we observed the peculiar spin depolarization in the energy region between 100 meV BE and E_F, which can be well explained by a theory predicting NQP states. We also found that the depolarization was noticeable below 150 K because the wide-range depolarization derived from the surface effects was suppressed at low temperature. These results show that the bulk-sensitive and low-temperature spin-resolved PES is a promising experimental technique to observe the NQP states.

We also investigated the spin-depolarization process in CrO_2(100) epitaxial films, by high-resolution SRPES. Two types of spin depolarizations were observed. Type I depolarization developed over the entire spin-polarized energy range at a constant rate with respect to temperature. The origin of type I depolarization was attributed to spin-wave excitation. Above 80 K, type II depolarization occurred in the close vicinity of E_F with an energy scale of several 10 meV. With the development of type II depolarization, a minority spin state hidden above E_F at lower temperatures appeared and was enhanced in the minority spin gap with elevating temperature, while the majority spin state was not changed significantly. The temperature dependence of the minority spin state was consistent with that of the NQP theories, which constituted spectroscopic evidence for the appearance of a minority tail state attributed to a many-body effect. A thorough investigation of the fine spin-resolved electronic structure of HMFs will be important for understanding the many-body effect in itinerant electron ferromagnets, and realizing complete spin polarization at room temperature, which may accelerate the development of spintronic devices.

5.5 References

[1] T. Moriya, J. Magn. Magn. Mater. **100**, 261 (1991).

[2] J. A. Hertz and D. M. Edwards, J. Phys. F: Metal Phys. **3**, 2174 (1973).

[3] J. A. Hertz and D. M. Edwards, J. Phys. F: Metal Phys. **3**, 2191 (1973).

[4] V. Yu. Irkhin and M. I. Katsnelson, J. Phys. C: Solid State Phys. **18**, 4173 (1985).

[5] V. Yu. Irkhin, M. I. Katsnelson, and A. I. Lichtenstein, J. Phys.: Condens. Matter **19**, 315201 (2007).

[6] M. I. Katsnelson, V. Yu. Irkhin, L. Chioncel, A. I. Lichtenstein, R. A. de Groot, Rev. Mod. Phys. **80**, 315 (2008).

[7] D. S. Hirashima, J. Phys. Soc. Jpn. **84**, 124707 (2015).

[8] V. Yu. Irkhin, J. Phys.: Condens. Matter **27**, 155602 (2015).

[9] L. Chioncel, Y. Sakuraba, E. Arrigoni, M. I. Katsnelson, M. Oogane, Y. Ando, T. Miyazaki, E. Burzo, and A. I. Lichtenstein, Phys. Rev. Lett. **100**, 086402 (2008).

[10]K. Miyamoto, A. Kimura, Y. Miura, M. Shirai, M. Ye, Y. Cui, K. Shimada, H. Namatame, M. Taniguchi, Y. Takeda, Y. Saitoh, E. Ikenaga, S. Ueda, K. Kobayashi, and T. Kanomata, Phys. Rev. B **79**, 100405(R) (2009).

[11]I. Žutić, J. Fabian, and S. Das Sarma, Rev. Mod. Phys. **76**, 323 (2004).

[12]R. J. Soulen Jr., J. M. Byers, M. S. Osofsky, B. Nadgorny, T. Ambrose, S. F. Cheng, P. R. Broussard, C. T. Tanaka, J. Nowak, J. S. Moodera, A. Barry, and J. M. D. Coey, Science **282**, 85 (1998).

[13]H. Fujiwara, M. Sunagawa, K. Terashima, T. Kittaka, T. Wakita, Y. Muraoka, and T. Yokoya, Appl. Phys. Lett. **106**, 202404 (2015).

[14]E. Y. Tsymbal and I. Žutić (eds.), Handbook of Spin Transport in Magnetism (CRC Press, Boca Raton, FL, 2012).

[15]R. Wang, Y. J. Jin, J. Z. Zhao, Z. J. Chen, Y. J. Zhao, and H. Xu, Phys. Rev. B **97**, 195157 (2018).

[16]H. Y. Hwang and S.-W. Cheong, Science **278**, 1607 (1997).

[17]S. S. Manoharan, D. Elefant, G. Reiss, and J. B. Goodenough, Appl. Phys. Lett. **72**, 984 (1998).

[18]J. M. D. Coey, A. E. Berkowitz, Ll. Balcells, and F. F. Putris, Phys. Rev. Lett. **80**, 3815 (1998).

[19]L. Chioncel, H. Allmaier, E. Arrigoni, A. Yamasaki, M. Daghofer, and M. I. Katsnelson,

Phys. Rev. B **75**, 140406(R) (2007).

[20]S. Souma, A. Takayama, K. Sugawara, T. Sato, and T. Takahashi, Rev. Sci. Instrum. **81**, 095101 (2010).

[21]T. Okuda, K. Miyamaoto, H. Miyahara, K. Kuroda, A. Kimura, H. Namatame, and M. Taniguchi, Rev. Sci. Instrum. **82**, 103302 (2011).

[22]K. Yaji, A. Harasawa, K. Kuroda, S. Toyohisa, M. Nakayama, Y. Ishida, A. Fukushima, S. Watanabe, C. Chen, F. Komori, and S. Shin, Rev. Sci. Instrum. **87**, 053111 (2016).

[23]K. P. Kämper, W. Schmitt, G. Güntherodt, R. J. Gambino, and R. Ruf, Phys. Rev. Lett. **59**, 2788 (1987).

[24]Yu. S. Dedkov, M. Fonine, C. König, U. Rüdiger, and G. Güntherodt, Appl. Phys. Lett. **80**, 4181 (2002).

[25]K. Iwai, Y. Muraoka, T. Wakita, M. Hirai, T. Yokoya, Y. Kato, T. Muro, and Y. Tamenori, J. Appl. Phys. **108**, 043916 (2010).

[26]P. D. Johnson, Rep. Prog. Phys. **60**, 1217 (1997).

[27]M. Hoesch, T. Greber, V.N. Petrov, M. Muntwiler, M. Hengsberger, W. Auwärter, and J. Osterwalder, J. Electron Spectrosc. Relat. Phenom. **124**, 263 (2002).

[28]A. Barry, J. M. D. Coey, L. Ranno, and K. Ounadjela, J. Appl. Phys. **83**, 7166 (1998).

[29]R. Skomski and P. A. Dowben, Europhys. Lett. **58**, 544 (2002).

[30]J.-H. Park, E. Vescovo, H.-J. Kim, C. Kwon, R. Ramesh, and T. Venkatesan, Phys. Rev. Lett. **81**, 1953 (1998).

[31]F. Hong and J. G. Che, Appl. Phys. Lett. **88**, 121903 (2006).

[32]S. M. Watts, S. Wirth, S. von Molnár, A. Barry, and J. M. D. Coey, Phys. Rev. B **61**, 9621 (2000).

[33]T. Takeda and H. Fukuyama, J. Phys. Soc. Jpn. **40**, 925 (1976).

[34]M. P. Seah and W. A. Dench, Surf. Interface Anal. **1**, 2 (1979).

[35]P. J. Feibelman and D. E. Eastman, Phys. Rev. B **10**, 4932 (1974).

[36]T. Kondo, M. Ochi, M. Nakayama, H. Taniguchi, S. Akebi, K. Kuroda, M. Arita, S. Sakai, H. Namatame, M. Taniguchi, Y. Maeno, R. Arita, and S. Shin, Phys. Rev. Lett. **117**, 247001 (2016).

[37]Z. Tao, C. Chen, T. Szilvási, M. Keller, M. Mavrikakis, H. Kapteyn, and M. Murnane, Science **353**, 62 (2016).

[38]K. Schwarz, J. Phys. F: M: Met. Phys. **16**, L211 (1986).

[39]W. von der Linden, M. Donath, and V. Dose, Phys. Rev. Lett. **71**, 899 (1993).

[40]F. Bisti, V. A. Rogalev, M. Karolak, S. Paul, A. Gupta, T. Schmitt, G. Güntherodt, V. Eyert, G. Sangiovanni, G. Profeta, and V. N. Strocov, Phys. Rev. X **7**, 041067 (2017).

[41]M. A. Korotin, V. I. Anisimov, D. I. Khomskii, and G. A. Sawatzky, Phys. Rev. Lett. **80**, 4305 (1998).

[42]H.-T. Jeng and G. Y. Guo, J. Appl. Phys. **92**, 951 (2002).

[43]T. Greber, T. J. Kreutz, and J. Osterwalder, Phys. Rev. Lett. **79**, 4465 (1997).

[44]H. Hopster, R. Raue, G. Güntherodt, E. Kisker, R. Clauberg, and M. Campagna, Phys. Rev. Lett. **51**, 829 (1983).

[45]W. Borgiel, W. Nolting, and M. Donath, Solid State Commun. **72**, 825 (1989).

[46]A. Gupta, X. W. Li, and G. Xiao, Appl. Phys. Lett. **78**, 1894 (2001).

[47]H. Y. Hwang and S.-W. Cheong, Nature **389**, 942 (1997).

[48]H. Y. Hwang and S-W. Cheong, Phys. Rev. Lett. **77**, 2041 (1996).

[49]J.-H. Park, E. Vescovo, H.-J. Kim, C. Kwon, R. Ramesh, and T. Venkatesan, Nature **392**, 794 (1998).

[50]V. Yu. Irkhin and M. I. Katsnelson, Eur. Phys. J. B. **30**, 481 (2002).

[51]G. Miao, G. Xiao, and A. Gupta, Phys. Rev. B **71**, 094418 (2005).

CHAPTER 6. HALF-METALLICITY AND SPIN-DEPENDENT CORRELATION EFFECTS IN CoS_2

6.1 Introduction

Producing a source of spin-polarized carriers has been a challenging topic of research of solid state physics since emergence of spintronics which manipulates spin degree of freedom of electrons [1,2]. Efforts for the realization of spin-polarized carriers have been strenuously made in studies on half-metallic ferromagnets (HMFs) [3–7]. HMF has metallic electronic structures with an energy gap at the Fermi level (E_F) for any one electronic spin state in the ground state, realizing 100% spin polarization at E_F.[8] Although many HMF candidates have been predicted for transition metal oxides and chalcogenides, Heusler alloys, and two dimensional materials,[9–13] CrO_2 has been a sole substance indicating approximately 100% spin polarization in both of point-contact Andreev reflection and spin-resolved photoemission spectroscopy experiments.[14–18] Further discovery and identification of half-metallic materials must be addressed in order to understand phenomena characteristics of HMF and to realized more thermally stable HMFs.

CoS_2 is a ferromagnetic metal whose ordered moment is reported to be approximately 0.9 μ_B/Co with an easy-axis along the [111] direction.[19–21] The ordered moment is close to 1 μ_B/Co in a low-spin state of Co^{2+} (configuration: $t_{2g}^6e_g^1$), suggesting that CoS_2 has a half-metallic electronic structure including completely spin polarized e_g bands crossing the Fermi level (E_F). The half-metallicity has been also supported by theoretical band structure calculated within generalized gradient approximation (GGA), an experimental study of the de Haas–van Alphen (dHvA) effect, and an optical study measuring reflectivity of CoS_2.[10,20,22] On the other hand, the results of band calculation within local spin-density approximation (LSDA), point-contact Andreev reflection (PCAR), x-ray magnetic circular dichroism, and photoemission spectroscopy measurements indicated that CoS_2 has a “nearly” half-metallic electronic structure in which a bottom of the minority spin e_g band touches or slightly crosses E_F near the R point.[10,23–28] This band-structure picture is also supported by PCAR studies on $Co_{1-x}Fe_xS_2$ in which the absolute value of spin polarization at E_F is enhanced by hole-doping.[29,30] However, although a polarized neutron-diffraction study indicating non-half-metallic electronic structure also, the electronic state obtained from the observed magnetization distribution, in which both spin states produced by mixing of the e_g and t_{2g} states cross E_F, conflicted with that obtained by photoemission spectroscopy and LSDA-calculation studies.[27,28,31] So far, there is no electronic-structure model describing comprehensively these experimental results.

In order to reveal the half-metallicity of CoS_2 experimentally, it has been indicated that measurements with energy resolution less than 10 meV are needed. A photoemission study reported that peak width of a structure attributed to a minority spin state was 6.5 meV which was narrower than that of a spectrum calculated from the density of states, several-10 meV, because of a mass renormalization due to the electron correlation and/or the coupling to spin excitations.[28] Clarifying the fine electronic structure with spin character can provide the decisive evidence for the half-metallicity of CoS_2.

In this work, we report the three-dimensional Fermi surface (FS) and the band structure of a CoS_2 single crystal including the spin character revealed by high-resolution spin- and angle-resolved photoemission spectroscopy (SARPES). We have found that both of majority and minority spin bands cross E_F along the ΓX line, unambiguously demonstrating that CoS_2 does not have the half-metallic electronic structure at least below 20 K. Furthermore, the minority spin bands breaking the half-metallicity are renormalized by an electron correlation effect, while the overall character of the majority spin band can be understood by the one-electron model. This indicates that the spin-dependent electronic correlation must not be neglected to understand the electronic structure of CoS_2. Based on the experimentally revealed electronic structure, we discuss (i) the half-metallicity in Section III. A and B, (ii) the spin-dependent electronic correlation effects from comparison with theoretical band structures in Section III. C, and (iii) the demagnetization process and the thermal decoherence of near-E_F bands in Section III. D.

6.2 Methods

Single crystals of CoS_2 were synthesized by the vapor transport method,[21] and were used for ARPES and SARPES measurements. ARPES experiments were carried out at beamline BL-28A of the Photon Factory (PF), KEK, using synchrotron radiation as the excitation light source. Circularly polarized light was used, except for the polarization-dependence ARPES measurements. The total energy and angular resolutions were set to approximately 20 meV and 0.3° (corresponding to ~0.02 Å), respectively. E_F of the samples was calibrated by measuring a gold foil that was electrically connected to the samples. The data were taken at $T = 50$ K. Laser-based ARPES and SARPES experiments were performed at the Institute for Solid State Physics, The University of Tokyo.[32] The *p*-polarized light with $h\nu = 6.994$ eV was used to excite the photoelectrons. Photoelectrons were analyzed with a combination of a ScientaOmicron DA30L analyzer and a very-low-energy-electron-diffraction (VLEED) type spin detector. The energy and angular resolutions were set to 6 meV and 0.3° (corresponding to ~0.005 Å) for spin-integrated ARPES and 10 meV and 1° (corresponding to ~0.02 Å) for SARPES, respectively. Calibration of E_F for the samples was achieved using a gold reference. The data were taken at $T = 40$ K, except for the temperature-dependence data in Fig. 6.7. Clean surfaces for all measurements were obtained by *in situ* cleaving of the samples. The high structural quality of a sample (100) surface was verified by low-energy electron diffraction (LEED), as shown in Fig. 6.1(a).

In order to obtain absolute values of spin polarization using the VLEED detector, we used the equation $P = (1/M_0S_{\rm eff})\,(I_+ - I_-)/(I_+ + I_-)$, where M_0 is ratio of the remnant magnetization of the sample to the saturated magnetization, a calibration factor in terms of magnetic domain, $S_{\rm eff}$ (=0.25) is the effective Sherman function of the apparatus and $I_{+(-)}$ is the intensity of the electrons reflected by the positively (negatively) magnetized target.[] Then, we obtain the majority ($I_\uparrow$) and minority ($I_\downarrow$) spin spectra using $I_{\uparrow(\downarrow)} = (1 +(-)\ P)(I_{\rm tot}/2)$, where $I_{\rm tot} = I_+ + I_-$.[33,34]

Band structure calculations were performed within LSDA, using the WIEN2k package.[35] We used the lattice parameters, $a = 5.5348$ and $u = 0.389$, taken from Wyckoff.[36]

6.3 Results and Discussion

6.3.1 Three-Dimensional Fermi Surface and Band Structure

In Figs. 6.1 (b)–(h), we gather our experimental information on the FS of CoS_2. First, in order to clarify the correspondence relation between the photon energy and the measuring k_z value, we determined the inner potential of CoS_2. The perpendicular component of the crystal wave vector k_z is not conserved across the crystal surface to vacuum interface, but instead can be found using the inner potential correction: $k_z = (2m[(E_i + h\nu - W)]\cos^2\theta + V_0)^{1/2}/\hbar$, where m is the rest mass of an electron, E_i is energy of initial state of the electron, W is the work function, θ is the emission angle of the photoelectron, V_0 is the inner potential.[37] From the equation, we can determine V_0 by observing the periodicity of E_i with respect to $h\nu$. Band structure along

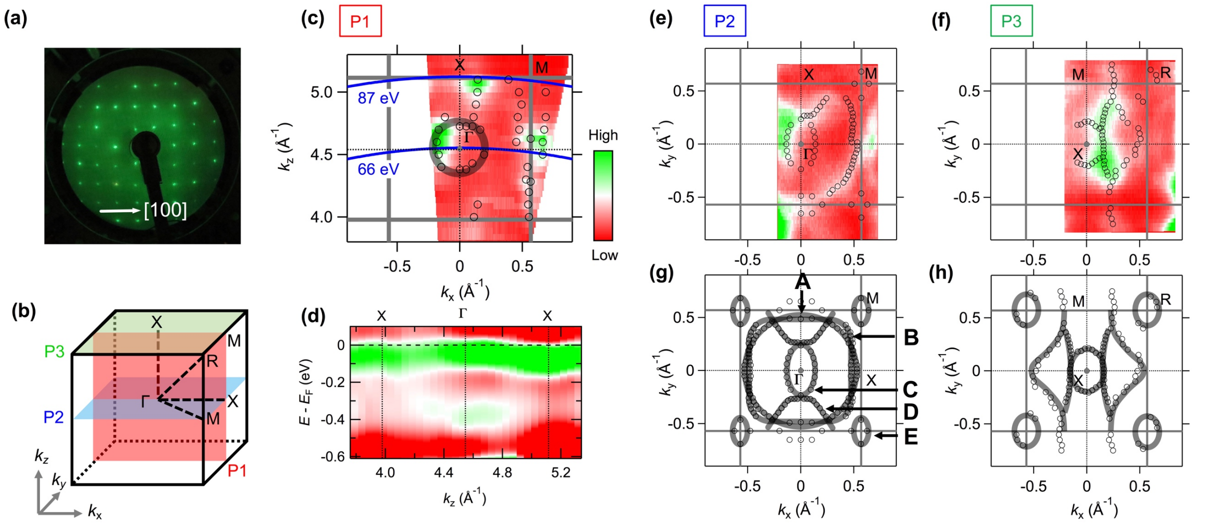

Fig. 6.1. **(a)** LEED pattern at an incident electron energy of 185 eV. **(b)** Brillouin zone of pyrite-type CoS$_2$. The k_z direction corresponds to that normal to the sample surface. **(c)** ARPES intensity map of the FS along P1 marked at (b), overlaid with the k_F plots determined by fitting the MDC peaks (black circles). Blue lines show measured k positions for the states near E_F estimated for $h\nu = 66$ eV and for $h\nu = 87$ eV. Gray shaded circle is guide for the eye. **(d)** Second derivative of ARPES intensity map as a function of energy to E_F and wave vector k_z. **(e),(f)** ARPES intensity maps of the FS measured at $h\nu = 66$ eV and at $h\nu = 87$ eV (corresponding to P2 and P3 marked at (b)), respectively, overlaid with the fitted MDC peak positions at E=E_F showing the k_F positions (black circles). **(g),(h)** k_F plots along P2 and P3, respectively, symmetrized by assuming a twofold symmetry with respect to the Γ point. The thick shaded lines are guides for the eye, respectively. The FSs in (c), (e), and (f) are obtained with an energy-integration window of ±0.01 eV.

the k_z direction shows clearly a high-intensity band localized between –0.1 eV and E_F. This band produces a hole pocket, as shown by the shaded circle in Fig. 6.1(c), which suggests that the center of the hole pocket, $k_z \sim 4.55$ Å^{-1}, corresponds to the Γ or the X point. Furthermore, the band structure along k_z also has an electron-like band with a bottom around $k_z \sim 4.55$ Å^{-1} at $E - E_F \sim -0.4$ eV. Theoretical band-structure studies on CoS$_2$ demonstrated that the electron-like band is centered at the Γ point.[10,21,23] Based on the correspondence, we determined the inner potential V_0 to be 18 eV. For $V_0 = 18$, the measured k_x–k_y planes for the states near E_F are the ΓXMX plane for $h\nu = 66$ eV and the XMRM plane for $h\nu = 87$ eV.

Figures 6.1(e)–(h) show the experimental in-plane FSs for the cut P2 and P3. We observed three pockets around the Γ point (FS A, B, and C), one pocket around the X point (FS D), and one pocket around the M point (FS E) in the cut P2. According to theoretical studies of FS, there are one hole pockets around the Γ point and one electron pocket near the M point [21,23]. The number of the pockets are much less than those of our experimental FS. Also in the cut P3, the shape of the theoretical FS is inconsistent with that of our experimental FS [21,23].

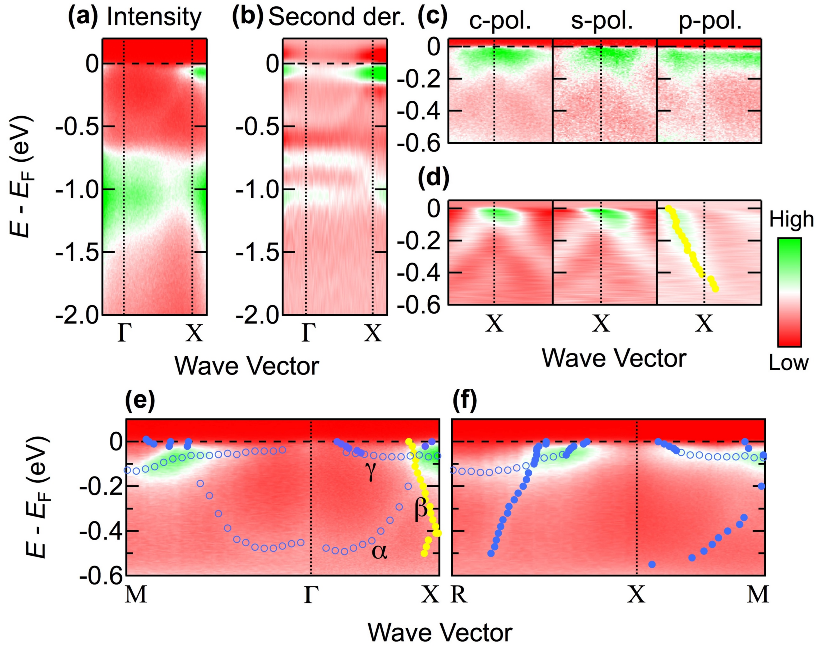

Fig. 6.2. **(a)** ARPES intensity map as a function of energy to E_F and wave vector. **(b)** Second derivative of ARPES intensity map in (b) with respect to energy. **(c)** Polarization-dependent ARPES intensity map around the X point: (left) circularly polarized light; (middle) *s*-polarized light; (right) *p*-polarized light. **(d)** Second derivatives of ARPES intensity maps in (c) with respect to wave vector. Yellow filled circles show MDC peak positions estimated from the right panel in (c). **(e),(f)** ARPES intensity maps along the MΓX and the RXM lines, respectively, overlaid with plots showing peak positions of EDCs (empty circles) and MDCs (filled circles). Yellow filled circles are the same as that in (d) but folded with respect to the X point.

A reason for the deviation can be understood by inspecting the band structures. Figures 6.2 (a) and (b) show the band structure along the ΓX line. We observed a peak structure located at –1.0 eV with a shoulder structure at –0.75 eV corresponding to the exchange-splitted t_{2g} bands. Furthermore, we observed bands located between –0.5 eV and E_F corresponding the e_g bands. The band with a bottom at –0.5 eV near the Γ point was observed along the in-plane k_x direction as well as the out-of-plane k_z direction. Around the X point, there are three bands near E_F: the band with a bottom around the Γ point, a light hole band, and a heavy band located just below E_F. Although the intensity derived from the hole band is quite small by the circularly polarized light, it becomes clearer by the *p*-polarized light, as shown in Figs. 6.2(c) and (d), because of an orbital selectivity of photoexcitation [38,39]. Based on these results, we summarize the band structure in Fig. 6.2(e). Along the ΓX line, the α, β, and γ bands cross E_F and constitute the FS A, B, and C, respectively. Comparing our experimental band structure with theoretical one [23]. the β band can be assigned to a majority spin hole band forming a hole pocket around the Γ point. The α band also corresponds to a majority spin band around the Γ point. However, the experimental α band crosses E_F although the theoretical electron band does not cross E_F. Furthermore, there is seemingly no theoretical band in the occupied states to which we can assign the γ and δ bands. These deviations of the band structure are the reasons partially why the experimental FS deviates from the theoretical FS. In order to clarify the character of the γ and δ bands, we investigated the spin-resolved band structure by high-resolution SARPES, as described below.

6.3.2 Spin-Resolved Band Structure

Our high-resolution SARPES results are summarized in Fig. 6.3. By the 7-eV laser, we observed bands located at –1 eV, –0.5 eV, –50 meV, near E_F, and a dispersive hole band corresponding to the β band. From Fig. 6.3(i), the bands located at –1 eV split into majority (lower energy) and minority (higher energy) spin bands. The minority spin spectra along cut 2 and cut 3 have the shoulder structure at –0.75 eV (black thick lines in Fig. 6.3(i)) which is observed by our ARPES measurements using synchrotron radiation (see Figs. 6.2(a) and (b)). These spectral features of the structure at –1 eV strongly support the picture that the t_{2g} bands split into the majority and minority spin bands as predicted by theoretical studies.[10,21,23]

For the e_g bands, we obtained the spin-polarized band structure more clearly. From the correspondence to the band structure obtained by our ARPES measurements, we named the e_g bands as shown in Figs. 6.3 (c) and (f). At –0.5 eV, the ARPES intensity map for the majority spin bands has a clear structure corresponding the α band shown in Fig. 6.2 (c), although that for the minority spin bands has no structure at –0.5 eV. In the same way, it is identified that the β band has the majority spin character. The result that the spin character of the α and β bands is the majority spin is consistent with the theoretical band structures.[10,21,23] On the other hand, the ARPES intensity map for the minority spin bands has clear band dispersion being in absolute agreement with the γ and δ bands. This demonstrates that the γ and δ bands have the minority spin character.

Here, we discuss the half-metallicity of CoS_2. We observed both of the majority and minority spin bands crossing E_F, as shown in Figs. 6.3 (c)–(h), providing spectroscopic evidence for 'normal' ferromagnetic metallicity, not half-metallicity, of CoS_2. The minority spin bands remain at least below 20 K as shown after in Fig. 6.7(a). This result is consistent with claims by Andreev reflection and photoemission studies.[25,27,28] The non-half-metallicity is also supported by the fact that the ordered moment $\mu_s \sim 0.9\ \mu_B$/Co at 2 K[19,20] is not exactly $\mu_s =$

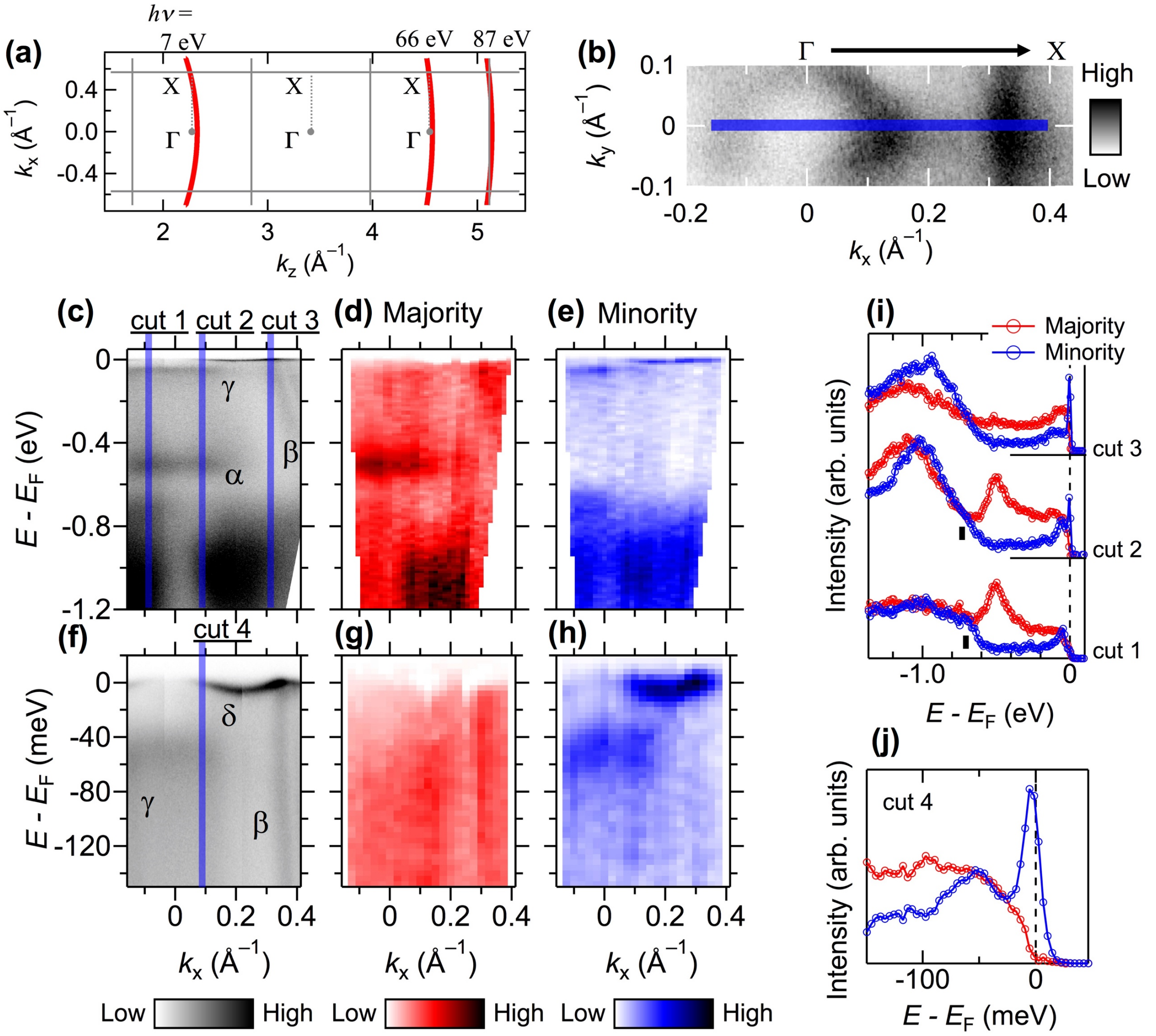

Fig. 6.3. **(a)** Two-dimensional Brillouin zone (gray lines) showing estimated measured *k* positions for the states near E_F (red curves) for each photon energy. **(b)** ARPES intensity map of the FS as a function of k_x and k_y measured by 7-eV laser. The FS is obtained with an energy-integration window of ±1 meV. **(c)–(e)** ARPES (c) and SARPES ((d): Majority spin bands; (e) Minority spin bands) intensity maps as a function of energy to E_F and k_x. **(f)–(h)** Same as (c)–(e) but measured in the vicinity of E_F. **(i),(j)** Spin-resolved EDCs at k points corresponding to the blue shaded line cuts in (c) and (f).

1 μ_B/Co which is the expected ordered moment when the e_g electrons are completely spin-polarized. However, our results are seemingly not in agreement with a dHvA-experiment study suggesting that the high-quality CoS$_2$ single crystal has the half-metallic electronic structure.[21] The dHvA-experiment study claimed mainly that the CoS$_2$ sample has a hole band with the majority spin character forming a large hole pocket around the Γ point. This claim is consistent with our results that there is the majority spin hole band (β band) around the Γ point.

As seen in Fig. 6.3(j), the δ band has a very narrow peak just below E_F. This structure was observed by high-resolution photoemission spectroscopy using the Xe Iα line below T_C [28]. Sato *et al*. interpreted the peak structure as evidence for the occupied minority spin state around the R point, supported by their band-structure calculation results. However, our high-resolution SARPES results show that the peak structure is observed at the Fermi wave vector (k_F) of the minority spin hole band around the Γ point. This band never exist as the occupied states shown in any band-structure calculation result [10,21,23]. Note that the minority spin hole band around the Γ point cannot be attributed to a surface band because the band shows dispersion with the periodicity of the bulk Brillouin zone along the k_z direction as shown as the intense band near E_F in Fig. 6.1 (d). For understanding the minority spin bands around the Γ point, we analyze a more detailed comparison of our experimental band structure with theoretical one, as discussed below.

6.3.3 Comparison with the Theoretical Band Structures

Figure 6.4 (a) shows a comparison of our experimental Co 3*d* bands with those calculated within LSDA. Although the energy and width of the theoretical bands do not fit closely with those of the experimental bands, the band shape of the spin-splitting t_{2g} bands, the majority spin e_g band ($e_g^\uparrow$) with a bottom at the Γ point are quite similar to those of the experimental bands. We therefore modified the theoretical band structure to reproduce the experimental band structure, as shown in Fig. 6.4 (b); for the t_{2g} bands, energy of the band center relative to E_F, approximately 1.86 eV, is shifted to 0.9 eV, and the bandwidth is narrowed by 50%; for the $e_g^\uparrow$ band, the bands are shifted by +0.21 eV; for the minority spin e_g bands ($e_g^\downarrow$), the bands, the bands are shifted by –0.16 eV. The bandwidths are not narrowed for the e_g bands. We also shifted down the $e_g^\downarrow$ for the conservation of the number of electrons in the system. The modified band structure describes the overall character of the Co 3*d* bands. This indicates again that the bands at –1.0 eV and at –0.75 eV are interpreted as the spin-splitting t_{2g} bands, and that the electron band around the Γ point (α band) and the heavy bands just below E_F are interpreted as the $e_g^\uparrow$ and $e_g^\downarrow$ bands, respectively, as shown in Figs. 6.4 (a)–(c).

In order to more clarify the consistency between the modified band structure and the experimental one in detail, we show ARPES intensity maps overlaid with the band plots showing the peak positions and with the modified bands in Figs. 6.4 (d) and (e). Along the ΓX line, the experimental band structure including the hole band (band β) is in good agreement

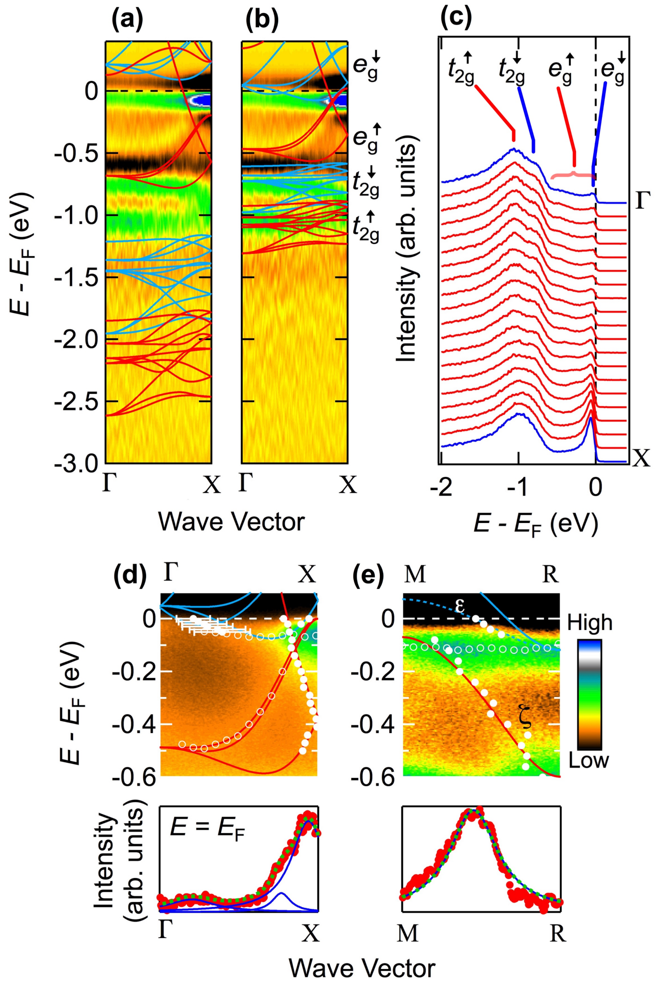

Fig. 6.4. Comparison of our experimental ARPES results with band structures calculated within LSDA. **(a)** Second derivatives of ARPES intensity map along the ΓX line overlaid with the theoretical bands. Red and blue band lines indicate majority and minority spin bands, respectively. **(b)** Same as (a) but overlaid with the calculated bands modified as to reproduce our experimental band structure. The width and energy position of the t_{2g} bands are halved. The $e_g^{\uparrow}$ and $e_g^{\downarrow}$ bands are shifted by +0.20 eV and –0.15 eV, respectively, but their width is not changed. **(c)** EDCs of the ARPES intensity map shown in Fig. 2(a). Blue spectra correspond to the points of symmetry, Γ and X. **(d)** (top) ARPES intensity map measured along the ΓX line overlaid with the band plots showing the peak positions of EDCs (white empty circles) and MDCs (white filled circles), and with the theoretical bands; (bottom) MDC at $E - E_F = 0$ with an energy window of ±0.01 eV (red dots). The green dotted line is the sum of the lorentzians (blue lines) corresponding to the modified theoretical bands crossing E_F. **(e)** Same as (d) but shown along the M–R line. The dashed blue line is obtained by shortening the bandwidth of the minority spin electron band around the R point.

with the modified band structure. Furthermore, it is demonstrated clearly that the modified band structure reproduces the spin character determined by our SARPES experiments. This strongly ensures validity of the modification of the theoretical band structure. The modification corresponds to reduction of the exchange splitting of the e_g bands, indicating that the amount

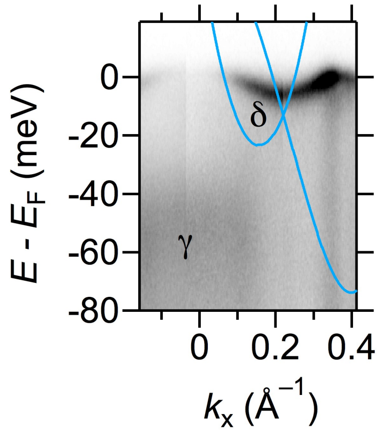

Fig. 6.5. Comparison of high-resolution ARPES intensity map along the ΓX direction taken by 7-eV laser with the bands calculated within LSDA. The theoretical bands are shifted as same as Fig. 6.4 (b).

of exchange splitting is overestimated for CoS$_2$ in LSDA calculation. This tendency of LSDA calculation revealed here implies that in terms of half-metallicity of a material, discussion based on spin-resolved electronic structure determined experimentally is absolutely necessary.

In Fig. 6.4 (e), the modified band structure also well-describes the overall character of the ζ band, while the k_F of the ε band experimentally observed deviates from that of the corresponding theoretical band. Disagreement of k_Fs of the theoretical and experimental minority spin electron band around the R point (ε band) can be improved by the bandwidth modification, as shown by the dashed blue line in Fig. 6.4 (e). Here, note that the experimental $e_g{}^\uparrow$ bands are in good agreement with the theoretical $e_g{}^\uparrow$ bands whose bandwidth is not modified. This suggests that spin-dependent renormalization can be occurred in CoS$_2$ by a difference of electron correlation for the majority spin and minority spin electrons.

In order to discuss the deviation of the experimental minority spin bands from the theoretical bands in more detail, a high-resolution ARPES intensity map overlaid with the theoretical bands is shown in Fig. 6.5. It is clearly found that bandwidth of the δ band is much (about tenth) smaller than that corresponding to the δ band, indicating that the agreement between experimental and theoretical band structure can be improved by shortening the bandwidth (i.e., renormalizing the carrier mass) just for the $e_g{}^\downarrow$ bands. However, the minority spin bands cannot be explained just by the modification of bandwidth. In Fig. 6.5, when the width of the theoretical bands is shortened in order to reproduce the δ band, there is no band explaining the γ band. Similarly, in Fig. 6.4(e), there is a band localized at –0.1 eV, which also cannot be reproduced by our modified theoretical band structure. These characteristics of the bands obtained experimentally cannot be understood even by band calculation within LSDA+U. The comparison of band structure calculated within LSDA with that calculated within LSDA+U ($U_{\mathrm{eff}} = 3.31$ eV) is shown in Fig. 6.6. By considering U, minority spin band gap between t_{2g} and e_g bands becomes larger for any wave vector. This tendency has been reported for other

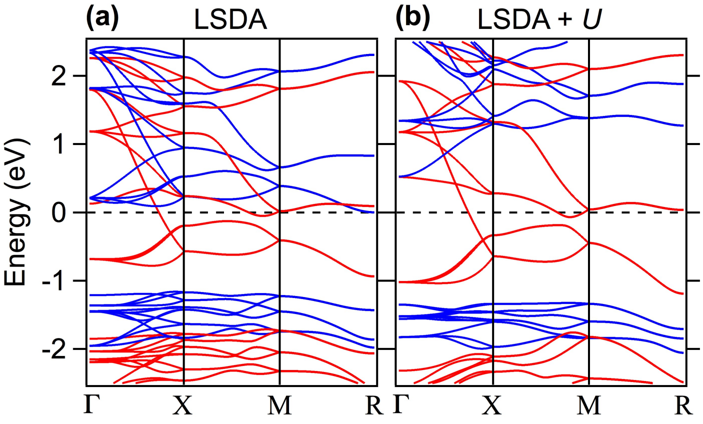

Fig. 6.6. Band structures calculated within LSDA **(a)** and within LSDA + U with $U = 4.2$ eV and $J = 0.89$ eV **(b)**. We used the lattice parameters, $a = 5.5348$ and $u = 0.389$.

candidates for half-metallic ferromagnets.[40,41] Moreover, bandwidth of the lowest energy $e_g{\downarrow}$ band becomes larger also. The change of the band structure by the LSDA+U calculation never complements the disagreement between our experimental results and LSDA calculation results.

Based on our SARPES and band calculation results, the effective mass of the observed minority spin bands in the close vicinity of E_F is renormalized significantly, although that of the observed majority spin bands is in good agreement with the mass estimated from our LSDA calculation. Such mass renormalization only for the minority spin electrons has been investigated as spin-dependent electronic correlation in studies on typical ferromagnetic metals.[42–44] One of the studies implies that the imaginary part of the self-energy Σ of Co indicates a significant spin-dependence.[44] Although the electronic states of Co obtained by SARPES measurements cannot be explained by the LSDA+U calculation, which is the tendency same as ours, their spectra simulated by LSDA+DMFT calculation within the 1-step model improve the description of the experimental photoemission data for Co. This suggests that the deviation of the experimental results from the modified theoretical band structure can be understood from a LSDA+DMFT calculation.

Note that the spin-dependent electronic correlation is different from an orbital-dependent correlation discussed for iron-based superconductors. For the case of $K_xFe_{2-y}Se_2$, the magnitude of electronic correlation depends on the orbital character of Fe 3d. For the case of the e_g bands in CoS_2, the magnitude depends on the spin character, because the band shape of the calculated $e_g{\uparrow}$ and $e_g{\downarrow}$ bands compared each other is the same, indicating that these bands splitting by an exchange interaction have the same orbital character.

Here, we compare the magnitude of the spin-dependent correlation of CoS_2 with that of typical ferromagnets. For the electron bands around the Γ point of Ni(110), $\eta^{\uparrow}/\eta^{\downarrow}$ is estimated to be 1.6, where $\eta^{\uparrow(\downarrow)}$ is a mass enhancement factor for majority (minority) spin band due to electron correlation defined by $\eta^{\uparrow(\downarrow)} = (k_F^{\uparrow(\downarrow)\mathrm{ARPES}} / k_F^{\uparrow(\downarrow)\mathrm{LSDA}})(v_F^{\uparrow(\downarrow)\mathrm{LSDA}} / v_F^{\uparrow(\downarrow)\mathrm{ARPES}})$ where $v_F^{\uparrow(\downarrow)\mathrm{ARPES(LSDA)}}$ is a Fermi velocity for a majority (minority) spin band obtained by ARPES (LSDA calculation).[42] For the electron bands around the R point of CoS_2 (namely, the ε and ζ bands), $\eta^{\uparrow}/\eta^{\downarrow}$ is estimated to be 1/3.2 = 0.31, where we assume that $\eta^{\uparrow} = 1$ because the ζ band does not have k_F and the ζ band shows good agreement with the corresponding theoretical band. From the fact, two indications are found: (i) The mass renormalization of the minority spin band in CoS_2 is larger than that of the majority spin band, while in Ni the magnitude relation of the mass renormalization is opposite. (ii) The ratio of $\eta^{\uparrow}$ and $\eta^{\downarrow}$ of CoS_2, 3.2, is much larger than that of Ni(110). This speculates us that near-E_F electronic structure constituted by no renormalized majority spin bands and anomalously large mass renormalization of minority spin bands are one of characteristic features of a nearly half-metallic ferromagnet. A study on a half-metallic ferromagnet CrO_2 reported a similar result that the majority spin t_{2g} bands can be well reproduced by LSDA calculation with $U_{\mathrm{eff}} \sim 1$ eV, although minority spin bands cannot be compared because no minority spin band crossing E_F is observed for CrO_2.[45] However, recently, it has been reported that minority spin bands of CrO_2 are broadened with growth of thermal fluctuation due to a correlation effect.[18] This suggests large correlation for the minority spin electrons, similar to the case of CoS_2. To investigate the correlation effect, we measured the temperature dependence of ARPES spectra for CoS_2, discussed below.

6.3.4 Temperature Dependence

In Fig. 6.7, we examine the temperature evolution of ARPES spectra. In Fig. 6.7 (a), the δ band gets broader rapidly with increasing temperatures up to T_C (= 122 K). Concomitantly, the β and γ bands are relatively enhanced. Except for the broadening, the band structure does not change significantly with increasing temperatures. Moreover, from the energy distribution curves (EDCs) shown in Fig. 6.7 (b) and (c), although the peak structure at E_F gets broader rapidly as seen in the ARPES intensity map, the peak structure does not disappear even above T_C. From wide spectra corresponding to the Co 3*d* bands shown in Fig. 6.7 (d), a peak structure corresponding to the α band shifts rapidly by +0.16 eV through T_C. Note that the temperature cycle of measurements was conducted to make sure that it is an intrinsic behavior, not because

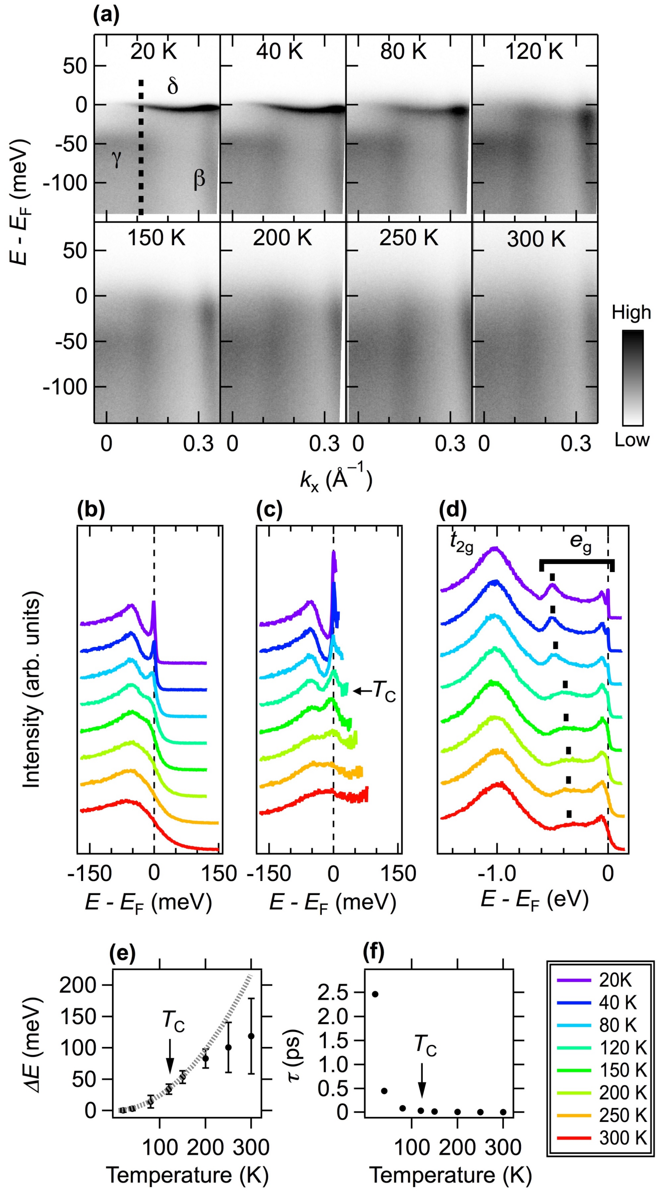

Fig. 6.7. **(a)** Temperature dependence of ARPES intensity map along the ΓX line taken by 7-eV laser. **(b),(c)** EDCs at a k_x point marked by the dotted line in (a), and those divided by the Fermi function at measured temperatures which is convoluted with a 6 meV gaussian corresponding to the energy resolution of the measurement. The EDCs are normalized by its intensity at –150 meV. **(d)** EDCs at a k_x point marked by the dotted line in (a). The EDCs are normalized by the peak height at 1.0 eV. Black thick lines show positions of the structure corresponding to the α band. **(e)** Temperature evolution of the width of the spectral peak at E_F (ΔE) shown in (c). The ΔE plots are obtained after subtracting the energy resolution of our measurement, 6 meV. The gray dotted line denotes a fit of $\Delta E = A + BT^2$, where A and B are fitting parameters and T is temperature, to the data in a temperature range of 20–120 K. **(f)** Temperature evolution of lifetime (τ) of the minority spin electrons occupying the δ band, estimated by $\tau = 2\hbar/\Delta E$.

of the surface aging. Based on our SARPES results which demonstrate that the α and β (γ and δ) bands are the $e_g^{\uparrow}$ ($e_g^{\downarrow}$) bands, the temperature dependence of the ARPES spectra demonstrate that the $e_g^{\uparrow}$ and $e_g^{\downarrow}$ bands are not degenerate even above T_C. This suggests that the origin of the demagnetization of CoS_2 is not the stoner damping but vanishment of the ferromagnetic long-range order by the spin fluctuation, as the case of iron.[46,47]

In a previous spin- and angle-integrated photoemission study, the broadening of the near-E_F peak was interpreted as a change from the ferromagnetic electronic structure to the paramagnetic one, that is, as damping of the exchange splitting.[28] However, by our spin- and angle-resolved measurements, we identified that the exchange splitting remains above T_C, although the magnitude reduced slightly. Therefore, the broadening of the δ band is attributed to reduction of lifetime of the minority spin electrons. Figure 6.7 (e) shows temperature evolution of the width of the spectral peak at E_F (ΔE) shown in (c). ΔE shows the T^2 dependence below T_C and deviates from the T^2 curve above T_C. Corresponding to the sharpening of the near-E_F peak, lifetime of the minority spin electrons (τ) rapidly increases, as shown in Fig. 6.7(f). The temperature evolution is nicely in line with that of the resistivity. Because the rapid broadening feature is characterized by T_C, it is found that scattering by magnetic fluctuations is a dominant component contributing the broadening of the near-E_F peak and the increase of the resistivity. Furthermore, the rapid broadening is significant for the δ band which is highly mass renormalized by correlation. This suggests that electron–electron scattering due to Coulomb interaction is also an indispensable component contributing the temperature dependence of the resistivity.

Finally, we discuss realization of half-metallic electronic structure at room temperature. The thermal broadening feature is quite similar to that predicted by DMFT calculations for half-metals.[13,41,48–50] DMFT calculations have demonstrated that by thermal fluctuations spectral function of electronic states for either one of spin state forming a gap at E_F is broadened and has a finite value at E_F. This state emerging near E_F as a result of thermal fluctuations is called a non-quasiparticle (NQP) state, which has been actually observed experimentally as breaking of the half-metallicity in CrO_2 and Co_2MnSi.[17,18,50] These facts suggest that although the spin-dependent correlation can be one of the universal characteristics of half-metals, as discussed above, the correlation between minority spin electrons break the half-metallicity at finite temperatures, unfortunately. Our results can be also interpreted that the sole $e_g{\uparrow}$ is well-described by one-electron picture despite $3d$ electron system, indicating that to produce half-metallic electronic structure, it can be important to produce weakly correlated majority spin electrons. The present study shows that the spin-dependent electronic correlation is one of the most important factors for realizing half-metallic electronic structure at higher temperatures.

6.4 Summary

We have investigated the electronic structure of pyrite-type CoS_2 by ARPES and high-resolution SARPES. We determined the inner potential to be 18 eV from the band dispersion along the k_z-direction. Along the ΓX line, we observed localized bands at –1 eV and dispersive bands between –0.5 eV and E_F. The overall character of the observed bands is in good agreement with the Co 3*d* bands calculated within LSDA, except for the energy positions with respect to E_F. In addition, a localized bands were observed near E_F. From our SARPES measurements, we unambiguously identified that the near-E_F bands had the minority spin character, while the LSDA calculations predicts that an occupied minority spin band exists solely around the R point. The deviations of the experimental band structure from theoretical one can be explained by shifting the theoretical bands to narrow the exchange splitting of the e_g band down, demonstrating that the LSDA calculations overestimated the exchange splitting of CoS_2. However, the modified band structure cannot explain the bandwidth of the minority spin bands; the experimental bandwidths of the minority spin bands is at least two times narrower than those of the theoretical bandwidths, although the bandwidths of the majority spin bands are in line with the theoretical bandwidths. This can be interpreted as a result of spin-dependent electronic correlation effects. From our temperature-dependent ARPES experiments, we observed a decoherence of the mass-renormalized minority spin electrons which is much more rapid than that of the majority spin hole band. The decoherence of the minority spin band is scaled by T_C of CoS_2, indicating that the decoherence originates from increase of scattering of the conducting minority spin electrons with magnetic excitation. As a significant variation of the majority spin bands, we observed an energy shift of the band bottom to the high energy direction with exceeding T_C. From the variation of the e_g bands, the majority and minority spin bands are not damped even above T_C, as seen in Fe metal. This indicates that the demagnetization of CoS_2 is due to spin fluctuation. Through our thorough electronic-structure study of “nearly” half-metallic ferromagnet CoS_2, we suggest that spin-dependent correlation must be understand for realizing “true” half-metallic ferromagnets.

6.5 References

[1] S. A. Wolf, D. D. Awschalom, R. A. Buhrman, J. M. Daughton, S. von Molnár, M. L. Roukes, A. Y. Chtchelkanova, and D. M. Treger, Science **294**, 1488 (2001).

[2] I. Žutić, J. Fabian, and S. Das Sarma, Rev. Mod. Phys. **76**, 323 (2004).

[3] H. Y. Hwang and S.-W. Cheong, Science **278**, 1607 (1997).

[4] A. Gupta and J. Z. Sun, J. Magn. Magn. Mater. **200**, 24 (1999).

[5] J. M. D. Coey and M. Venkatesan, J. Appl. Phys. **91**, 8345 (2002).

[6] M. Jourdan, J. Minár, J. Braun, A. Kronenberg, S. Chadov, B. Balke, A. Gloskovskii, M. Kolbe, H. J. Elmers, G. Schönhense, H. Ebert, C. Felser, and M. Kläui, Nature Commun. **5**, 3974 (2014).

[7] Y. Ando, Jpn. J. Appl. Phys. **54**, 070101 (2015).

[8] R. A. de Groot, F. M. Mueller, P. G. van Engen, and K. H. J. Buschow, Phys. Rev. Lett. **50**, 2024 (1983).

[9] K. Schwarz, J. Phys. F: M: Met. Phys. **16**, L211 (1986).

[10] T. Shishidou, A. J. Freeman, and R. Asahi, Phys. Rev. B **64**, 180401(R) (2001).

[11] S. J. Hashemifar, P. Kratzer, and M. Scheffler, Phys. Rev. Lett. **94**, 096402 (2005).

[12] Y.-W. Son, M. L. Cohen and S. G. Louie, Nature **444**, 347 (2006).

[13] M. I. Katsnelson, V. Yu. Irkhin, L. Chioncel, A. I. Lichtenstein, and R. A. de Groot, Rev. Mod. Phys. **80**, 315 (2008).

[14] R. J. Soulen Jr., J. M. Byers, M. S. Osofsky, B. Nadgorny, T. Ambrose, S. F. Cheng, P. R. Broussard, C. T. Tanaka, J. Nowak, J. S. Moodera, A. Barry, and J. M. D. Coey, Science **282**, 85 (1998).

[15] Y. Ji, F. Y. Yang, C. L. Chien, J. M. Byers, A. Anguelouch, G. Xiao, and A. Gupta, Phys. Rev. Lett. **86**, 5585 (2001).

[16] H. Fujiwara, M. Sunagawa, K. Terashima, T. Kittaka, T. Wakita, Y. Muraoka, and T. Yokoya, Appl. Phys. Lett. **106**, 202404 (2015).

[17] H. Fujiwara, M. Sunagawa, K. Terashima, T. Kittaka, T. Wakita, Y. Muraoka, and T. Yokoya, J. Electron Spectrosc. Relat. Phenom. **220**, 46 (2017).

[18] H. Fujiwara K. Terashima, M. Sunagawa, Y. Yano, T. Nagayama, T. Fukura, F. Yoshii, Y. Matsuura, M. Ogata, T. Wakita, K. Yaji, A. Harasawa, K. Kuroda, S. Shin, K. Horiba, H. Kumigashira, Y. Muraoka, and T. Yokoya, Phys. Rev. Lett. **121**, 257201 (2018).

[19] H. S. Jarrett, W. H. Cloud, R. J. Bouchard, S. R. Butler, C. G. Frederick, and J. L. Gillson,

Phys. Rev. Lett. **21**, 617 (1968).

[20] H. Hiraka and Y. Endoh, J. Phys. Soc. Jpn. **63**, 4573 (1994).

[21] A. Teruya, F. Suzuki, D. Aoki, F. Honda, A. Nakamura, M. Nakashima, Y. Amako, H. Harima, M. Hedo, T. Nakama, and Y. Ōnuki, J. Phys. Soc. Jpn. **85**, 064716 (2016).

[22] R. Yamamoto, A. Machida, Y. Moritomo, and A. Nakamura, Phys. Rev. B **59**, 7793(R) (1999).

[23] G. L. Zhao, J. Callaway, and M. Hayashibara, Phys. Rev. B **48**, 781 (1993).

[24] S. K. Kwon, S. J. Youn, and B. I. Min, Phys. Rev. B **62**, 357 (2000).

[25] L. Wang, T. Y. Chen, and C. Leighton, Phys. Rev. B **69**, 094412 (2004).

[26] V. N. Antonov, O. V. Andryushchenko, A. P. Shpak, A. N. Yaresko, and O. Jepsen, Phys. Rev. B **78**, 094409 (2008).

[27] T. Takahashi, Y. Naitoh, T. Sato, T. Kamiyama, K. Yamada, H. Hiraka, Y. Endoh, M. Usuda, and N. Hamada, Phys. Rev. B **63**, 094415 (2001).

[28] T. Sato, S. Souma, K. Sugawara, K. Nakayama, S. Raj, H. Hiraka, and T. Takahashi, Phys. Rev. B **76**, 113102 (2007).

[29] I. I. Mazin, Appl. Phys. Lett. **77**, 3000 (2000).

[30] C. Leighton, M. Manno, A. Cady, J. W. Freeland, L. Wang, K. Umemoto, R. M. Wentzcovitch, T. Y. Chen, C. L. Chien, P. L. Kuhns, M. J. R. Hoch, A. P. Reyes, W. G. Moulton, E. D. Dahlberg, J. Checkelsky, and J. Eckert, J. Phys.: Condens. Matter **19**, 315219 (2007).

[31] P. J. Brown, K.-U. Neumann, A. Simon, F. Ueno. and K. R. A. Ziebeck, J. Phys.: Condens. Matter **17**, 1583 (2005).

[32] K. Yaji, A. Harasawa, K. Kuroda, S. Toyohisa, M. Nakayama, Y. Ishida, A. Fukushima, S. Watanabe, C. Chen, F. Komori, and S. Shin, Rev. Sci. Instrum. **87**, 053111 (2016).

[33] P. D. Johnson, Rep. Prog. Phys. **60**, 1217 (1997).

[34] M. Hoesch, T. Greber, V.N. Petrov, M. Muntwiler, M. Hengsberger, W. Auwärter, and J. Osterwalder, J. Electron Spectrosc. Relat. Phenom. **124**, 263 (2002).

[35] P. Blaha, K. Schwarz, G. K. H. Madsen, D. Kvasnicka, J. Luitz, R. Laskowski, F. Tran, and L. D. Marks, WIEN2K, ISBN 3-9501031-1-2.

[36] R. W. G. Wyckoff, Crystal Structures (Interscience, New York, 1965), Vol. 1.

[37] A. Damascelli, Phys. Scr. **T109**, 61 (2004).

[38] Y. Zhang, F. Chen, C. He, B. Zhou, B. P. Xie, C. Fang, W. F. Tsai, X. H. Chen, H. Hayashi, J. Jiang, H. Iwasawa, K. Shimada, H. Namatame, M. Taniguchi, J. P. Hu, and D. L. Feng,

Phys. Rev. B **83**, 054510 (2011).

[39] M. Sunagawa, K. Terashima, T. Hamada, H. Fujiwara, T. Fukura, A. Takeda, M. Tanaka, H. Takeya, Y. Takano, M. Arita, K. Shimada, H. Namatame, M. Taniguchi, K. Suzuki, H. Usui, K. Kuroki, T. Wakita, Y. Muraoka, and T. Yokoya, J. Phys. Soc. Jpn. **85**, 073704 (2016).

[40] H. -T. Jeng and G. Y. Guo, J. Appl. Phys. **92**, 951 (2002).

[41] L. Chioncel, E. Arrigoni, M. I. Katsnelson, and A. I. Lichtenstein, Phys. Rev. Lett. **96**, 137203 (2006).

[42] M. Higashiguchi, K. Shimada, K. Nishiura, X. Cui, H. Namatame, and M. Taniguchi, Phys. Rev. B **72**, 214438 (2005).

[43] J. Sánchez-Barriga, J. Fink, V. Boni, I. Di Marco, J. Braun, J. Minár, A. Varykhalov, O. Rader, V. Bellini, F. Manghi, H. Ebert, M. I. Katsnelson, A. I. Lichtenstein, O. Eriksson, W. Eberhardt, and H. A. Dürr, Phys. Rev. Lett. **103**, 267203 (2009).

[44] J. Sánchez-Barriga, J. Braun, J. Minár, I. Di Marco, A. Varykhalov, O. Rader, V. Boni, V. Bellini, F. Manghi, H. Ebert, M. I. Katsnelson, A. I. Lichtenstein, O. Eriksson, W. Eberhardt, H. A. Dürr, and J. Fink, Phys. Rev. B **85**, 205109 (2012).

[45] F. Bisti, V. A. Rogalev, M. Karolak, S. Paul, A. Gupta, T. Schmitt, G. Güntherodt, V. Eyert, G. Sangiovanni, G. Profeta, and V. N. Strocov, Phys. Rev. X **7**, 041067 (2017).

[46] E. Kisker, K. Schröder, W. Gudat, and M. Campagna, Phys. Rev. B **31**, 329 (1985).

[47] R. Kurzawa, K. -P. Kämper, W. Schmitt, and G. Güntherodt, Solid State Commun. **60**, 777 (1986).

[48] V. Yu. Irkhin, M. I. Katsnelson, and A. I. Lichtenstein, J. Phys.: Condens. Matter **19,** 315201 (2007).

[49] L. Chioncel, H. Allmaier, E. Arrigoni, A. Yamasaki, M. Daghofer, M. I. Katsnelson, and A. I. Lichtenstein, Phys. Rev. B **75**, 140406(R) (2007).

[50] L. Chioncel, Y. Sakuraba, E. Arrigoni, M. I. Katsnelson, M. Oogane, Y. Ando, T. Miyazaki, E. Burzo, and A.I. Lichtenstein, Phys. Rev. Lett. **100**, 086402 (2008).

CHAPTER 7. SUMMARY AND OUTLOOK

This dissertation thoroughly investigates spin-resolved electronic structures of half-metals in order to clarify the fundamental mechanism of the precipitous thermal spin depolarization in half-metal-based tunneling magnetic junctions. To accomplish this work, we used two advanced SARPES techniques: Bulk-sensitive SARPES and high-resolution SARPES techniques. Through the electronic-structure studies on CrO_2, we revealed the intrinsic electronic structure, and directly observed NQP states in the close vicinity of E_F. From the study on CoS_2, we discovered an anomalously large spin-dependent correlation effect as a possibly universal characteristic of half-metals. In this chapter, we summarize the findings in this work and describe future outlook.

1. Intrinsic spin-polarized electronic structure of CrO_2 revealed by bulk-sensitive SARPES

(1) In construction of our SARPES apparatus, we have prepared Bi(111) films on Si(111) substrates and evaluate surface of the films. We built a new chamber in which we were able to prepare films and evaluate surface of the films. By measuring the spin polarization of Bi(111) thin films by SARPES measurements, we found the effective Sherman function S_{eff} of our SARPES apparatus to be 0.10 ± 0.006 that is a typical value of S_{eff} of Mott spin detectors, showing that unknown spin polarization can be determined by our SARPES apparatus.

(2) After the determination of S_{eff} of our SARPES apparatus, we have prepared high quality CrO_2(100) epitaxial films and investigated the temperature dependence of the spin-dependent electronic structure of the CrO_2 epitaxial films by bulk-sensitive SARPES. A clear Fermi edge and spin polarization of about 100 %, and a band gap of 0.5 eV in the spin down states were observed at 40 K, providing the spectroscopic evidence for the half-metallicity of CrO_2 at low temperatures, at least in the probed momentum region of the Brillouin zone. In addition, the Fermi edge and spin polarization of 40 % near E_F was observed at 300 K, which is consistent with earlier reports of resistivity measurements and our magnetization curves. The comparison of the SARPES spectra with LSDA+U band calculations suggests that the electronic

correlation U must be considered in order to discuss the electronic states of CrO_2. These results also indicate that bulk-sensitive spin-resolved PES is a very powerful experimental tool to investigate intrinsic spin-resolved electronic states of half-metallic ferromagnets.

2. Thermal fine spin depolarization in CrO_2 revealed by high-resolution SARPES

(1) We performed low-energy bulk-sensitive SRPES measurements on CrO_2 (100) epitaxial films to observe the NQP states. At 100 K, we observed the peculiar spin depolarization in the energy region between 100 meV binding energy and E_F, which is possibly explained by a theory predicting NQP states. We also found that the depolarization was noticeable below 150 K because the wide-range depolarization derived from the surface effects was suppressed at low temperature. For observing NQP states, bulk-sensitive, high-resolution, and low-temperature SRPES is a promising experimental technique to observe the NQP states.

(2) We also investigated the spin-depolarization process in CrO_2(100) epitaxial films, by high-resolution SARPES. In order to conduct high-resolution SARPES experiments at ISSP, we developed a sample magnetization system in the laser-based SARPES apparatus. From high-resolution SARPES measurements, two types of spin depolarizations were observed. Type I depolarization developed over the entire spin-polarized energy range at a constant rate with respect to temperature. The origin of type I depolarization was attributed to spin-wave excitation. Above 80 K, type II depolarization occurred in the close vicinity of E_F with an energy scale of several 10 meV. With the development of type II depolarization, a minority spin state hidden above E_F at lower temperatures appeared and was enhanced in the minority spin gap with elevating temperature, while the majority spin state was not changed significantly. The temperature dependence of the minority spin state was consistent with that of the NQP theories, which provides spectroscopic evidence for the appearance of a minority tail state attributed to a many-body effect.

3. Spin-dependent electronic correlation in CoS_2

(1) We have investigated the electronic structure of pyrite-type CoS_2 by ARPES and high-resolution SARPES. We determined the inner potential to be 18 eV from the band dispersion along the k_z-direction. Along the ΓX line, we observed localized bands at –1 eV and dispersive bands between –0.5 eV and E_F. The overall character of the observed bands is in good agreement with the Co 3*d* bands calculated within LSDA, except for the energy positions with respect to E_F. In addition, a localized bands were observed near E_F. From our SARPES measurements, we unambiguously identified that the near-E_F bands had the minority spin character, which provides spectroscopic evidence for 'nearly' half-metallicity of CoS_2.

(2) We found that the minority spin band crossing E_F is a hole band around the Γ point, while the LSDA calculations predicts that an occupied minority spin band exists solely around the R point. The deviation of the experimental band structure from theoretical one can be explained by shifting the theoretical bands to narrow the exchange splitting of the e_g band down, demonstrating that the LSDA calculations overestimated the exchange splitting of CoS_2. However, the modified band structure cannot explain the bandwidth of the minority spin bands; the experimental bandwidths of the minority spin bands is at least two times narrower than those of the theoretical bandwidths, although the bandwidths of the majority spin bands are in line with the theoretical bandwidths. This can be interpreted as a result of spin-dependent electronic correlation effects. The magnitude of the spin-dependent electronic correlation is anomalously larger than that of normal ferromagnetic metals such as Ni and Co. This suggests that the anomalously large spin-dependent electronic correlation must be considered for understanding electronic structures of half-metallic ferromagnets.

(3) From our temperature-dependent ARPES experiments, we observed a decoherence of the mass-renormalized minority spin electrons which is much more rapid than that of the majority spin hole band. The decoherence is scaled by T_C of CoS_2, indicating that the decoherence originates from increase of scattering of the conducting minority spin electrons with magnetic excitation. From analogy with the situation of 'true' half-metal CrO_2, the decoherence originates from the many-body effect due to electron–magnon

interaction. This shows that the spin-dependent electronic correlation plays a crucial role in realizing half-metallic electronic structure at finite temperatures. As a significant variation of the majority spin bands, we observed an energy shift of the band bottom to the high energy direction with exceeding T_C. From the variation of the e_g bands, the majority and minority spin bands are not damped even above T_C, as seen in Fe metal. This indicates that the demagnetization of CoS_2 is due to spin fluctuation.

4. Future outlook

While several important characteristics of electronic structure in half-metals at finite temperatures have been revealed in this dissertation, this study also raises a question. Besides, there are some questions which remain to be unanswered. In particular, I consider that the following points are very important and must be addressed in the future studies.

(1) ***E-k*** band structure of NQP states in CrO_2

For application of CrO_2 for spintronics devices, it is important to clarify where the NQP states appear in the Brillouin zone, because we might obtain higher spin polarization by choosing the orientation not parallel to the momentum direction of the NQP states. Therefore, band dispersion of the NQP states observed by ARPES measurements or inverse ARPES provides important information for achieving higher spin polarization at room temperature.

(2) Controlling anisotropy gap of the magnon spectrum for higher spin polarization

The NQP states are one of the origins of the thermal spin depolarization which cannot be explained from the macroscopic magnetization. Therefore, we can obtain higher spin polarization at room temperature by suppressing the NQP states. Based on the NQP theories, it is effective to widen the anisotropy gap of the magnon spectrum by material design techniques. This not only leads to achieving higher spin polarization at room temperature but also further verifies the NQP theories.

(3) Electron–boson coupling in CoS_2

In this work, although spin-dependent correlation derived from electron–electron Coulomb interaction was observed for CoS_2, kink structures originating from electron–boson coupling were not observed clearly. It is expected that the electron–boson coupling shows spin dependence similar to the electron–electron interaction. For further understanding of the correlation effects characteristic of half-metals, we must investigate the spin-dependent electron–boson coupling through kink structures and its temperature dependence.

Finally, although leaving the issues above, this study demonstrates that bulk-sensitive and high-resolution spin-resolved photoemission spectroscopy is a powerful tool for the research of the thermal spin depolarization in half-metals. I hope that the present study contributes fundamental science (many-body physics) and applied physics (performance advances of potential spintronic devices) in some way.

APPENDIX A. SURFACE METALLICITY OF CrO_2(001) EPITAXIAL FILMS

Abstract

Half-metallic ferromagnet CrO_2(001) film is a promising material for integration into magnetic memories because of its magnetocrystalline easy axis perpendicular to the film surface. However, for the conducting properties of the (001) surface, there exist two suggestions on theoretical studies; insulating or half-metallic. The argument has not yet been settled experimentally because it is difficult to determine the intrinsic electronic states of CrO_2(001) surface due to surface contaminants. In this study, we performed emission angle-dependent photoelectron spectroscopy measurements for CrO_2(001) epitaxial films with few contaminants to reveal the surface metallicity. The obtained energy distribution curve shows the surface states at $E_B = 0.5$ eV and the Fermi level (E_F), providing evidence for the metallic behavior of the (001) surface. Observations of metallic surface states and our (1×1) low-energy electron diffraction pattern are consistent with the theoretical study for the unreconstructed (001) surface which predicts the half-metallic surface states.

I. Introduction

The great potential of half-metallic ferromagnetic systems as a key material for spintronics devices has motivated investigation of their spin-polarized electronic structure [1–4]. In addition, it has been predicted that topological superconducting phases are induced in half-metal/superconductor heterostructures and Majorana fermions are produced at the edges of the heterostructures. These imply that half-metals can be used as a fundamental material to investigate topological physics [5–7]. Chromium dioxide (CrO_2) has been theoretically predicted to be a half-metallic ferromagnet [8]. As a notable advantage, CrO_2 always shows almost 100% spin polarization at low temperatures, which is the highest value exhibited by a candidate half-metals [9–13]. Because of the reliable half-metallicity and the fact that its Curie temperature (~ 400 K)[14] is greater than room temperature, CrO_2 is an attractive material for spintronics devices such as spin valves [15,16] and magnetic memories using a magnetic tunnel junction [17–19].

CrO_2 (001) films have the magnetocrystalline easy axis (*c* axis [20]) perpendicular to the film surface, which is an ideal condition for integration of magnetic memories [21]. However, the surface half-metallicity is still an open question. It has been expected that a (001) surface of a rutile structure is reconstructed from octahedral configuration to tetrahedral configuration [22] or forms faceted surfaces [23], because the unrelaxed (001) surface of the rutile-type structure has an energy larger than that of the (100), (110), and (101) surfaces according to a theoretical study [24]. Band calculations indicate that electronic structure of the reconstructed CrO_2(001) surface has a band gap at E_F produced by the lower majority e_g bands and the higher majority t_{2g} bands [22]. In addition, another theoretical study found that a strain-induced surface effect making the spin texture antiferromagnetic occurred at the surface of three-layer and thicker CrO_2 epitaxial thin films grown on TiO_2 (001) substrates [25]. On the other hand, it is predicted that the unrelaxed (001) surface maintains a half-metallic electronic structure [26]. Although scanning tunneling microscopy / spectroscopy (STM/STS) can directly observe the surface-atomic image and the density of states (DOS) [27], the surface studies of CrO_2(001) based on STM/STS have not succeeded most probably because of a critical difficulty of CrO_2: The surface of CrO_2 tends to change to the antiferromagnetic insulator Cr_2O_3 [28]. This tendency also prevents from obtaining a clean surface of pure CrO_2 by annealing and sputtering [29]. In previous photoelectron spectroscopy (PES) studies of CrO_2(100) films, insulating-like PES spectra with Cr_2O_3-derived spectral structures were reported, which is inconsistent with the metallic behavior of its resistivity [29–31]. However, it was reported that high-quality CrO_2 (100) films with few Cr_2O_3 contaminants were prepared by a closed system chemical vapor deposition (CVD) method [20]. PES spectra of samples prepared with the method show clear Fermi edges and peaks at 1 eV derived from Cr 3*d* bands even by surface sensitive PES measurements [11–13,20], characteristic of bulk electronic structure of CrO_2 as revealed by bulk-sensitive soft X-ray PES [32,33]. Therefore, it is expected that CrO_2 (001) films prepared by the closed-system CVD method may open a pathway for investigation of the intrinsic electronic states of the (001) surface.

In this work, we have prepared unrelaxed CrO_2 (001) epitaxial films by the closed-system CVD method and investigated the surface electronic states by emission angle-dependent PES. This method enables us to study bulk and surface electronic structures in materials [34,35]. The greater the emission angle θ for the axis normal to the sample surface is, the more surface sensitive the PES measurement is, because the escape depth λ is proportional to $1/\cos\theta$. The emission angle dependence shows enhancement of the PES intensity at a binding energy (BE) of 0.5 eV and at E_F at the surface sensitive configuration. This indicates that the (001) surface

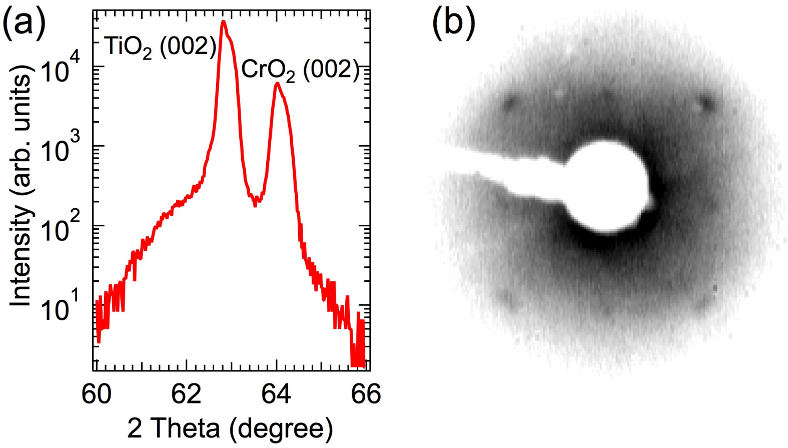

Fig. 1. (a) XRD pattern of a CrO_2 film on TiO_2 (001). (b) LEED pattern of the CrO_2 film. The energy of incident electrons was set at 46 eV.

is intrinsically metallic. This result is consistent with band calculations that assume that the (001) surface is not reconstructed into a tetrahedral arrangement.

II. Experimental

The CrO_2 (001) epitaxial films (rutile-type crystal structure; a = 4.419 Å; c = 2.915 Å) were prepared on rutile-type TiO_2 (001) substrates (a = 4.592 Å; c = 2.959 Å) with the CVD technique [20]. Cr_8O_{21} was used as a precursor. Powdered Cr_8O_{21} and TiO_2 (001) substrates were heated at 300 °C and 390 °C, respectively, for 2.5 h in a sealed-vacuum quartz tube. Figure 1(a) shows the X-ray diffraction (XRD) pattern of the CrO_2 (001) film. The 2θ peak positions for TiO_2 (002) and CrO_2 (002) are 62.9° and 64.1°, respectively, consistent with the results from a previous study [36]. The thickness of the film was estimated to be approximately 200 nm from comparison of the 2θ peak position for CrO_2 (002) in our XRD measurement with that in a previous study [36]. After the synthesis, the CrO_2 film was removed from the quartz tube and introduced into an ultra-high vacuum for the PES measurements with ~ 5 min exposure to atmosphere. The quality of the prepared CrO_2 film surface was evaluated by low-energy electron diffraction (LEED) at HiSOR BL-5, as shown in Fig. 1(b). The square-like pattern characteristics of the rutile-type (1×1) structure[37] was confirmed on the sample surface without any cleaning procedures.

The PES measurements for the valence band were performed in an angle-resolved PES (ARPES) system at UVSOR. Linear polarized radiation light of $h\nu$ = 33 eV was used as excitation light. The energy resolution was set to 15 meV. Emission angle-dependent PES

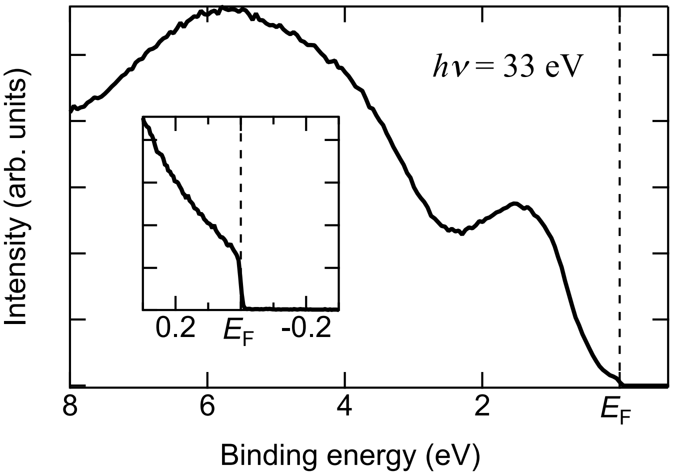

Fig. 2. Valence band PES spectrum for a CrO_2 epitaxial film on TiO_2 (001) taken at $h\nu$ = 33 eV at 12 K. Inset shows a magnified view of the near-E_F region.

measurements were carried out in an ARPES system with a base pressure of 5 × 10^{-9} Pa at Okayama University. The He I resonance line ($h\nu$ = 21.2 eV) was used as excitation light. We measured emission angle-dependent PES by rotating our sample with respect to the analyzer normal. The rotating direction is perpendicular to the analyzer slit. The energy resolution was set to 30 meV. In both measurements, the acceptance angle of the analyzer at ±15° along the [110] direction was used.

III. Results and Discussion

Figure 2 shows the valence band PES spectrum of the CrO_2 (001) film as a function of the BE at $h\nu$ = 33 eV. The Fermi level position was determined by measuring the Fermi edge of gold. Because the escape depth of photoelectrons with the kinetic energy of 33 eV is known to be in the range of 5–10 Å,[38] the spectrum includes electronic structures derived from electrons in a depth of 2–4 unit cells of CrO_2 (c = 2.915 Å) from the surface. The peak at 1.5 eV BE is primarily from the Cr 3d band, and the broad band located at 8–3 eV results from the O 2p band, consistent with a previous study using CrO_2 (100) epitaxial films prepared by the same CVD method.[20] A clear Fermi edge was also observed, as seen in the inset. These data indicate that at least the vicinity of the surface comparable to the escape depth of photoelectrons contains metallic states.

Next, we discuss the metallicity of the surface layer of the CrO_2 (001) film. Figure 3(a) shows the emission angle dependence of the PES spectra. The structure at 1 eV BE is owing to the bulk bands of CrO_2, as demonstrated by soft X-ray PES[32,33] and low-energy bulk-

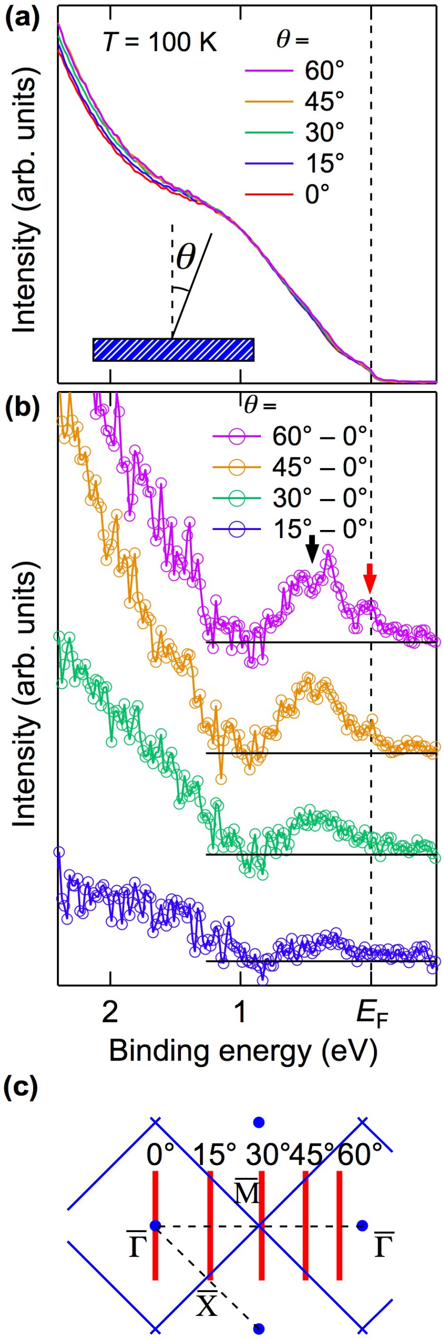

Fig. 3. **(a)** Emission angle dependence of PES spectra for a CrO_2 epitaxial film on TiO_2 (001) at 100 K measured by He I line (21.2 eV) over the angle range of 0°–60°. These spectra are normalized by the intensity at 1.0 eV BE, corresponding to the bulk electronic states. (b) The surface states of the CrO_2 (001) film determined from the difference between spectra acquired at 15°, 30°, 45°, and 60° and that acquired at 0°. Red and black arrows mark the significant structures (see text). (c) Brillouin zone of CrO_2 (001) surface (blue lines) and the detecting region of our emission angle-dependent PES measurements at each angle (red lines).

sensitive spin-resolved PES [11,12]. Therefore, the PES spectra in Fig. 3(a) are normalized by the intensity at 1 eV BE to emphasize the change in the spectral shape resulting from the existence of surface states. With increasing emission angle relative to the axis normal to the sample surface, the intensities in the energy region greater than 1.5 eV BE increased systematically. Part of this structure is attributed to the presence of Cr_2O_3 on top of the film because the energy position of Cr 3*d* bands in Cr_2O_3 is located at around 2 eV BE [29]. The existence of Cr_2O_3 may be in line with the amount of background in the LEED image shown in Fig. 1(b). Because the Cr 3*d* bands of Cr_2O_3 have a band gap more than 1 eV below E_F, the intensity variation near E_F is not caused by the existence of Cr_2O_3 and can be attributed to the (001) surface states. The difference spectra in Fig. 3(b), which were obtained by subtracting the normalized intensities of $\theta = 0^\circ$ from those of $\theta = 15^\circ$, 30°, 45°, and 60°, are shown to clarify the details of the surface states. The bulk sensitivity is the highest at $\theta = 0^\circ$ and the lowest at $\theta = 60^\circ$, so that subtracting the spectrum of $\theta = 0^\circ$ from the other spectra reduces the contribution of the bulk bands. In the difference spectra, it is clear that the difference intensity at 0.5 eV BE and E_F increases systematically with increasing emission angle. These structures can be attributed to the surface states of CrO_2 (001) because the structures are enhanced with increasing surface sensitivity. As the other possible origins of the emission-angle variation, there are following three effects: (i) angular dispersions of the energy distribution curves, (ii) tails of the surface contaminants extending toward E_F, and (iii) formation of faceted surfaces. Before assigning the two structures to the surface states, we discuss the contribution of these possible origins to our emission angle-dependent PES spectra.

First, we discuss spectral changes with increasing emission angle originating from band dispersions. One might wonder if the spectral change marked by a red arrow in Fig. 3(b) is due to observing an electron pocket somewhere in the Brillouin zone (BZ). If the spectral change was derived from the band dispersion, the intensity of the structure should be changed with the periodicity of the BZ of CrO_2(001) surface. In our angle-dependent spectra with various angles, although the photoelectron intensity at E_F is enhanced, the periodicity of the photoelectron intensity does not follow that expected from BZ of CrO_2(001) surface, as shown in Figs. 3(b) and 3(c). Furthermore, the peak position of a structure marked by a black arrow in Fig. 3(b) are also not changed within experimental accuracy, although the peak position should be changed with the BZ periodicity if the emergence of the structure is derived from band dispersion. Therefore, the contribution of the effect of band dispersion to the changes of the difference spectra can be negligible.

Second, we discuss the effects of the surface contaminations. We assume that the non-negligible secondary-electron-like background (BG) from the surface contaminants such as Cr_2O_3, which has no Fermi edge, exists just below E_F as shown in Figs. 4(a) and 4(b). Actually, this background has been observed by spin-resolved PES measurements.[13] With increasing θ, the BG is enhanced relative to the signals derived from the CrO_2 bulk state. Normalizing the simulated spectra, which include the BG and the metallic bulk state, by the intensity at 1 eV

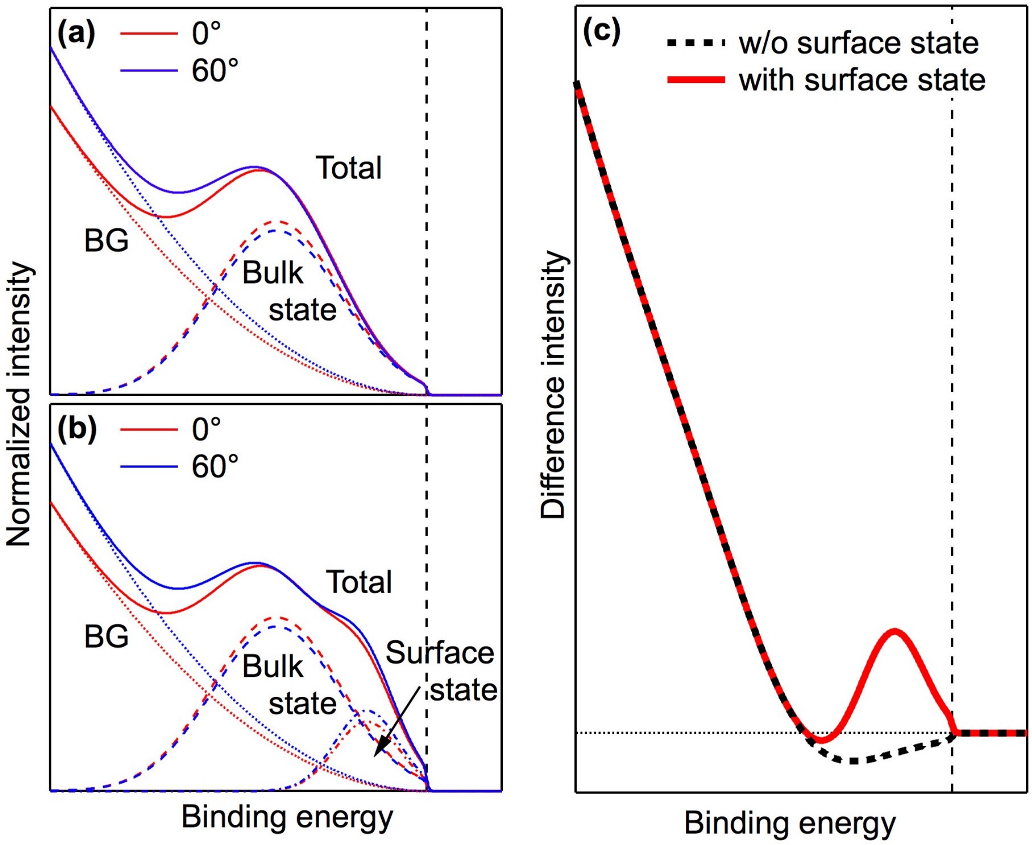

Fig. 4. **(a)** Simulated spectra at 0˚ and 60˚ in which it is assumed that there exist only bulk CrO_2 states and background from the surface contaminants as Cr_2O_3. **(b)** Similar to (a) but including a metallic surface state. **(c)** Difference spectra obtained by subtracting the spectrum at $\theta = 0˚$ from that at $\theta = 60˚$. Dashed black line and solid red line correspond to the situations in (a) and (b), respectively.

BE, the intensity of the metallic bulk state may be decreased relatively with increasing θ, as shown in Fig. 4(a). As a result, the difference spectrum is expected to show a negative Fermi edge and a negative structure in the energy region between 1 eV BE and E_F. This feature is inconsistent with that obtained by our measurements. Figure 4(b) shows simulated PES spectra including a surface state as well as a bulk state and BG. A red solid line shown in Fig. 4(c) represents the simulated difference spectra obtained by subtracting the simulated spectrum at $\theta = 0˚$ from that at $\theta = 60˚$. The line shape of the red solid line is closely in line with that of the experimental difference spectrum. Therefore, in order to reproduce our experimental results, there must be a structure located between 0.5 eV BE and E_F which enhance at the surface-sensitive configuration.

Third, we consider the possible influence from the faceted surface. A previous LEED study reported that faceted (0*n*1) and (*n*01) surfaces (where *n* is a rational number) were produced in CrO_2 (001) surfaces [37]. The LEED pattern in the previous study has the fourfold symmetry expected from its bulk crystal structure, with additional features derived from the faceted surfaces. A theoretical investigation shows that the surface energy of rutile-type TiO_2 (001), the same crystal structure as CrO_2, is higher than those of the (100) and (110) surfaces, supporting the formation of the faceted surfaces on CrO_2 (001) in the LEED study [24]. If such faceted surfaces exist, the sample surface would no longer be perpendicular to the [001] direction. However, in our LEED pattern shown in Fig. 1(b), such additional features do not appear, unlike the previous LEED study. This indicates that our CrO_2 (001) samples have few faceted surfaces, consistent with the monotonic variation of our PES spectra with respect to emission angle. Thus, we conclude that the surface sensitivity increases with increasing emission angle in our emission angle-dependent PES.

The difference between our LEED pattern and the previous one can be attributed to the methods of preparing samples and the cleaning procedures. Faceted surface structures were also reported in LEED studies of TiO_2 (001) [23,39–41]. In studies of TiO_2 (001), the area of the faceted surfaces depends on the cleaning procedure. For instance, faceted surfaces of TiO_2 (001) were partially produced after Ar^+ ion sputtering and annealing at 970 K for 5 min, although areas of unfaceted surface remained. After annealing at 1160 K for 5 min, the area with faceted surfaces increased [40]. Our CrO_2 (001) samples were prepared by the closed-system CVD method, in which a Cr_8O_{21} precursor and a TiO_2 substrate are vacuum encapsulated in a quartz tube and measured without any cleaning procedures, including sputtering or annealing, although the samples in Ref. 37 were prepared using a modified Ishibashi process under flowing oxygen in a chamber connected to a LEED-measurable chamber and measured *in situ*. Annealing at 390 °C in 2 mTorr O_2 for 30 min was found to restore the CrO_2 (001) surface to the faceted surface structure, indicating that formation of the faceted surface on CrO_2 (001) is also related to the annealing process. Therefore, our experimental procedures, without surface cleaning, seem to keep the unfaceted surface.

From the emission angle-dependent PES, we observed two surface states, at 0.5 eV BE and at E_F. The observation of the surface states at E_F indicates the metallic nature of the CrO_2 (001) surface. To further elucidate the electronic states of the (001) surface, we compared the surface states obtained from our PES measurements with those of band calculations [22,25]. Previous band calculations, assuming that oxygen atoms at the CrO_2 (001) surface are reconstructed into a tetrahedral arrangement, predict that surface bands constituted by e_g bands not crossing E_F are formed in the energy region between 0.7 eV and 0.2 eV BE, inconsistent with the metallic behavior observed by our measurements. However, a band calculation assuming that the oxygen atoms remain in an octahedral arrangement predicts a half-metallic band structure in the surface layer of CrO_2 (001) film [26]. Our PES results are more correspondent to the half-metallic band structure than the electronic structure of the reconstructed surface. The LEED pattern shown in Fig. 1(b) does not contain spots derived from the tetrahedral arrangement mentioned above, showing that the octahedral arrangement remains up to the surface of our sample. The consistency of our PES results and the band calculations in Ref. 26 suggests that the half-metallicity can be sustained up to the surface of the (001) film. However, we note that the band calculations in Ref. 26 cannot completely be in line with the surface states obtained in our PES measurements, in particular the structure at 0.5 eV BE. As a reason for the difference, the amount of electronic correlation U considered in the band calculation in Ref. 26 cannot be appropriate, although including of U is extremely valuable for understanding the electronic states of CrO_2 [11,32,42]. The spectral characteristics of our PES fit more closely with DOS calculated within LSDA+U method using $U = 3$ eV [43] rather than the bulk DOS in Ref. 26. Therefore, to understand the surface states of CrO_2 (001), advanced theoretical calculations of the surface states taking into account optimized U value are highly desired.

IV. Summary

We have investigated the surface metallicity of CrO_2 (001) epitaxial films by emission angle-dependent PES, which had been arduousness due to the surface contaminant. We observed the intensity increased at E_F for the measurements of surface-sensitive configurations, which is understood by considering the existence of the metallic surface electronic state. In addition, surface electronic states located at 0.5 eV BE were also observed. These are consistent with theoretical band structure assuming that the (001) surface is not reconstructed into a tetrahedral arrangement. This consistency indicates that the (001) surface sustains an octahedral arrangement of oxygen atoms around Cr atoms without reconstructions and consequently holds half-metallic electronic states up to the surface. Through the present PES study, we demonstrate that we can obtain information of CrO_2(001) surface by using samples prepared by the closed-system CVD method. Since PES cannot focus on the first layer, direct observations of the atomic arrangement and DOS by STM/STS are desired as a next-step investigation. The present work also suggests that the CrO_2 (001) films prepared by the CVD method are promising for application in spintronics devices.

Acknowledgments

The authors thank T. Fukura for valuable discussions, T. Fujii for XRD measurements, and A. Ino for ARPES data analysis program. Part of this work was supported by the Use-of- UVSOR Facility Program (BL7U, 2015) of the Institute for Molecular Science. This work was partially supported by the Program for Promoting the Enhancement of Research Universities and a Grant-in-Aid for Young Scientists (B) (No. 25800205) and for Japan Society for the Promotion of Science Fellows (No. 16J03208) from the Ministry of Education, Culture, Sports, Science and Technology of Japan. LEED measurements at HiSOR were conducted under the project (BL-5-14-A6).

References

[1] R. A. de Groot, F. M. Mueller, P. G. van Engen, and K. H. J. Buschow, Phys. Rev. Lett. **50**, 2024 (1983).

[2] M. I. Katsnelson, V. Yu. Irkhin, L. Chioncel, A. I. Lichtenstein, and R. A. de Groot, Rev. Mod. Phys. **80**, 315 (2008).

[3] I. Žutić, J. Fabian, and S. D. Sarma, Rev. Mod. Phys. **76**, 323 (2004).

[4] S. A. Wolf, D. D. Awschalom, R. A. Buhrman, J. M. Daughton, S. von Molnár, M. L. Roukes, A. Y. Chtchelkanova, D. M. Treger, Science **294**, 1488 (2001).

[5] M. Duckheim, and P. W. Brouwer, Phys. Rev. B **83**, 054513 (2011).

[6] S. B. Chung, H. -J. Zhang, X. -L. Qi, and S. -C. Zhang, Phys. Rev. B **84**, 060510(R) (2011).

[7] S. Mironov, and A. Buzdin, Phys. Rev. B **92**, 184506 (2015).

[8] K. Schwarz, J. Phys. F: Met. Phys. **16**, L211 (1986).

[9] R. J. Soulen Jr., J. M. Byers, M. S. Osofsky, B. Nadgorny, T. Ambrose, S. F. Cheng, P. R. Broussard, C. T. Tanaka, J. Nowak, J. S. Moodera, A. Barry, and J. M. D. Coey, Science **282**, 85 (1998).

[10] Y. Ji, F. Y. Yang, C. L. Chien, J. M. Byers, A. Anguelouch, G. Xiao, and A. Gupta, Phys. Rev. Lett. **86**, 5585 (2001).

[11] H. Fujiwara, M. Sunagawa, K. Terashima, T. Kittaka, T. Wakita, Y. Muraoka, and T. Yokoya, Appl. Phys. Lett. **106**, 202404 (2015).

[12] H. Fujiwara, M. Sunagawa, K. Terashima, T. Kittaka, T. Wakita, Y. Muraoka, and T. Yokoya, J. Electron Spectrosc. Relat. Phenom. **220**, 46 (2017).

[13] H. Fujiwara, K. Terashima, M. Sunagawa, Y. Yano, T. Nagayama, T. Fukura, F. Yoshii, Y. Matsuura, M. Ogata, T. Wakita, K. Yaji, A. Harasawa, K. Kuroda, S. Shin, K. Horiba, H. Kumigashira, Y. Muraoka, and T. Yokoya, Phys. Rev. Lett. **121**, 257201 (2018).

[14] B. L. Chamberland, Crit. Rev. Solid State Mater. Sci. **7**, 1 (1977).

[15] S. Sugahara, and M. Tanaka, Appl. Phys. Lett. **84**, 2307 (2004).

[16] A. Singh, S. Voltan, K. Lahabi, and J. Aarts, Phys. Rev. X **5**, 021019 (2015).

[17] A. M. Bratkovsky, Appl. Phys. Lett. **72**, 2334 (1998).

[18] A. Barry, J. M. D. Coey, and M. Viret, J. Phys. : Condens. Matter **12**, L173 (2000).

[19] A. Gupta, X. W. Li, and G. Xiao, Appl. Phys. Lett. **78**, 1894 (2001).

[20] K. Iwai, Y. Muraoka, T. Wakita, M. Hirai, T. Yokoya, Y. Kato, T. Muro, and Y. Tamenori, J. Appl. Phys. **108**, 043916 (2010).

[21] N. Nishimura, T. Hirai, A. Koganei, T. Ikeda, K. Okano, Y. Sekiguchi, and Y. Osada, J. Appl. Phys. **91**, 5246 (2002).

[22] F. Hong, and J. G. Che, Phys. Rev. Lett. **96**, 167206 (2006).

[23] U. Diebold, Surf. Sci. Rep. **48**, 53 (2009).

[24] H. Perron, C. Domain, J. Roques, R. Drot, E. Simoni, and H. Catalette, Theor. Chem. Acc. **117**, 565 (2007).

[25] X. Huang, X. H. Yan, Z. H. Zhu, Y. R. Yang, and Y. D. Guo, J. Appl. Phys. **109**, 064319 (2011).

[26] H. van Leuken, and R. A. de Groot, Phys. Rev. B **51**, 7176 (1995).

[27] T. Hasegawa, and K. Kitazawa, Jpn. J. Appl. Phys. **29**, L434 (1990).

[28] R. Cheng, B. Xu, C. N. Borca, A. Sokolov, C. -S. Yang, L. Yuan, S. -H. Liou, B. Doudin, and P. A. Dowben, Appl. Phys. Lett. **79**, 3122 (2001).

[29] C. A. Ventrice Jr., D. R. Borst, H. Geisler, J. van Ek, Y. B. Losovyj, P. S. Robbert, U. Diebold, J. A. Rodriguez, G. X. Miao, and A. Gupta, J. Phys.: Condens. Matter **19**, 315207 (2007).

[30] K. P. Kämper, W. Schmitt, G. Güntherodt, R. J. Gambino, and R. Ruf, Phys. Rev. Lett. **80**, 4181 (1987).

[31] Yu. S. Dedkov, M. Fonine, C. König, U. Rüdiger, G. Güntherodt, S. Senz, and D. Hesse, Appl. Phys. Lett. **80**, 4181 (2002).

[32] M. Sperlich, C. König, G. Güntherodt, A. Sekiyama, G. Funabashi, M. Tsunekawa, S. Imada, A. Shigemoto, K. Okada, A. Higashiya, M. Yabashi, K. Tamasaku, T. Ishikawa, V. Renken, T. Allmers, M. Donath, and S. Suga, Phys. Rev. B **87**, 235138 (2013).

[33] F. Bisti, V. A. Rogalev, M. Karolak, S. Paul, A. Gupta, T. Schmitt, G. Güntherodt, V. Eyert, G. Sangiovanni, G. Profeta, and V. N. Strocov, Phys. Rev. X **7**, 041067 (2017).

[34] W. A. Fraser, J. V. Florio, W. N. Delgass, and W. D. Robertson, Surf. Sci. **36**, 661 (1973).

[35] M. Pijolat, and G. Hollinger, Surf. Sci. **105**, 114 (1981).

[36] X. Zhang, X. Zhong, P. B. Visscher, P. R. LeClair, and A. Gupta, Appl. Phys. Lett. **102**, 162410 (2013).

[37] P. G. Ivanov, and K. M. Bussmann, J. Appl. Phys. **105**, 07B107 (2009).

[38] M. P. Seah, and W. A. Dench, Surf. Interface Anal. **1**, 2 (1979).

[39] L. E. Firment, Surf. Sci. **116**, 205 (1982).

[40] K. Fukui, R. Tero, and W. Iwasawa, Jpn. J. Appl. Phys. **40**, 4331 (2001).

[41] Y. Ikuma, H. Tajiri, K. Ishiguro, S. Anandan, K. Niwa, O. Sakata, and K. Nakata,

Transactions of the Materials Research Society of Japan **36**, 535 (2011).

[42] T. Tsujioka, T. Mizokawa, J. Okamoto, A. Fujimori, M. Nohara, H. Takagi, K. Yamaura, and M. Takano, Phys. Rev. B **56**, R15509 (1997).

[43] K. A. Korotin, V. I. Anisimov, D. I. Khomskii, and G. A. Sawatzky, Phys. Rev. Lett. **80**, 19 (1998).

APPENDIX B. LIST OF PUBLICATIONS AND CONFERENCES

Publications relevant to this thesis

1. "Spin-dependent electronic structure and correlation effects in "nearly" half-metallic ferromagnet CoS_2"
   H. Fujiwara, K. Terashima, T. Wakita, Y. Yano, W. Hosoda, N. Kataoka, N. Takemori, H. O. Jeschke, A. Teruya, M. Kakihana, M. Hedo, T. Nakama, Y. Ōnuki, K. Yaji, A. Harasawa, K. Kuroda, S. Shin, K. Horiba, H. Kumigashira, Y. Muraoka, and T. Yokoya
   In Preparation.

2. "Possible Surface Metallicity of CrO_2(001) Epitaxial Films Revealed by Emission Angle-Dependent Photoelectron Spectroscopy"
   H. Fujiwara, M. Sunagawa, T. Kittaka, T. Wakita, K. Terashima, T. Nagayama, M. Ogata, Y. Matsuura, F. Yoshii, S. Ideta, K. Tanaka, Y. Muraoka, and T. Yokoya
   Submitted.

3. "Origins of Thermal Spin Depolarization in Half-Metallic Ferromagnet CrO_2"
   H. Fujiwara, K. Terashima, M. Sunagawa, Y. Yano, T. Nagayama, T. Fukura, F. Yoshii, Y. Matsuura, M. Ogata, T. Wakita, K. Yaji, A. Harasawa, K. Kuroda, S. Shin, K. Horiba, H. Kumigashira, Y. Muraoka, and T. Yokoya
   Phys. Rev. Lett. **121**, 257201 (2018).

4. "Observation of intrinsic half-metallic behavior of CrO_2 (100) epitaxial films by bulk-sensitive spin-resolved PES"
   H. Fujiwara, M. Sunagawa, K. Terashima, T. Kittaka, T. Wakita, Y. Muraoka, and T. Yokoya
   J. Electron Spectrosc. Relat. Phenom. **220**, 46 (2017).

5. "Intrinsic spin polarized electronic structure of CrO_2 epitaxial film revealed by bulk-sensitive spin-resolved photoemission spectroscopy"
   H. Fujiwara, M. Sunagawa, K. Terashima, T. Kittaka, T. Wakita, Y. Muraoka, and T. Yokoya
   Appl. Phys. Lett. **106**, 202404 (2015).

Publications concerning other topics

1. "Direct observation of double valence-band extrema and anisotropic effective masses of the thermoelectric material SnSe"
   T. Nagayama, K. Terashima, T. Wakita, H. Fujiwara, T. Fukura, Y. Yano, K. Ono, H. Kumigashira, O. Ogiso, A. Yamashita, Y. Takano, H. Mori, H. Usui, M. Ochi, K. Kuroki, Y. Muraoka, and T. Yokoya
   Jpn. J. Appl. Phys. **57**, 010301 (2018).

2. "Evolution of the remnant Fermi-surface state in the lightly doped correlated spin-orbit insulator $Sr_{2-x}La_xIrO_4$"
   K. Terashima, M. Sunagawa, H. Fujiwara, T. Fukura, M. Fujii, K. Okada, K. Horigane, K. Kobayashi, R. Horie, J. Akimitsu, E. Golias, D. Marchenko, A. Varykhalov, N. L. Saini, T. Wakita, Y. Muraoka, and T. Yokoya
   Phys. Rev. B **96**, 041106 (2017).

3. "Unusual upper critical field behavior in Nb-doped bismuth selenides"
   K. Kobayashi, T. Ueno, H. Fujiwara, T. Yokoya, and J. Akimitsu
   Phys. Rev. B **95**, 180503(R) (2017).

4. "Ce 4f electronic states of $CeO_{1-x}F_xBiS_2$ studied by soft x-ray photoemission spectroscopy"
   T. Wakita, K. Terashima, T. Hamada, H. Fujiwara, M. Minohara, M. Kobayashi, K. Horiba, H. Kumigashira, G. Kutluk, M. Nagao, S. Watauchi, I. Tanaka, S. Demura, H. Okazaki, Y. Takano, Y. Mizuguchi, O. Miura, K. Okada, Y. Muraoka, and T. Yokoya
   Phys. Rev. B **95**, 085109 (2017).

5. "Observation of a Hidden Hole-Like Band Approaching the Fermi Level in K-Doped Iron Selenide Superconductor"
   M. Sunagawa, K. Terashima, T. Hamada, H. Fujiwara, T. Fukura, A. Takeda, M. Tanaka, H. Takeya, Y. Takano, M. Arita, K. Shimada, H. Namatame, M. Taniguchi, K. Suzuki, H. Usui, K. Kuroki, T. Wakita, Y. Muraoka, and T. Yokoya
   J. Phys. Soc. Jpn. **85**, 073704 (2016).

6. “Comparaive ARPES studied of $LaO_xF_{1-x}BiS_2$ (x=0.23 and 0.46)”
   K. Terashima, T. Wakita, M. Sunagawa, H. Fujiwara, T. Nagayama, K. Ono, H. Kumigashira, M. Nagao, S. Watauchi, I. Tanaka, H. Okazaki, Y. Takano, Y. Mizuguchi, H. Usui, K. Kuroki, Y. Muraoka, and T. Yokoya
   J. Phys: Conference Series **683**, 012002 (2016).

7. “Bulk sensitive angle-resolved photoelectron spectroscopy on $Nd(O,F)BiS_2$”
   K. Terashima, J. Sonoyama, M. Sunagawa, H. Fujiwara, T. Nagayama, T. Muro, M. Nagao, S. Watauchi, I. Tanaka, H. Okazaki, Y. Takano, Y. Mizuguchi, H. Usui, K. Suzuki, K. Kuroki, T. Wakita, Y. Muraoka, and T. Yokoya
   J. Phys: Conference Series **683**, 012003 (2016).

8. “Pressure-dependent magnetization and magnetoresistivity studies on tetragonal FeS (mackinawite): revealing its intrinsic metallic character”
   S. J. Denholme, H. Okazaki, S. Demura, K. Deguchi, M. Fujioka, T. Yamaguchi, H. Takeya, M. ElMassalami, H. Fujiwara, T. Wakita, T. Yokoya, and Y. Takano
   Sci. Technol. Adv. Mater. **15**, 055007 (2014).

Presentations relevant to this thesis

International Conferences

1. "Fundamental mechanisms of spin depolarization in half-metallic ferromagnet CrO_2 revealed by high-resolution spin-resolved photoemission spectroscopy"
   H. Fujiwara, K. Terashima, M. Sunagawa, Y. Yano, T. Nagayama, T. Fukura, F. Yoshii, Y. Matsuura, M. Ogata, T. Wakita, K. Yaji, A. Harasawa, K. Kuroda, S. Shin, Y. Muraoka, and T. Yokoya
   International Conference on Magnetism 2018, San Francisco, July 2018.

2. "Intrinsic electronic structure of high-quality CrO_2 epitaxial film prepared by a closed-system CVD method"
   H. Fujiwara (Invited)
   Energy Materials and Nanotechnology Meeting on Epitaxy 2018, Vienna, June 2018.

3. "Finite Temperature Effects in Half-metal CrO_2 Studied by Bulk-sensitive Spin-resolved Photoemission Spectroscopy"
   H. Fujiwara, M. Sunagawa, K. Terashima, T. Kittaka, M. Ogata, T. Wakita, Y. Muraoka, and T. Yokoya
   International Workshop on Superconductivity and Related Functional Materials 2016, Tsukuba, December 2016.

4. "Observation of Intrinsic Half-metallic Behavior of CrO_2 (100) Epitaxial Films by Bulk-sensitive Spin-resolved PES"
   H. Fujiwara, M. Sunagawa, K. Terashima, T. Kittaka, T. Wakita, Y. Muraoka, and T. Yokoya
   The 39th International conference on Vacuum Ultraviolet and X-ray Physics, Zürich, July 2016.

5. "Bulk sensitive spin- and angle-resolved photoemission spectroscopy of half-metallic ferromagnet CrO_2"
   H. Fujiwara, M. Sunagawa, T. Kittaka, K. Terashima, T. Wakita, Y. Muraoka, and T. Yokoya
   Ushimado International Workshop on Physics and Chemistry of Novel Superconductors and Related Materials, Okayama, November 2014.

Domestic Meetings

1. "Clarification of electronic structures of CoS_2 by high-resolution spin-resolved ARPES"
   H. Fujiwara, K. Terashima, T. Wakita, Y. Yano, W. Hosoda, N. Kataoka, A. Teruya, M. Kakihana, M. Hedo, T. Nakama, Y. Ōnuki, K. Yaji, A. Harasawa, K. Kuroda, S. Shin, K. Horiba, H. Kumigashira, Y. Muraoka, and T. Yokoya
   JPS 2018 Autumn Meeting, Doshisha University, September 2018.
   (*Student Presentation Award of the Physical Society of Japan, Division 5.*)

2. "Observation of electronic structure of half-metal candidate CoS_2 by high-resolution spin-resolved ARPES"
   H. Fujiwara, K. Terashima, T. Wakita, Y. Yano, W. Hosoda, N. Kataoka, A. Teruya, M. Kakihana, M. Hedo, T. Nakama, Y. Ōnuki, K. Yaji, A. Harasawa, K. Kuroda, S. Shin, K. Horiba, H. Kumigashira, Y. Muraoka, and T. Yokoya
   JPS 2018 Autumn Meeting, Doshisha University, September 2018.

3. "Origins of spin depolarization in half-metal CrO_2: High-resolution spin-resolved photoemission spectroscopy study"
   H. Fujiwara, K. Terashima, M. Sunagawa, Y. Yano, F. Yoshii, Y. Matsuura, M. Ogata, K. Yaji, A. Harasawa, K. Kuroda, S. Shin, T. Wakita, Y. Muraoka, and T. Yokoya
   The 65th JSAP Spring Meeting, Waseda University, March 2018.

4. "Observation of spin depolarization in half-metal CrO_2 by high resolution spin-resolved photoemission spectroscopy"
   H. Fujiwara, K. Terashima, M. Sunagawa, Y. Yano, M. Ogata, K. Yaji, A. Harasawa, S. Shin, T. Wakita, Y. Muraoka, and T. Yokoya
   JPS 2017 Autumn Meeting, Iwate University, September 2017.

5. "Observation spin depolarization due to thermal fluctuation in half-metal CrO_2: High-resolution spin-resolved PES"
   H. Fujiwara, M. Sunagawa, K. Terashima, M. Ogata, K. Yaji, A. Harasawa, S. Shin, T. Wakita, Y. Muraoka, and T. Yokoya
   JPS 2017 Spring Meeting, Osaka University, March 2017.

6. "Intrinsic half-metallicity of CrO_2 revealed by bulk-sensitive spin-resolved photoemission spectroscopy"
   H. Fujiwara, M. Sungawa, K. Terashima, T. Kittaka M. Ogata, T. Wakita, Y. Muraoka, and T. Yokoya
   The 77th JSAP Autumn Meeting, Toki Messe (Niigata), September 2016.

7. "Observation of metallic surface states on CrO_2 (001) films by depth-resolved photoemission spectroscopy"
   H. Fujiwara, M. Sunagawa, T. Kittaka, T. Wakita, K. Terashima, T. Nagayama, M. Ogata, Y. Matsuura, F. Yoshii, S. Ideta, K. Tanaka, Y. Muraoka, and T. Yokoya
   The 77th JSAP Autumn Meeting, Toki Messe (Niigata), September 2016.

8. "Intrinsic half-metallic electronic states of CrO_2: Bulk-sensitive spin-resolved photoemission spectroscopy"
   H. Fujiwara, M. Sungawa, K. Terashima, T. Kittaka, M. Ogata, T. Wakita, Y. Muraoka, and T. Yokoya
   Annual Meeting of Chugoku-Shikoku chapter of JSAP 2016, Okayama, July 2016.
   (*Incentive Award of the 21th JSAP Fall Meeting*)

9. "Surface metallicity of half-metal CrO_2 (001) films"
   H. Fujiwara, M. Sunagawa, K. Terashima, T. Nagayama, T. Kittaka, M. Ogata, S. Ideta, K. Tanaka, T. Wakita, Y. Muraoka, and T. Yokoya
   JPS 2016 Spring Meeting, Tohoku Gakuin University, March 2016.

10. "Half-metallicity of CrO_2 revealed by bulk-sensitive spin-resolved photoemission spectroscopy"
   H. Fujiwara, M. Sunagawa, K. Terashima, T. Kittaka, M. Ogata, T. Wakita, Y. Muraoka, and T. Yokoya
   JCS West Japan Chemistry Forum 2015, Okayama University, November 2015.

11. "Intrinsic electronic states of ferromagnetic metal CrO_2 revealed by bulk-sensitive spin-resolved photoemission spectroscopy"
   H. Fujiwara, M. Sunagawa, K. Terashima, T. Kittaka, M. Ogata, T. Wakita, Y. Muraoka, and T. Yokoya
   JPS 2015 Autumn Meeting, Kansai University, September 2015.

12. "Bulk sensitive spin-resolved photoemission spectroscopy of half-metallic ferromagnet CrO_2 II"
   H. Fujiwara, M. Sunagawa, T. Kittaka, M. Ogata, K. Terashima, T. Wakita, Y. Muraoka, and T. Yokoya
   JPS 2015 Spring Meeting, Waseda University, March 2015.

13. "Bulk sensitive spin-resolved photoemission spectroscopy of half-metallic ferromagnet CrO_2"
   H. Fujiwara, M. Sunagawa, T. Kittaka, K. Terashima, T. Wakita, Y. Muraoka, and T. Yokoya
   JPS 2014 Autumn Meeting, Chubu University, September 2014.